Characterization of calcium signals generated by activation of the two excitatory synaptic inputs in Purkinje neurons

Karima Ait Ouares

Communauté
UNIVERSITÉ Grenoble Alpes

THÈSE

Pour obtenir le grade de

DOCTEUR DE LA COMMUNAUTE UNIVERSITE GRENOBLE ALPES

Spécialité : **Physique pour les sciences du vivant**

Arrêté ministériel : 25 mai 2016

Présentée par

Karima AIT OUARES

Thèse dirigée par **Marco CANEPARI, CR Inserm,** Université Grenoble Alpes et CNRS UMR 5588

Préparée au sein du **Laboratoire Interdisciplinaire de Physique** dans **l'École Doctorale de Physique de Grenoble**

Caractérisation des signaux calciques générés par l'activation des deux voies synaptiques excitatrices des neurones de Purkinje

Thèse soutenue publiquement le **11 Avril 2019** ,
devant le jury composé de :

Mr Boris, BARBOUR
DR CNRS – ENS Paris, Rapporteur
Mr Philippe, LORY
DR CNRS – IGF Montpellier, Rapporteur
Mme, Micaela, GALANTE
MC – Université Paris Sud, Membre
Mme, Cécile, DELACOUR
CR CNRS – Institut Néel Grenoble, Membre
Mr, Claude, VERDIER
DR CNRS – LIPhy Grenoble, Président

I would like to express my immense gratitude to all those who have made this thesis possible.

Firstly, I would like to thank my supervisor Marco Canepari for giving me the opportunity to further my academic career. Thank you for your infinite patience and confidence.

I would like to thank "MOTIV" team for welcoming me and for allowing me to be part of the team.

Finally, I owe my deepest gratitude to my family and my friends. There are no words that can describe all the support that you have given me.

Contents

Abstract (English)

In the cerebellum, the interplay between PFs and CF inputs generates supralinear Ca^{2+} signals that provide the information on their concomitant occurrence. These phenomena trigger both short- and long-term depression at PF-PN synapses associated with motor learning and coordination, i.e. the primary functions of the cerebellum. While activation of PFs elicits local Ca^{2+} transients that are confined to activated spines, the activation of the CF generates a large depolarization that spreads passively into the dendrites. The CF-mediated transient dendritic depolarization, not localized, plays a fundamental role in dendritic integration and in regulating local PF signals and their plasticity at distal sites. The study carried out in my thesis addressed two crucial questions of this problem: the dendritic ion channels activated by the CF-mediated dendritic depolarization at different initial V_m and the mechanisms underlying dendritic supralinear Ca^{2+} signals associated with concomitant PF and CF activity. The results reported here were obtained using recent optical methods of V_m imaging and ultrafast Ca^{2+} imaging with low affinity Ca^{2+} and high affinity Ca^{2+} indicators combined with pharmacological analysis.

During the first part of my work, I characterized the behavior of the dendritic Ca^{2+} and K^+ channels activated by CF-EPSPs at different initial dendritic V_m, using optical measurements of V_m and Ca^{2+} transients. We found that two different sets of ion channels are selectively activated at different states. When the dendrite is hyperpolarized, CF-EPSPs mainly activate T-type voltage-gated Ca^{2+} channels (VGCCs), SK channels and A-type voltage-gated Ca^{2+} channels (VGKCs) that limit the transient V_m below ~0 mV. When in contrast the dendrite is depolarized, T-type VGCCs and A-type VGKCs are inactivated and CF-EPSPs activate P/Q-type VGCCs, high-voltage activated VGKCs and BK channels, initiating Ca^{2+} spikes. We demonstrated that A-type VGKCs play a crucial role in controlling the second set of

channels. Indeed, these channels limit the activation of P/Q-type VGCCs and associated K^+ channels, preventing Ca^{2+} spikes.

During the second part of my work, we demonstrated that the concomitant activation of PF and CF triggers two different types of supralinear Ca^{2+} signals. The activation of one or the other path depends on the delay between the activation of the two inputs which is the crucial discriminator of the mechanisms involved in the generation of supralinear Ca^{2+} signals. We found that when CF-EPSPs occur near the end of a burst of PFs, the associated supralinear Ca^{2+} transients are independent of the activation of mGluR1 and are produced by a combined effect of two mechanisms: the increased Ca^{2+} influx through P/Q-type VGCCs enabled by PF-depolarization inactivating A-type VGKCs; and the transient saturation of endogenous Ca^{2+} buffers during the PF-EPSP burst amplifying free Ca^{2+} concentration. When CF-EPSPs occur at longer delays after the end of the PF burst, the associated supralinear Ca^{2+} transients are mGluR1-dependent and do not involve the mechanisms underlying the generation of mGluR1-independent supralinear Ca^{2+} transients. Instead, an entirely different mechanism is recruited. We found that, the supralinear Ca^{2+} transients were correlated with an increase in mGluR1-dependent Ca^{2+} influx via the slow mGluR1-activated cation conductance.

The results reported here advance our understanding of the generation of supralinear Ca^{2+} transients associated with the concomitant PF and CF activity with respect to the potential molecular mechanisms that are involved. Nevertheless, we were not able to provide a definitive answer on the nature of the Ca^{2+} influx mediating mGluR1-depedent supralinear Ca^{2+} signals. This issue must be further explored in future experiments.

Abstract (French)

Dans le cervelet, l'interaction entre l'activité des fibres parallèles (FPs) et celle de la fibre grimpante (FG), les deux principaux inputs excitateurs des neurones de Purkinje (NPs), engendre des signaux calciques supra-linéaires procurant des informations sur leur activité concomitante. Ce phénomène déclenche des mécanismes synaptiques qui induisent la dépression à court- ou à long-terme des synapses FP-NPs. L'activation des FPs génère des signaux calciques locaux confinés aux épines activées tandis que l'activation de la FG génère une dépolarisation qui se propage passivement dans les dendrites. Cette dépolarisation transitoire qui n'est pas locale joue un rôle important dans la régulation de la signalisation locale des FPs et leur plasticité. L'étude menée durant ma thèse s'est focalisée sur deux principaux points : les canaux dendritiques des NPs activés par la dépolarisation transitoire générée par l'activation de la FG et les mécanismes responsables de la génération des signaux dendritiques supra-linéaires associés à l'activité concomitante des FPs et de la FG. Les résultats reportés ici ont été obtenus en utilisant des méthodes optiques récemment développés.

Nous avons caractérisé le comportement des canaux ioniques dendritiques qui sont activés par la dépolarisation dendritique générés par l'activation de la FG. Nous avons découvert que deux différents groupes de canaux ioniques sont sélectivement activés selon le potentiel membranaire initial. En effet, quand les dendrites sont hyperpolarisées, les CF-EPSPs activent principalement des canaux calciques voltage-dépendant (CCVDs) de type T, des canaux SK et des canaux potassiques voltage-dépendant (CPVDs) de type A. Ces derniers maintiennent le potentiel membranaire en dessous de ~0 mV. En revanche, quand les dendrites sont dépolarisées, les CCVDs de type T et les CPVDs de type A s'inactivent complètement et les CF-EPSPs activent des CCVDs de type P/Q, des CPVDs et des canaux BK. L'activation de cet ensemble de canaux déclenche des spikes calciques. Notamment, nous avons établi l'importance des CPVDs de type A dans le control du

deuxième ensemble de canaux. En effet, ils limitent l'activation des CCVDs de type P/Q et les canaux potassiques associés empêchant le déclenchement des spikes calciques.

Nous avons démontré que l'activation occurrente de la FG et des FPs induit deux différents types de signaux calciques supra-linéaires. L'induction de l'un ou de l'autre dépend du temps entre l'activation des deux inputs, qui est aussi un principal déterminant des mécanismes impliqués dans la génération des ces signaux calciques. Nous avons trouvé que quand les CF-EPSPs se produisent à de courts délais après la fin du burst des FPs, les signaux calciques supra-linéaires associés sont indépendant de l'activation des mGluR1 et sont générés par l'effet combiné de deux mécanismes : l'augmentation du flux calcique via les CCVDs de type P/Q activés par la dépolarisation membranaire médiée par l'activation de FPs inactivant les CPVDs de type A; et la saturation transitoire des buffers calciques endogènes durant le burst des PF-EPSPs amplifiant les concentrations du Ca^{2+} libre. Quand les CF-EPSPs se produisent à de longs délais après la fin du burst des PF-EPSPs, les signaux calciques supra-linéaires associés dépendent de l'activation des mGluR1 et n'impliquent aucun des mécanismes précédents. Dans ce cas, nous avons démontré que les signaux calciques supra-linéaires sont corrélés avec l'augmentation du flux calcique via les conductances cationiques associées à l'activation des mGluR1.

Les résultats reportés ici ont avancé notre compréhension sur la génération des signaux calciques supra-linéaires associés à l'activité concomitante des PFs et de la FGs ainsi les mécanismes qui y sont impliqués. Néanmoins, nous n'avons pas pu procurer une réponse définitive sur la nature du flux calcique médiant les signaux calciques supra-linéaires dépendant de l'activation des mGluR1s.

Chapter 1:

Introduction

1.1 The cerebellum, its anatomy and its circuitry

1.1.1 Brief overview on historical studies of the cerebellum

The seminal progress in understanding the anatomy of the cerebellum and its function was the result of decades of standard anatomical, physiological, and pathological research. By the end of the eighteenth century, accurate anatomical description of the cerebellum has been established and hypothesis about its function have begun to emerge. First experimental evidences regarding cerebellar function from animals and patients have been provided during the nineteenth century. Luigi Rolando (1773–1831) showed that animals with cerebellar lesions exhibited essentially impairment in motor function but no evident alterations in vital or cognitive function. He thereby assigned to the cerebellum the role of movement initiation (Rolando, 1809). Pierre Flourens (1794-1867) noted that animals, after cerebellum ablation, were not completely paralyzed but rather displayed alterations in movement regularity and coordination. He further demonstrated that recovery from cerebellar damage was possible (Flournes, 1824). Together, Luigi Rolando and Pierre Flourens proposed the principle of “the cerebellum working as a whole”.

A further advance in elucidating cerebellar function came from Luigi Luciani (1840-1919) who, using more improved techniques, characterized motor dysfunction symptoms following total or partial cerebellectomy. He described them as muscular weakness, lack of muscular tone and defective stability of the muscular contractions and further classified them in a triad of symptoms namely atonia, asthenia, and astasia, which are still used nowadays for clinical diagnosis in cerebellar impairment (Luciani, 1891). Joseph Babinski (1857-1932) further detailed cerebellar lesions symptoms by identifying deficits in rapid and complex movement sequence (Babinski, 1902). He recognized dysmetria as a unique characteristic sign of cerebellar diseases. Thereafter, Gordon Holmes (1876-1965) made use of the experimental observations and conclusions of Luciani and produced important clinical observation

from patients with cerebellar tumors and soldiers wounded during the First World War that confirmed the general functional alterations resulting from cerebellar lesions (Holmes, 1917). He noted that many of these patients displayed voluntary tremors and diskinesia leading to the identification of the concept of ataxia.

The early twentieth century was marked by the initial cerebellar network characterization and the emergence of a new theory stating the existence of functional localization within the cerebellar cortex. The concept of function-structure relationship was based on precise comparative anatomical observations. Lodewijk Bolk (1866-1930) compared the cerebellum of several mammals, identified and characterized four principal regions in the cerebellum namely anterior and posterior vermis and the two hemispheres (Bolk, 1906). Particularly, his work emphasized a sagittal continuity of the cerebellar cortex within the folia chains of the vermis and hemispheres, and a transverse continuity between vermis and hemispheres that is maintained by the parallel fibers (PFs). He pioneered the first single somatotopic map on the surface of the cerebellum on the basis of a careful phylogenetic comparison and made the assumption that proximal muscles are controlled by the vermis whereas distal ones are controlled by the hemispheres. The concept of single somatotopic map was contradicted by the work of Edgar Adrian (1889-1977) who characterized two somatotopic maps, in the anterior lobe and in the paramedian lobule (Adrian 1943). Bolk also contributed to the cerebellar nomenclature. Olof Larsell (1886-1964) expanded the numbering scheme for the vermis initially developed by Bolk and subdivided the vermis into ten lobules (Larsell, 1952).

The major advancement towards the characterization of the cellular organization and the connectivity within the cerebellar network arise from the histological analysis carried out in the middle to late of the nineteenth century. The new discoveries have driven subsequent work that shed light on some of the functional aspects of the cerebellar network which have been interpreted within a motor control viewpoint. Jan Evangelista Purkinje (1787-1869) described for the first

time the large neurons in the cerebellar cortex which bear his name and reported his work in a paper published in 1838 (Purkinje, 1838). Back then, the lack of better methods for tissues fixing and staining slowed down the progress in histological study of the cerebellum. In 1873, Camillo Golgi (1843-1926) developed selective silver staining of nervous tissues and described the whole cerebellar network which was presented in a work published in 1874 entitled “on the fine anatomy of human cerebellum” (Golgi, 1874). He made basic assumptions on cell connectivity and function. Santiago Ramon y Cajal (1852–1934), by refining Golgi staining methods, extended the histological analysis of the cerebellar network and provided an ultimate picture of its cellular organization characterizing the morphological feature and the connections of each neuronal type and proposed a diagram of neuronal pathways. He described the two fundamental afferents to the cerebellar cortex: the mossy fiber and the climbing fiber (CF). He studied in particular cerebellar glomeruli, which he described as vacuolar dendritic cytoplasmatic islands containing granule cells dendrites, Golgi cell axons and mossy fibers rosettes (terminals). Moreover, he described the deep cerebellar nuclei and the inferior olive and their fundamental relationships with the Purkinje neurons (Ramón y Cajal, 1888, 1889a,b).

Later in the 20th century, there has been a new era in cerebellar physiology research. Steps ahead occurred in the 1960 and 1970 through the development of electron microscopy and microelectrode recording which allowed morphological analysis and electrophysiological studies to be achieved. The seminal work performed by John Eccles (1903-1997) using electrophysiological recording yielded to the identification of the excitatory and inhibitory nature of each cell type of the cerebellar cortex (Eccles et *al.*, 1967). Janos Szentágothai (1912-1994), using silver impregnation method to detect degenerating fiber, demonstrated that the CF originates solely in the inferior olive (Szentágothai and Rajkovitz, 1959). Masao Ito (1928-2018) demonstrated that Purkinje neurons (PNs) are the sole output from the cerebellar cortex and their projections are inhibitory contrasting the dogma that neurons with long axons are excitatory (Ito, 1984). These studies led to the discovery

that all other neurons in the cerebellar cortex are inhibitory except granule cells and to the conclusion that the cerebellum serves as an inhibitory loop controlling the deep cerebellar nuclei, in which excitatory information are transmitted to PNs through the mossy fiber–granule cell–PF pathway and the inferior olive–CF pathway (Ito, 1982). David Marr (1945-1980) presented a very powerful model of cerebellar function (Marr, 1969) which was further expanded by the engineer James Albus (1935-2011), by studying extensively the structural organization of PNs and their inputs and outputs connectivity within the cerebellar cortex, provided an original description of the modular organization in the cellular connectivity and characterized the functional somatotopie of the modular information processing which challenged the principal of "the cerebellum working as a whole" (Albus, 1971).

The classical functional theory of the cerebellar function assigns a role to the CF input as a supervising teacher implying that CF input carries instructive signals that calibrate PNs electrical response which mediate the adaptive modification in motor learning (Marr, 1969; Albus, 1971; Ito, 1978). In fact, CF input carries information about the activity of interneuron in the spine and brainstem providing information about error movement. Thus, they initiate mechanisms that weaken the strength of PN response to PF input. Ito (Ito, 1982) was the first who demonstrated that a coincident CF and PF inputs onto PN induces long-term depression (LTD) of the PF synapse that underlie motor learning. At present, the associative learning mechanisms based on concomitant PFs and CF activity are still under investigation and the work presented in this thesis addresses this issue.

1.1.2 The anatomy of the cerebellum

Understanding cerebellar functions relies primarily on understanding its anatomical organization and connectivity. The cerebellum is a distinct subregion of the vertebrate brain and the word cerebellum comes from the Latin “little brain”. It is situated at the caudal part just above the brainstem. It is an intricate uniform multi-foliated structure which serves as an important part of the vertebrate motor system and has been implicated in higher cognitive function (Thach *et al.,* 1992; Schmahmann, 2000). The cerebellum has conserved its basic structural and functional organization through evolution although it differs across all mammalian species in term of size and shape (Sultan and Glickstein, 2007; Butler and Hodos, 2005). Although it constitutes only 10 % of the total brain weight, it comprises roughly half of all the neurons in the brain (Lange, 1975; Herculano-Houzel, 2010). The cerebellar circuitry is highly stereotyped, uniformly arranged throughout the entire structure and sensorimotor information is processed in a similar way. Yet the cerebellum is highly compartmentalized into anatomically distinct and functionally specialized regions (Groenewegen *et al.,* 1979; Voogd *et al.*, 1981, Buckner *et al.,* 2011; Lu *et al.*, 2007).

The cerebellum (see Figure 1.1) consists of two principal structures: a folded layer of cortex (gray matter) and the deep cerebellar nuclei located within the white matter situated underneath the cortex. Commonly, the cerebellar cortex has a central structure, the vermis, extending along the anteroposterior axis surrounded by two hemispheres that extend on the caudal and rostral side which are further divided into an intermediate (paravermis) and lateral hemispheres (Glickstein *et al.*, 2011). On the anteroposterior axis, the cerebellar surface is divided by numerous curved transverse fissures which give it a laminated appearance. The main fissures split the cerebellum into three lobs. While the primary fissure on the dorsal surface separates the anterior

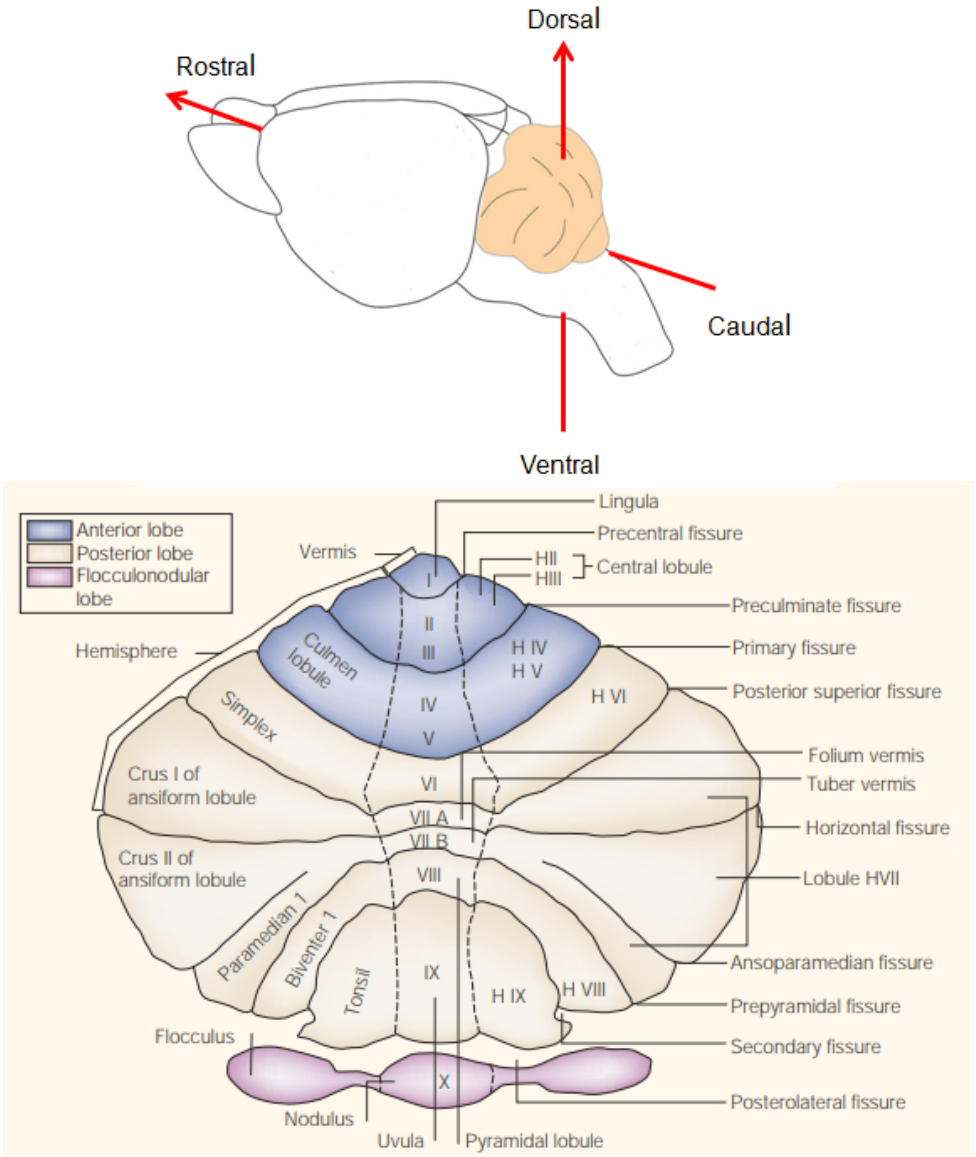

NATURE REVIEWS | NEUROSCIENCE VOLUME 5 | MARCH 2004 | 241

Figure 1.1: Anatomy of the cerebellum

Top, positioning of the cerebellum in the mouse brain and representation of rostro-caudal and ventro-dorsal axis.

Bottom, anatomical organization of the cerebellum illustrating the central vermis and the lateral hemispheres. The primary fissures devide the cerebellum into anterior and posterior lobes. The posterolateral fissure separates the flocculonodular lobe. Shallower fissures divide the anterior and posterior lobes into ten lobules.

and posterior lobes, the posterolateral fissure on the ventral surface fissure separates the flocculonodular lobe from the posterior lobe (Armstrong *et al.*, 1973). These regions are further subdivided by finer fissures into 10 individually named lobules each composed of shallow folds, folia (Larsell, 1937; 1952). The vermis and the hemispheres receive different afferents and give rise to different efferents which represent the different functional subdivisions (Brodal, 1954; Groenewegen and Voogd, 1977; Groenewegen *et al.*, 1979; Voogd *et al.*, 1981). The white matter of the cerebellum is formed by afferents and efferents nerve fibers and contains three pairs of deep nuclei namely the dentate (lateral), the interposed (itself composed of two nuclei, the globose and emboliform), and the fastigial (medial) nuclei with each cerebellar nucleus has characteristic efferent targets. There is a specific pattern of innervations between the cerebellar cortex and deep cerebellar nuclei. The most lateral parts of the cerebellar cortex are connected to the lateral nucleus; the intermediate parts are connected to the interposed nucleus and the most medial parts are connected to the medial nucleus (see Figure 1.2)

1.1.3 The functional organization of the cerebellum

On functional basis, the cerebellum has three major subdivisions (see Figure 1.2) depending on its afferent/afferent connections and phylogeny (Gravel and Hawkes, 1990; Groenewegen and Voogd, 1977; Groenewegen *et al.*, 1979; Voogd and Glickstein, 1998).

The vestibulocerebellum or flocculonodular lobe of the cerebellum is phylogenically the oldest part of the cerebellum. It receives the largest amount of its input directly from the vestibular apparatus and from the visual system. Thus its function is restricted to only control equilibrium and eye movements (vestibular reflexes). Its output from PNs projects back to the lateral vestibular nuclei without passing the deep cerebellar nuclei forming a closed loop (Gerrits *et al.*, 1985).

The spinocerebellum (paleocerebellum) comprises mainly the vermis and the medial part of the two hemispheres (paravermis) (lobules I–V of the vermis), so named because it receives extensive inputs form the spinal cord. It receives mainly visual, auditory and vestibular information. PNs in the vermis project to the fastigial nucleus, and those in the intermediate zone project to the interposed nucleus. Both nuclei include projection to the cortical and brainstem regions. Its primary task consists of regulating body and limb movement. In fact, it continuously monitors movement and provides feedback signals to control muscle tone and adjust ongoing movements (Coffman *et al.*, 2011).

The pontocerebellum (Cerebrocerebellum) is the largest part of the cerebellar cortex and consists of the lateral part of hemispheres. It receives the vast majority of its input from the cerebral cortex through the pons nuclei. The pontine nuclei project exclusively through the middle cerebellar peduncles to the cerebellum, where these axons terminate as mossy fibers. PNs in the cerebrocerebellum project back to the dentate nucleus and via the thalamus to the premotor cerebral cortex and to additional regions of the cerebral cortex. It is principally involved in higher cognitive function (visiospatial perception and modulation of emotion), motor control such as planning, initiation, and timing of movements (Watson, 2014; Wattand and Mihailoff, 1983; Grodd *et al.*, 2001).

Remarkably, the fundamental function of the cerebellum are accomplished by the vermis which is the primitive part seen in many species whereas the lateral hemispheres which are relatively large in mammals particularly in humans are implicated in more sophisticated functions such as cognition and emotion. The increase in the size of these parts paralleled the evolution of cerebellar cortex and reflects the importance of cerebrocerebellar afferents and efferents in cerebellar function (Grodd *et al.*, 2001).

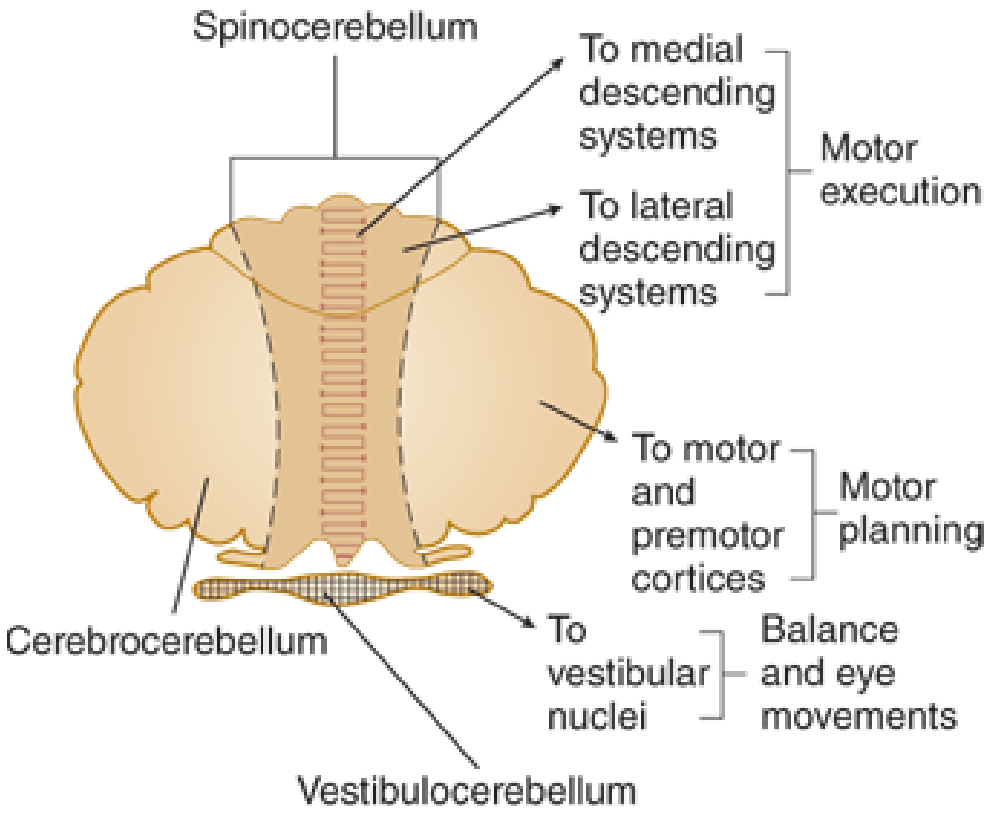

Figure 1.2 Functional division of the cerebellum

Representation of the three functional divisions of the cerebellum (the vestibulocerebellum, the spinocerebellum, and the cerebrocerebellum) with their outputs

Source: Kim E Barrett; Susan M Barman; Scott Boitano; Heddwen Brooks Ganong's Review of Medical Physiology 25th Edition.

1.1.4 The layers of the cerebellar cortex

Histologically, the cerebellar cortex is uniformly arranged in three layers (see Figure 1.3) named essentially after the principal cell body of the neurons they comprise (Ghez and Thach, 2000, Apps and Garwicz, 2005). They are classified from the outer side to the deeper side:

The molecular layer consists mainly of the dendritic arborization of PNs, parallel fibers which are the axons of the granule cells crossing perpendicularly the flat tree, some CF terminals and the cell bodies of stellate and basket cell interneurons.

The Purkinje cell layer consists exclusively of the soma of PNs surrounded by somata of Bergmann glia.

The granular layer consists of large number of densely packed somata of granule cells receiving from mossy fibers terminals on their dendrites in the cerebellar glomeruli and different types of interneurons.

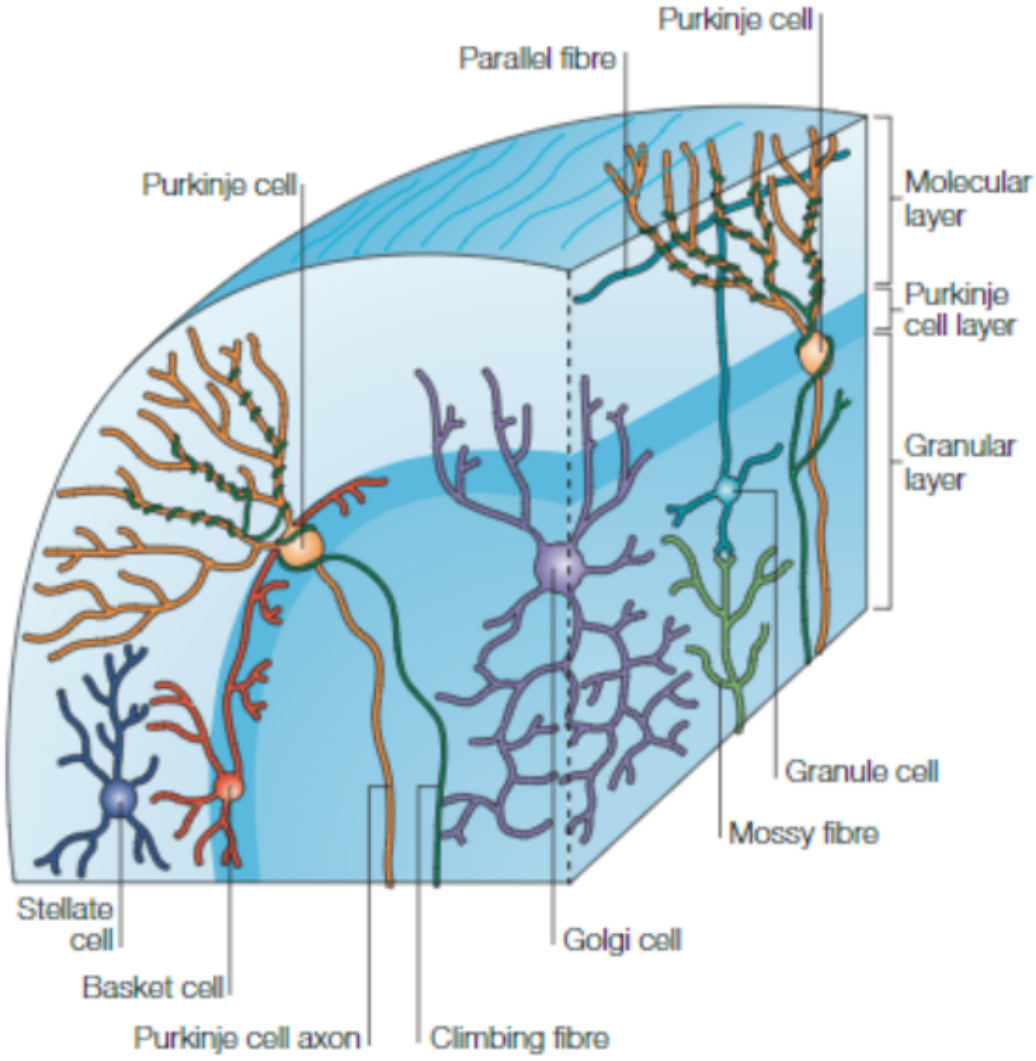

NATURE REVIEWS | NEUROSCIENCE VOLUME 6 | APRIL 2005 | 297

Figure 1.3 Layers and cell types of the cerebellar cortex

1.1.5 The excitatory circuitry of the cerebellar cortex

Sensorinformation are supplied to the cerebellar cortex via two distinct types of afferents: directly from olivocerebellar CFs and indirectly from mossy fiber via granular neurons, whose axons are the parallel fibers. The CF and PF inputs form excitatory synapses on the dendrites of PNs. The final inhibitory output of PNs is modulated by the GABAergic inhibitory interneurons. Only excitatory pathways to granule cells and PNs are further discussed.

Olivocerebellar climbing fiber afferent

CFs were discovered and described for the first time by Ramon y Cajal, 1911 using the Golgi impregnation technique. They arise solely from neurons in the inferior olive nucleus situated in the medulla of the brain stem which receives sensory and motor information from several structure mainly the spinal cord, the midbrain and the cerebral cortex (Szenthgothai Rajkovits, 1959; Eccles, 1967; Llinas and Sasaki, 1989). The axons of the CF, moderately thin and myelinated, enter the cerebellum, penetrate through the granular layer and finally terminate on the molecular layer where they make extensive synaptic contacts with the proximal dendrites of PNs, while don't make contact with distal dendrites. The term "climbing fiber" refers to the manner that these fibers make connections on the dendritic tree. CFs connect in a uniform way with the cerebellar cortex forming the olivocerebellar projections which are remarkably characterized by highly specific pattern of innervations that underlie the modular organization of the cerebellar cortex. In fact, a group of neurons of a given nucleus in the inferior olive project their fibers topographically into a narrow parasagittaly aligned band of PNs. These fibers give off collaterals that also project topographically to neurons located in a specific area in the deep cerebellar nuclei. Neurons of that area receive their afferents from the same zone of Purkinje neurons contacted by the fibers from the same inferior olive neurons (Andersson and Oscarsson, 1978). These connections form a topographically organized olivo-cortico-

nuclear closed loop in which sets of PNs may exert control on their own CF afferents. The olivo-cerebellar organization reflects a consistency in the way information is processed in the cerebellar cortex. CF inputs make contact with PNs in different lobules of the cerebellum (Voogd and Ruigrok, 2004).

In early stages of development, PNs are transiently innervated by several CFs. As the cerebellar cortex matures, the number diminishes and the adult Purkinje neuron is contacted by only one single CF. While one CF appears to innervate roughly one to ten PNs, each PNs receives substantial synaptic connections from one single CF. Indeed, one CF makes 500 hundreds synaptic contact with the proximal part of dendritic tree with high release probability (Harvey and Napper, 1991). This extensive connection is reflected by the powerful excitatory synaptic action of CFs on PNs. At the time of the pioneering studies by Eccles, the CF was referred as the most powerful and specific excitatory synapse yet discovered in the mammalian central nervous system (Eccles *et al.*, 1966). CF collaterals also innervate the molecular layer inhibitory interneurons and their activation modulates the frequency and the rhythmicity of PNs simple spikes discharge (Dizon and Khodakhah, 2011). Indeed, in vitro, repetitive stimulation of CF and the subsequent spillover of glutamate may activate interneurons (Szapiro and Barbour, 2007) which in turn cause short or long pauses in the simple spikes leading to progress reduction and ultimately to a net inhibition of PNs (Dizon and Khodakhah, 2011).

The olivo-cerebellar connections are one of the most conserved cerebellar circuitry through evolution of the vertebrate nervous system reflecting the prominent role of CF inputs in a number of theories regarding the cerebellar motor learning and coordination. CF input triggers the complex spike; regulates PN spontaneous and evoked firing pattern and synaptic plasticity. Over the last decade, considerable amount of research has been dedicated to shed light on the CF functions, yet some of the theory regarding CF function are still controversial and under heated debate.

Mossy fibers

In contrast to CF input, mossy fibers originate from many sources namely from neurons located within the brainstem, the spinal cord and from sensory peripheral nerves. They are myelinated and reach the cerebellar cortex crossing the cerebellum rostrally and terminate in the granular layer where they project mostly bilaterally and form glutamatergic synapses on dendrites of several granule cells forming cerebellar glomeruli.

Granule cells are the smallest and the most abundant neurons in the cerebellar cortex. They are glutamaergic neurons and they have 3 to 5 short dendrites that terminate in the glomeruli. Each dendrite receives excitatory input from mossy fiber terminals through only four to five excitatory synapses (Eccles *et al.*, 1967; Chadderton et *al.*, 2004).

Ascending and parallel Fibers

The thin unmyelinated axons of granule cells originating from either their cell body or more often from one of their dendrites, ascend through the PN layer to the molecular layer where they bifurcate giving rise to parallel fiber that richly synapse with dendrites of PN. They may synapse with PNs before bifurcating and in this cases synapses are referred as “ascending fibres”. The activity in the granule layer directly modulates the electrical activity of PN or indirectly through molecular layer interneurons which inhibit the activity of PNs (Dizon and Khodakhah, 2011). Indeed, each granule cell collect and sample information from different input from mossy fiber and associated them in a pattern that will be only discriminated later by PNs (Chadderton *et al.*, 2004). The ascending axons of granule protrude along the medio-lateral axis of the molecular layer perpendicularly bifurcating later in T-shape manner giving rise to two PF branches. From the point of bifurcation, the tow branches extend for a couple of millimeters (2-3 mm) across the transverse plan of

the cerebellar cortex innervating several hundred of PN at the same time. The number of PFs that cross the dendrite and makes contact with a single PN was estimated to be roughly 200 000 in rodents (Napper and Harvey, 1991).

1.1.6 Purkinje neurons

Purkinje neurons were described for the first time as an oval objects by Johannes Evangeliste Purkinje in a paper on the histology of the nervous system presented in Prague in 1837. Their characteristic morphology was further described by Ramón y Cajal in 1911 by refining Golgi's techniques. PNs are the central neurons of the cerebellum as they serve as a fundamental processing and integrating unit. They are the largest neurons and have a very distinctive morphology characterized by a wide soma, long axons and extensively branched dendritic trees. Their cell bodies line up in a single row all over the cerebellar cortex forming a distinct monolayer of several millions of cells situated between the molecular layer and the granular layer. Their elaborate dendritic tree, oriented in the anteroposterior axis, is flat and extends outward into the molecular layer. It is divided into one or less often two primary branches which then are divided into secondary, tertiary and quaternary thin branchelets. Proximal parts of the dendritic tree are relatively smooth and receive CF projections. Distal parts are covered by spines (Spiny branchlets) and receive synapses from the terminals of parallel fibers. Several inhibitory neurons form synapse with PNs, in particular stellate and basket cells contact PNs in the dendrites.

PNs are GABAergic neurons and form the sole output of the cerebellar cortex. Hence, they are the final step of information processing in the cerebellar cortex (Ito, 1984). Both excitatory and inhibitory neurons modulate the electrical properties of PNs and contribute to shaping the final output which is relayed to cerebellar and vestibular nuclei. PNs send inhibitory signals through their myelinated axons that penetrate through the granular layer and continue into the white matter to terminate in the cerebellar and vestibular nuclei. On average, one PN projects to 30–50

different cerebellar nuclei cells and one cerebellar nuclei cell is innervated by 20–30 different PNs (Chan-Palay, 1977). In turn, the deep cerebellar and the vestibular nuclei project to motor area in the cerebral cortex and the brain stem (Rand, 1954; Sastry *et al.*, 1997). PNs are cells that were studied in this thesis and their properties are introduced in the next paragraph.

1.2 Properties of Purkinje neurons

Currently, a considerable amount of information describing PN electrical responsiveness is available. This was obtained from electrophysiological and morphological studies later integrated into reliable computational models. One of the most striking features of PNs is their large highly branched dendritic tree and their intrinsic passive properties that mostly shape both the spontaneous firing and the responsiveness following the activation of excitatory inputs. Additionally, the complex electrical responsiveness of PN relies on a variety of ion channels expressed at the soma and dendrites, their differential distribution and their biophysical properties. The contribution of these ions channels to shaping the electrical properties of PN is well documented. All these characteristics confer PNs the ability to fire high frequency Na^{+} spikes in the axon and Ca^{2+} spikes in the dendrites.

1.2.1 Passive properties of Purkinje neurons

The propagation and summation of subthreshold synaptic potentials are mainly determined by the passive membrane properties. The fundamental biophysical parameters, such as membrane resistances and the capacitance, underlie passive membrane properties (Roth and Hausser, 2001). Several factors influence these parameters. In PNs, with development, the dendritic tree increases in surface and becomes progressively more branched. Adult PNs are characterized by a phenomenal ramification in their dendrites generating a large number of dendritic terminals and high spines densities (McKay and Turner, 2005). The distribution of ion channels across the somatodendritic axis is not uniform determining a spatial pattern of membrane resistance (Vetter *et al.*, 2001).

The remarkable dendritic tree of PNs determines the electrical propagation of membrane potentials (Roth and Hausser, 2001). Indeed, when potentials spread from the soma to the dendrites, the thick proximal dendrites allow static potentials to be distributed uniformly in the entire neuron (Stuart and Hausser, 1994). This is a very important concept since it has permitted the calibration of voltage-sensitive dyes imaging experiments reported in Chapter 3. Furthermore, the high resistance of thin dendrites and the high branching density generates considerable attenuation in the fast voltage changes while spreading from the soma into the dendrites (Rapp *et al.*, 1994; Roth and Hausser, 2001). In the other direction (from the dendrites to the soma), the absence of a long primary dendrite, such as in pyramidal neurons of the brain, limits the attenuation and provides a faithful transfer of synaptic information to the soma. Notably, EPSPs from thinner dendrites are larger at the site of origin because of the larger local impedance, but they attenuate more with respect to those from thicker dendrites (Roth and Hausser, 2001).

The propagation of active events is also disfavored. At ramification point, because the surface is bigger and the capacitance is larger, the change in voltage is slowed and attenuated thus is not capable to reach thresholds required for sustained spike generation (Goldstein and Rail, 1974; Vetter *et al*., 2001). Consequently, Na^+ spikes generated in the axons are poorly and passively spread into the dendrites (Stuart and Hausser, 1994; Vetter *et al.*, 2001). This concept is relevant for the protocols used in the experiments reported in Chapter 3. On the other hand, transient potential generated by dendritic inputs are affected by these factors and are expected to attenuate even more significantly. PF-EPSPs generated in the spiny dendrites considerably attenuate while propagating to the soma (Roth and Hciusser, 2001), and brief action potentials in the dendrites don't forward propagate to the soma (Vetter *et al.*, 2001). For this reason voltage-sensitive imaging experiments are crucial to reveal the dynamics of membrane potential in the dendrites.

1.2.2 Active properties in the soma and axon of Purkinje neurons

Voltage-dependent sodium channels (Nav) drive the large, inward currents that underlie fast action potentials in neurons. Presently, ten voltages gated sodium channels (Nav1.1–1.9, Nax) have been identified in the mammalian brain (Catterall, 2000; Goldin, 2001). These channels display differences in developmental pattern expression, level of abundance and subcellular localization throughout the brain (Felts *et al.*, 1997; Trimmer & Rhodes, 2004). Cerebellar PNs express high level of Nav1.6 and Nav1.1 channels, although some Nav1.2 are also found (Felts et *al.,* 1997; Vega-Saenz de Miera *et al.*, 1997; Shah *et al.*, 2001; Schaller and Caldwell, 2003; Kalume *et al.*, 2007). The sodium currents measured in dissociated Purkinje cell somata display three main components. A large transient current characterized by rapid activation and inactivation, a resurgent current generated following depolarizing inactivating step, and a persistent non inactivating current. The subthreshold resurgent and persistent currents contribute to generating spontaneous action potentials (Raman and Bean, 1997, 1999, 2001; Khaliq *et al.*, 2003; de Ruiter et *al.*, 2006; Fry, 2006).

The resurgent current, a brief sodium current and initially identified in cerebellar PNs (Raman and Bean, 1997, 1999), is unique in that it activates after strong depolarization when the membrane is repolarized. This current is due to a recovery of sodium channels from inactivation proceeding through open states (Raman and Bean, 2001). The resurgence mechanism underlying this current accelerates return of membrane potential to the threshold level after an action potential immediately depolarizing the cell again which generates the typical high frequency firing of PNs (Raman and Bean 1997; Khaliq *et al.*, 2003). Furthermore, voltage clamp of dissociated Purkinje somata to an action potential train demonstrated that the major inward current flowing between spikes is the resurgent current with a minor contribution of the persistent current (Raman and Bean, 1997, 1999; Fry, 2006).

Nav1.6 channels, highly expressed in PNs, are particularly important because they are localized at the initial segments of axons where action potentials are initiated (Waxman and Quick, 1978; Kaplan *et al.* 2001; Royeck *et al.* 2008; Hu *et al.* 2009). NaV1.6 channels play a major role in conducting subthreshold sodium currents in Purkinje neurons. They are the main source, but not exclusive, of resurgent current and contribute also to the generation of the persistent current (Kay et *al.*, 1998; Raman and Bean, 2001; Fry, 2006). The Nav1.6-mediated subthreshold current play a prominent role in both spontaneous peacemaking and the generation of high frequency spontaneous action potential in Purkinje cells which are important processes in motor coordination (Raman *et al.*, 1997; Taddese & Bean, 2002; Khaliq *et al.*, 2003; Martina *et al.*, 2003; Chen et *al.*, 2008). Indeed, in mice lacking Nav1.6 channels expression, the resurgent current was drastically diminished preventing spontaneous firing (Kohrman *et al.*, 1996a; Raman *et al.*, 1997; Khaliq *et al.*, 2003; Levin *et al.*, 2006). Nevertheless, the persistent current was only slightly reduced suggesting that this current is carried by other Nav channels. Moreover, these animals exhibited alterations in limb coordination and motor reflexes (Raman *et al.*, 1997; Kalume *et al.*, 2007). On the other hand, knockout of Nav1.1 reduced sodium currents but did not affect the characteristics of resurgent current and only slowed spontaneous spiking (Kalume *et al.*, 2007).

In cerebellar PNs, sodium channels expression are essentially restricted to the axon and soma, yet dendrites display some level of expression (Llinás and Sugimori, 1980a, b; Stuart & Hausser, 1994). The membrane properties of PNs disfavor the propagation of Na^+ action potentials which greatly diminish in amplitude and time course while spreading into the dendrite (Stuart & Hausser, 1994; Vetter *et al.*, 2001). Furthermore, the complex spikes generated in the soma by CF activation are maintained in the dendrite after sodium current reduction via the compensatory balance of currents mediated by the activation of VGCCs (Llinás and Sugimori, 1980a, b; Swensen and Bean, 2003).

Most of the electrophysiological studies conducted in order to study PNs emphasize the uniqueness of their electrical responsiveness and the importance of their firing pattern in shaping the sole output of the cerebellar cortex onto deep cerebellar nuclei and in cerebellum functions. PNs are capable of firing spontaneous actions potentials.

PNs fire spontaneous action potentials in the *in vitro* slice preparation (Llinas and Sugimori, 1980a, b; Hounsgaard and Midtgaard, 1988; Hausser and Clark, 1997) and in vivo (Granit and Phillips, 1956; Eccles *et al.*, 1966; Thach, 1967; Armstrong and Rawson, 1979). The firing pattern of PNs varies depending on whether the recording is performed in slice preparation or in vivo. In both cases, the action potential are very sharp (0.2 ms) and characterized by fast rising (reaching ~0 mV) at physiological temperature. They are mediated by TTX sensitive sodium channels (Llinas and Sugimori, 1980a, b). These action potentials can occur in tonic (high frequency) mode and occasionally in burst mode with silent periods. In tonic mode, PNs fire 'simple spike' action potentials at high frequency (~50 kHz) *in vivo*. The same rate of firing has been observed in different preparations including cultured PNs, acute cerebellar slices and isolated soma of PN even synaptic inputs have been blocked indicating that the process of simple spike generation in this case relies on the intrinsic excitability of PNs (Llinas and Sugimori, 1980a, b; Hausser and Clark, 1997). In the *in vitro* slice preparation, the spontaneous firing occurs at fixed rate, whereas *in vivo* the spike firing becomes highly irregular at rest and during the execution of movement. This indicates that the irregularity is controlled by the activity of excitatory and inhibitory inputs (Llinas and Sugimori, 1980a, b; Hausser and Clark, 1997).

The intrinsically generated simple spike firing of PNs is essentially driven by a variety of conductances active at subthreshold membrane (Llinas and Sugimori, 1980a, b; Edgerton and Reinhart, 2003; Swensen and Bean, 2003; McKay and Turner, 2004; Womack and Khodakhah, 2004). A major conductance is Nav, highly

expressed in the soma that opens briefly during repolarization and allow the membrane to depolarize immediately ensuring the spontaneous firing of PNs (Raman and Bean, 1997; Afshari *et al.*, 2004; Aman and Raman, 2007). Notably, the resurgent current cooperates with Kv3.3 current in promoting the high frequency firing. The fast activation and deactivation kinetics of Kv3 channels support this fact. Additionally, genetic deletion of Kv3.3 channels considerably reduced the rate of spontaneous action potential firing (Akemann and Knöpfel, 2006). The hyperpolarization-activated I_h current involved in the restoration of the resting membrane potential also plays an important role in the control of tonic firing of PNs. In fact, this current maintains a membrane potential in a range that favors the activation of resurgent current responsible for the generation of spontaneous actions potentials (Williams *et al.*, 2002).

Other channels modulating firing properties are low threshold T-type voltage-gated Ca^{2+} channels (VGCCs), mainly expressed in the dendrites and spines, but that still contribute to the regulation of the frequency of firing. Their activation may drive the membrane potential up to levels required for sodium channels activation and subsequent spike generation. P/Q-type VGCCs, also highly expressed in the dendrites, contribute to the spontaneous firing precision and rate (Mark *et al.*, 2011). Calcium influx through P/Q- and T-type channels activates Ca^{2+} activated K^+ channels that are highly involved in the regulation of PN spontaneous firing (Edgerton and Reinhart, 2003).

Beside the high basal rate of spontaneous firing, PNs display an intrinsic firing bistability that can be evoked spontaneously or after modulation of intrinsic conductances. In vitro experiment, PNs are able to alternate between up-states characterized by high-frequency firing rate (depolarized states) and down-states characterized by long pauses of firing (hyperpolarized sates) (Llinas and Sugimori, 1980; Williams *et al.*, 2002). Subsequent experimental and modeling studies have identified several factors that governs the transition from UP to DOWN states

including inhibitory interneuron (Oldfield *et al.*, 2010), excitatory input climbing fibers (Loewenstein *et al.*, 2005; Yartsev *et al.*, 2009) and by brief depolarizing and hyperpolarizing current steps. Upregulation and downregulation of firing rates provides bidirectional inhibitory control of PN target neurons in deep cerebellar nuclei. Sensory-evoked CF inputs serve as a toggle switch inducing Up- Down-state transitions. It has been suggested that this phenomenon has a key role short-term processing and storage of sensorimotor information in the cerebellar cortex (Lowenstein *et al.*, 2005). Additionally, Bergmann glia modulate PNs intrinsic excitability by regulating K^+ concentration through Ca^{2+} -dependent K^+ uptake mechanisms (Wang *et al.*, 2012).

1.2.3 Active properties of Purkinje neuron dendrites.

Dendrites of PNs express P/Q-type Ca^{2+} channels that are high-voltage activated VGCCs. The activation of these channels above their threshold gives rise to depolarizing events with similar kinetics of Na^+ action potentials. Thus, PN dendrites can be classified as excitable membranes generating "Ca^{2+} spikes". In addition, the spread of these events from the site of generation is controlled by BK Ca^{2+}-activated K^+ channels. Dendritic spikes can be produced by PF inputs and can trigger bursts of somatic action potentials, but silenced spontaneous somatic action potentials after a burst (Rancz and Hausser, 2010). Thus, it appears that PF-evoked spikes can transform into a transient temporal code for concomitant PF inputs, while providing a negative feedback for the frequency code mediated by sparse and continuous PF inputs. Dendritic spikes can be also produced by the large dendritic depolarization mediated by the CF input (Chan *et al.*, 1989). The study reported in Chapter 3 addresses in detail the channels underlying dendritic Ca^{2+} spikes triggered by a CF-EPSP. Thus, in the next paragraphs, we address the properties of the ion channels involved in this signal.

1.3 Ion channels of cerebellar Purkinje neurons

Ion channels are complex proteins that conduct the movement of ion from one side to the other side of a membrane leading to transient changes in local concentrations and electrical potential across the membrane. They play an important role in diverse physiological processes. PNs are richly endowed with such ion conductances as demonstrated by immunohistochimical and electrophysiological studies. The non-uniform distribution of these conductances across the dendro-somatic axis is greatly responsible for the differential electrical responsiveness and functional properties of PNs. Dendrites of PNs express high levels of Ca^{2+} and K^{+} channels and very low levels of Na^{+} channels. The activation and the synergistic interplay among these channels play a crucial role in determining the electrical properties of PNs in both spontaneous and evoked firing and are involved in transmission and integration processes at synaptic inputs levels contributing to shape the final output of PNs. Using electrophysiological, imaging techniques and specific pharmacological tools, the contribution of each channel to the overall electrical behavior of PNs has been the main interest of several studies for decades.

1.3.1 Fundamentals of Voltage Gated Calcium channels (VGCCs)

VGCCs channels are multisubunit membrane proteins, characterized by biophysical, pharmacological and functional properties that vary from one type to another. The first biochemical purification of VGCCs from skeletal muscle (Catteral, 2000) revealed that functional VGCCs are complex proteins consisting of five subunits (α1, β, $\alpha_2\delta$ and γ) encoded by multiple genes (Tanabe *et al.*, 1987).

The α1 subunit: is the pore subunit as its expression alone is enough to form a functional channel. It accounts primarly for the diversity of VGCCs channels as it carries most channel biophysical, modulation and pharmacological properties**.** The protein sequence of the α1 subunit has ~2000 amino acids residues which are

arranged in four homologous hydrophobic distinct domains (I, II, III and IV). Each of the four domains comprises six putative membrane spanning segments (S1-S6). The segment four, in each domain, acts as voltage sensor and contains five to six regularly arranged, positively charged amino acids forming part of the voltage sensing domain which is a key element in determining the voltage sensitive gating of the channels. The linker between segments 5-6 in each domain form the channel pore and contribute to the selectivity of the channel to Ca^{2+}. Ten genes encoding for the different α1 subunits have been characterized in mammals. Based on their sequence homology, their biophysical properties and functional roles, these 10 isoforms are assigned to three families namely Cav1, Cav2 and Cav3. Cav1 channels conduct L-type currents, Cav2.1, Cav2.2 and Cav2.3 of the Cav2 channels conduct P/Q-, N-, and R-type calcium currents, respectively (Olivera *et al.*, 1994) and Cav3 channels (Cav3.1, Cav3.3 and Cav3.3) conduct T-type currents (Nowycky *et al.*, 1985). Based on the membrane threshold of their activation, theses families are further classified into two majors groups: High Voltage Activated (HVA, Cav1 and Cav2) and Low Voltage Activated (LVA, Cav3) VGCCs (Tsien *et al.*, 1987; Randall and Tsien, 1995; Ertel *et al.*, 2000; Catterall, 2000; Pietrobon, 2002; Catterall *et al.*, 2005).

The auxiliary subunits: The classical auxiliary subunits comprise the β subunits (β1, β2, β3 and β4), the extracellular $\alpha_2\delta$ subunit ($\alpha_2\delta$ -1, -2, -3, -4), and in skeletal muscle an integral membrane protein, the γ subunit. The combination and the dynamic interaction between the α1 subunit and the auxiliary subunits modulate the preexistent biophysical properties and further enhance the molecular and functional diversity of the VGCCs. The auxiliary subunits are crucial for VGCC function, their trafficking and assembly. They are regulated by different protein kinases.

1.3.2 HVA-VGCCs in Purkinje neuron dendrites

In PNs, soma highly expresses Na^+ channels which underlie the generation of the somatic actions potentials whereas VGCCs channels are barely detectable. Conversely, as the dendrites express very low level of Na^+ channels, the dendritic excitability is principally determined by HVA-VGCCs channels. In fact, several techniques mainly immunohistochemistry, electrophysiology and Ca^{2+} imaging have revealed that VGCCs are highly enriched in dendrites of PNs and constitute one of the main source of Ca^{2+} influx (Usowicz *et al.*, 1992; Mouginot *et al.*, 1997; Raman & Bean, 1999; Isope & Murphy, 2005; Indriati *et al.*, 2013). They are the primary contributor to synaptic Ca^{2+} signaling pathways coupling electrical activity with Ca^{2+} influx and play crucial roles in intrinsic membrane properties, firing pattern, synaptic transmission and dendritic integration at the somatodendritic axis.

The large majority of HVA-VGCCs in PN dendrites are P/Q-type (Llinás *et al.*, 1989; Usowicz *et al.*, 1992; Raman & Bean, 1999; Regan *et al.*, 1991). These channels have a prominent role in the control of neurotransmitter release from presynaptic terminals, those expressed at postsynaptic site are essentially involved in the generation of dendritic spike. They contribute to synaptic transmission, integration and synaptic plasticity (Catterall *et al.*, 2005). They are insensitive to DHPs and ω-CgTx but are potentially blocked by ω-Aga IVA, a toxin isolated from the venom of the funnel web spider *Agelenopsis aperta* (Llinas *et al.*, 1989; Mintz *et al.*, 1992). They display distinct kinetic, pharmacological, and modulatory properties (Bourinet *et al.*, 1999). P and Q- type channels display trivial differences in the pharmacological and the electrophysiological properties.

An early study on dendritic excitability assumed that dendrites express a high density of channels with P-type like properties (Llinas & Sugimori, 1980) where they were initially identified. Interestingly, it has been shown that P/Q channels co- cluster with Ca^{2+} activated K^+ channels in dendritic nanodomains in PNs (Hillman et *al.,*

1991; Womack *et al.*, 2004; Indriati *et al.*, 2013). They contribute to control the firing pattern of PNs and are essentially required for sustained spontaneous bursting. They underlie Ca^{2+} spike generation in response to CF activation or strong PF activation that is implicated in endocannabinoid release and short-term synaptic plasticity (Tank *et al.*, 1988; Davie *et al.*, 2008; Rancz and Häusser, 2006).

The requirement of P/Q channels in normal function of PNs and synaptic plasticity has been investigated in mice lacking functional P/Q channels. Indeed, ataxic mice models (Rolling-Nagoya, tottering, Rocker and Leaner), all carrying mutations in the gene encoding α1A subunit of P/Q-type Ca^{2+} channels, displayed aberrant motor behavior and common impaired cerebellar functions namely irregularity and reduction of the electrical responsiveness of PNs, considerable decrease in the density of Ca^{2+} currents causing reduction in synaptic transmission at PF-CF synapse, imbalance between PF and CF inputs to PNs and enhanced inhibitory transmission (Matsushita *et al.*, 2002; Zhou *et al.*, 2003; Kodama *et al.*, 2006; Liu and Friel, 2008). Furthermore, P/Q-type Ca^{2+} channels play an important role at early stages of postnatal development and competitive synaptic wiring which was supported by the observation that genetic deletion or mutation in the α1A subunit of P/Q channels was further associated with abnormal arborization of PN dendrites, aberrant CF multiple innervations and regression of CF territory to the proximal part of PNs dendrites (Miyazaki *et al.*, 2004; Kodama *et al.*, 2006; Hashimoto *et al.*, 2011).

Other HVA-VGCCs types have been shown to be expressed in PNs but at very low densities (Regan, 1991; Mintz *et al.*, 1992; Raman and Bean, 1999). R-type Ca^{2+} channels (Cav2.3 isoform) has been shown to be expressed in PNs but its functional role has not been yet elucidated (Yokoyama *et al.*, 1995). L-type Ca^{2+} channels (Cav1.2 and Cav1.3) appear to be expressed at early stage of development and their level decreases during PNs maturation (Raman and Bean 1999; Liljelund *et al.*, 2000) in contrast to pyramidal neurons where they are highly expressed (Markram *et al.*, 1995).

1.3.3 LVA-VGCCs in Purkinje neuron dendrites

Electrophysiological recording and immunecytochemistry experiments have shown that dendrites of PNs express low threshold T-type channels which plays an important role in synaptic transmission, integration and the induction of synaptic plasticity (Bossu *et al.*, 1989; Mouginot *et al.*, 1997; Talley *et al.*, 1999; Isope & Murphy 2005; Isope *et al.*, 2012; Ly *et al.*, 2013).Three Cav3 T-type channel subunits have been identified with unique biophysical and pharmacological properties: Cav3.1, Cav3.2 and Cav3.3 (Perez-Reyes, 2003). Immunofluorescence and electron microscopy have further demonstrated that T- type channels are highly concentrated in dendritic spines of PF synapses (Hildebrand *et al.*, 2009) and that all the three T-type Ca^{2+} channels isoforms are expressed in PNs, displaying differential subcellular localization (McKay *et al.*, 2006; Hildebrand *et al.*, 2009). Pharmacologically, Mibefridil was the first generation of antagonist to be characterized for T-type Ca^{2+} channels (Zamponi *et al.*, 1996). More selective molecules namely ML218 and NNC550396) were recently characterized as highly selective T-type channels blockers (Huang *et al.*, 2004; Xiang *et al.*, 2011) and thus were used in the experiments presented in Chapter 3.

Specific biophysical properties allow T-type VGCCs to being activated in response to subthreshold membrane potentials. They are implicated in the control of interspike and interburst intervals during spontaneous burst firing in Purkinje cells (Pouille *et al.*, 2000; Womack and Khodakhah, 2004). They are also involved in both PF and CF mediated electrical reponse (Cavelier *et al.*, 2008; Ly *et al.*, 2016) more specifically in the generation of low threshold Ca^{2+} spike upon PF stimulation that might boost P/Q-type dependent Ca^{2+} spikes generation (Cavalier *et al.*, 2002; Isope & Murphy, 2005). Remarkably, it has been reported that at PF-PN synapses, T-type Ca^{2+} channels (Cav3.1 isoform) and mGluR1 are co-localized in spines and are functionally coupled. Indeed, the activation of mGluR1 potentiates Ca^{2+} transients meditated by T-type Ca^{2+} channels (Hildebrand *et al.*, 2009). Furthermore, they are functionally and

structurally coupled with BK channels to reduce synaptically evoked neural firing (Womack *et al.*, 2004; Engbers *et al.*, 2013; Turner and Zamponi, 2014). T-type Ca^{2+} channels activated by repetitive PF stimulation provides at least a part of Ca^{2+} influx required for LTP induction (Ly *et al.*, 2016). However, the block of T-type Ca^{2+} channels does not alter the induction of LTD and in contrast to P/Q-type channels; they play a minor role in motor coordination and learning.

While P/Q-type and T-type Ca^{2+} channels are responsible for up to 95% of the total Ca^{2+} currents in PNs (Usowicz *et al.*, 1992; Isope & Murphy, 2005; Isope *et al.*, 2010), other VGCCs types may be responsible for the remaining 5% of the total Ca^{2+} current (Regan, 1991; Mintz *et al.*, 1992; Raman & Bean, 1999).

1.3.4 Voltage-activated K^+ channels in Purkinje neuron dendrites

Potassium channels drive an outward current that cooperate with inward currents to shape the firing pattern of neurons. Activation of K^+ channels tends to drive membrane potential toward its resting state, thus regulating neuronal excitability (Latorre *et al.*, 1989; Vergara *et al.,* 1998; Coetzee *et al.,* 1999).

K^+ channels are the largest and the most diverse group of mammalian channels in term of structure and function. They are involved in a myriad of neuronal functions and in fact the specific role fulfilled by each channel is determined by their biophysical properties as well as their subcellular localization and molecular interaction. K^+ channels exist as multi-subunits formed by the coassembly of the principal α subunits with a variable number of auxiliary subunits. The principal α subunit is a transmembrane polypeptide that contains the selective pore and it is necessary to form a functional channel. Based on the membrane topology of their principal subunits, K^+ channels are subdivided into three groups. “Inward rectifiers” have two transmembrane domains and one pore, “leak” channels have four transmembrane domains and two pores and “voltage-activated” and “Ca^{2+}-activated”

K^+ channels have 6 transmembrane domains and one pore (Patel and Honoré, 2001). Each of the three groups is further subdivided into subgroups. Additionally, the association of the principal α subunit with auxiliary subunits yields to the immense diversity in their intrinsic functional and biophysical properties as well as the pattern of expression, the subcellular distribution and modulation (Moczydlowski *et al.*, 1988; Rudy, 1988; Jan and Jan, 2012). PNs dendrites express high densities of voltage-gated K^+ channels (VGKCs) which further restrict the spread of membrane depolarization into distal dendrites. K^+ channels in proximal dendrites can be activated by depolarization generated by the passive spread of action potentials and by the activation of the CF (Martina *et al.*, 2003). As for VGCCs, VGKCs can be divided into HVA and LVA and PN dendrites express both. Among HVA-VGKCs, Kv3.3 are highly expressed in PN dendrites (Goldman-Wohl *et al.*, 1994), and these channels are known to regulate dendritic Ca^{2+} spikes (Zagha *et al.*, 2010; Veys *et al.*, 2013).

The transient A-type potassium current that activates at subthreshold membrane potential and inactivates within tens of milliseconds, and quickly recover from inactivation (Coetzee *et al.*, 1999; Jerng *et al.*, 2004) is due to the LVA-VGCs Kv4 (Baldwin *et al.*, 1991; Serôdio *et al.*, 1994, 1996; Tsunoda and Salkoff, 1995). Three mammalian genes have been identified encoding for three Kv channels namely Kv4.1, Kv4.2, and Kv4.3 and are particularly localized in dendrites and soma of neurons (Baldwin *et al.*, 1991; Rudy *et al.*, 1991; Serôdio *et al.*, 1994). In PNs, evidences regarding the expression of A-type current in the somatodendritic compartment have been reported as well (Wang *et al.*, 1991; Midtgaard, 1995; Bushell *et al.*, 2002; Sacco & Tempia, 2002; Wang & Schreurs, 2006). In Turtle PNs, Midtgaard and collaborators showed that dendritic current injection and the subsequent slow development of depolarization inactivates A-type currents and this current regulate the occurrence of dendritic Ca^{2+} spikes generated in response to CF or strong parallel fiber stimulation. He further demonstrated that the block of A-type current significantly increases the spread of dendritic excitability (Midtgaard *et al.*,

1993; Midtgaard, 1995). It has been shown that Kv4.3 subunits were expressed throughout the molecular layer suggesting that PNs may also express these subunits. In this case, the generation of A-type currents is most probably mediated by Kv4.3 channels (Serodio and Rudy, 1998; Sacco and Tempia, 2002; Wang & Schreurs, 2006). A more recent study demonstrated that increased inactivation of A-type channels by activity dependent, signals (depolarization and mGluR1 activation) unlocks Ca^{2+} spike assuming a crucial involvement of A-type current in the induction of synaptic plasticity mediated by the co-activation of PF and CF inputs (Otsu *et al.*, 2014).

1.3.5 Ca^{2+} activated K^+ channels in Purkinje neuron dendrites

The elevation of intracellular Ca^{2+} during membrane depolarization activates a group of K^+ channels namely Ca^{2+} activated K^+ channels. Based on their single channels conductance, three types of Ca^{2+} activated K^+ channels have been characterized and classified into: Big conductance (BK), intermediate conductance (IK) and small conductance channels (SK) channels (Latorre *et al.*, 1989). While BK channels are both voltage and calcium dependent, SK and IK are exclusively Ca^{2+} dependent.

In the cerebellum, both SK and BK are expressed in somata and dendrite of PNs (Sah and Faber, 2002) where they serve distinct specifics functions in the electrical responsiveness of these neurons. They contribute to shaping action potentials, to regulating the firing pattern and are involved in synaptic transmission and plasticity (Faber and Sah, 2002; Womack and Khodakhah, 2002a, 2003 Edgerton and Reinhart, 2003; Canepari and Ogden, 2006). Additionally, modeling studies that combined morphological and electrophysiological characteristic of PNs have further demonstrated that density of Ca^{2+} activated K^+ channels are main determinants of the firing pattern and synaptic integration and that interaction between Ca^{2+} and

Ca^{2+}-activated K^+ channels have to be well balanced to maintain PN firing patterns (De Schutter and Bower, 1994; Anwar *et al.*, 2010).

BK channels conduct large currents and their activation is gated by the combined action of membrane potential depolarization and Ca^{2+} concentration (Salkoff *et al.*, 2006). These channels comprise a principal α subunit known as *Slo1* and 3 auxiliary subunits (β1, β2/3, β4). While α subunit alone can from a functional channel, its co-assembly with the auxiliary β subunits confers the diversity in the biophysical and functional properties and in the sensitivity to voltage and Ca^{2+} (Sah and Faber, 2002). Single channels recordings from inside-out patches demonstrated that neurons expresses two types of BK channels; a rapidly activating and inactivating Iberiotoxin-sensitive current, and a slowly activating, non-inactivating Iberiotoxin-insensitive current (Sah and Faber, 2002, Benton *et al.*, 2013). Numerous studies, performed in PN isolated somata, in cultured PNs or in PNs in cerebellar slices, have shown their somata and dendrites express BK channels (Knaus *et al.*, 1996; Jacquin & Gruol, 1999; Benton *et al.*, 2013). Both inactivating and non-inactivating BK currents are expressed in PNs but the inactivating is dominantly expressed (Widmer *et al.*, 2003; Haghdoost *et al.*, 2008). In PNs, BK channels are activated by intracellular increase in Ca^{2+} concentration via both calcium influx through VGCCs channels and calcium release from internal stores (Womack and Khodakhah, 2002b; Canepari *et al.*, 2006). Additionally, BK channels require membrane depolarization for their activation (Latorre, 1994; Salkoff *et al.*, 2006). In fact, as voltage-gated K^+ channels, BK channels possess a voltage sensor domain and a large cytoplasmic C-terminal domain that bind Ca^{2+}. Ca^{2+} binding and voltage sensors activation, two mechanisms that act independently to gate BK channels via allosteric coupling (Horrigan & Aldrich, 2002). The regulation of BK channels by both Ca^{2+} and membrane potential variation confers to these channels a powerful influence on neuronal excitably (Sah & Faber, 2002). They participate in many aspects of PN electrical activity (Edgerton and Reinhart, 2003, McKay and Turner, 2004, Womack and Khodakhah, 2003, Womack and Khodakhah, 2004).

The identification of a specific role of BK channels in the firing pattern of PNs was challenged by the structural and functional diversity of BK channels on one hand, the complexity and the developmental change in firing mode of PNs on the other hand. Both somatic and dendritic BK channels contribute to control the frequency, the regularity and the pattern of spontaneous firing in PNs (Edgerton & Reinhart, 2003; Womack and Khodakhah, 2002b; Womack et al., 2009). They may be involved in the regulation of the efficacy of the coupling between soma and dendrites (Womack and Khodakhah, 2002b). They also contribute to regulate and shape Na^+ and Ca^{2+} spikes and to their subsequent fast afterhyperpolarization suggesting a very important role with respect to CF response characterized by a burst of Na^+ spikes and a dendritic Ca^{2+} spike (Edgerton and Reinhart, 2003; Sausbier *et al.*, 2004). The fast hyperpolarization also serves to limit the spread of dendritic Ca^{2+} spikes (Rancz and Hausser, 2006). In keeping with these various roles, genetic deletion of BK channels affected the regularity and the frequency of the spontaneous firing of PNs, induced a reduction in the generation of afterhyperpolarization and the animals showed cerebellar ataxia phenotypes (Sausbier *et al.*, 2004; Cheron *et al,*. 2009). BK channels are often functionally coupled with voltage gated calcium channels (Robitaille *et al.*, 1993; Marrion & Tavalin, 1998; Prakriya & Lingle, 2000). In PN, BK channels couple with P/Q-type channels that provide the Ca^{2+} required for their activation. In turn, the activation of BK channels restricts the duration of membrane depolarization and Ca^{2+} influx serving as negative feedback. The interaction between BK and P/Q-type channels generates regular oscillation in membrane potential (Regan, 1991; Womack and Khodakhah, 2002b).

In contrast to BK channels, SK channels are voltage independent and are exclusively activated by an increase in Ca^{2+} concentration in the cytosol (Köhler *et al.* 1996; Stocker, 2004). Given their high sensibility to Ca^{2+}, SK channels are activated even by very low Ca^{2+} concentration (Vergara *et al.*, 1998). Three types of SK channels subunits have been characterized; they are widely distributed throughout the brain namely SK1, SK2 and SK3 and display the same sensitivity

level to Ca^{2+} concentration (Köhler *et al.*, 1996; Xia *et al.*, 1998; Stocker and Pedarzani, 2000). SK channels conduct small currents and are formed by homo- or heteromultimers of SK1, SK2 or SK3 subunits (Stocker, 2004). Among the three subunits, PNs express predominantly SK2 as demonstrated by *in situ* hybridization (Stocker and Pedarzani, 2000; Cingolani *et al.*, 2002; Sailer *et al.*, 2002) and immunohistochemical studies (Sailer *et al.*, 2004; Ballesteros-Merino *et al.*, 2014a). *In situ* hybridization studies, at both mRNAs and proteins levels, showed that SK channels are highly expressed at birth. After that, their level of expression undergoes significant downregulation during the three first weeks after birth displaying weak expression in adulthood (Cingolani *et al.*, 2002). Remarkably, the downregulation of SK expression parallels the upregulation of BK channels suggesting that BK channels are more involved in the regulation of the excitability in mature PNs. However, a later electrophysiological study showed that under physiological condition, even thought the expression level of SK channels is lower in adult PNs; they still contribute to regulate the spontaneous firing rate in the same way as in young PN (Womack and Khodakhah, 2003). Remarkably, in a more recent work conducted on rat PNs, staining showed that SK2 channels are expressed during development and throughout adulthood (Hosy *et al.*, 2012).

Studies conducted to identify the precise SK channels functions in cerebellar PNs have demonstrated that while somatic SK channels essentially regulate the basal firing frequency during spontaneous activity, dendritic SK channels regulate not only the spontaneous firing rate but also control the efficacy of electrical coupling between the soma and dendrites (Edgerton and Reinhart, 2003; Womack and Khodakhah, 2003, 2004). The Block of somatic SK by apamin disrupts the regularity and the stability of the spontaneous firing causing PNs to fire high frequency bursts and increases the number of action potential evoked by current injections (Cingolani *et al.*, 2002; Edgerton and Reinhart, 2003; Womack and Khodakhah, 2003, 2004; Stocker *et al.*, 1999). Similarly, the block of dendritic SK channels increases their firing rate also, but only where somatic action potentials do not backpropagate to

cause significant Ca^{2+} influx. Thus, it has been suggested that the source of Ca^{2+} for the dendritic SK channels is the resting dendritic Ca^{2+} and not that generated by Ca^{2+} spike (Womack and Khodakhah, 2003). Interestingly, pharmacological enhancement of SK current using 1-ethyl-2-benzimidazolinone (EBIO) rescued spontaneous firing irregularity and the tendency to fire high frequency burst caused by the absence of SK or by mutations in P/Q-type VGCCs (Cingolani *et al.*, 2002; Walter *et al.*, 2006). Furthermore, in vivo perfusion of EBIO into the cerebellum improved motor performance dysfunctions and alleviated the ataxic phenotype in mice harboring mutations in P/Q-type VGCCs (Walter *et al.*, 2006). Similarly, the oral administration of SK2 selective agonists to mice model of ataxia (spinocerebellar ataxia type 2) ameliorated their motor performances and restored the basal spontaneous firing of PNs (Kasumu *et al.*, 2012a).

In PNs, in contrast to BK channels that are involved in the repolarization following individual action potentials, SK channels contribute to the slow after hyperpolarization mediated by repetitive action potentials in the tonic firing (Stocker *et al.,* 1999; Pedarzani *et al.,* 2001; Edgerton & Reinhart, 2003). Indeed, the block of SK does not affect the after hyperpolarization following Na^{+} and Ca^{2+} spike in burst firing (Edgerton and Reinhart, 2003). In PNs, it has been shown that SK channels are activated by P/Q-type VGCCs to control spontaneous firing in PCs (Womack *et al.*, 2004). Nevertheless, the coupling of SK with voltage gated calcium channels during electrical response to CF stimulation has not been investigated. The functional coupling between SK channels and the channels providing the Ca^{2+} is accomplished by molecular interaction. A study using a proteomic approach demonstrated that SK channels form macromolecular complexes with VGCCs channels (Fakler and Adelman, 2008).

1.4 Synaptic signaling by mGuR1 in Purkinje neurons

1.4.1 Type-1 metabotropic glutamate receptors

Glutamate is the neurotransmitter of the vast majority of fast excitatory synapses in the central nervous system (CNS) and plays an important role in a large number of neuronal functions (Curtis *et al.*, 1959). It exerts its effect on the postsynaptic membrane through activation of two major classes of receptors which are the iontropic glutamate receptors (iGluRs) and the metabotropic glutamate receptors (mGluRs) (Sugiyama *et al.*, 1987). While glutamate binding to iGluRs induces fast excitation, the effects of glutamate binding to mGluRs are slower. iGluRs, including AMPA- (α-amino-3-hydroxy-5-methyl-4-isoxazolepropionic acid), NMDA receptors (*N*-methyl *D*-aspartate receptors) and kainate receptors, are ligand-gated cation channels (Dingledine *et al.*, 1999) and were established as the primary mediators of excitatory synaptic transmission in the CNS (Monaghan *et al.*, 1989). Later, it was also reported that glutamate also elicits metabolic actions through G protein coupled receptors, namely mGluRs.

mGluRs belong to the G-protein-coupled receptors (GPRC), the largest receptors gene family in the human genome. In contrast to iGluRs, they do not form ion permeable pore and couple via G-protein to intracellular signaling pathways providing a mechanism by which glutamate can modulate synaptic transmission by second messenger. mGluRs are widely distributed in the central nervous system and are homodimers. Each monomer characterized by the presence of seven transmembranes domains, a large N-terminal ligand binding domain (LBD), an intracellular C-terminal domain interacting with the trimeric G-protein and in multiple ways with proteins of the postsynaptic density (PSD) (Tu *et al.*, 1998; Tu *et al.*, 1999).

mGluRs are divided in eight types: mGluR1 to mGluR8 (Conn and Pin, 1997) divided into three groups based on the amino acid sequence homology and downstream

signal transduction mechanisms, group I (mGluR1 and mGluR5, mainly located at the postsynaptic sites), group II (mGluR2 and mGluR3), and group III (mGluR4, mGluR6, mGluR7, and mGluR8) (Nakanishi, 1992). Group I, in particular mGluR1, are expressed in PNs. mGluR1 couple G_q proteins and may lead to phospholipase C (PLC) activation and generation of inositol - 3 - phosphate (InsP3) and diacylglycerol (DAG), as well as activation of protein kinase C (PKC) (Conn and Pin, 1997). Intensive work has been dedicated to studying mGluR1 expression and functions. mGluR1 is expressed differentially throughout the mammalian central nervous system (Shigemoto *et al.*, 1992; Martin *et al.*, 1992; Baude *et al.*, 1993; Ryo *et al.*, 1993; Fotuhi *et al.*, 1993; Nusser *et al*. 1994; Gravius *et al*. 2010) with high expression in the olfactory bulb, dentate gyrus, and cerebellum (Fotuhi *et al.*, 1994; Romano *et al.*, 1996a; lein *et al.*, 2007; Luscher and Huber, 2010) and is involved in a variety of physiological functions including memory, cognition, the sensation of pain and fear. They are relatively concentrated at the post synaptic densities of excitatory glutamatergic synapses; although, there is also evidence for presynpatic localization and presynaptic targeted actions via endogenous retrograde signaling (Maejima *et al.*, 2001; Niswender and Conn, 2010). At the subcellular level, mGluR1 is localized in the extrasynaptic regions of dendritic spines, and together with other postsynaptic proteins including Homer, Shank, and postsynaptic density protein form a multi-protein signaling complex (Lujan *et al.*, 1996; Tu *et al.*, 1999; Nakamura *et al.*, 2004). In the following, we focus on mGluR1 function in PNs.

1.4.2 mGluR1 in Purkinje neurons

PNs express only mGluR1 and mGluR5 which exhibits somatodendritic localization. In contrast to mGluR5 which are moderately expressed, mGluR1 are highly expressed and located perisynaptically in their dendritic spines (Shigemoto *et al.*, 1992; Nusser *et al.*, 1994; Mateos *et al.*, 2000; lein *et al.*, 2007).

mGluR1s signaling pathways are crucial for normal cerebellar functioning, a statement that was highlighted through different reports linking the disregulation of mGluR1 signaling to severe cerebellar dysfunction. In Human, Aaraneoplastic cerebellar degeneration, a type of cerebellar ataxia in which patients showed sever deficit in motor coordination, is caused by autoantibodies directed against mGluR1 (Sillevis-Smitt *et al.*, 2000; Coesmans *et al.*, 2003). More recently, a mutation in mGluR1s was associated with an Autosomal-recessive congenital cerebellar ataxia characterized by degeneration or abnormal development of cerebellum and patient showed severe deficit in gait (Guergueltcheva *et al*., 2012). In mice models, genetic deletion of mGluR1 caused severe ataxia in mice which exhibited impaired motor behaviors (Aiba *et al.*, 1994; Conquet *et al.*, 1994). At cellular level, mGluR1 signaling also plays a central role in PN synaptic wiring. Indeed, mGluR1 deletion was associated with developmental alteration in synaptic innervation of cerebellar PNs. Adult mice lacking mGluRs showed abnormal climbing fiber multiple innervations indicating that mGluR1 signaling is indispensable for eliminating the persistent multiple climbing fiber innervations during postnatal development in order to establish the mono-innervation by single climbing fibers (Kano *et al.*, 1997; Levenes *et al.*, 1997; Offermanns *et al,*. 1997). Furthermore, mice lacking mGluR1s were not able to eliminate PF synapses from proximal dendrites, a phenomenon which is important for PF and CF inputs segregation during early postnatal development (Ichikaw *et al.*, 2016). Remarkably, rescue of these cerebellar deficits was possible using PN-specific expression of mGluR1 in mice lacking mGluR1 which exhibited apparent normal motor behaviors (Ichise *et al.*, 2000). Chronic activation of mGluR1s restricted

PN dendritic arborization growth indicating that mGluR1 signaling may control the mechanism underlying the proper growth of the PN dendritic tree. It has been also reported that a gain-of-function of mGluR1 signaling also led to ataxia. In SCA28 mouse model, PNs exhibit excessive cytosolic Ca^{2+} levels due to alterations in mitochondrial Ca^{2+} handling. Interestingly, the ataxic phenotype is rescued by reducing mGluR1 expression in the SCA28 mice (Maltecca *et al.*, 2015). Finally, the signals downstream of mGuR1 activation such as G-proteins, PLC, and $InsP_3$, are necessary for normal Long-term Depression (LTD) and motor coordination. This was supported by the observation that mice lacking $InsP_3$ receptor displayed motor discoordination, severe ataxia and LTD was abolished in these animals (Inoue *et al.*, 1998).

LTD is believed to constitute the molecular substrate for motor coordination and learning (Ito, 1982; 1984; 2001). Numerous studies have been conducted seeking to elucidate the role of mGluR1 in the induction of LTD. Using antibodies directed against mGluR1s led to the block of mGluR1-dependent intracellular Ca^{2+} increase and of LTD (Shigemoto *et al.*, 1994). Genetic deletion of mGluR1s was associated with LTD deficiency at PF-PN synapse (Aiba *et al.*, 1994; Conquet *et al.*, 1994). Moreover, application of mGluR1 blocker in vivo prevented LTD induction (Gao *et al.*, 2003). In the mGluR1-rescue mice, cerebellar LTD was restored (Ichise *et al.*, 2000). A recent study reported the importance of mGluR1 in the induction of LTD by demonstrating that combined mGluR1 activation and depolarization unlocked dendritic Ca^{2+} spikes mediated by P/Q-type Ca^{2+} channels through inactivation of the A-type K^+ channels in the distal dendrites of Purkinje cells (Otsu *et al.*, 2014).

In conclusion, all this finding emphasized the curial role of mGluR1 in motor control, learning and synaptic plasticity. Indeed, they play crucial roles in development, modulation, and plasticity of cerebellar synapses as well as motor learning and motor coordination.

1.4.3 Specificity of mGluR signaling at PF-PN synapse

As mature Purkinje neurons don't express functional NMDARs (Shin and Linden, 2005), AMPAR and mGluR1 are the main mediator of synaptic transmission between parallel fibers and Purkinje cells (Konnerth *et al.*, 1990; Llano *et al.*, 1991). AMPAs and mGluR1 receptors show different localization at the postsynaptic sites which determines the mode of activation of these receptors. AMPARs are located at the centre of the postsynaptic spine in front of PF synaptic terminals (Nusser *et al.*, 1994) and low levels of glutamate released by PF terminals are enough to activate AMPARs and depolarize the membrane. In contrast, mGluR1s are located at perisynaptic sites (Baude *et al.*, 1993; Nusser *et al.*, 1994) and they are only activated in case of high glutamate accumulation in the synaptic cleft. In this case, mGluR1 recruitment occurs only during high frequency burst stimulation of parallel fibers (Batchelor & Garthwaite, 1997; Tempia *et al.*, 2001). The activation of granule cells which project through PF on the dendrites fires action potentials (APs) with relatively high frequencies leading to mGluR1 activation under physiological conditions. Under non physiological conditions, fast application of glutamate by photolysis or applications of selective mGluR1 agonists activate mGluR1 independently of presynaptic activation (Canepari *et al.*, 2001).

Synaptic activation of mGluR1s initiates two distinct pathways through intracellular chemical messenger signaling that segregate after G-protein activation (Canepari and Ogden, 2006), both leading to intracellular Ca^{2+} transients. The first one leads to Ca^{2+} release from intracellular stores and the second one leads to slow Ca^{2+} influx from the extracellular space which appears to be mediated mediated by TRPC3 channels (Hartmann *et al.*, 2008).

In the first pathway, mGluR1s activate phospholipase Cβ (PLCβ), via heterotrimeric G-proteins Gq/G_{11} which triggers the hydrolysis of phosphatidyl-inositol-bisphosphate to inositol 1,4,5-trisphosphate ($InsP_3$) and diacyl-glycerol (DAG) an activator of PKC. $InsP_3$ receptors in smooth endoplasmic reticulum (SER) bind InsP3 allowing release of Ca^{2+} (Finch and Augustine, 1998). At the PF-PN synapse, Ca^{2+} release from internal stores is restricted to small spino-dendritic domains (Finch and Augustine, 1998; Takechi *et al.*, 1998). Mimicking mGluR1 activation by flash photolysis of $InsP_3$ led also to Ca^{2+} release in spines and dendrites which was associated with a generation of an outward K^+ current that slowly hyperpolarizes the PN with the subsequent reduction of membrane excitability (Khodakhah & Ogden, 1993). The InsP3-mediated Ca^{2+} response in dendritic spine has been shown to play a crucial role in triggering LTD at PF-PN synapse (Miyata et al., 2000; Kano *et al.*, 2008; Hartmann *et al.*, 2011; Finch *et al.*, 2012).

In the second pathway, mGluR1 activation generates a slow inward current mediated by a non-selective cation conductance (Batchelor *et al.*, 1997; Canepari *et al.*, 2001). This conductance exhibits Ca^{2+} permeability and a relatively low conductance estimated as 0.6 pS (Canepari *et al.*, 2004). Studies aiming to elucidate the mechanisms linking activation of mGluR1 to the slow EPSC have reported that the generation of slow current necessitates G-proteins Gq. This was suggested by the observation that inhibition of protein tyrosine phosphatase (PTP) was able to eliminate the mGluR1-dependent sEPSC (Tempia *et al.*, 1998; Canepari and Ogden, 2003; Hartmann *et al.*, 2004). Additionally, in $G\alpha_q$-deficient mice, mGluR1 responsiveness has been altered and the sEPSCs could not be evoked. Furthermore, the inhibition of PLC did not prevent the slow EPSC which indicates its independence of phophoinositide metabolism (Hirono *et al.*, 1998; Tempia *et al.*, 1998; Canepari *et al.*, 2006). The identification of the channel underlying the slow mGluR-dependent EPSP has been the objective of several studies for more than a decade.

Initial reports have suggested that TRPC1 cation channels underlie the slow EPSC (Kim *et al*., 2003). Later, another study has contrasted this finding providing strong evidences that the channel responsible for the slow EPSC is TRPC3 and not TRPC1. In fact, the mGluR1 mediated sEPSC is suppressed in mice lacking TRPC3 and remained unaffected in mice lacking TRPC1 (Hartmann *et al*., 2008). The Ca^{2+} increase through mGluR1-dependent TRPC3 activation would be then specific to individual spine activated in contrast to the wider spread of action of $InsP_3$ release from stores by $InsP_3$ as demonstrated in PN dendrites because of the high cytosolic diffusion coefficient of $InsP_3$ relative to Ca^{2+} (Allbritton *et al.*, 1992; Finch and Augustine,1998). Even though the increase in intracellular Ca^{2+} is less than the Ca^{2+} released from intracellular stores (Canepari *et al*., 2004), its requirement for the induction of LTD induction has been reported (Chae *et al*., 2012). A more recent study has however provided indications that the orphan GluD2 receptor forms functional channels that are triggered by mGluR1 activation in PNs (Ady *et al*., 2014), indicating that the origin of the mGluR1-dediated slow EPSP may be more complex. Both TRPC3 and GluD2 have been found to be crucial in PN function. In addition, mGluR1s, TRPC3 and GluD2 associate at molecular level in PNs (Kato *et al*., 2012).

1.5 Open questions that motivated my experiments

The coincidence activity of multiple signals at a signals synaptic site is believed to drive lasting functional changes that underlie several form of associative synaptic plasticity. One best candidate site where this phenomenon occurs is the dendrite of PNs receiving two excitatory inputs, namely PFs and CF. The activation of the PF inputs triggers local Ca^{2+} influx confined to a small number of spiny branchlets being activated whereas the activation of the CF input evkoes a transient depolarization that spreads passively into the dendrite and activates a set of ion channels eliciting Ca^{2+} transients in PF input territory. Therefore I initially characterized, with the maximal precision allowed by the experimental tools I utilized, the ion channels activation associated with the CF-EPSP in the dendrites where PF synapses are formed. These experiments are reported in Chapter 3.

Ca^{2+} signaling mediated by PF activation leads to mechanisms of synaptic plasticity at PF-PN synapses that are crucial for cerebellar function. These mechanisms are mostly homosynaptic since they occur exclusively at the synapses that are activated. Yet, the CF-mediated Ca^{2+} signaling acting as a global signal plays a key role in controlling synaptic plasticity at PF-PNs synapses. It is therefore obvious that the CF activity works in combination with synapse-dependent mechanisms that are triggered by PF activity generating Ca^{2+} transients, and these are key signals involved in the mechanism of synaptic plasticity. This rise a fundamental question: how can such a global CF signal interact with local PF signaling? Considerable amount of work has been dedicated to shed light on this important issue, yet conclusive answers have not been yet provided. I therefore investigated in detail the signaling associated with the pairing of PF and CF activation, focusing on protocols leading to synaptic plasticity.

Chapter 2:

Materials and methods

2. Materials and methods

2.1 Mice and ethics for animal experimentation

C57/B16 wild type mice (male/female) aging from 21 to 35 days were used in my experiments. They were purchased from Janvier Company (Saint-Berthevin Cedex, France), housed and fed in Biology department of Saint Martin d'Heres.

Experiments were ethically reviewed and carried out in accordance with European Directives 2010/63/UE on the care, welfare and treatment of animals. Procedures were reviewed by the ethics committee affiliated to the animal facility of the university (D3842110001). During my PhD I attended the 81 hours compulsory training and the Level 1 Diploma for *Animal Experiments* that entitled me to perform the experiments presented in Chapters 3 and 4.

2.2 Slice preparation

Mice were anesthetized with Isoflurane and decapitated. The cerebellum was quickly removed out and immediately placed in an ice-cold cutting extracellular solution (4°C) bubbled to saturation (at least 20 minutes) with a gas mixture (95% O_2 and 5% $CO_{2)}$. The extracellular solution contained (in mM): 125 NaCl, 26 $NaHCO_3$, 1 $MgSO_4$, 3 KCl, 1 NaH_2PO_4, 2 $CaCl_2$ and 20 glucose. After a maximum of two to three minutes, the cerebellum was removed from the solution using a spatula then gently placed on filter paper to dry quickly then firmly glued on a stage on a sagittal side and the ensemble was placed in a slicing chamber containing the same ice-cold cutting extracellular solution. Using a vibratome slicer (Leica VT1200, Wetzlar, Germany), parasagittal slices of 250 µm thick were prepared. After each cut, the parasagittal

slice was immediately transferred into an oxygenated solution maintained in a water bath at 37 °C and left to incubate for roughly 30 to 40 minutes. Thereafter, the slices holder was removed from the water bath and maintained at room temperature for at least 60 minutes before starting the experiments. All recordings were done at near physiologal temperature (32-34 °C)

2.3 Electrophysiology

After incubation, the slices were transferred to a recording chamber placed right under the microscope and mechanically stabilized at the bottom with a grid. The microscope was used for wide-field imaging experiments and it is an Olympus BX51 microscope (Tokyo, Japan) equipped with a 60×/1.0 NA Nikon (Tokyo, Japan) objective. The recording chamber was constantly perfused with the external solution at constant flow rate of about 2ml/mn in order to maintain the slice stability and the temperature was held at 32/34 °C. Patch-clamp experiments were performed following the procedures described below.

We used electrodes with an open tip resistance of 3–4 MΩ obtained by pulling borosilicate pipettes with 1.5 mm external diameter and 1.17 mm internal diameter without filament having a tip of diameter of ~1 µm. In addition to the standard composition reported below, the solution uses to fill pipettes contained the fluorescent probes. The intracellular solution contained (in mM): 125 $KMeSO_4$, 5 KCl, 8 $MgSO_4$, 5 Na_2-ATP, 0.3 Tris-GTP, 12 Tris-Phosphocreatine, 20 HEPES, adjusted to pH 7.35 with KOH. Each patch pipette was frontfilled with the solution not containing the indicators and then backfilled with the same solution containing the indicator. While approaching the neurons, different pressure were applied to the electrode which was controlled with a manometer. First, a weak positive pressure of

~10 to 12 mbar was applied on the patch pipette, this pressure was necessary to maintain the tip of the pipette clean. Then a stronger pressure of about 80 to 100 mbar was applied for a few seconds before the electrode is attached to the cell. The goal of this procedure was to avoid the leak of the solution containing the indicators before forming the seal, i.e. to avoid the unwanted staining of tissues in the slice other then the recording cell (Canepari *et al.*, 2008).

After establishing the whole cell configuration, series resistances were monitored. Recordings were performed using a Multiclamp 700A amplifier (Molecular Devices, Sunnyvale, CA). The neuron was initially held at resting membrane potential or at different membrane potentials using current injections under current clamp. Recordings of somatic membrane potential were acquired at 20 kHz using the A/D board of the charge-coupled device (CCD) camera. Somatic V_m, recorded via the patch pipette, was corrected for a junction potential of -11 mV, calculated for the composition of the intracellular solution (Canepari *et al.*, 2010).

The stimulation of the two excitatory inputs (CF and PFs) was carried out using borosilicate patch pipettes filled with the external solution. To stimulate PF inputs, the glass pipette was placed in the molecular layer on the top of dendrites. To stimulate the CF input, the glass pipette was placed near the soma, in the granule cell layer. PF and CF EPSPs were generated by stimulating pulses of 100 µs duration and of 5-20 µA amplitude delivered by an IS4 stimulator (SC-Devices, Switzerland) through the glass pipette. Pulses were generated by a Master_8 (A.M.P.I, Jerusalem, Israel).

2.4 Neuronal loading and staining

The fluorescent dyes used in the experiments were the Ca^{2+} indicators Oregon Gren BAPTA-5N (OG5N), FuraFF and Fura-2 and the water soluble voltage sensitive dye (VSD) JPW1114. These were added to the intercellular solution at different final concentrations according to the specific experiment. Ca^{2+} indicator are available as water soluble potassium salts. In order to avoid the spill over of the dye into the extracellular medium while approaching the neuron and the resulting large background fluorescence, it was necessary to first fill the patch pipette from the tip with dye-free intracellular solution by applying a negative pressure using 10 ml syringe for a period of 20 to 30 seconds, as reported before. This time depends on numerous parameters of the patch pipette, namely the shape and the size of the type and glass type and dimension. The glass pipette was then back-filled with the intracellular solution containing the fluorescent indicator at a precise concentration. Once the fluorescent dye reached the cytosol after establishing the whole-cell configuration, neuronal staining was accomplished by diffusion from the soma into the dendrites while the neurons was held at -70 mV in voltage clamp. The dye can equilibrate in the cytosol at the given concentration providing quantitative estimate of Ca^{2+} signals. The optimal staining time depends on the shape and dimensions of the cell and was determined by measuring the resting fluorescence from the soma at low excitation light intensity since overexposure of the neuron to strong intensity light produces photo damages. Ca^{2+} dyes diffuse through the cytosol and equilibrate relatively quickly. However, we routinely waited 30 minutes to allow dye equilibration in PN dendrites. The staining for the VSD JPW1114 is different. Although dissolved in the intracellular solution, this molecule immediately binds to somatic membranes as it outcomes from the pipette. Thus, staining occurs via dye diffusion through the

membrane, a process that is slower than cytosolic diffusion. Thus, because dye equilibration in PN dendrites takes more than 1h, the patch electrode was cautiously detached from the cell by forming an outside-out patch after ~30 minutes. In order to help preserving the health conditions of the cell, this initial staining patch was performed at room temperature when it is necessary. After the first patch, the temperature was reset to 32-34 °C and neurons were left to rest for about 10 minutes and repatched again using the internal solution containing only the Ca^{2+} indicator.

2.5 The imaging system

The imaging system consisted of a camera and different light sources and was designed to monitor either Ca^{2+} signals alone or to sequentially record Ca^{2+} and V_m signals which can be obtained with negligible optical cross-talk between the two signals (Canepari *et al.*, 2008) and negligible photo-damage of the preparation. The camera is a dual head NeuroCCD-SMQ camera (RedShirtimaging, Decatur, GA) with 80*80 pixels per head that is capable to acquire at the fast rate of 5 kHz (Figure 2A). The illumination source, either a UV/blue/green light-emitting diode (LED) or a green solid state laser was provided through the epifluorescence port of the microscope and allowed by different dichroic mirrors depending on the fluorescent dye. A 385 nm or a 470 nm LED was used for Ca^{2+} dye excitation, (Fura or OG5N, respectively), and was controlled by an OptoLED (Cairn Research, Faversham, United Kingdom). During continuous illumination, the protection circuit of the OptoLED limits the power of the LED to ~50 mW at the objective. Intrestingly, blue illumination at ~30 mW for longer periods (seconds) elicit the opening of ion channels, a phenomenon that can be attributed to a transient temperature change and that is characterized in the report included in the annex (see paper published in *Eur. J. Neurosci.*). A 532 nm-300 mW solid state laser (model MLL532; CNI,

Changchun, China) was used to excite the VSD in experiments reported in Chapter 3 through a custom-made unit designed to allow wide-field illumination of the preparation from above the objective. The laser was kept constantly on and illumination was controlled by a TTL-triggered shutter (Vincent Associates, Rochester, NY). An output channel of the A/D board of the NeuroCCD-SM was used to control the shutter and to trigger the Master-8 which used to control the UV/blue illumination. In contrast, in experiments reported in Chapter 4, the VSD was excited using a 530 nm LED. This choice was motivated by the fact that these recordings lasted at least 200 ms and exposure to the full power of the laser for such long duration causes considerable photodamage. Thus, the light intensity of the LED was only 20% of that of the laser, but also was more stable and triggerable with a TTL without the need of using a shutter. As illustrated in Figure 2, the excitation light from the epifluorescence was first filtered by two excitation filters (ex1 and ex2) and then directed to a dichroic mirror reflecting to a water immersion objective Nikon 60X NA = 1). Different dichroic mirrors were used according to the dye used. The emission light was filtered before being captured by the camera. Fluorescent images were de-magnified by a ~0.2X projection lens and splitted into one or the other 80 × 80 pixel chip of the NeuroCCD camera according to the color, using an additional dichroic irror (dic 3). In this way, the area projected to each chip of the dual camera was ~150 × 150 μm.

In all experiments, the exposure time for a single trial was either 20 or 200 ms except in DHPG experiments where the exposure time could last up to 400 ms for a single trial. The time between two consecutive trials was 20 second or more in the case of V_m imaging (30 ms) to limit photodamages of the neuronal preparation and to allow recovery of initial conditions. Optical signals associated with paired CF and PF EPSPs were recorded for 200 ms (1000 frames) and optical signals associated with

CF-EPSPs were recorded for 20 ms (100 frames). Individual trials were saved and checked for exact temporal matching of the somatic electrical signal in each trial to verify their consistency. This was necessary to correlate V_m and Ca^{2+} signals, but also to average trials. Indeed, four trials (Ca^{2+} signals) or 9 (V_m signals) were averaged to improve the signal-to-noise ratio (S/N). Finally, slow changes in fluorescence due to bleaching of the dye were corrected by subtracting an appropriate exponential function derived from the recording trials with no stimulation fluorescence or directed that filtered trial.

2.6 Fluorescent indicators

JPW1114 also called di-2-ANEPEQ was purchased from Molecular Probes Invitrogen (Carlsbad, CA). It belongs to aminostyryl pyridinium class of fast potentiometric membrane dyes that undergo a large charge shift upon excitation and display a strictly linear electrochromic response to membrane potential in the range of −100 mV to 100 mV (Loew and Simpson 1981; Loew *et al.*, 1992). They are lipophilic but still sufficiently water soluble to be used for micro-injection. Individual neurons were loaded with 0.2–0.5 mg/mL which gives no toxic effect on the neuron. A stock solution in H_20 at a concentration of 20 mg/mL was prepared and kept at 4ºC. The day of experiments, the stock was diluted in the internal solution containing the Ca^{2+} dye at the desired final concentrations.

Ca^{2+} indicators: OG5N, FuraFF and Fura2

A stock solution at 20 mM was prepared for each dye and small aliquots were stocked at −20ºC. The day of experiment, an aliquot was diluted in intracellular solution at the desired final concentration.

OG5N: this is the main low affinity Ca^{2+} indicator (OG5N, K_D = 35 µM) used to record fast Ca^{2+} signals. It was initially used to develop the technique of Ca^{2+} current imaging (Jaafari *et al.*, 2014; 2015) then my preliminary experiments, during my PhD, aimed at extending this technique to PN neurons (see the paper in J Neurosci Methods included in the Annex).

FuraFF: this is the alternative low affinity Ca^{2+} dye (K_D = 10 µM) that was used in combination with membrane potential imaging, since OG5N emission overlaps with that of the VSD (Canepari *et al.*, 2008). As all Fura dyes, FuraFF is ratiometric and, when excited above its isosbestic wavelength (~360 nm), the changes of fluorescence associated with an increase in Ca^{2+} concentration are negative.

Fura-2: is the high affinity Ca^{2+} indicator (K_D = 0.2 µM) that was used, in combination with OG5N, to mimic the binding of Ca^{2+} ions to endogenous buffers and therefore monitoring this scenario. To this purpose, in comparison with the low affinity indicators, it was used at a much lower concentration (200 µM).

2.7 Membrane potential calibration and signals interpretation

The direct quantifications of V_m signals in experiments reported in Chapter 3 were provided by the calibration of $\Delta F/F_0$ V_m on an absolute scale (mV). This quantification is crucial to compare V_m signals associated with CF-EPSP obtained from different dendritic regions and to allow the analysis of the voltage gating of Ca^{2+} channels associated with the CF-EPSP at the same region where Ca^{2+} transients were recorded. Nevertheless, the absolute calibration of $\Delta F/F_0$ V_m signals is not a straightforward procedure. Indeed, VSD fluorescence is not only generated by the dye bound to the plasma membrane (active dye), but also to the dye bound to

internal membranes (inactive dye). Noteworthy, the inactive dye contributes only to the resting fluorescence whereas the active dye contributes both to the resting fluorescence and to the fluorescence change. Because membrane potential (V_m) signal is always measured as a fluorescence change relative to the resting fluorescence ($\Delta F/F_0$), this signal will depend, in each pixel, on the ration between the active and inactive dye, a variable that cannot be measured. Consequently, the sensitivity of VSD- $\Delta F/F_0$ recordings differs from one site to another site in the cell. Importantly, the fact that $\Delta F/F_0$ corresponding to a given V_m signal from a given site is quite stable in many acquisition trials and thus, a calibration of the VSD- $\Delta F/F_0$ signal in terms of V_m is possible if an electrical signal that has a known amplitude is obtainable at all recordings sites. The action potential signal can be used to calibrate $\Delta F/F_0$ of the VSD in some cell types. For instance, in mitral cells of the olfactory bulb, as the axo-somatic actions potentials propagate without attenuation throughout the whole apical dendrite, they are used to calibrate the amplitudes of V_m optical signals (Djurisic et *al.*, 2004). PNs do not fire actions potentials that propagate into the dendrites. Therefore, in the case of this cell type, a prolonged hyperpolarizing pulse that propagates from the soma to the dendrites with slight amplitude attenuation constitutes an alternative approach to calibrate the $\Delta F/F_0$ of VSD (Stuart and Häusser, 1994). Assuming that the resting V_m is identical over the entire cell and once the PN is held at resting V_m, we injected via the recording patch pipette a hyperpolarizing or depolarizing current pulses of 1s duration to the soma and the corresponding V_m change was recorded. In this case, as the somatic hyperpolarization propagates into the dendrites with insignificant attenuation, the recording of somatic V_m are used to convert the dendritic VSD-$\Delta F/F_0$ signals to values expressed in mV in order to quantify the dendritic V_m transients associated with the CF-EPSP. On the contrary, the somatic depolarization attenuates while

spreading along the dendrites; therefore, it cannot be used to calibrate VSD-$\Delta F/F_0$ signals. However, since the fluorescence change is linear with the V_m change, once the calibration is obtained for hyperpolarizing pulse, it is then possible to estimate the correct dendritic V_m corresponding to the depolarizing pulses. In this way, in our experiments, we could systematically assess the initial V_m at any region of interest, as well, in the case of depolarizing states. A full explanation of this calibration method is detailed in Chapter 3. Finally, it must be noted that VSD signal reported in Chapter 4 were not calibrated. In fact, while the intrinsic photon noise of these signals produced by LED fluorescence excitation was larger than that of signals in Chapter 3, the calibration was not critical for the scientific conclusions of this particular investigation.

2.8 Pharmacology

Chemical blockers: All chemicals were purchased either from Tocris (Bristol, UK), Hello Bio (Bristol, UK) or Sigma-Aldrich (St. Louis, MO). Full names of utilised chemicals in order of appearance in the Results are the followings: **ML218**: 3,5-dichloro-*N*-[[(1α,5α,6-exo,6α)-3-(3,3-dimethylbutyl)-3-zabicyclo[3.1.0]hex-6-yl]methyl]-benzamide-hydrochloride.**NNC550396**: (1*S*,2*S*)-2-[2-[[3-(1*H*-Benzimidazol-2-yl)propyl]methylamino]ethyl]-6-fluoro-1,2,3,4-tetrahydro-1-(1-methylethyl)-2-naphthalenyl-cyclopropanecarboxylate-dihydrochloride; **Isradipine**: 4-(2,1,3-Benzoxadiazol-4-yl)-1,4-dihydro-2,6-dimethyl-3,5-pyridinecarboxylic acid methyl 1-methylethyl ester; **PD173212**: *N*-[[4-(1,1-Dimethylethyl)phenyl]methyl-*N*-methyl-L-leucyl-*N*-(1,1-dimethylethyl)-*O*-phenylmethyl)-L-tyrosinamide;**CPCCOEt**: 7-(Hydroxyimino)cyclopropa[*b*]chromen-1a-carboxylate ethyl ester**;** **DHPG**: (*RS*)-3,5-Dihydroxyphenylglycine **U73122** : 1-[6-[[(17β)-3-Methoxyestra-1,3,5(10)-trien-17-

yl]amino]hexyl]-1*H*-pyrrole-2,5-dione; **IEM1460:** *N*,*N*,*H*,-Trimethyl-5-[(tricyclo[3.3.1.13,7]dec-1-ylmethyl)amino]-1-pentanaminiumbromide hydrobromide

Toxins : ω-Agatoxin IVA, AmmTx3, Iberiotoxin and apamin were purchased from Smartox Biotechnology (St Martin d'Hères, France).

Noticably, in experiments reported in Chapter 3, chemicals or toxin were locally applied by a using a pipette, wherease in experiments reported in Chapter 4, these were applied in the entire chamber through regular perfusion. In the case of pressure application of DHPG, which precisely synchronized with the optical recordings, this was achieved using a commercial ejector PDES-2DX (npi electronic, Tamm, Germany)

2.9 Optical data analysis

All data were analysed with dedicated software written in Matlab (The MathWorks Inc., Natick, MA, USA). V_m and Ca^{2+} signals were performed at 5 kHz and initially expressed as fractional changes of fluorescence ($\Delta F/F_0$) calculated after subtraction of the autofluorescence background.

2.10 Statistics

Statistics were calculated in Excel (Microsoft Office 2007) and averages are presented as the mean ± standard deviation (SD). The significance of all quantified changes, for instance produced by addition of a channel blocker or another inhibitor or by stimulating the CF alone or paired with previous PF activation, was assessed using paired Student's *T*-test. The probabilities associated with the two tests were reported below or above a certain value to assess its statistical significance. In

general, a change was defined as "significant" if $p < 0.01$, but in several cases lower values of p were reported in the individual cases described in the two following chapters. In contrast, we reported a non detectable change when $p > 0.1$.

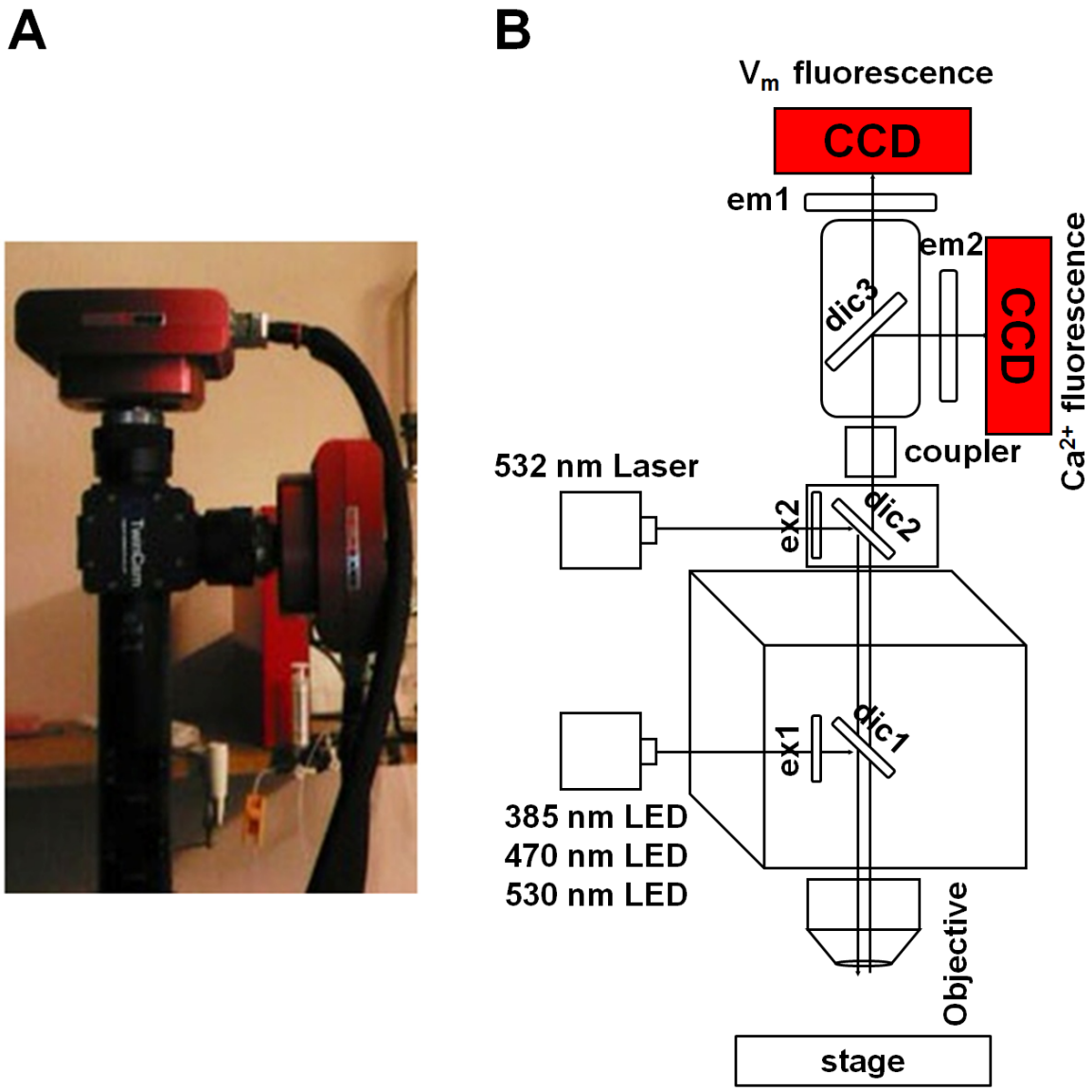

Figure 2.A. The dual NeuroCCD camera manufactured by RedshirtImaging for this type of measurement. **B.** Schematic drawing of the apparatus for sequential voltage and Ca^{2+} imaging using the VSD JPW1114 and the Ca^{2+} indicator FuraFF or for Ca^{2+} imaging only using OG5N; Light from a 385 nm or a 470 nm LED via the epifluorescence port of a commercial microscope is reflected by a 495 nm long-pass dichroic mirror (dic1); 532 nm laser light via the top of the microscope is reflected by a 560 nm dichroic mirror. (dic2); fluorescence images are demagnified and separated by a 565 nm long-pass dichroic mirror (dic3); The V_m image and the Ca^{2+} images are filtered by a 610 nm long-pass (em1) and by a 510±42 nm band-pass filter (em2) respectively, then acquired by two CCD cameras.

Chapter 3: *Dendritic Ca^{2+} and K^{+} channels activated by the CF-EPSP*

3. Dendritic Ca^{2+} and K^{+} channels activated by the CF-EPSP in PN neurons

The climbing fiber (CF), originating in the inferior olive, forms excitatory synapses with PNs in the cerebellar cortex. It makes hundreds thousands contacts in the soma and in the initial part of the PN dendritic tree (Napper & Harvey, 1991) providing a very large excitatory input in the cerebellar cortex. The CF to PN synapse is a strong neuronal connection characterized by an extremely high release probability of neurotransmitters (glutamate) (Silver *et al.*, 1998). Consequently, the excitation of CF evokes a powerful excitatory response, the large all-or-nothing complex spike EPSP (Eccles *et al.*, 1967). The activation of the CF-PN synapse has been shown to be involved in the induction of LTD at the PF-PN synapse which underlies motor learning in the cerebellum (Ito, 1984). The large somatic and peri-somatic CF-EPSP propagates into the dendritic tree with strong attenuation (Llinás and Sugimori, 1980). It has several components that are the consequence of the summation of several events. Indeed, the glutamate released from CF terminals activates AMPA receptors present in the soma and proximal dendrite of the PN generating a depolarization which triggers the first spike. The depolarization mediated by Na^{+} influx invades the dendritic tree, activates voltage-gated Ca^{2+} channels (VGCCs) leading to Ca^{2+} entry into the cell and produce slow spikelets (Schmolesky *et al.*, 2002). Dendrites of PNs lack dendritic sodium channels and therefore the sodium spike does not back-propagates into the dendrites (Stuart & Häusser, 1994) while dendritic calcium spikes may propagate towards the soma (Llinás and Nicholson, 1976). The dendritic Ca^{2+} transients evoked by the CF-EPSP are mediated by a large Ca^{2+} influx through VGCCs that are expressed abundantly in the dendrites of PNs. The intracellular elevation of Ca^{2+} activates Ca^{2+}-activated K^{+} channels which contribute to the repolarization. The dendritic depolarization induced by the CF-EPSP activates voltage-gated K^{+} channels (VGKCs). The biophysical properties of these ion channels as well their distribution

are crucial determinants of the electrical properties of the PN. Their contribution into shaping the waveform of the complex spike mirrors the direct control of the CF over the output of the cerebellar cortex. Studying the activation of these channels in their physiological environment is therefore fundamental in understanding the role they play while CF input fulfills its function in transmitting information to the PN dendrite.

The optical approach I used in my experiments has been recently developed and improved at the laboratory and I contributed to the latest stages of these developments. It consists in combining voltage imaging using the voltage sensitive dye JPW1114 and fast Ca^{2+} imaging using the low affinity indicator FuraFF or, alternatively, fast Ca^{2+} imaging only using the low affinity indicator OG5N (see Material and Methods). The imaging device used in these experiments allows acquiring optical signals at high temporal resolution (5 kHz). Initially, this optical approach has been applied on CA1 hippocampal pyramidal neurons to record Ca^{2+} currents optically. Our team has reported a first study of local dendritic Ca^{2+} current during back-propagating action potentials based on direct optical measurements (Jaafari and Canepari, 2016). At the beginning of my PhD, I contributed to the extension of this approach to investigate Ca^{2+} signals in PNs (Ait Ouares *et al.*, 2016). We thus took advantage of this optical tool to characterize, for the first time, the Ca^{2+} transients and the large depolarization associated with the CF-EPSP. We first reported the first measurements of the dendritic V_m and Ca^{2+} transients associated with the CF-EPSP at different initial V_m state. The analysis of the correlation between dendritic V_m signal and Ca^{2+} transient allows investigating Ca^{2+} transients as they occur in their physiological environment. We then sought to characterize separately the activation of dendritic Ca^{2+} or K^+ ion channels during the CF-EPSP. To this purpose, we used highly selective pharmacological blockers to inhibit VGCCs, SK and BK which are Ca^{2+}-activated K^+ channels and A-type VGKCs then we examined the change in V_m and Ca^{2+} transients at different initial V_m.

3.1 Dendritic depolarization and Ca^{2+} transients associated with the CF-EPSP

CF stimulation generates an EPSP in the cell body and in the proximal area of the dendrites that propagates into the more distal dendritic tree. The subsequent depolarization activates dendritic VGCCs channels and evokes transient a Ca^{2+} influx into the cytosol. The amplitude of the dendritic Ca^{2+} transients varies according to the initial V_m. The main objective of this first experimental investigation was to assess the dendritic V_m and the Ca^{2+} signals associated with the CF-EPSP at different initial states of the V_m. To this aim, we combined V_m and Ca^{2+} imaging measurements as described in the Material and Methods. We loaded PNs with the VSD JPW1114 after establishing the whole cell configuration and left the indicator equilibrating 1 hour. Then, we repatched the cells in order to load them with 1 mM of the Ca^{2+} indicator FuraFF. The recording of V_m and Ca^{2+} signals was performed at 5 kHz and data were originally expressed as $\Delta F/F_0$. To improve the signal-to-noise ratio, nine trials for V_m signals and four trials for Ca^{2+} signals were averaged.

We first proceeded to a direct quantification of V_m signals which is provided by the calibration of $\Delta F/F_0$ V_m on an absolute scale (mV). This quantification is crucial to compare V_m signals associated with CF-EPSP obtained from different dendritic regions and to allow the analysis of the voltage gating of Ca^{2+} channels associated with the CF-EPSP at the same region where the Ca^{2+} signals transients are recorded. Nevertheless, the absolute calibration of $\Delta F/F_0$ V_m signals is not a straightforward procedure and the exact calibration is impossible. Indeed, the fractional change of VSD fluorescence is not only relative to V_m, but also to the ratio of inactive dye to active dye which is not known. While the inactive dye contributes only to the resting fluorescence and it is bound to membranes that are not activated and other organelles, the active dye is bound to the excitable membranes that are activated and the light from this active dye carries the signal and contributes to the

resting fluorescence as well. Consequently, the sensitivity of VSD- $\Delta F/F_0$ recordings differs from one site to another site of the cell. The fact that $\Delta F/F_0$ corresponding to a given V_m signal from a given site is quite stable in many acquisition trials, permits a calibration of the VSD- $\Delta F/F_0$ signal in terms of V_m if an electrical signal that has a known amplitude is obtainable at all recordings sites. The action potential signal can be used to calibrate $\Delta F/F_0$ of the VSD in some cell types. For instance, in mitral cells of the olfactory bulb, as the axo-somatic actions potentials propagate without attenuation throughout the whole apical dendrite, they are used to calibrate the amplitudes of V_m optical signals (Djurisic *et al.*, 2004). PNs do not fire actions potentials that propagate into the dendrites. Therefore, In the case of this cell type, a prolonged hyperpolarizing pulse that propagates from the soma to the dendrites with slight amplitude attenuation constitutes an alternative approach to calibrate the $\Delta F/F_0$ of VSD (Stuart and Häusser, 1994). Figure 3.1.1 illustrates an example of this calibration. We assume that the resting V_m is identical over the entire cell. Once the PN is held at resting V_m, we inject via the recording patch pipette a hyperpolarizing or depolarizing current pulses of 1s duration to the soma and the corresponding V_m change is recorded. In this case, since the somatic hyperpolarization propagates into the dendrites with negligible attenuation, the recording of somatic V_m are used to convert the dendritic VSD-$\Delta F/F_0$ signals to values expressed in mV in order to quantify the dendritic V_m transients associated with the CF-EPSP. On the contrary, the somatic depolarization attenuates while spreading along the dendrites; therefore, it cannot be used to calibrate VSD-$\Delta F/F_0$ signals. However, since the fluorescence change is linear with the V_m change, once the calibration is obtained for hyperpolarizing pulses, it is possible to estimate the correct dendritic V_m corresponding to the depolarizing pulses. In this way, in our experiments, we could systematically assess the initial V_m at any region of interest, as well in the case of depolarizing states. An important aspect of combined V_m and Ca^{2+} imaging is the interpretation of Ca^{2+} optical signals, which depends on the indicator Ca^{2+} buffering capacity relative to the cell endogenous buffering capacity and on how much the Ca^{2+}

indicator perturbs the physiological Ca^{2+} homeostasis. PNs have an especially high dendritic K_{cell} estimated at ~2,000 (Fierro and Llano, 1996).

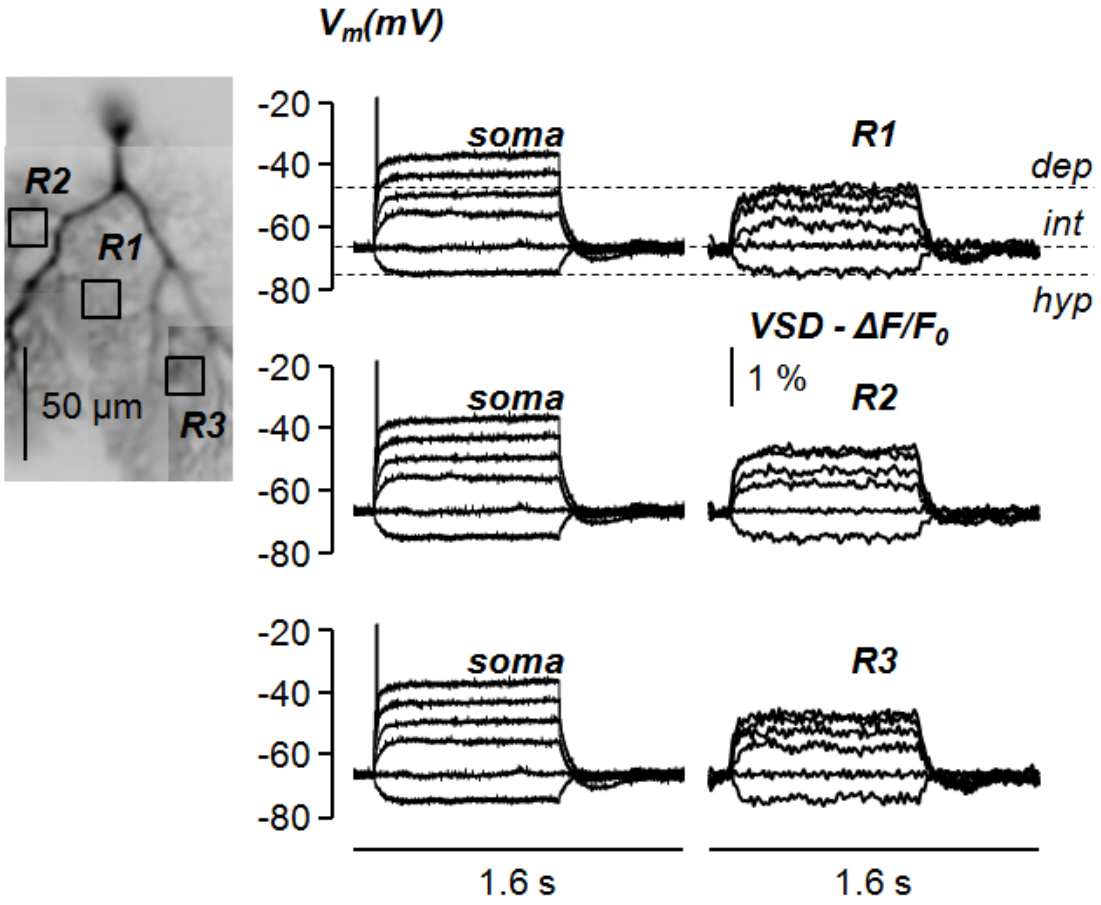

Figure 3.1.1: calibration Protocol for dendritic V_m

On the left, the fluorescence reconstruction of a PN loaded with the voltage sensitive dye JPW1114 indicating the three regions of interest (R1, R2 and R3) where the V_m signals were calibrated. On the right, the somatic V_m associated with long hyperpolarizing and depolarizing pulses and the corresponding dendritic VSD-$\Delta F/F_0$ from the three regions of interest. The hyperpolarization step was used to calibrate the VSD $\Delta F/F_0$ signals because it spreads to the dendrites with minimal attenuation. The depolarization step was used to estimate the initial V_m in the dendrites when the cell is depolarized by somatic current injection.

In our experiments, the addition of a low affinity Ca^{2+} indicator, such as FuraFF (Kd ~10), even at millimolar concentrations, generates minor impact on the physiological Ca^{2+} homeostasis and validates the condition of $K_{cell} \gg K_{dye}$ (see Materials and Methods). The initial somatic V_m was set at resting values by current injection and the CF was stimulated at different initial V_m by increasing the intensity of the current injected. The initial V_m were: the hyperpolarized V_m state (*hyp*, blue trace) around -80 mV, the intermediate V_m (*int*, green trace) close to the resting V_m (-65 mV) and the depolarized state (*dep*, red trace) > -55 mV as indicated in Figure 3.1.2A. Dendritic V_m and Ca^{2+} transients associated with the CF-EPSP at the three different initial V_m states were analyzed in the two regions of interest R1 and R2 (~17X17 μm^2, 3X3 pixels) and the results are reported in Figure 3.1.2B. For both regions, the dendritic V_m associated with the CF-EPSP evoked at initial *hyp*, *int* and *dep* states was -83, -64 and -54 mV, respectively. In R1, the dendritic V_m associated with the CF-EPSP evoked at initial *hyp* state reached a peak value of -17 mV whereas, at initial *int* and *dep* state, it reached a peak value of +10 mV. In R2, the dendritic V_m associated with the CF-EPSP evoked at initial *hyp* state reached a peak of -20 mV whereas at initial *int* and *dep* state, it reached a peak value of +5 mV. Interestingly, in both regions, the dendritic V_m increased in peak from the initial *hyp* state to the initial *dep* state displaying a second sharp peak at the *dep* state. Likewise, the corresponding FuraFF-$\Delta F/F_0$ signals increased in amplitude from the initial *hyp* state to the initial *dep* state and exhibited a second sharp peak at the *dep* state. Next, we further extended the analysis of the results obtained from the region R1 by performing a quantitative analysis as illustrated in figure 3.1.2C. For both dendritic V_m and Ca^{2+} signals ($-\Delta F/F_0$), we measured the peak occurring during the first 4 ms after the CF stimulation (first peak) and the peak occurring between 4 and 14 ms after the CF stimulation (second peak).

Figure 3.1.2: Combined V_m and Ca^{2+} transients associated with the CF-EPSP at different initial holding V_m.

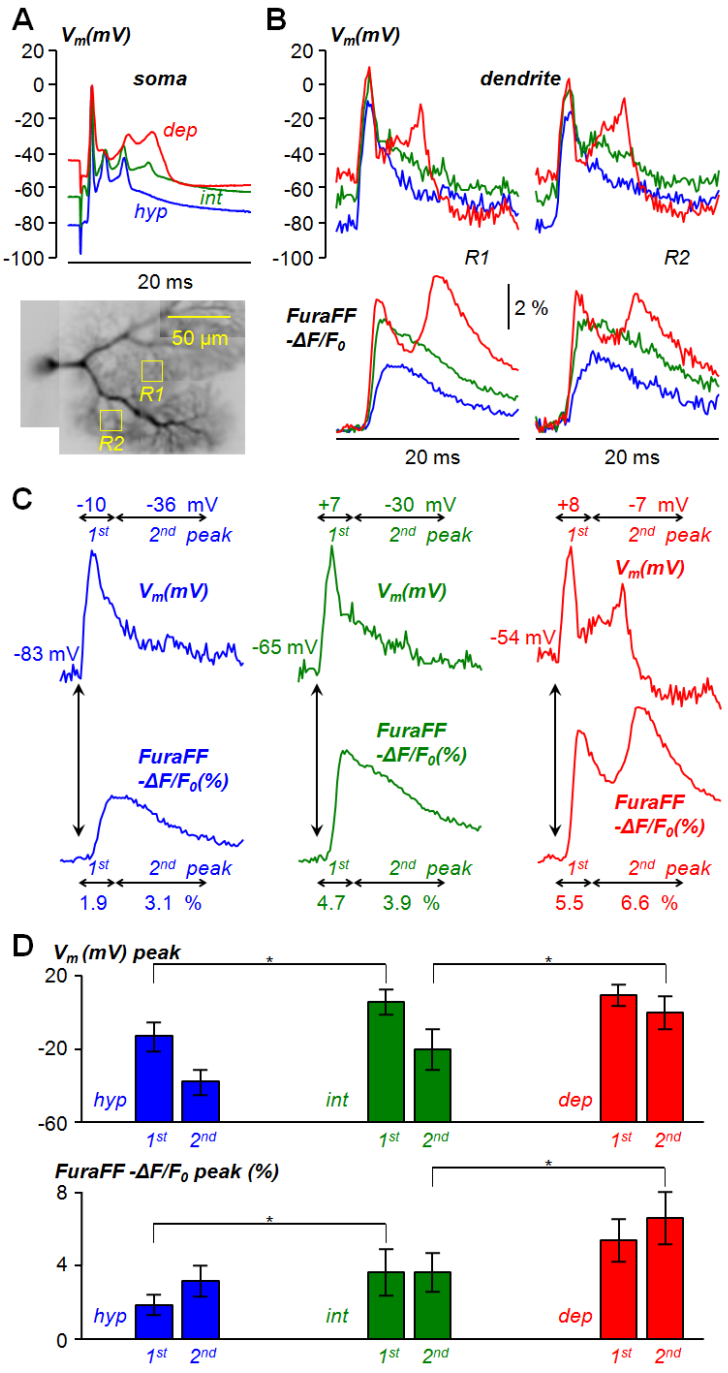

A. On the top, the electrophysiological traces of the somatic V_m associated with the CF-EPSPS held at three different initial V_m, *hyp* (blue traces) with initial V_m between -87 mV and -74 mV, *int* (green traces) with initial V_m between -68 mV and -61 mV, *dep* (red traces) with initial V_m between -54 mV and -46 mV. On the bottom, PN fluorescence reconstruction indicating the two regions of interest (R1 and R2) where the signals were analyzed. The PNs is loaded with the VSD JPW1114 and 1 mM FuraFF. **B.** On the top, the calibrated dendritic V_m for the R1 and R2; on the bottom, the corresponding FuraFF-$\Delta F/F_0$ signals. **C.** Quantitative analysis of the V_m signals (top) and Ca^{2+} signals (bottom) recorded in R1 (B). On the right, at *hyp* V_m state (blue traces). In the middle, at *int* V_m state (green traces). On the right, at *dep* V_m state (red traces). The analysis is performed on the first and second peak of V_m and Ca^{2+} signals. The first peak is calculated within the first 4 ms after the CF stimulation and the second peak is calculated between 4 and 14 ms after the CF stimulation. **D.** Mean ± SD for 19 regions in 12 cells analysed as illustrated in panel *C.* the significant increase in the peak is designated by the asterisk symbol ($p < 0.005$, paired t-test).

At the *hyp* state (corresponding to initial V_m of -83 mV), the first V_m peak was -10 mV and the second V_m peak was -36 mV, whereas the first Ca^{2+} signal peak was 1.9 % and the second Ca^{2+} signal peak was 3.1 %. At the *int* state (corresponding to initial V_m of -65 mV), the first V_m peak was -7 mV and the second V_m peak was -30 mV, whereas the first Ca^{2+} signal peak was 4.7 % and the second Ca^{2+} signal peak was 3.9 %. Finally, at the *dep* state (corresponding to initial V_m of -54 mV), the first V_m peak was +8 mV and the second V_m peak was -7 mV, whereas the first Ca^{2+} signal peak was 5,5 % and the second Ca^{2+} signal peak was 6.6 %. Figure 3.1.2D illustrates the statistic (mean ± SD) for 19 regions in the 12 cells analysed. At *hyp* states (with initial V_m between -87 mV and -74 mV), the first and the second V_m peaks were -13 ± 8 mV and -38 ± 7 mV respectively, while the Ca^{2+} signals peaks were 1.83 ± 0.55 % and 3.14 ± 0.85 % respectively. At *int* states (with initial V_m between -68 mV and -61 mV), the first and the second V_m peaks were 6 ± 7 mV and -21 ± 11 mV respectively, while the Ca^{2+} signal peaks were 3.65 ± 1.27 % and 3.65 ± 1.05 % respectively. Finally, at *dep* states (with initial V_m between -54 mV and -46 mV), the first and the second V_m peaks were 9 ± 6 mV and -1 ± 9 mV respectively, while the Ca^{2+} signals peaks were 5.36 ± 1.17 % and 6.59 ± 1.42 % respectively. The first peak of both V_m and Ca^{2+} signals significantly increased from the *hyp* state to the *int* state ($p < 0.005$, paired t-test), while the second peak of both the V_m and Ca^{2+} signals significantly increased from the *int* state to the *dep* state ($p < 0.005$, paired t-test). Additionally, when the dendrites were more depolarized, V_m and Ca^{2+} signals exhibited two dendritic spikes that occur in 18 ms after the CF stimulation. These results indicate that the amplitude of dendritic V_m and the Ca^{2+} signals increases with the increase in the initial V_m state. Moreover, dendritic spikes occur only at depolarized membrane potentials. The dendritic depolarization is produced by the passive spread of the CF-EPSP from the site of origin into the dendrites that activates VGCCs and VGKCs. The subsequent Ca^{2+} influx activates Ca^{2+}-activated K^+ channels. In order to characterise in detail all the relevant channels responsible of

the behavior observed in the experiments reported above, we analysed pharmacologically in detail Ca^{2+} transients associated with the CF-EPSP.

3.2 Dendritic VGCC channels activated during CF-EPSP at different initial V_m state

The passive propagation of the CF-EPSP into the dendrites of PNs activates VGCCs that mediate Ca^{2+} influx. Intracellular Ca^{2+} elevation is a fundamental process in neuronal integration and it is involved in the induction of LTD at PF-PN synapse (Ito, 1984). A wide range of VGCCs are expressed in the dendrites of PNs with different biophysical and pharmacological properties. They underlie electrical excitably, calcium signaling and signal integration processes. The dendrites of PNs express predominantly P/Q- and T- types VGCCs and the large fraction of the Ca^{2+} entering during active events is mediated by T- and P/Q-type Ca^{2+} channels (Raman and Bean, 1999), although N-, L-, and R-type channels seem to be also present but with lower level of expression (Regan, 1991). VGCCs contribute to shape the output of PN in response to the stimulation of synaptic inputs. P-type channel, originally identified in PNs ("P" refers to Purkinje) (Llinas *et al.*, 1989; Usowicz *et al.*, 1992) is a high-threshold activating channel displaying slow inactivation kinetics (Regan, 1991). While P-channels (now more commonly defined P/Q channels), expressed at presynaptic terminals, play a pivotal role in neurotransmitter release, P/Q-channels presents at somatodendritic membrane contribute essentially to neuronal excitability and integration (Catterall *et al.*, 2005). In PNs, P/Q-type channels display high level of expression in the dendrites (Llinás *et al.*, 1989; Usowicz *et al.*, 1992). They are activated by membrane depolarization evoked by the stimulation of CF inputs and strong stimulation of PFs. They are fundamentally involved in the generation of dendritic Ca^{2+} spikes and the slow Ca^{2+} plateau potentials (Llinas and Sugimori 1980; Konnerth *et al.,* 1992; Regehr and Mintz 1994; Regan, 1991).

In this first section of the pharmacological experiments, we investigated the activation of P/Q-type VGCC during the CF-EPSP at different initial V_m states. We examined the change in the dendritic Ca^{2+} associated with CF-EPSP induced by the blockade of P/Q-type VGCC by ω-Aga-IVA (AgaIVA). AgaIVA, a component of the venom of the funnel-web spider, Agelenopsis aperta, is a potent inhibitor of P-type channels, with an IC_{50} of <1 nM and has no effect on T-type, L-type, or N-type currents in a different central and peripheral neurons (Mintz *et al.*, 1992). Furthermore, AgaIVA was used during the experiment at relatively high concentration for such selective toxin (1 µM), which block both P- and Q- types VGCC channels. In fact, this concentration is necessary since the toxin was applied locally, on the slice surface and the actual concentration reaching the dendrite is likely lower. In these experiments, we loaded PNs with 2 mM of OG5N and left equilibrating for about 20 to 30 minutes. In order to locally block P/Q-type VGCC channels, a glass pipette was placed next to the region R1 to deliver 1 µM of the AgaIVa toxin as indicated in Figure 3.2.1A. P/Q-type channels are present at presynaptic terminals and their blockade would affect the CF synaptic transmission. In our experiments, when applying AgaIVA, any small spillage could affect the P/Q channels present at presynaptic terminals. Thus, a region R2 situated > 50 µm away from the site of AgaIVA application was used as a control as indicated in Figure 3.2.1A. CF-EPSPs were evoked at a *hyp* state (blue trace), at an *int* state (green trace) or at a *dep* state (red trace) and the associated OG5N-$\Delta F/F_0$ signals were recorded and analysed in R1 and R2 before and after the application of AgaIVA as reported in Figure 3.2.1A. The action of AgaIVA was observed during the first few milliseconds following CF stimulation. In R1, the blockade of P/Q-type VGCC channels by AgaIVA produced a reduction in the Ca^{2+} signal associated with the CF-EPSP at *hyp and int* states and the toxin blocked almost entirely the Ca^{2+} signal at the *dep* state. Additionally, the block of P/Q-type channels was associated with a change in the kinetics of Ca^{2+} transients.

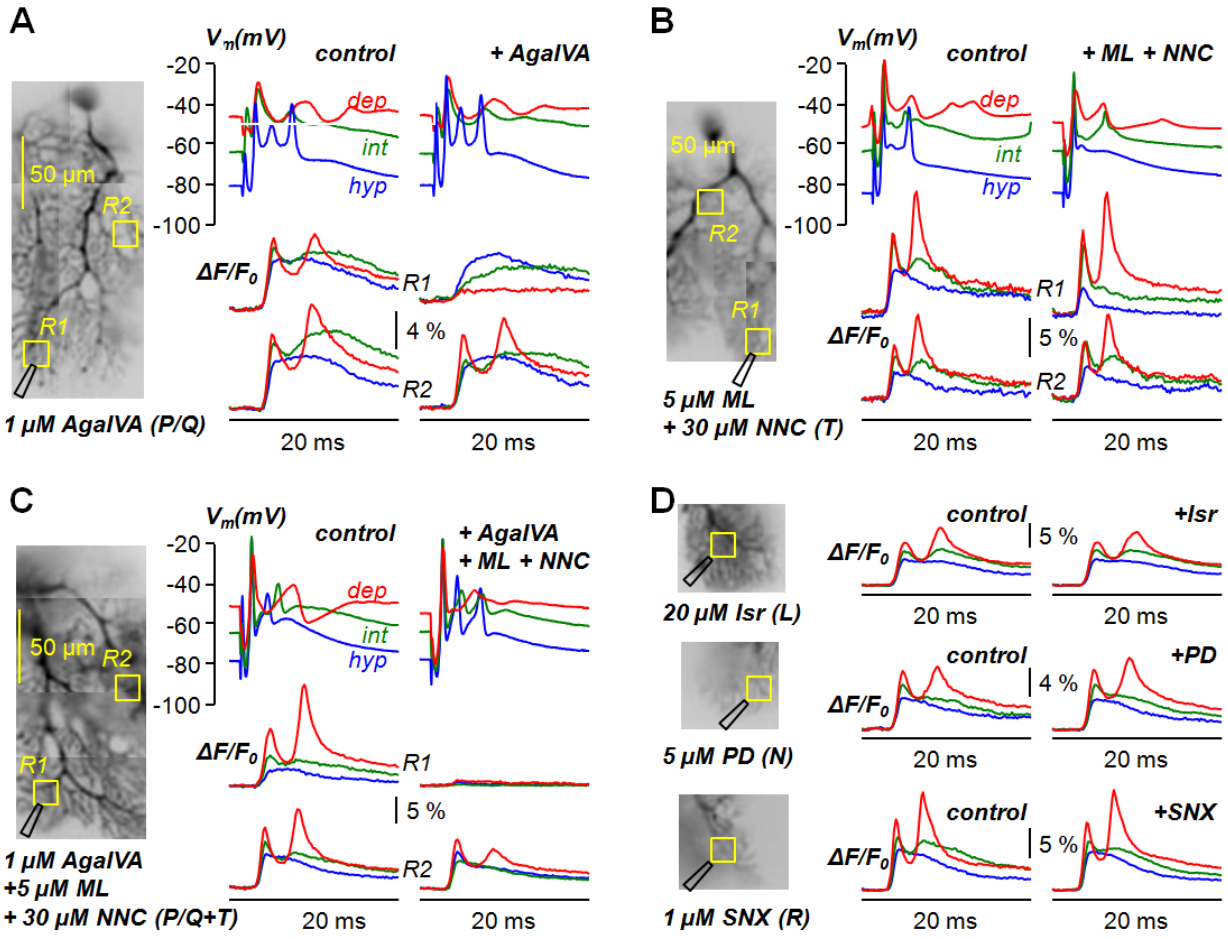

Figure 3.2.1: dendritic VGCCs activated during CF-EPSP at different initial states of V_m.

A. Right, fluorescence reconstruction of a PN filled with 2 mM of OG5N displaying tow regions of interest R1 and R2. A glass pipette is placed in the R1 to deliver 1 µM of the P/Q-type VGCC blocker AgaIVA and the R2, control region, is >50 µm away from the application pipette. Left, on the top, somatic V_m associated with CF-EPSPs in control conditions and after local application of AgaIVA at three different initial V_m: *hyp* (blue trace); *int* (green trace); *dep* (red trace).in the middle and on the bottom the corresponding OG5N-$\Delta F/F_0$ signals for R1 and R2 respectively. **B.** The same as in A, but in another PN and the pipette is placed in the R1 to deliver 5 µM of ML and 30 µM of NNC, tow T-type VGCCs selective blockers. **C.** Same as in A, in another PN, the pipette delivers both P/Q-type VGCC blockers (AgaIVA) and T-type VGCC blockers (ML + NNC) with the same concentration used above. **D.** Right, Fluorescence reconstruction of three PNs indicating a region of interest where the pipette is positioned to deliver 20 µM of the L-type VGCC blocker ISR (top), 5 µM of the N-type VGCC blocker PD (middle) or 1 µM of the R-type VGCC blocker SNX (bottom). Left, are reported the OG5N $\Delta F/F_0$ signals associated with CF-EPSPs at the three initial V_m state in control conditions and after local application of ISR (top), PD (middle) or SNX (bottom).

In R2, however, both the somatic CF-EPSP and the associated dendritic Ca^{2+} signals remained unaffected at the three initial V_m states demonstrating that AgaIVA had no effect on the presynaptic P/Q type VGCCs or on the CF-synaptic transmission in this protocol that utilises a local application of the channel blocker.

The low thresholds T-type VGCCs are also expressed in the soma and dendrites of PNs with a particular high density in the spine of PF synapse (Ly *et al.,* 2016; Isope and Murphy 2005). They are characterized by fast activation and relatively fast inactivation kinetics (with respect to P/Q channels). They entirely inactivate at depolarized V_m. These channels underlie regenerative low threshold spikes and contribute to burst firing (Kaneda *et al.*, 1990; Llinas *et al.,* 1992). At PF-PN synapse, they activate in response to subthreshold depolarization mediating Ca^{2+} influx into the spines and are critically involved in synaptic transmission at these synapses (Isope and Murphy 2005). Furthermore, by their depolarizing action, they contribute to bring membrane potential to a level required to boost P/Q-type channel activation (Llinas *et al.,* 1992; Watanabe *et al.,* 1998; Otsu *et al*., 2014). Given their important role, we investigated the activation of T-type channels during the CF-EPSP. To this end, we examined the change in the dendritic Ca^{2+} signals associated with CF-EPSPs evoked at the three initial V_m state produced by the block of T-type VGCCs by a cocktail of ML218 (ML, 5µM) and NNC550396 (NNC, 30 µM), both highly selective T-type channels blockers (Huang *et al.,* 2004; Xiang *et al.,* 2011).In another PN, the same procedure, as in the P/Q channels blockade, was performed as represented in Figure 3.2.1B. The OG5N-$\Delta F/F_0$ signals associated with the CF-EPSPs at three initial V_m states were analyzed in R1 and in R2 before and after the block of T-types VGCCs and the results are reported in the Figure 3.2.1B. In R1, while the blockade of T-type VGCC produced an observable reduction in the amplitude and a change in the kinetics of Ca^{2+} signals associated with CF-EPSP evoked at initial *hyp* and *int* states, it had no effect on the Ca^{2+} signal at the *dep* state. In R2, the Ca^{2+} signals and the somatic CF-EPSPs remained unaffected at the

three initial V_m state suggesting that neither T-type VGCC at presynaptic terminals nor the CF synaptic transmission was affected by the block of T-type channels. P/Q- and T-type VGGC conduct the large majority of the calcium current in PNs (Regan, 1991; Usowicz *et* al., 1992; Kaneda *et al.*, 1990; Bean *et al.*, 2003). We therefore examined the change in Ca^{2+} signals associated with CF-EPSP produced by the block of

P/Q- and T-type VGCC together. Again, in another PN, a glass pipette was positioned near R1 to deliver locally both P/Q- and T-type VGCC blockers (AgaIVA + ML + NNC) at the same concentration used above. The OG5N-$\Delta F/F_0$ signals associated with CF-EPSP evoked at the three initial V_m states are reported in the Figure 3.2.1C. In R1, the block of P/Q- and T-type VGCC completely abolished the Ca^{2+} signals at all initial V_m states. However, the Ca^{2+} signals in R2 remained unaffected indicating that the CF mediated transmission was not affected by the VGCC blockers. Because other types of VGCCs (L-,R- and N-type) are found to be expressed in PNs with minor contribution to the Ca^{2+} current (Raman and Bean, 1999), we investigated the activation of these channels during the CF-EPSP. We thus examined the change in Ca^{2+} signals associated with the CF-EPSP at the three initial V_m produced by using potent selective blockers specific for these three channels. L-type channels are sensitive to Isradipine (Isr, Ruegg and Hof 1990); N-type channels are sensitive to PD 173212 (PD, Hu *et al.*, 1999) and finally R-type channels are sensitive to SNX 482 (SNX, Newcomb *et al.*, 1998). In three different PNs, we blocked separately L-, N- or R-type VGCC by local application of 20 µM of Isr, 5 µM of PD or 1 µM of SNX respectively and the OG5N-$\Delta F/F_0$ signals associated with the CF-EPSP evoked at the three initial V_m before and after the blockade of these channels were analysed as reported in Figure 3.2.1D. The block of all other channels had no effect on the Ca^{2+} transient associated with the CF-EPSP at all initial states of V_m. All the results reported in Figure 3.2.1 were consistently observed in all cells tested with each VGCC blockers. We again performed a quantitative

analysis on the $\Delta F/F_0$ signals associated with CF-EPSP recorded in control conditions and after the block of VGCC channels. We similarly calculated the first peak occurring during the first 4 ms after the CF stimulation and the second peak occurring between 4 ms and 14 ms after the CF stimulation in both conditions. Then, we calculated the % of change between the first and the second peak of $\Delta F/F_0$ signals produced by the block of VGCCs and the first and the second peak in control conditions. From two representative cells where either AgaIVA or ML + NNC were locally applied, $\Delta F/F_0$ signals at the three initial V_m in control conditions (*hyp*: blue trace, *int*: green trace, *dep*: red trace) are superimposed with $\Delta F/F_0$ signals after the block of either P/Q or T-type channels at each initial V_m state (gray traces) as illustrated in Figure3.2.2, on the left. The % of change values for both the first and the second peak of $\Delta F/F_0$ signals at the three initial V_m are reported above or below the arrows. At *hyp* states, local application of AgaIva reduced the first peak by 44 % and the second peak by 6 % while local application of T-type blockers reduced the first peak by 40 % and the second peak by 75 %. At *int* states, local application of AgaIva reduced the first peak by 81 % and the second peak by 57% while local application of T-type blockers reduced the first peak by 2 % and the second peak by 52 %. Finally, at *dep* states, local application of AgaIVA reduced the first peak by 82 % and the second peak by 86 % while local application of T-type blockers affect neither the first peak nor the second peak. Figure 3.2.2, on the left, illustrates the statistics (mean + SD) of the % of change values for the first peak (gray columns) and for the second peak (White columns) of $\Delta F/F_0$ signals at the three initial V_m after the block of P/Q-type VGCCs (AgaIVA), or T-type VGCC (ML + NNC) or P/Q-type and T-type VGCCs together (AgaIVA + ML + NNC) in six cells for each case and after the block of L-type VGCCs (Isr), or N-type VGCC (PD) or R-type VGCCs (SNX) in 4 cells for each case. The block of P/Q-type VGCC channels significantly reduced the first peak of the Ca^{2+} signal at the three V_m states with up to 80% of reduction in the first peak at initial *dep* state whereas it only significantly reduced the second peak at *dep* state.

Figure 3.2.2: Ca^{2+} channels activated by the CF-EPSP at different initial V_m state.

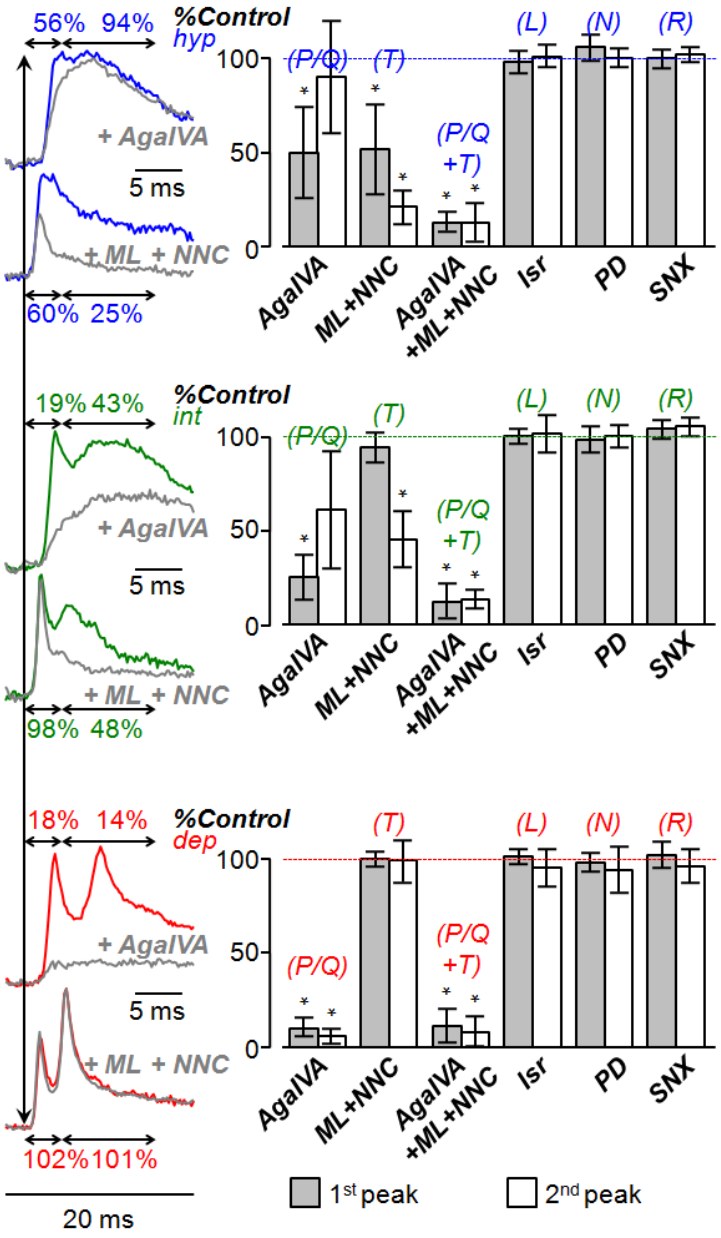

Quantitative analysis of the Ca^{2+} signals obtained from two representative cells where either 1 µM of the P/Q-type VGCC blocker AgaIVA or of the T-type VGCC blockers ML (5 µM) and NNC (30 µM) are applied. On the right, OG5N-$\Delta F/F_0$ signals associated with the CF-EPSP in control conditions at three different initial V_m: *hyp* (blue trace); *int* (green trace); *dep* (red trace), superimposed (gray traces) are the OG5N-$\Delta F/F_0$ signals associated with the CF-EPSP after local application of the VGCC blockers at three different initial V_m. For $\Delta F/F_0$ signals obtained before and after application of the blockers, the first peak of the Ca^{2+} transient is calculated within the first 4 ms and the second peak is calculated between 4 and 14 ms after the CF stimulation. The % of change in $\Delta F/F_0$ Ca^{2+} signals after application of the blockers relative to control $\Delta F/F_0$ Ca^{2+} signals for the first and second peak are reported above or below the arrows. Right, mean ± SD of the % of change from control $\Delta F/F_0$ peaks after application of the VGCC inhibitors AgaIVA (N = 6 cells), ML+NNC (N + 6 cells), AgaIVA+ML+NNC (N = 6 cells), Isr (N = 4 cells), PD (N = 4 cells) or SNX (N = 4 cells). Gray columns are the statistics of the 1st peak; white columns are the statistics of the 2nd peak; the significant change in the peak is de designated by the asterisk symbol "*" ($p < 0.005$, paired t-test).

.

The block of T-type VGCCs significantly reduced the first peak only at initial *hyp* state while it significantly reduced the second peak at both initial *hyp* and *int* states. The block of P/Q and T-type VGCCs together dramatically reduced both the first and the second peak Ca^{2+} signals associated with the CF-EPSP at the three initial V_m states. These effects were observed in each cell tested. The block of other VGCCs channels (R-, N-, L-type) had no effect on both the first and the second peak of Ca^{2+} signals associated with the CF-EPSPS at the three initial V_m state and thus in each cell tested ($p < 0.005$, paired t-test, see Table 1).

Signal (% control) / **Channel block**		*Hyp*		*Int*		*Dep*	
		1st max	2nd max	1st max	2nd max	1st max	2nd max
P/Q	+1 µM AgaIVA (N = 6 cells)	50 ± 24*	90 ± 30	25 ± 12*	61 ± 31	10 ± 5*	6 ± 4
T	+5 µM ML+30 µM NNC (N = 6 cells)	52 ± 24*	21 ± 9*	94 ± 8	45 ± 15*	100 ± 4	99 ± 11
A	+1 µM AmmTx3 (N = 6 cells)	151 ± 34*	187 ± 44*	114 ± 8*	160 ± 33*	102 ± 4	102 ± 5
BK	+1 µM iberiotoxin (N = 5 cells)	97 ± 5	99 ± 5	98 ± 3	98 ± 4	98 ± 9	106 ± 5
SK	+1 µM apamin (N = 6 cells)	101 ± 9	101 ± 10	100 ± 8	99 ± 6	103 ± 7	97 ± 8

Table 1

Comparison of the percentage of the control Ca^{2+} transient (mean ± SD of the 1st and 2nd maxima) produced by the pharmacological block of a channel type. The number of cells used for the statistics is indicated.

During the experiments, while applying the VGCC blockers, the possible block of the VGCCs expressed at the site of release of CF synapse affects the CF transmission and alters the interpretation of our results. To rule out any effect of the application of the VGCC blockers on the CF transmission, the change in Ca^{2+} signals were assessed in another region situated more than 50 µm away from the site of application. In all experiments, the block of VGCC channels had no effect on the CF synaptic transmission. The block of both P/Q and T-type VGCC suppressed almost completely the Ca^{2+} signals associated with the CF-EPSP at all initial V_m states while the block of all other VGCCs had no effect on the Ca^{2+} signals. These results demonstrate that the CF-EPSP evoked Ca^{2+} transients are exclusively mediated by P/Q- and T-type VGCC and confirm the fact that these channels, predominantly expressed on the dendrites of PNs, are responsible of the Ca^{2+} current in response to the activation of CF synaptic input. On the other hand, they demonstrate that the concentrations at which the blockers were applied are enough to block selectively the targeted VGCC channels. Notably, there was variability in the change of the Ca^{2+} signals associated with the CF-EPSP produced by either application of AgaIVA or ML + NNC at the three initial V_m states. The application of AgaIVA produced a significant reduction in the Ca^{2+} signals at all V_m states with a maximal reduction at *dep* states. This result indicates that P/Q-type channels are already activated in response to the CF-EPSP at initial *hyp* and *int* states, but they reach maximal activation only at more depolarized V_m to trigger Ca^{2+} spikes. The application ML+ NNC, on the other hand, reduced the Ca^{2+} signal associated with the CF-EPSP at *hyp* and *int* states, but had no effect on the Ca^{2+} signal at *dep* states. This result confirms that T-type channels are capable to activate in response to a CF-EPSP exclusively at *hyp* and *int* states, while they fully inactivate as the V_m becomes more positive. Moreover, the quantitative analysis performed on the Ca^{2+} signals associated with the CF-EPSP before and after the block of Ca^{2+} channels indicated that the application of AgaIVA produced a significant reduction mostly in the first peak of the Ca^{2+} signals while the application of ML+NNC produced a significant reduction mostly in the second peak.

The Ca^{2+} signals at all initial V_m displays a first component that peaks fast (first peak) and a second component that peaks slower (second peak). P/Q-type channels exhibit fast activation kinetics whereas T-type channels display slow activation and inactivation kinetics. The block of P/Q-type channels affects mostly the first peak indicating that the fast component of Ca^{2+} signals associated with the CF-EPSP is mediated by these VGCCs while the block of T-type channels affects mostly the slow component of the Ca^{2+} signals indicating that the slow component is mediated by these other channels.

3.3 Dendritic Ca^{2+}-activated K^+ channels activated by the CF-EPSP

In PNs, CF-EPSP mediated intracellular Ca^{2+} rise through VGCCs activates Ca^{2+}-activated K^+ channels (Jacquin *et al.*, 1999, Womack & Khodakhah, 2002). In central neurons, Ca^{2+}-activated K^+ channels are involved in the modulation of membrane excitability through the regulation of the firing properties (Sah et *al.*, 1996). Both type of Ca^{2+}-activated K^+ channels are expressed in PNs (BK and SK channels) where they play a distinct and fundamental role in the generation of PNs electrical behavior (Jacquin *et al.*, 1999; Cingolani *et al*., 2002). Beside their involvement in firing activity of PNs, they also contribute to CF-meditaed signaling (Womack & Khodakhah, 2002a, 2003; Edgerton & Reinhard, 2003). BK channels are expressed in the soma and in the dendrites of PNs (Gahwiler and Llano 1989; Gruol *et al.*, 1991). ‘’B’ stands for ‘big’ since they conduct large inward currents. To be maximally activated under physiological condition, BK channels necessitate both intracellular Ca^{2+} increase and membrane depolarization (Womack and Khodakhah, 2002). Given their voltage dependence, BK channels are mostly active during the peak of APs and less active near resting membrane potentials. They play an essential role in APs repolarization and they contribute to fast after-hyperpolarization (AHP) generated by somatic and dendritic calcium spikes (Edgerton and Reinhart,

2003; Womack & Khodakhah, 2002b). The AHP is important to limit the spread of dendritic Ca^{2+} spike (Rancz and Hausser, 2006). Additionally, when PN are depolarized, PLC-dependent store-released Ca^{2} selectively activates BK channels (Canepari and Ogden, 2006).

We first investigated the activation of BK channels during the CF-EPSP. To this end, we examined the change in Ca^{2+} signals associated with the CF-EPSP produced by the block of BK channels by Iberiotoxin, a selective blocker of BK channels (Galvez *et al.*, 1990), at different initial states of V_m. In PNs filled with 2 mM of OG5N, a glass pipette was positioned near a region of interest to deliver 1 µM Iberiotoxin. Figure 3.3A. reports Ca^{2+} signals associated with the CF-EPSP at different initial V_m: *hyp* V_m state (blue trace); *int* V_m state (green trace); *dep* V_m state (red trace) before and after Iberiotoxin application. While blocking BK channels had no effect on Ca^{2+} signals at *hyp* and *int* state, it induced a third spike in Ca^{2+} signals at *dep* states. We next investigated the activation of SK channels during the CF-EPSP. Among the three subunits of SK channels, PNs express only SK2 channels which are highly sensitive to Ca^{2+} (Cingolani *et al.*, 2002; Stocker and Pedarzani, 2000). In contrast to BK channels, SK channels conduct very small currents, are exclusively activated by intracellular Ca^{2+} elevation and don't require membrane depolarization for their activation (Kohler *et al.*, 1996; Xia *et al.*, 1998). At the functional level, SK channels regulate primarily spike firing frequency and unlike BK, they contribute to the slow after-hyperpolarization (AHP) current (Pedarzani et *al.*, 2001; Hosy et *al.*, 2011; Edgerton and Reinhard, 2003; Womack *et al.*, 2003). We examined the change in Ca^{2+} signals associated with the CF-EPSP produced by the block of SK channels by Apamin, a highly selective blocker of SK channels (Van der Staay *et al.*, 1999). The same protocol was performed as in the block of BK channels. A glass pipette was placed in the region of interest to deliver 1 µM of Apamin and Ca^{2+} signals associated with the CF-EPSP at the three initial V_m before and after local application of Apamin were analysed and reported in Figure 3.3B.

Figure 3.3: Dendritic Ca^{2+}-activated K^+ channels activated by the CF-EPSP.

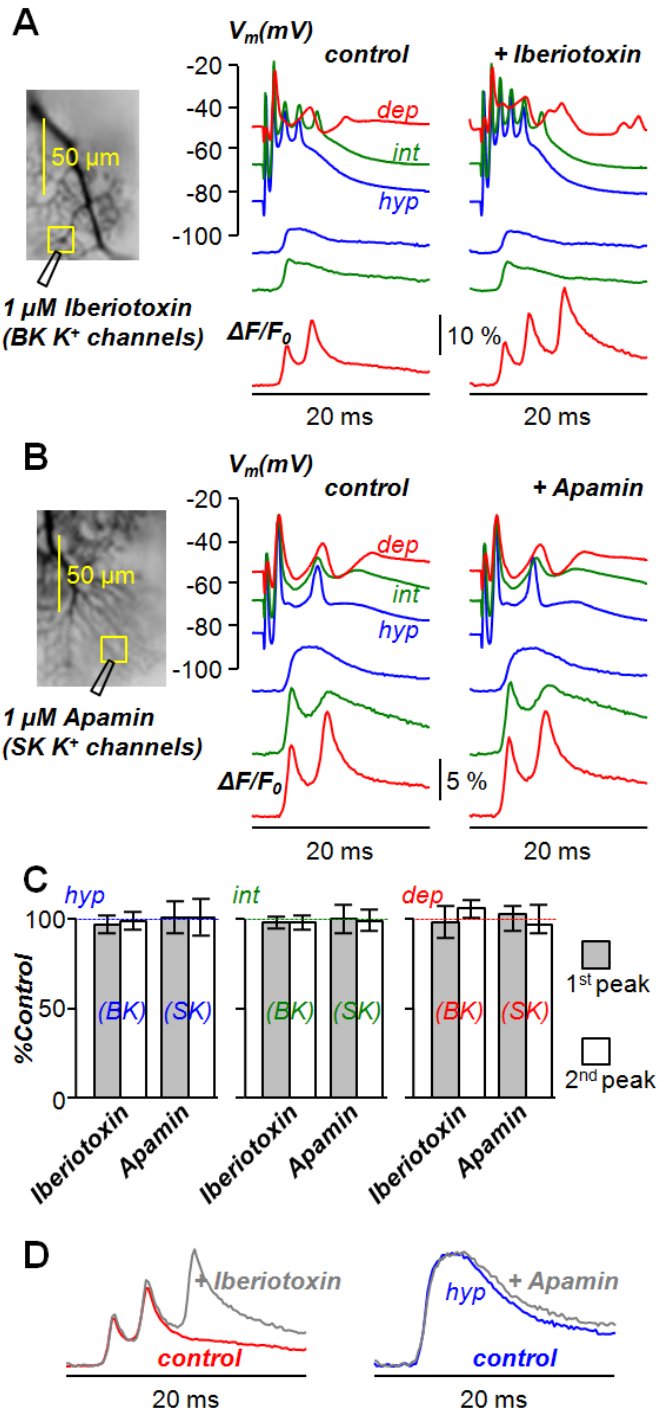

A. Left, fluorescence reconstruction of a PN filled with 2 mM of OG5N indicating a region of interest where a glass pipette is positioned to deliver locally 1 µM of the BK channel blocker Iberiotoxin. Right, on the top, somatic V_m associated with the CF-EPSPs in control conditions and after local application of Iberiotoxin at three different initial V_m states, *hyp* V_m state (blue trace); *int* V_m state (green trace); *dep* V_m state (red trace). On the bottom, the corresponding OG5N-$\Delta F/F_0$ signals. **B.** In another PN filled with 2 mM of OG5N as in **A,** except the pipette positioned in the region of interest deliver 1 µM of the SK channel blocker Apamin. **C.** Bargraphs of mean ± SD of the percentages of change between $\Delta F/F_0$ Ca^{2+} signals before and after application of Iberiotoxin (N = 5 cells) or Apamin (N = 6 cells); gray columns are the statistics of the first peak; white columns are the statistics for the second peak. **D.** On the left, from the cell in *A*, are superimposed the OG5N-$\Delta F/F_0$ signal associated with the CF-EPSP at *dep* state in control condition (red trace) and that after addition of Iberiotoxin (gray trace). On the right, from the cell in *B*, are superimposed the OG5N-$\Delta F/F_0$ signal associated with the CF-EPSP at *hyp* state in control condition (bleu trace) and that after addition of Apamin (gray trace).

Local block of SK channels had no effect on Ca^{2+} signals associated with the CF-EPSP at all initial V_m states. We again performed a quantitative analysis on Ca^{2+} signals obtained from all the cells tested with Iberiotoxin and Apamin. We calculated the first peak occurring during the first 4 ms after CF stimulation and the second peak occurring between 4 ms and 14 ms after CF stimulation. We then calculated the % of change between the first and second peaks of Ca^{2+} signals associated with the CF-EPSP before and after local application of Iberiotoxin and Apamin at the three initial V_m (Data not shown). The statistics (mean ± SD) of the % of change are reported in Figure 3.3C. Gray columns represent the first peak and white columns represent the second peak.

Neither Iberiotoxin nor Apamin produced any change in the first and the second peak of the Ca^{2+} signals at all initial V_m states, a result observed in N = 5 cells tested with Iberiotoxin and N = 6 cells tested with Apamin. In order to see clearly the effect of the block of BK and SK channels, the Ca^{2+} signals associated with the CF-EPSP at *dep* V_m state before and after Iberiotoxin application are superimposed, similarly the Ca^{2+} signals associated with CF-EPSP at *hyp* V_m state before and after Apamin application are superimposed as illustrated in Figure 3.3D. The block of BK channels increased the number of Ca^{2+} spikes from 2 to 3 at *dep* state, a result observed in 5/5 cells tested whereas the block of SK channels produced a slight yet observable decrease in the decay of the OG5N-$\Delta F/F_0$ signal at *hyp* state, a result observed in 4/6 cells tested. The change in the Ca^{2+} transients associated with the CF-EPSP produced by the block of BK or SK channels displays voltage dependence. This indicates that BK and SK channels are recruited at different V_m during the CF-EPSP suggesting distinct role for BK and SK channels during CF activation. While BK channels activate at depolarized V_m, SK channels are likely active at hyperpolarized V_m. BK channels, as their activation necessitates both Ca^{2+} increase and membrane depolarization, open during the CF-EPSP when the dendrites are depolarized. Since P/Q-type channels are highly active at depolarized V_m, they are the primary source of

the Ca^{2+} required for BK channels activation. In this case, BK channels contribute substantially to the repolarization of V_m limiting the number of Ca^{2+} spikes. SK channels, on the other hand, as they activate at hyperpolarized V_m following the CF-EPSP, are likely activated mainly by T-type VGCCs and they contribute to the V_m repolarization, although this contribution appears to be merely auxiliary. Notably, it has been shown that SK channels activation is V_m independent and consequently it should equally occur at hyperpolarized and depolarized membrane potentials (Kohler *et al.,* 1996; Vergara *et al.,* 1998). In our experiments, however, the block of SK channels did not have any effect on the Ca^{2+} transients associated with the CF-EPSP at *dep* V_m. This evidence suggests that either SK channels are not recruited at depolarized V_m or that SK channels are activated but as they conduct small current, it is of minor contribution to the CF-EPSP at depolarized V_m.

3.4 Dendritic A-type VGKC activation by the CF-EPSP

A-type K^+ channels belong to the Shal subfamily of voltage-gated K^+ channels (VGKC). Active at relatively low membrane potential, they conduct fast transient and rapidly inactivating outward currents. A-type VGKCs are localized in the soma and dendrites of neurons (Hoffman *et al*., 1997; Sheng *et al.*, 1992) where they are essentially involved in the regulation of membrane excitability and hence play a central role in synaptic transmission and integration (Hille, 2001). PN dendrites and soma possess A-type VGKCs that operate at subthreshold membrane potential and inactivate quickly as the membrane depolarizes (Gahwiler and Llano, 1989; Sacco and Tempia, 2002). Their biophysical properties allow them to tightly control the subthreshold dendritic excitability and thus shaping the firing pattern of PNs (Sacco and Tempia, 2002). In pyramidal neurons, A-type VGCCs are expressed at high density in the dendrites and attenuate the dendritic depolarization carried by active events (back-propagating action potentials) and limit their propagation into the distal regions of the dendritic tree. However, as they are inactivated by local synaptic

potentials (Johnston *et al.*, 2000, Migliore *et al.*, 1999), propagating action potentials are boosted promoting synaptic plasticity via increasing Ca^{2+} influx and unblocking NMDA receptors (Hoffman *et al.,* 1997). While in pyramidal neurons dendritic excitability is principally due to active propagation of action potential mediated by sequential activation of sodium channels, in the dendrites of PNs, dendritic excitation occurs by activation of VGCCs leading to calcium spikes. The transient subthreshold A-type K^+ current modulates the dendritic Ca^{2+} transient and it is responsible for spike acceleration (Hounsgaard & Midtgaard, 1988; Midtgaard *et al.*, 1993).

The aim of this part of the experiments is to investigate the activation of A-type VGKCs during the CF-EPSP. Thus, we examined the change in Ca^{2+} signals associated with the CF-EPSP produced by the block of A-type VGKC at three initial V_m states. AmmTx3, isolated from the venom of the scorpion Androctonus mauretanicus (Maffie *et al.*, 2013), is a pore blocker of Kv4.2 and Kv4.3 and was used in our experiment to block A-type VGKC. During my thesis, I contributed to further characterize this toxin in a recently published report (Zoukimian *et al.*, 2019). After loading PNs with 2 mM of OG5N for about 20 to 30 minutes, 1 µM of AmmTx3 was locally applied via a glass pipette positioned in the region of interest as indicated in Figure 3.4A. OG5N-$\Delta F/F_0$ signals associated with the CF-EPSP before and after application of AmmTx3 at the three initial V_m state were analyzed and reported in Figure 3.4A. Local application of AmmTx3 drastically increased Ca^{2+} signals associated with the CF-EPSP at initial *hyp* and *int* states while it had no effect on the Ca^{2+} signal at the initial *dep* stat. Notably, although AmmTx3 was locally applied, its effect was observed not only in the area close to the region of application. Indeed, A-type VGKC restricts the spread of active events into longer distances thereby blocking these channels allowed Ca^{2+} signals increase even in distant regions. We performed the same quantitative analysis on the Ca^{2+} signals associated with the CF-EPSP at the three initial V_m obtained from the cell in A.

Figure 3.4: Dendritic A-type VGKCs activation by the CF-EPSP

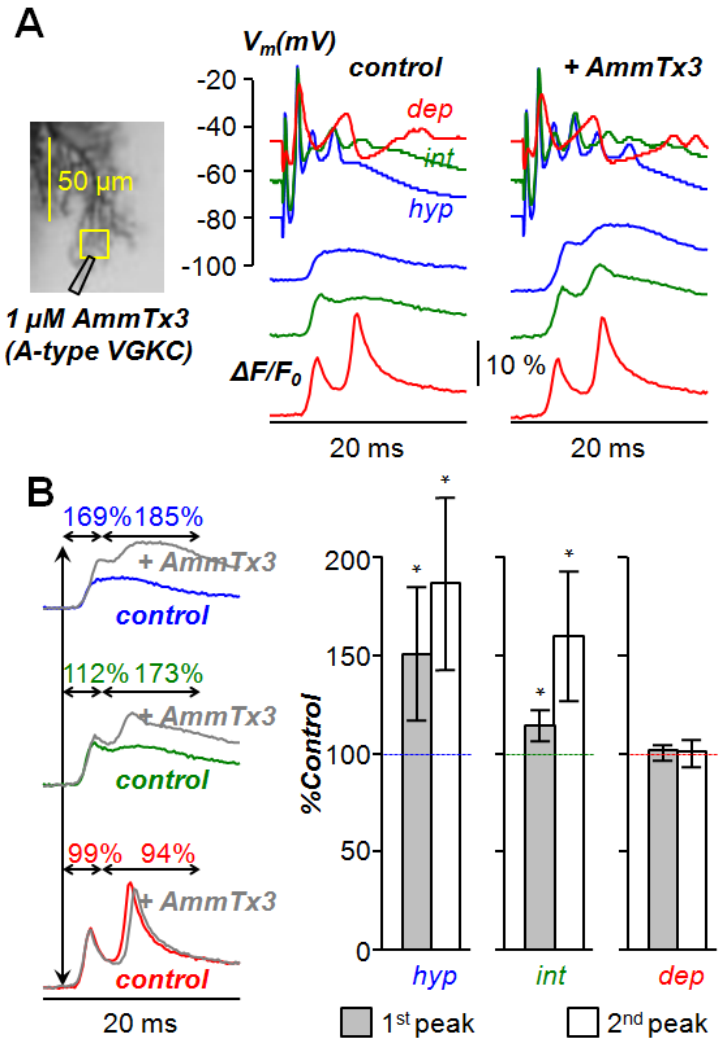

A. Left, fluorescence reconstruction of a PN filled with 2 mM of OG5N indicating a region of interest where a glass pipette is placed to deliver 1 µM of the A-type VGKC blocker AmmTx3. Right; on the top, somatic V_m associated with the CF-EPSPs before and after local application of AmmTx3 at three different initial V_m states: *hyp* state (blue traces); *int* state (green traces); *dep* state (red traces). On the bottom, the corresponding OG5N-$\Delta F/F_0$ signals. **B.** On the left, from the cell in A, Quantitative analysis of the first and the second peak of Ca^{2+} signals associated with the CF-EPSPs at the three initial V_m, *hyp* state (bleu traces), *int* state (green traces) and *dep* state (red traces). The first peak is calculated within the first 4 ms after the CF stimulation and the second peak is calculated between 4 and 14 ms after the CF stimulation. Superimposed (gray traces) are the OG5N-$\Delta F/F_0$ signals after local application of 1 µM AmmTx3 at the three initial V_m. The percentages of change between the first and second peak of the $\Delta F/F_0$ signals before and after application of AmmTx3 are calculated and reported above the arrows. On the right, statistics (mean ± SD, N = 6 cells) of the % between the first and second peak of the $\Delta F/F_0$ signals before and after application of AmmTx3; gray columns represent the statistics of the first peak, white columns represent the statistics of the second peak; the significant change is indicated by the asterisk symbol "*" ($p < 0.005$, paired t-test).

We measured the first peak that occurs during the first 4 ms after the CF stimulation and the second peak that occurs between 4 and 14 ms after the CF stimulation. Then, we calculated the % of change between the first and the second peak before and after application of AmmTx3 and the results are reported above the arrows as indicated in Figure 3.4B. The block of A-type VGKCs increased the first peak and the second peak of the Ca^{2+} signals by 169% and 185% respectively at *hyp* state and by 112 % and 173 % respectively at the *int* state whereas it had no effect on the first peak nor did on the second peak of the Ca^{2+} signals at *dep* state.

The statistics (mean ± SD) in 6 cells of the % of change are reported on the right in the Figure 3.4 B. At *hyp* states, the block of A-type VGKC increased the first peak of Ca^{2+} signals by 150% and the second peak by 170%; at *int* states, the block of A-type VGKC increased the first peak of the Ca^{2+} signals by 110% and the second peak by 160%; at *dep* state the block of A-type VGKC had no effect on the Ca^{2+} signals. While the block of A-type VGKC significantly increased the first and the second peak of Ca^{2+} signals associated with the CF-EPSP at *hyp* and *int* states, it had no effect on the Ca^{2+} signals at *dep* states. In contrast to the test on VGCCs and similarly to what observed in the tests of Ca^{2+}-activated K^+ channels, the effect of blocking of A-type currents was not restricted to the dendritic area adjacent to the pipette delivering the toxin (date not shown). This was likely due to the fact that the V_m changes due to inhibiting K^+ channels are not local. These experiments confirm the fact that A-type VGKCs fully activate at V_m levels that are below the inactivation threshold, in this way limiting P/Q-type channel activation and Ca^{2+} spike generation (Midtgaard *et al.*, 1993). As the V_m depolarizes (V_m > -55 mV), A-type VGKCs inactivate. Thus, the pharmacological block of these channels doesn't affect the Ca^{2+} signals that, under this condition, are fully mediated by P/Q-type VGCCs as demonstrated above.

3.5 Conclusions

The experiments reported in this chapter were performed in order to investigate the activation of ion channels following the activation of the CF input using the optical approaches newly developed in the laboratory. The activation of CF generates the complex spike and transiently depolarizes the dendrites of PNs. The passive spread of the CF-EPSP from the site of origin activates voltage-gated Ca^{2+} channels (VGCCs) and voltage-gated K^+ channels (VGKCs). Ca^{2+} influx via VGCCs activates Ca^{2+} activated K^+ channels (BK and SK). We found that two different sets of channels are selectively activated at different initial V_m. When the dendrite is hyperpolarized (V_m ~ -80 mV), the transient depolarization produced by the CF-EPSP activates T-type VGCCs that enhance the distal dendritic V_m depolarization produced by the spread of the EPSP. The dendritic V_m is however is kept below ~10 mV by the K^+ current via A-type VGKCs, limiting the opening of HVA Ca^{2+} and K^+ channels. Under this condition, Ca^{2+} influx activates SK channels that regulate V_m repolarization and that appear selectively linked to T-type VGCCs, presumably by molecular coupling (Stocker, 2004). When in contrast the dendrite is depolarized (V_m ~ -50 mV), T-type VGCCs and A-type VGKCs are fully inactivated and the CF-EPSP can drive the dendrite to more positive V_m values that activate first P/Q-type VGCCs and then HVAKs leading to Ca^{2+} spikes. In this case, Ca^{2+} influx activates BK channels that fasten V_m repolarization limiting the number of Ca^{2+} spikes. The role of BK channels is to dampen the generation of Ca^{2+} spikes, which are typically only two when these channels are active. Finally, significant activation of both sets of channels occurs only at intermediate initial V_m (~ -65 mV). The scheme of activation of the two distinct sets of functionally-coupled channels is illustrated in Figure 3.5.

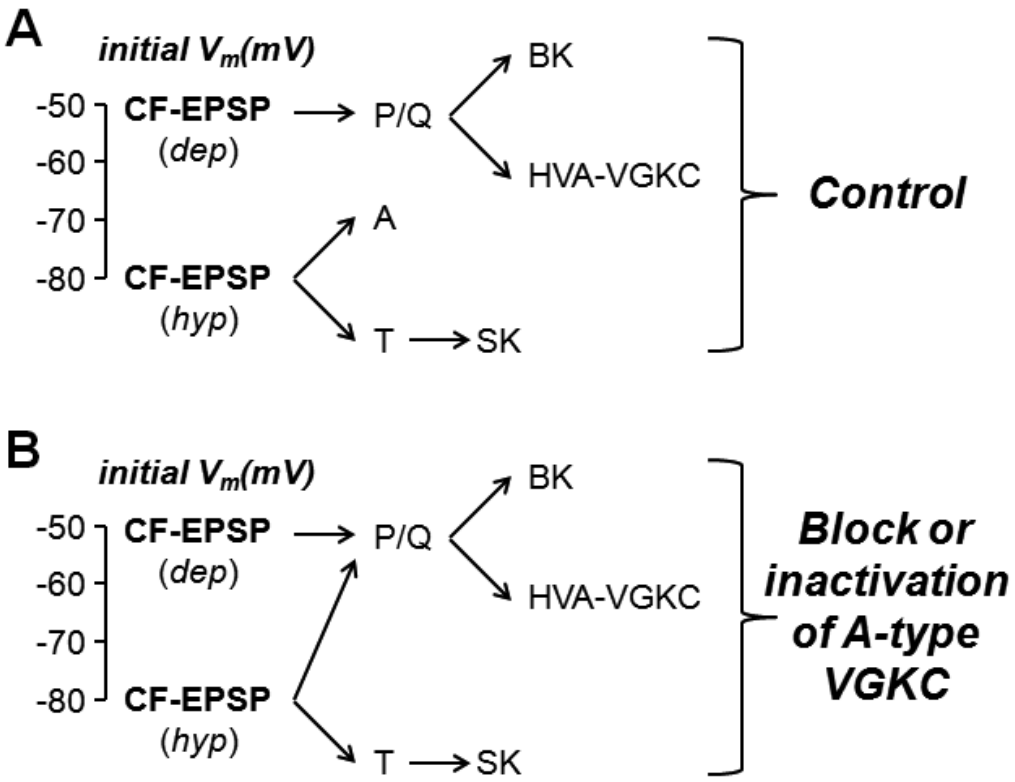

Figure 3.5: The scheme of activation of the two distinct sets of functionally-coupled channels.

Channel activation following CF-EPSPs at hyperpolarized and depolarized states. ***A***, In control conditions, at *hyp* state, the CF-EPSP activates T-type channels, that activate SK channels and A channels that limit activation P/Q and HVAK channels; at *dep* state, the CF-EPSP activates P/Q-type channels, that activate BK channels and HVAK channels, while T-type channels and A-type channels are inactivated. ***B***, when A-type channels are blocked or inactivated, at hyp state, the CF-EPSP also activates P/Q-type channels that activate BK channels, and HVAK channels.

Chapter 4: *Dendritic supralinear Ca^{2+} signal underlying concomitant PF and CF activity*

4.1 Dendritic Ca^{2+} signals associated with pairing PF-CF stimulation

Many types of neurons possess an extensive dendritic arbor which integrates and processes a large amount of information received from thousand of synaptic inputs. PNs have one of the most intricate dendritic trees in the mammalian brain receiving nearly 200,000 excitatory inputs from cerebellar granule cells (Napper and Harvey, 1988). Functionally, these inputs can be classified as “ascending” fibers (i.e. en passant contacts from ascending granule cell axons) and “parallel” fibers (PFs), i.e. contacts formed after the bifurcation of granule cell axons along the axonal bundles that run perpendicularly to the PN dendritic tree (Marcaggi and Atwell, 2006). Here, we refer to PFs generically to indicate all synaptic inputs from cerebellar granule cells. The other excitatory input to PN is the CF that was extensively analyzed in the previous chapter. The interplay between PFs and the CF produces a complex pattern of Ca^{2+} dynamics in the Purkinje cell dendritic tree and shapes the electrical response of PN which provides the final output of the cerebellar cortex. While the CF excitatory input activation leads to an all-or-none complex spike (Eccels, 1969) generating a widespread calcium transient detectable across the entire dendritic tree (Tank *et al*., 1988; Knöpfel *et al.*, 1991; Konnerth *et al.*, 1992; Miyakawa *et al.*, 1992, but see also Chapter 3), PF excitatory input activation generates Ca^{2+} signals which are confined to the region comprising the spines that are activated (Wang *et al.*, 2000; Brenowitz and Regehr, 2005). The Ca^{2+} signals associated with the CF activation was analyzed in detail in Chapter 3. Here, we analyze the CF-mediated Ca^{2+} signal in combination with the PF activity.

At PF-PN synapses, the coactivation of PF and CF strongly enhances the Ca^{2+} influx which can act as an associative signal for synaptic plasticity. Indeed, it was shown that the large Ca^{2+} transient provides the signal that underlies the coincident detection between PFs and CF inputs (Wang *et al.,* 2000) leading to short-term

(Brenowitz and Regehr, 2003, Rancz and Häusser, 2006) and long-term (Ito and Kano, 1996; Konnerth *et al*., 1992; Augustine *et al*., 2003) synaptic change at PF-PN synapses. Long-term depression of the PF transmission is a plastic change that underlies motor learning mechanisms in the cerebellum (Ito, 1984; 2006). Furthermore, it has been demonstrated that the relative timing between the interactions of the two excitatory inputs is a crucial determinant in the generation of the Ca^{2+} signals and in the induction of long-term depression (Safo and Regehr, 2005). Understanding the nature and the functional properties of Ca^{2+} signals generated by pairing PF and CF activation have been the subject of great debates and extensive studies. Yet, the precise molecular mechanisms that lead to the Ca^{2+} signals underlying the coincident detection of PF-CF dependant plastic change remain poorly understood (Vogt and Canepari, 2010). The purpose of the experiments reported in this chapter was to shed new light on this pivotal aspect of cerebellar physiology.

In this section of experiments, we initially characterized the Ca^{2+} signals associated with the coactivation of PF and CF excitatory inputs, using pairing protocols, similar to those utilized by Brenowitz and Regehr (2005), which were associated with short-term plasticity of PF-EPSPs. In detail, we used a train of 5 PF-EPSPs and one CF-EPSP delayed at different intervals, and we explored the change in Ca^{2+} signals associated with the CF-EPSP produced by paired PF-CF stimulation. We tested three different delays between the first PF-EPSP in the train and the CF stimulation, namely 60, 100 and 150 ms. Since the Ca^{2+} signal associated with paired PF-CF activation has a key role in the induction of synaptic plasticity at PF-PN synapses, it is of great importance to elucidate the biophysical mechanisms underlying the generation of these Ca^{2+} signals, which is the main goal of these experiments. In detail, 9 PNs were filled with 2 mM of OG5N through the patch pipette and two glass pipettes were used to independently stimulate the PFs and the CF inputs, as depicted in the example of Figure 4.1A.

Figure 4.1: Dendritic Ca^{2+} signals associated with pairing PF-CF activation

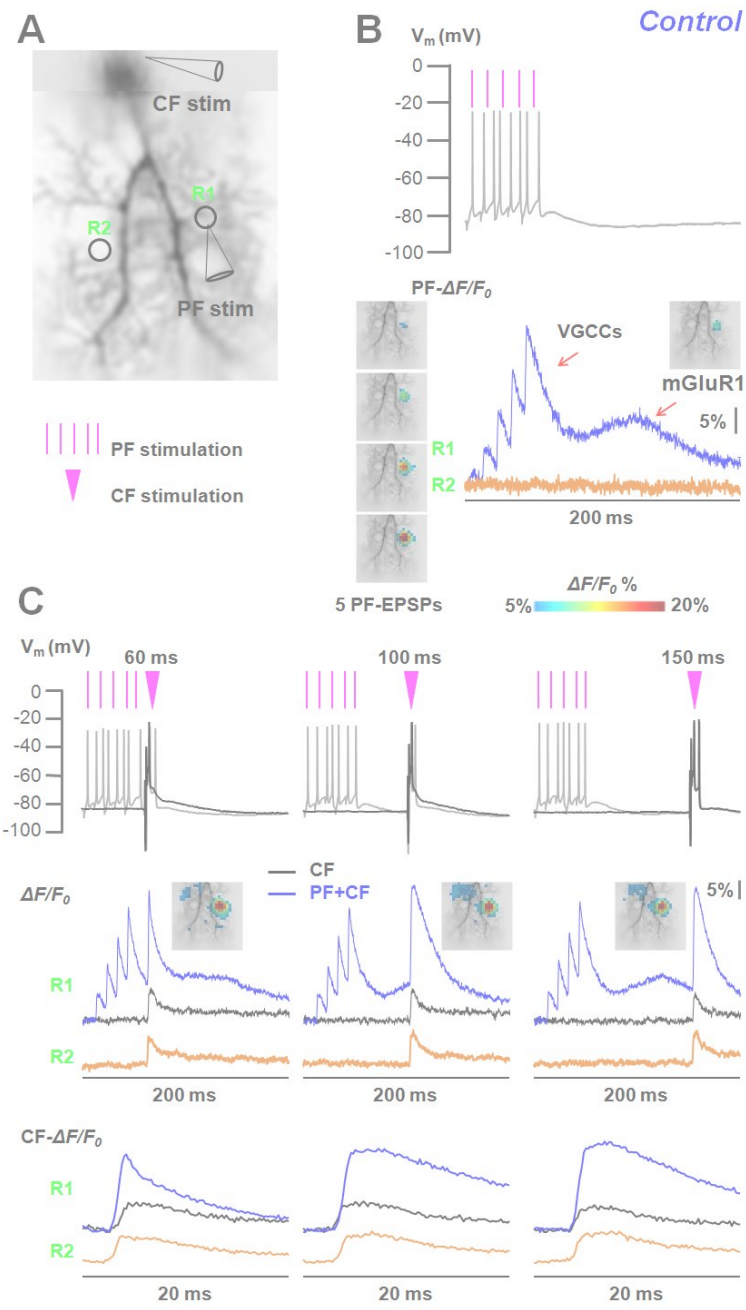

A. Fluorescence reconstruction of a PN loaded with 2 mM OG5N indicating a region of interest R1 where a glass pipette is placed to simulate the PF inputs and another region R2 as a control where the PF inputs are not stimulated. Another glass pipette is placed above the soma to stimulate the CF input. **B.** On the top, the somatic V_m following 5 PF stimuli delivered at 100 Hz (5 PF-EPSPs). On the bottom, the corresponding OG5N-$\Delta F/F_0$ signals in R1 (blue trace) and in R2 (orange trace) are superimposed. Color-coded OG5N-$\Delta F/F_0$ signals corresponding to the 2^{nd}-5^{th} PF-EPSP (left) and to the metabotropic EPSP (right) depicts the localization of these signals in the dendritic tree **C.** On the top, the somatic V_m following CF-EPSP impaired (black traces) and the somatic V_m following paired PF-CF stimulation (gray traces) with the CF-EPSP delayed by 60, 100 or 150 ms in respect to the first PF-EPSP are superimposed. In the middle, the OG5N-$\Delta F/F_0$ signals associated with the CF-EPSP impaired (black traces) and the OG5N-$\Delta F/F_0$ signals associated with the paired PF-CF stimulation in R1 for the three delays (blue traces) and bellow the OG5N-$\Delta F/F_0$ signals associated with the paired PF-CF stimulation in R2 (orange traces) are superimposed. Color-coded OG5N-$\Delta F/F_0$ signals corresponding to the CF-EPSP during pairing protocols depict the localization of the supralinear Ca^{2+} signals associated with the three delays. On the bottom, the corresponding CF-$\Delta F/F_0$ signals in R1 and in R2.

The pairing stimulation protocol consisted of a train of 5 stimuli delivered to the PFs at 100 Hz (5 PF-EPSPs) followed by one stimulus delivered to the CF (CF-EPSP) which was delayed by either 60, 100 or 150 ms. Figure 4.1A illustrates a representative PN indicating two regions of interest (R1 and R2, 2X2 Pixels, ~11X11 μm^2) where 3-4 trials of OG5N-$\Delta F/F_0$ signals were systematically averaged and compared. R1 next to the glass pipette contains the spines that are activated by PFs stimulation and R2 (as control) contains other spines that are not activated. The first step consisted of delivering a train of 5 stimuli at 100 Hz to the PF while the PN is held at around -80 mV. The corresponding OG5N-$\Delta F/F_0$ signals analyzed in R1 and R2 are reported in Figure 4.1B. While the stimulation of PF inputs generated Ca^{2+} signals (blue trace) in the region comprising the spines that were activated, it did not produce any signal in the region comprising the spines that were not activated (orange traces) indicating that the PN response to PF stimulation was restricted to the spines that were stimulated (Brenowitz and Regehr, 2005). The local Ca^{2+} transient associated with 5 FP-EPSP had a fast and a slow component. While the fast component was mediated by Ca^{2+} influx through T-type VGCCs activated by AMPARs-dependant depolarization (Ly *et al*., 2016), the slow component peaking more than 100 ms later was mediated by mGluR1s (Batchelor *et al*., 1994). Considering the fact that both the area of stimulation and the Ca^{2+} signals associated with the PF-EPSP increase when increasing the intensity of the stimulation (Canepari and Ogden, 2006), we set the intensity of stimulation to a level that allows restricting the amount of PF inputs stimulated and obtaining physiological Ca^{2+} signals that are comparable in amplitude. Next, we stimulated the CF alone (CF-EPSP impaired) or after a train 5 PF-EPSPs at 100 Hz with the CF-EPSP delayed by 60, 100 or 150 ms with respect to the first PF-EPSP (paired PF-CF stimulation) and we compared the corresponding Ca^{2+} signals in R1 and R2. Figure 4.1C reports the OG5N-$\Delta F/F_0$ signals associated with the CF-EPSP impaired (black traces) or with the paired PF-CF stimulation with the CF-EPSP occurring at delays of 60, 100 or 150 ms in R1 (blue traces) and in R2 (orange traces). While in R1, the Ca^{2+} signals associated with

CF-EPSP occurring at delays of 60, 100 or 150 ms after 5 PF-EPSPs (paired protocols) increased strongly in comparison with the Ca^{2+} signals associated with the CF-EPSP impaired, in R2, the Ca^{2+} signals associated with the CF-EPSP during paired PF-CF stimulation were identical to the Ca^{2+} signals associated with the CF-EPSP impaired at all delays. We therefore concluded that pairing PF-CF activation generates Ca^{2+} supralinear increase associated with the CF-EPSP at all delays tested (60, 100 or 150 ms) after the first PF-EPSP. Notably, these effects were localized exclusively in the area where the PF train alone produced a detectable Ca^{2+} transient, indicating that, at any delay between the PF and the CF stimulation, the supralinear Ca^{2+} signals associated with the CF-EPSP were spatially correlated with PF-induced signaling. Importantly, while the CF-Ca^{2+} transient at 100-150 ms after the first PF-EPSP coincides with the mGluR1-mediated slow Ca^{2+} influx, the CF Ca^{2+} signals at 60 ms occurs before this event. Thus, in the next set of experiments, we investigated the effect of the block of mGluR1 on the supralinear Ca^{2+} signals.

4.2 mGluR1 contribution to the supralinear Ca^{2+} signals associated with paring PF-CF stimulation

At PF-PN synapses, while the stimulation of PFs activates AMPARs and the subsequent depolarization activates VGCCs leading to a fast Ca^{2+} influx, multiple stimulation of PFs activates mGluR1 triggering a slow EPSP that develops in 100 to 200 milliseconds and lasts for about 1 second (Batchelor and Garthwaite 1993; 1997; Tempia *et al*., 1998) accompanied by a slow Ca^{2+} influx through non-selective ion channels activated by mGluR1 (TRPC3, Hartmann *et al.*, 2008). Type I metabotropic glutamate receptors (mGluR1) are G protein-coupled receptors and are abundantly expressed at the extrasynaptic site of the PF-PN synapses (Shigemoto *et al.*, 1992; Martin *et al.*, 1992). Functional mGluR1 activation is pivotal for normal cerebellar function. It is required for the induction of long-term depression (LTD) and plays a pivotal role in motor coordination and motor learning (Conquet *et al.*, 1994;

Aiba *et al.*, 1994; Ichise *et al.*, 2000; Sillevis-Smitt *et al.*, 2000; Nakao et *al*. 2007). Because mGluR1 is activated by PF stimulation, we sought to elucidate how mGluR1 activation influences the observed supralinear Ca^{2+} signals associated with the CF-EPSP produced by pairing PF-CF stimulation.

To this aim, we investigated the contribution of mGluR1 to the supralinear Ca^{2+} signals associated with the CF stimulation after bursts of PF stimulation. We examined the change in the supralinear Ca^{2+} signals associated with pairing PF-CF activation produced by the application of CPCCOEt, a potent antagonist of mGluR1 (Annoura *et al.*, 1996; Litschig *et al.*,1999). In 6/9 PNs from the experiments in paragraph 4.1, 20 µM of CPCCOEt was bath applied after a control recording and the same paired stimulation protocol was applied (CF stimulated either alone or after 5 PF-EPSP). Figure 4.2A shows the same representative PN from Figure 4.1 A where CPCCOEt was bath applied indicating the same region of interest next to the stimulating pipette (black circle). We delivered a train of 5 stimuli at 100 Hz to the PF and the corresponding OG5N-$\Delta F/F_0$ signals in the presence of CPCCOEt (red traces) superimposed with the OG5N-$\Delta F/F_0$ in the absence of CPCCOEt (dashed blue trace) are reported in Figure 4.2B. The application of CPCCOEt inhibited the slow Ca^{2+} transient as expected for a signal mediated by mGluR1. We then stimulated the CF alone or after 5PF-EPSPs with delays of 60, 100, 150 ms with respect to the first PF-EPSP and the corresponding OG5N-$\Delta F/F_0$ signals in the presence of CPCCOEt (red traced) superimposed with those obtained in the absence of CPCCOEt from Figure 4.1 C (dashed blue traces) are reported in Figure 4.2C. While the block of mGluR1 by CPCCOEt decreased the supralinear Ca^{2+} signals associated with CF-EPSPs occurring at delays of 100-150 ms after the first PF-EPSPs, it had only a minimal effect on the supralinear Ca^{2+} signal associated with CF-EPSPs occurring at a delay of 60 ms after the first PF-EPSP.

Figure 4.2: The effect of the block of mGluR1 on the CF-supralinear Ca^{2+} signals associated with pairing PF-CF stimulation

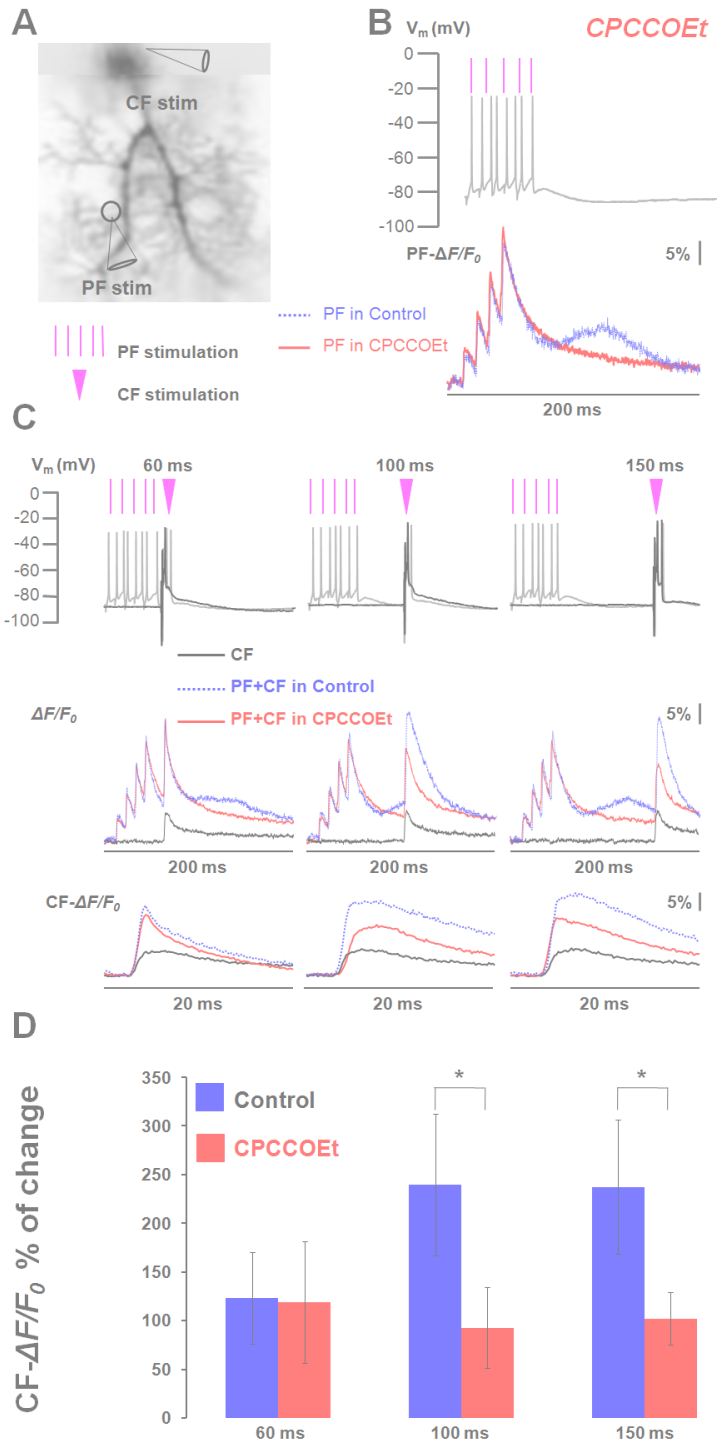

A. The same cell from figure 4.1 after bath application of 20 µM of CPCCOEt, a selective blocker of mGluR1, indicating a region of interest next to the stimulating pipette (black circle). **B.** On the top, the somatic V_m following a train of 5 PF stimuli delivered at 100 Hz; on the bottom, the corresponding OG5N-$\Delta F/F_0$ signals before (dashed blue traces) and after bath application of CPCCOEt (red traces). **C.** On the top, the somatic V_m following CF-EPSP impaired (black traces) and the somatic V_m following paired PF-CF stimulation with the CF-EPSP delayed by 60, 100 or 150 ms (gray traces) with respect to the beginning of the PF burst are superimposed. In the middle, the OG5N-$\Delta F/F_0$ signals associated with the CF-EPSP impaired (black traces) and the OG5N-$\Delta F/F_0$ signals associated with the paired PF-CF with the CF-EPSP occurring at the three delays before (dashed blue traces) and after bath application of CPCCOEt (red traces) are superimposed. On the bottom, the corresponding CF-$\Delta F/F_0$ signals. **D.** Statistics (mean ± sd, N = 6 cells) of the % of change in CF-$\Delta F/F_0$ signals produced by paired PF-CF stimulation with the CF-EPSP occurring at delays of 60, 100 or 150 ms relative to the CF-$\Delta F/F_0$ signals associated with the CF-EPSP impaired in the absence (blue columns) and in the presence of CPCCOEt (red columns). The symbol "*" indicates the significant effect of the block of mGluR1 ($p < 0.001$, paired t-test).

In Figure 4.2D, we report the statistics in the 6 cells tested (mean ± sd) of the % of change in CF-$\Delta F/F_0$ signals produced by pairing PF-CF with the CF-EPSP delayed by 60, 100 or 150 ms relative to the CF-$\Delta F/F_0$ signal associated with the CF-EPSP impaired in the absence (blue columns) and in the presence of CPCCOEt (red columns). The asterisk symbol indicates the significant decrease in the supralinear Ca^{2+} signals after the block of mGluR1 by CPCCOEt, estimated using a paired t-test with $p<0.001$. The inhibition of mGluR1 significantly decreased the CF-evoked supralinear Ca^{2+} signals associated with pairing PF-CF activation when the CF-EPSP occurs at delays of 100 or 150 ms from 240% ± 73% to 93% ± 42% and from 238% ± 69% to 102% ± 27% respectively. In contrast, after mGluR1s were blocked, CF-evoked supralinear Ca^{2+} signals changed from 123% ± 47% to 119% ± 60% non significantly. To summarize, Pairing PF and CF activation generates supralinear increases in the Ca^{2+} signals associated with the CF-EPSP occurring at all delays tested (60, 100 and 150ms) after the first PF-EPSP. A crucial difference between the supralinear Ca^{2+} signal at 60 ms and those at 100-150 ms is that the former was resistant to bath application of the mGluR1 antagonist CPCCOEt whereas the others were not. As stated above, understanding the mechanisms that underlie the generation of the supralinear Ca^{2+} is crucial for the comprehension of the induction of PF synaptic plasticity. In the experiments reported in next parts, we explored different possible hypotheses that may explain the generation of the mGluR1-dependant and independent supralinear Ca^{2+} signals.

4.3 Physiological mGluR1-dependant supralinear Ca^{2+} signals are not due to A-type K^+ channels inactivation and P/Q-type channels activation

4.3.1 The effect of direct chemical stimulation of mGluR1s on the Ca^{2+} signal associated with the CF-EPSP

We have shown that during paired PF-CF simulation, physiological activation of mGluR1 significantly contributes to the generation of supralinear Ca^{2+} transients associated with CF activation occurring at long delays (100-150 ms) after PF activation. Since mGluR1-dependent supralinear Ca^{2+} signals are critically involved in the induction of LTD, it is of crucial importance to elucidate the mechanisms underlying mGluR1-dependent supralinear Ca^{2+} signals. In a recent study, it has been shown that chemical stimulation of mGluR1 by DHPG substantially increased Ca^{2+} transients associated with CF activation and that P/Q-type VGCCs are the primary contributors to CF-evoked Ca^{2+} transient amplification. In fact, it has been demonstrated that the activation of mGluR1 acts in synergy with dendritic depolarization mediating A-type VGKC inactivation and unlock P/Q-type VGCCs. Remarkably, they also demonstrated that mGluR1-dependent slow EPSP doesn't contribute to this synergistic effect (Otsu *et al.*, 2014).

Thus, we decided to further investigate the contribution of A-type K^+ channels inactivation and P/Q-type channels activation in the generation of the supralinear Ca^{2+} transients during paired PF and CF activation. We first examined the change in Ca^{2+} transients associated with the CF-EPSP produced by direct chemical stimulation of mGluR1 receptors with DHPG, a selective agonist of mGluR1s (Schoepp *et al.*, 1994). To this aim, we loaded 6 PN with 2 mM OG5N through the patch pipette and left equilibrating. Then, 100 µM DHPG was applied by a puffing pipette placed next to the region of interest (black circle) to activate mGluR1s. In

parallel, a glass pipette was placed above the soma to stimulate the CF input, as illustrated in the representative PN in Figure 4.3.1A. The PN was held at around -80 mV and the OG5N-$\Delta F/F_0$ signals associated with the CF-EPSP before (black traces) and after DHPG application (blue traces), recorded and analyzed in the region of interest (4*4 pixels), were reported in Figure 4.3.1B. The activation of mGluR1 through a pressure application of DHPG produced a membrane depolarization that developed in ~100 ms, observable on the somatic recoding, as reported in a previous study (Canepari *et al.*, 2001). Direct stimulation of mGluR1 by DHPG substantially increased the Ca^{2+} signals associated with the CF-EPSP. In Figure 4.3.1C. we reported the statistics (mean ± sd, n =6 cells) of the % of change in CF-$\Delta F/F_0$ Ca^{2+} signals after DHPG application relative to CF-$\Delta F/F_0$ Ca^{2} signals associated with CF-EPSP stimulation alone. Chemical stimulation of mGluR1 increased Ca^{2+} transients associated with CF-EPSPs by 120 ± 80 %. Both chemical and physiological (during paired PF and CF) stimulation of mGluR1s generated a substantial increase in the Ca^{2+} signals associated with the CF-EPSP. However, there was a clear difference in the kinetics of the Ca^{2+} transient between the two cases. In order to quantify the observed kinetics difference of the Ca^{2+} transient associated with the CF-EPSP paired either with DHPG application or with PF-EPSP trains, we calculated the time derivative of OG5N-$\Delta F/F_0$ signals ($d(\Delta F/F_0)/dt$) filtered with the same Savitzky-Golay algorithm used in a previous study (Jaafari *et al.*, 2014). In Figure 4.3.1D. we report the Ca^{2+} signals associated with CF-EPSP alone (black traces) superimposed with the Ca^{2+} signals associated with CF-EPSP after DHPG application or occurring at delays of 60, 100 or 150 ms after the first PF-EPSP. To quantify the kinetics of the Ca^{2+} transients, the time derivative was normalized to the positive peak and the negative peak, which depends on the decay rate of the signal, was measured. The $d(\Delta F/F_0)/dt$ negative peak of the Ca^{2+} signals associated with the CF-EPSP in the presence of DHPG or occurring at a delay of 60 ms after the first PF-EPSP were larger with respect to those associated with the CF-EPSP alone.

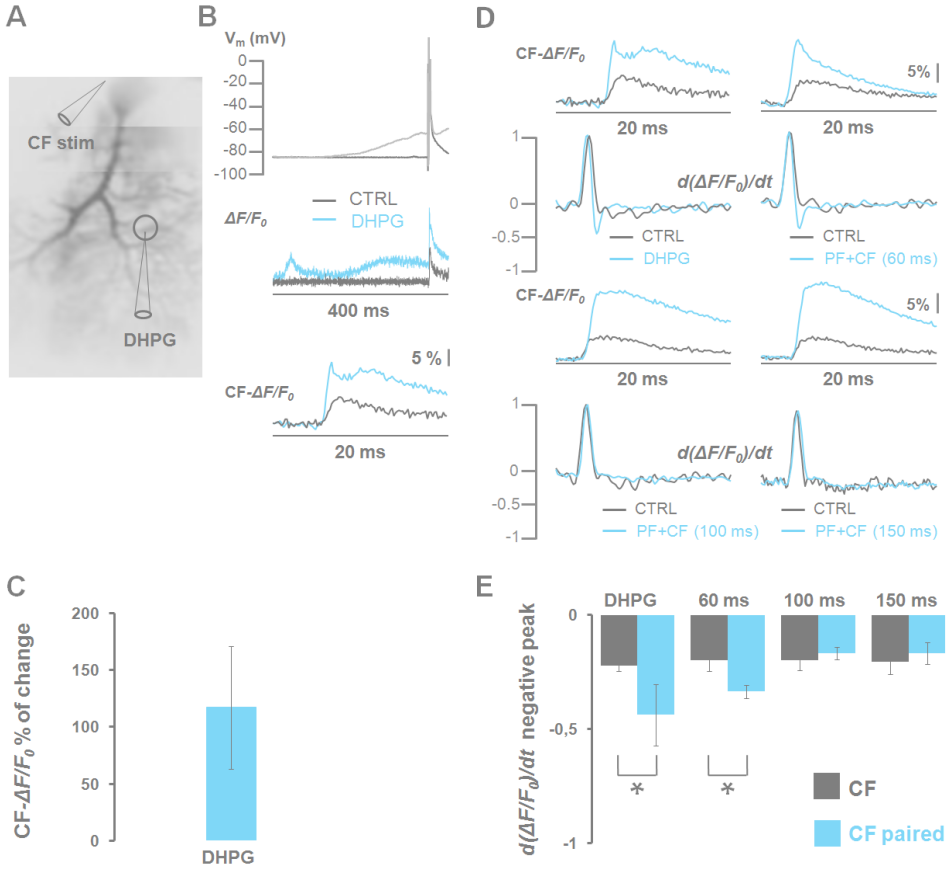

Figure 4.3.1: The effect of the direct chemical stimulation of mGluR1 on the Ca^{2+} signals associated with the CF-EPSP.

A. Reconstruction of a PN filled with 2 mM of OG5N indicating the stimulating pipette for the CF and a region of interest (black circle) where a glass of pipette is positioned to deliver, by pressure, 100 µM of DHPG, a selective agonist of mGluR1. **B**. On the top, the somatic V_m associated with the CF-EPSP in the absence (gray trace) and in the presence of DGPH (gray trace) are superimposed; on the bottom, the OG5N-$\Delta F/F_0$ signals associated with the CF-EPSP in the absence (black trace) or in the presence of DHPG (blue trace). **C.** Statistics (mean ± sd, n =7 cells) of the % of change in CF-$\Delta F/F_0$ signals produced by chemical stimulation of mGluR1. **D.** The CF-$\Delta F/F_0$ signals associated with the CF-EPSP alone (black traces) and CF-$\Delta F/F_0$ signals associated with the CF-EPSP paired either with DPGH application or with 5 PF-EPSPs with the CF-EPSP delayed by 60, 100 or 150 ms (blue traces) are superimposed; below the time derivative of CF- $\Delta F/F_0$ signals filtered and normalized to the positive peak are reported; the negative peak was measured in order to quantify the kinetics difference. **E.** Statistics (mean ± sd, n=7 cells) of the negative peak of the time derivative of CF- $\Delta F/F_0$ signals associated with the CF-EPSP impaired (black columns) or paired with DPGH application or with 5 PF-EPSPs with the CF-EPSP delayed by 60, 100 or 150 ms (blue columns). The symbol "*" indicates a significant difference in the value of *d(ΔF/F$_0$)/dt negative peak* ($p<0.01$, paired t-test).

In contrast, the $d(\Delta F/F_0)/dt$ negative peaks of the Ca^{2+} signals associated with the CF-EPSP occurring at delays of 100-150 ms after PF-EPSP were comparable with those associated with the CF-EPSP alone. The statistics (mean ± sd) of the normalized $d(\Delta F/F_0)/dt$ negative peaks in 6 cells were reported in Figure 4.3.1F. The values of the $d(\Delta F/F_0)/dt$ negative peak of the Ca^{2+} transient associated with the CF-EPSP before and after DHPG application were - 0.22 ± 0.04 and 0.44 ± 0.13 respectively. The values of $d(\Delta F/F_0)/dt$ negative peak of the Ca^{2+} transient associated with the CF-EPSP impaired and occurring at a delay of 60ms were -0.20 ± 0.05 and 0.34 ± 0.04 respectively. The values of $d(\Delta F/F_0)/dt$ negative peaks of the Ca^{2+} transient associated with the CF-EPSP alone or occurring at a delay of 100 ms were 0.20 ± 0.05 and 0.17 ± 0.04 respectively. The values of the $d(\Delta F/F_0)/dt$ negative peak of the Ca^{2+} transient associated with the CF-EPSP impaired and occurring at a delay of 150 ms were 0.21 ± 0.05 and 0.17 ± 0.05 respectively. While the values of the $d(\Delta F/F_0)/dt$ negative peak of the Ca^{2+} transients associated with CF-EPSPs in the presence of DHPG or occurring at a delay of 60 ms after the first PF-EPSP were significantly different with respect to those of the Ca^{2+} transients associated with CF-EPSPs alone, they did not differ in the case of CF-EPSPs occurring at delays of 100 -150 ms after the first PF-EPSP.

To summarize this set of experiments, chemical activation of mGuR1 potentiated the Ca^{2+} transients associated with CF activation in agreement with the results obtained by Otsu et al., 2014, who showed that this potentiation resulted from A-type K^+ inactivation and P/Q-type VGCCs activation. Nevertheless, in our experiments, we demonstrated that the kinetics of the Ca^{2+} transients generated by chemical stimulation of mGluR1s were different of that of the supralinear Ca^{2+} transients signal associated with the CF-EPSP occurring at long delays (100-150ms) which are dependent on mGluR1 activation. In detail, the $d(\Delta F/F_0)/dt$ negative peaks were significantly different in the first case and not in the second case suggesting that the mechanisms underlying the physiological mGluR1-dependent supralinear Ca^{2+}

signals are different and do not involve A-type K^+ channels inactivation and P/Q-type channels activation. Interestingly, the same change of kinetics of that observed in the case of DHPG application was observed in the experiments, reported in the previous chapter, where A-type K^+ channels were blocked by the toxin AmmTx3. Another interesting finding is that, supralinear Ca^{2+} transients associated with the CF-EPSP occurring at short delays after burst of PF stimulation displayed comparables kinetics with that of the Ca^{2+} transient associated with chemical stimulation of mGluR1 making A-type K^+ channels inactivation and P/Q-type channels activation a likely candidate to explain the supralinearity of Ca^{2+} transients in this case. This hypothesis was assessed in the experiments reported in the next paragraph.

4.3.2 Combined imaging of V_m and Ca^{2+} signals associated with PF-CF paired stimulation

While supralinear Ca^{2+} signals associated with CF activation occurring at short delays after burst PF stimulation (60 ms) were resistant to CPCCOEt and therefore independent of physiological mGluR1 activation, the kinetics of the potentiated signal was comparable to that of the Ca^{2+} transient signal associated with CF-EPSP paired with DHPG application which is mediated by A-type K^+ channels inactivation and P/Q-type channel activation (Otsu *et al.*, 2014). Pairing CF-EPSP with dendritic depolarization inactivates A-type VGKC leading to maximal activation of P/Q channels and to larger Ca^{2+} transients (see Chapter 3). Glutamate release following PF stimulation activates AMPARs present at the postsynaptic site of PF-PN synapses and the subsequent depolarization could inactivate A-type VGKC leading to P/Q–type VGCCs channels activation which may contribute to the mGluR1-independent supralinear Ca^{2+} transient. In order to better clarify this scenario, we investigated the change in dendritic V_m associated with the CF-EPSP paired with a train of 5 PF-EPSP. We thus performed V_m and Ca^{2+} imaging using the VSD JPW1114 and FuraFF respectively (Canepari *et al.*, 2008), similarly to the

experiments reported in Chapter 3, we loaded 6 PNs with JPW1114 via the patch pipette and left equilibrating for ~ 1 hour. Then, we repatched PNs in order to fill them with 1 mM of the low-affinity indicator FuraFF. Figure 4.3.2A. illustrates a representative PN indicating the stimulating pipette placed near the region of interest (black circle) to stimulate PF inputs and another pipette was placed above the PN soma to stimulate the CF input. We stimulated the CF alone (impaired CF-EPSP) or after a train of 5 PF-EPSPs (paired PF-CF stimulation) with delays of 60 or 100 ms with respect to the first PF-EPSP. The corresponding JPW1114-$\Delta F/F_0$ and FuraFF-$\Delta F/F_0$ are reported in Figure 4.3.2B. Dendritic CF-$\Delta F/F_0$ V_m and CF- $\Delta F/F_0$ Ca^{2+} signals associated with CF-EPSP paired with 5 PF-EPSP at delays of 60 and 100 ms and with CF-EPSP impaired are reported in Figure 4.3.2C. In the case of paired stimulation, while the initial dendritic V_m associated with the CF-EPSP occurring at a delay of 60 ms after the first PF-EPSP was more positive with respect to the initial dendritic V_m associated with the CF-EPSP alone, the initial dendritic V_m associated with the CF-EPSP occurring at a delay of 100 ms was not visually different from the initial dendritic initial V_m associated with the CF-EPSP. However, the CF-EPSP stimulation after 5 PF-EPSP was associated with supralinear Ca^{2+} signals at all delays. We report in Figure 4.3.2D, on the top, the statistics (mean ± sd, n = 6 cells) of the difference (ΔV_m %) between the initial (black columns) and the peak (gray columns) of JPW-$\Delta F/F_0$ associated with CF-EPSPs alone and CF-EPSPs paired with 5 PF-EPSPs with delays of 60 and 100. When CF-EPSP occurs with a delay of 60 ms, initial and peak ΔV_m were 0.95% ± 0,35% and 0.3% ± 0.35% respectively whereas when the CF-EPSP occurs with a delay of 100 ms, initial and peak ΔV_m were 0.015% ± 0,004% and 0.25 % ± 0.38 % respectively. We reported in Figure 4.3.2D, on the bottom, the statistics (mean ± sd, n = 6 cells) of the % of change in Ca^{2+} signals associated with CF-EPSP following paired PF-CF stimulation with the CF-EPSP delayed by 60 or 100 ms relative to the Ca^{2+} signals associated with the CF-EPSP impaired.

Figure 4.3.2: Combined imaging of dendritic V_m and supralinear Ca^{2+} signals associated with PF-CF paired stimulation.

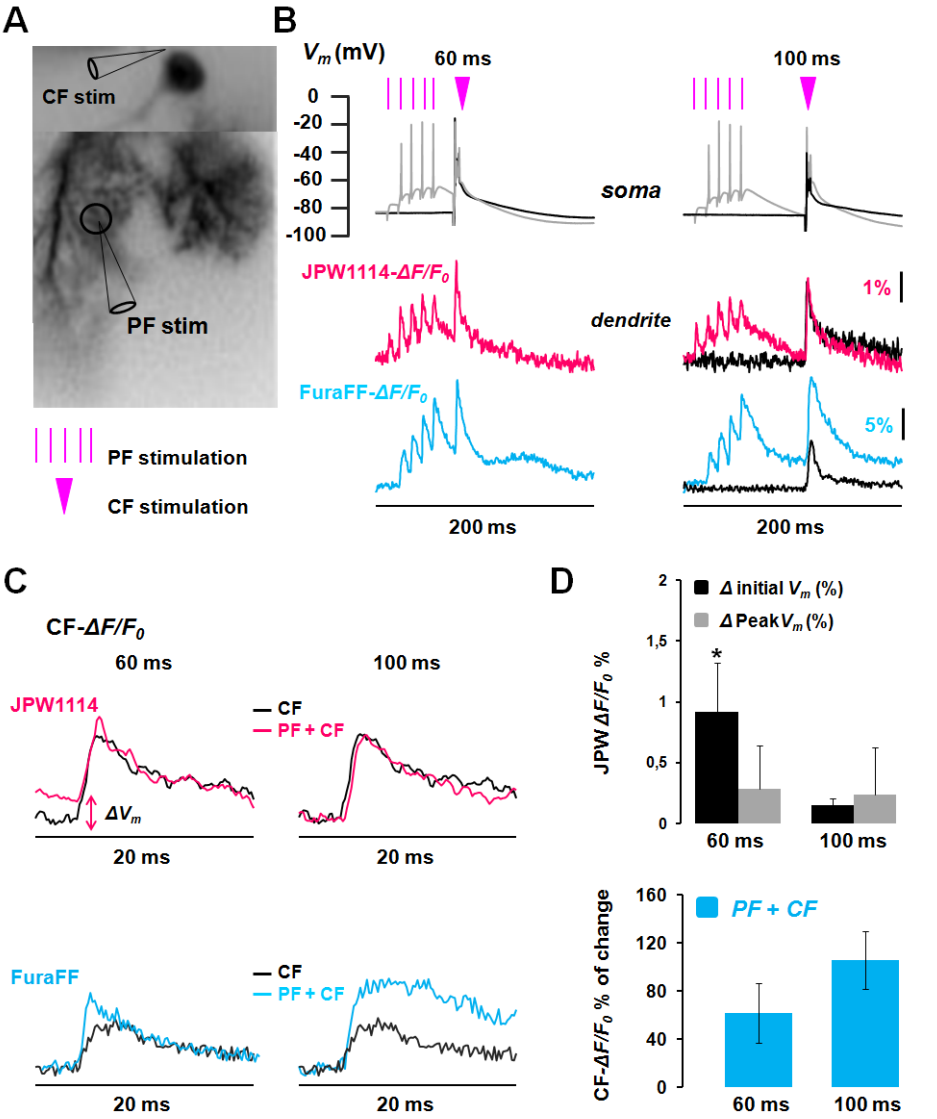

A. Fluorescence reconstruction of a PN loaded with JPW1114 and 1 mM of FuraFF indicating the region of interest and the position of the tow stimulating pipette. **B.** On the top, the somatic V_m following CF-EPSP impaired (black traces) and paired with 5 PF-EPSPs (gray traces) with delays of 60 or 100 ms in respect to the first PF-EPSP, superimposed; in the middle and on the bottom, the corresponding dendritic JPW-$\Delta F/F_0$ signals (CF impaired, black traces; CF paired, red traces) and FuraFF-$\Delta F/F_0$ signals (CF impaired, black traces, CF paired blue traces) respectively. **C.** On the top, dendritic CF JPW -$\Delta F/F_0$ signals associated with the CF-EPSP impaired (black traces) or with CF-EPSP paired with 5PF-EPSPs with delays of 60 or 100 ms (red traces) in respect to the first PF-EPSP, superimposed; on the bottom, dendritic CF FuraFF-$\Delta F/F_0$ signals associated with the CF-EPSP impaired (black traces) or with CF-EPSP paired with delays of 60 or 100 ms (blue traces) in respect to the first PF-EPSP, superimposed. **D.** On the top, statistics (mean ± sd, n = 6 cells) of the Δ between the initial (black columns) and the peak (gray columns) of JPW -$\Delta F/F_0$ values associated with CF-ESPS paired (delays of 60 and 100 ms) and with CF-ESPS alone. **D.** Statistic (mean ± sd, n = 6 cells) of the % of change in CF-$\Delta F/F_0$ signals associated with CF-EPSP paired with 5 PF-EPSPs delayed by 60 or 100 ms in respect to the first PF-EPSP relative to the CF-$\Delta F/F_0$ signals associated with CF-EPSP impaired.

The Ca^{2+} signals associated with CF-EPSPs occurring at delays of 60 after the first PF-EPSP increased by 62 % ± 25 % and the Ca^{2+} signals associated with CF-EPSPs occurring at delays of 100 ms after the first PF-EPSP increased by 105 % ± 24%. When CF-EPSPs occur at short delays after burst PF stimulation, the associated initial V_m associated increased by roughly 1% with respect to that associated with the CF stimulation alone. Since, the fractional change in light intensify (*JPW1114-$\Delta F/F_0$*) is proportional to V_m, this result indicates a larger depolarization transient. This depolarization is consistent with additional recruitment of P/Q-type which led to larger Ca^{2+} transient. However, the amplitude of the CF-Ca^{2+} signal associated with the CF-EPSP paired with depolarized initial V_m was smaller, as determined in Chapter 3, and cannot fully explain the supralinearity observed in CF-Ca^{2+} signals associated with CF-EPSPs occurring at 60 ms after PF stimulation. Thus, it is likely that other factors may be involved in this case. In contrast, when CF-EPSPs occur at 100 ms delay after PF burst stimulation which coincided with mGuR1 activation, the associated initial dendritic V_m was not significantly different from that associated with the CF activation alone which was roughly equal to resting membrane potential values. This implies a compensatory hyperpolarizing mechanism since the mGluR1-dependent slow EPSPs developing around tens ms should depolarize the dendrites, and this phenomenon was not detected by membrane potential imaging. One plausible explanation would be that the mGluR1-depandent slow depolarization is counteracted by the K^+ channels-dependant after hyperpolarization following PF depolarization preventing A-type K^+ inactivation and P/Q channels activation. To summarize, while supralinear Ca^{2+} transients associated with CF-EPSPs occurring at short delays after burst PF activation, independent of mGluR1 activation, are partially mediated by A-type K^+ channels inactivation and P/Q-type channels activation, mGluR1-dependent supralinear Ca^{2+} signals does not involve this mechanism confirming the previous observation.

4.4 Physiological mGluR1-dependant supralinear Ca^{2+} signals are not due to the transient saturation of endogenous Ca^{2+} buffers

So far, we demonstrated that in contrast to mGluR1-independant supralinear Ca^{2+} signals that are partially due to A-type K^+ channels inactivation and P/Q-type channel activation, in the case of physiological mGluR1-dependent Ca^{2+} signals, this mechanism is not implicated. We thus explored other potential factors that may be involved in this phenomenon. PNs express a high level of mobile endogenous Ca^{2+} buffer (ECB) including calbindin-D28K (CB) and parvalbumin (Baimbridge *et al.*, 1992; Bastianelli *et al.*, 2003). Their physiological role consists essentially in regulating Ca^{2+} homeostasis in neurons through buffering mechanisms. They in fact determine the amplitude and the time course of Ca^{2+} transients in spine and dendrites and control the diffusion of Ca^{2+} (Baimbridge *et al.*, 1992; Schwaller & Eilers, 2003; Schmidt and Eilers, 2009) thereby shaping the spatiotemporal dynamics of Ca^{2+} signaling which is a crucial aspect in the electrical responsiveness of PN, in intracellular signaling pathway and in synaptic plasticity (Bastianelli *et al.*, 2003; Blatow *et al.*, 2003). In contrast to parvalbumin, Calbindin-D28K (Calbindin) which displays high and medium Ca^{2+} affinity is characterized by relatively fast kinetics and is the major determinant of the high buffering capacity (~2000, see Fierro and Llano, 1996). It is in principle able to saturate during fast Ca^{2+} influx leading to an increase in free Ca^{2+} (Fierro and Llano, 1996; Blatow *et al.*, 2003). The potential role of ECBs for cerebellar function was highlighted in Calbindin knockout mice. In fact, targeted genetic deletion of the gene encoding Calbindin profoundly altered the dynamics of dendritic postsynaptic Ca^{2+} signaling in response to synaptic input activation causing abnormal firing patterns of PN and alteration in the morphology of spine. Moreover, these animals displayed impairments in motor coordination (Airaksinen *et al.*, 1997; Vecellio *et al.*, 2000; Barski *et al.*, 2003; Schwaller *et al.*, 2004; servais *et al.*, 2005; Farré-Castany et *al.*, 2007). Interestingly, the induction of LTD at PF-PN synapses was not prevented in mice lacking Calbindin (Barski *et al.*, 2003). In my

experiments, a quantitative evaluation of the PN endogenous buffers effect on the kinetics of the Ca^{2+} transients was performed at the beginning of my PhD (Ait Ouares *et al.*, 2016). Since Ca^{2+} binding proteins in PN dendrites have higher affinity with respect to OG5N, transient saturation of these molecules would increase the availability of Ca^{2+} ions to bind to the indicator resulting in a supralinear Ca^{2+} transient. Thus, Canepari & Vogt (2008) demonstrated that burst PFs stimulation can locally saturate ECBs leading to supralinear summation of intracellular free Ca^{2+} concentration.

In line with this finding, we investigated whether the saturation of ECBs was at the origin of mGluR1-independent and independent supralinear Ca^{2+} signals associated with CF-ESPSs paired with PF stimulation. To this aim, we examined the change in Ca^{2+} signals associated with CF-EPSP paired with 5 PF-EPSP using an internal solution containing 2 mM of the low affinity indicator OG5N and 200 µM of the high affinity indicator Fura-2. Since the K_D of Fura-2 is in the range of 100 nM, this concentration displays comparable buffering capacity as ECB and can act as an exogenous calcium buffer that effectively mimics what the endogenous proteins do during PF and CF Ca^{2+} influx. We loaded 6 PN with both indicators and left equilibrating for 20 to 30 minutes. Figure 4.4A. illustrates a representative example of a PN indicating a region of interest (black circle) near a pipette used to stimulate PF inputs. The other pipette depicted was used to stimulate the CF. We stimulated the CF alone (CF-EPSP alone) or after a train of 5 PF-EPSP (paired PF-CF stimulation with either 60 ms or 130 ms delay) and the corresponding OG5N-$\Delta F/F_0$ (blue traces) and Fura-2-$\Delta F/F_0$ (green traces) were reported in Figure 4.4B. Figure 4.4C shows CF-OG5N and CF-Fura-2 $\Delta F/F_0$ signals associated with the CF-EPSP alone or paired with 5 PF-EPSPs with the CF-EPSP delayed by either 60 ms or 130 ms superimposed.

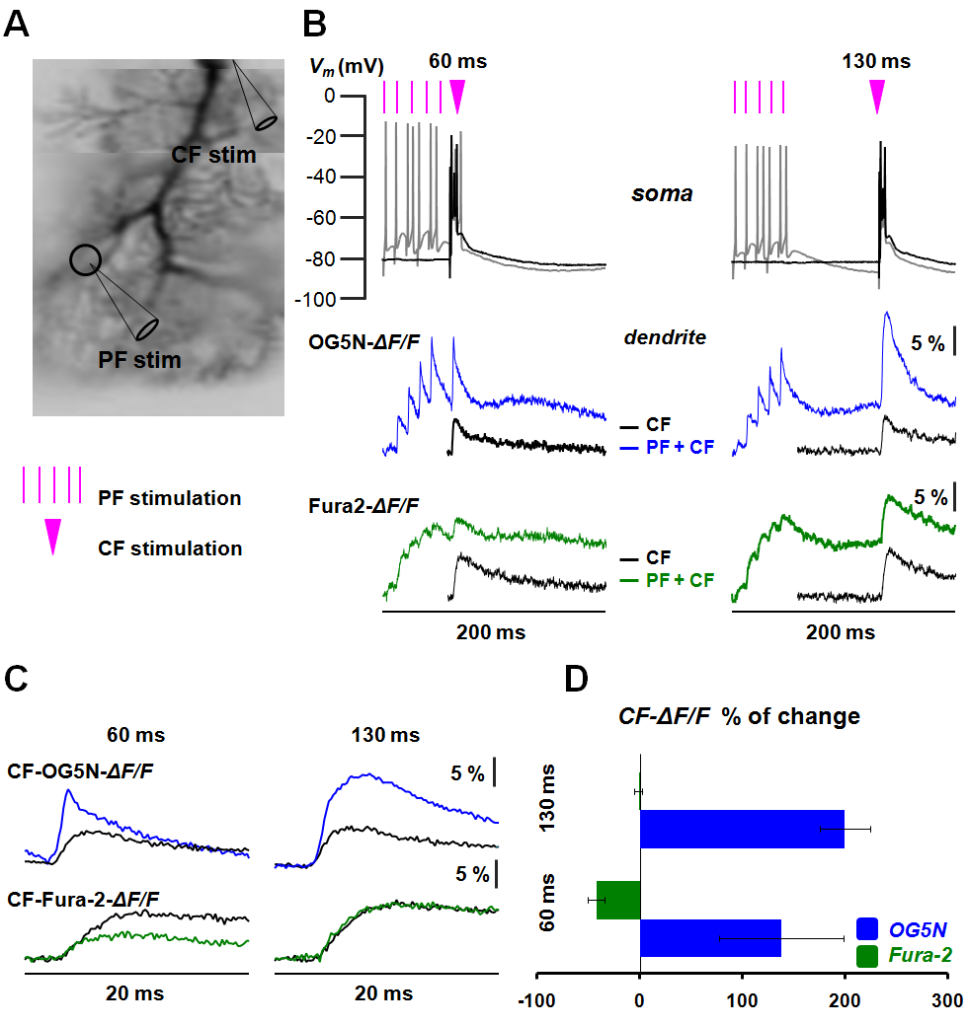

Figure 4.4 Imaging supralinear Ca^{2+} signal associated with PF-CF paired stimulation using a low affinity indicator and a high affinity indicator.

A. Fluorescence reconstruction of a PN loaded with 2 mM OG5N, a low affinity indicator and 200 µM Fura-2, a high affinity indicator; A region of interest (black circle) and the position of the two stimulating electrodes are indicated. **B.** On the top, the somatic V_m following a CF-EPSP alone (black traces) or paired with PF-CF stimulations with the CF stimulus delayed by 60 or 130 ms with respect to the first PF-EPSP (gray trace) superimposed; on the bottom, the corresponding dendritic OG5N- $\Delta F/F_0$ signals (CF alone, black traces; paired CF, blue traces) and Fura-2-$\Delta F/F_0$ signals (CF alone, black traces; paired CF green traces). **C.** On the top, CF OG5N-$\Delta F/F_0$ signals associated with the CF-EPSP alone (black traces) and paired with 5PF-EPSPs at 60 or 130 ms delay with respect to the first PF-EPSP, superimposed (blue traces); on the bottom, CF Fura-2-$\Delta F/F_0$ signals associated with the CF-EPSP alone (black traces) or paired at 60 or 130 ms delays with respect to the first PF-EPSP, superimposed (green traces). **D.** Statistics (mean ± sd, n = 6 cells) of the % of change in CF-$\Delta F/F_0$ signals associated with CF-EPSP paired with 5 PF-EPSPs delayed by 60 or 130 ms with respect to the first PF-EPSP relative to the CF-$\Delta F/F_0$ signals associated with CF-EPSP alone.

In the case of OG5N signals, pairing CF-EPSP with 5 PF-EPSPs at both delays was associated with supralinear Ca^{2+} signals (blue traces), similarly to the experiments performed without the other Ca^{2+} indicator. In contrast, in the case of Fura-2 signals, pairing CF-EPSP with 5 PF-EPSP reduced the CF-$\Delta F/F_0$ signal associated with the CF-EPSP occurring at the delay of 60 ms after the first PF-EPSP, similarly to what reported in Canepari and Vogt 2008. The CF-$\Delta F/F_0$ signal associated with the CF-EPSP occurring at 130 ms delay with respect to the first PF-EPSP (green traces), however, was comparable to CF-$\Delta F/F_0$ signal associated with the CF-EPSP alone (black traces). We report in Figure 4.4D the statistics (mean ± sd, N = 6 cells) of the % of change of CF-OG5N-$\Delta F/F_0$ signals (blue columns) and of the CF Fura-2 $\Delta F/F_0$ signals (green columns) produced by paired PF-CF stimulation relative to CF-$\Delta F/F_0$ signals associated with CF-EPSP alone. In the case of OG5N signals, the CF-$\Delta F/F_0$ associated with the CF-EPSP occurring at 60 ms delay increased by 138% ± 61%, whereas the CF-$\Delta F/F_0$ associated with the CF-EPSP occurring at 130 ms delay increased by 200% ± 24 %, relative to the CF-$\Delta F/F_0$ associated with CF-EPSP alone. In the case of Fura-2 signals, the CF-$\Delta F/F_0$ associated with the CF-EPSP occurring at 60 ms delay decreased by 43% ± 8%, whereas the CF-$\Delta F/F_0$ associated with CF-EPSP occurring at 130 ms delay remained almost unchanged (1% ± 3%) relative to the CF-$\Delta F/F_0$ associated with the CF-EPSP alone.

Since the Ca^{2+} binding to Fura-2 mimics that to the principal molecules forming the endogenous Ca^{2+} buffer, monitoring potential saturation of the high-affinity indicator gives a strong indication on what happens physiologically to Ca^{2+} binding proteins. In our experiments, in contrast to the low affinity indicator OG5N which displays buffering capacity smaller than that of the endogenous buffer, Fura-2 at relatively low concentration never exhibits supralinear Ca^{2+} signals, but in the specific case of the signal associated with the CF delayed by 60 ms the amplitude of Ca^{2+} signal in paired PF-CF activation was strongly reduced. In fact, the elevation of fast Ca^{2+} signals generated by PF stimulation mediated by VGCCs saturates the free

Fura-2 concentration reducing its availability for further binding caused by delayed Ca^{2+} influx. Hence, the observed reduction in Fura-2 $\Delta F/F_0$ signals amplitude associated with CF-EPSPs occurring at 60 ms delay with respect to Ca^{2+} signals associated with CF-EPSP alone is due to the saturation of Fura-2. In contrast, Ca^{2+} influx mediated by mGluR1 activation is very slow and diffusion rapid enough to maintain the free Fura-2 concentration constant. Consequently, Fura-2 does not saturate and is available for binding during the CF evoked Ca^{2+} signals. As a result, Fura-2 $\Delta F/F_0$ signals associated with CF-EPSPs occurring at 130 ms after burst PF stimulation which coincide with the onset of mGluR1 activation did not decrease in amplitude with respect to the Ca^{2+} signals associated with CF-EPSP alone.

Two principal factors determine how mobile ECBs buffer Ca^{2+} influx. First, since Calbindin and Parvalbumin have more than one Ca^{2+} binding site, their kinetics of binding differentially regulates the spatiotemporal dynamics of Ca^{2+} signals. Calbindin, for instance, possesses two high affinity binding sites and two medium affinity binding sites. Second, the diffusion rate is variable depending on the kinetics of Ca^{2+} source. In particular, fast occurring episodes of Ca^{2+} signals do not give the time for ECB diffusion and, as a consequence ECBs saturate. In contrast, slow and persistent Ca^{2+} influx binds more slowly to ECBs allowing equilibration of these proteins and preventing their saturation (Schmidt *et al.*, 2003a). Physiologically, PF-evoked high frequency Ca^{2+} influx are able to saturate the ECB (Canepari *et al.*, 2008) leading to supralinear summation of intracellular free Ca^{2+}. Consequently, during paired PF-CF activation, when the CF-EPSP occurs at short delays after PF stimulation, the observed supralinear Ca^{2+} signals in this case are partly due to the saturation of ECBs, in addition to the mechanism of recruitment of P/Q-type Ca^{2+} channels that we previously demonstrated. In contrast, PF-mediated mGluR1 activation triggers slow Ca^{2+} influx that can only minimally saturate ECB. Thus, our result excludes the hypothesis that ECB saturation is the principal mechanism underlying the very large supralinear Ca^{2+} signal occurring at longer delays after

burst PF stimulation. In summary, mGluR1 independent supralinear Ca^{2+} transients mediated by A-type K^+ inactivation and P/Q t-type channels activation are due to the saturation of ECBs. These two mechanisms, however, are not at the base of the observed mGluR1-dependent supralinear Ca^{2+} transient.

4.5 Physiological mGluR1-dependant supralinear Ca^{2+} signals are not due to $InsP_3$-mediated Ca^{2+} release from stores

Activation of mGluR1 induces an increase in intracellular Ca^{2+} levels through two distinct signaling pathways that diverge after common G protein activation leading to Ca^{2+} mobilization from internal or external space (Canepari and Ogden, 2006). One of the pathways involves the activation of PLC via heterotrimeric G-proteins Gq/G_{11} which triggers the hydrolysis of phosphatidyl-inositol-bisphosphate (PIP) to inositol 1,4,5-trisphosphate ($InsP_3$) and diacyl-glycerol (DAG) an activator of PKC. The ensuing binding of $InsP_3$ to their receptors $insP_3R$ leads to Ca^{2+} release from smooth endoplasmic reticulum (SER) (Finch and Augustine, 1998) that is restricted to the spines activated (Takechi *et al.*, 1998; Canepari *et al.*, 2006). It has been shown that $InsP_3$-mediated Ca^{2+} release plays an important role in the induction of LTD that at PF-PN synapses (Khodakhah & Armstrong, 1997; Finch & Augustine, 1998; Inoue *et al.*, 1998). Since we demonstrated that mGluR1 activation is mediating the generation of supralinear Ca^{2+} signals associated with CF stimulation paired with burst PF stimulation it was necessary to investigate the contribution of $InsP_3$-mediated Ca^{2+} release to the generation of supralinear Ca^{2+} transients during co-activation of PF and CF inputs.

We thus examined the change in the supralinear Ca^{2+} signals associated with pairing PF-CF activation in the presence of U73112 introduced into the cytosol through the patch pipette to suppress $InsP_3$-mediated Ca^{2+} release. In fact, U73112, by inhibiting PLC, prevents the hydrolysis of PPI to IP3 (Bleasdale *et al.*, 1990) and

the consequent signal cascade. We loaded 6 PNs with 2mM of OG5N and 5 µM U73112 in order to block PLC and left equilibrating for at least 30 minutes. Figure 4.5A illustrates a representative example of a PN indicating the position of the two stimulating pipettes used to stimulate CF and PFs inputs and a region of interest (black circle, 2*2 pixels) where the PFs were stimulated. We stimulated the CF alone (CF-EPSP impaired) or after 5PF-EPSP with delays of 60 or 100 ms (Paired PF-CF stimulation). The corresponding OG5N-$\Delta F/F_0$ signals are reported in Figure 4.5B. In Figure 4.5C, we reported the CF- $\Delta F/F_0$ signals associated with CF-EPSP occurring at delays of 60 and 100 ms after the first PF-EPSP (orange traces) superimposed with CF- $\Delta F/F_0$ signals associated with CF-EPSP alone (black traces).

Supralinear Ca^{2+} signals associated with CF-EPSP occurring at both delays were not apparently affected by blocking PLC which suppresses Ca^{2+} release from internal stores via $InsP_3$ receptors. In Figure 4.5D, we reported the statistics obtained from six cells (mean ± sd) of the % of change in CF-$\Delta F/F_0$ signals produced by pairing PF-CF activation with the CF-EPSP delayed by 60 or 100 ms relative to the CF-$\Delta F/F_0$ signal associated with the CF-EPSP alone, in control condition from paragraph 4.2 (blue columns) and in the presence of U73122 (orange columns). In the presence of U73122, Ca^{2+} signals associated with CF-EPSP occurring at delays of 60 and 100 ms with respect to the first PF-EPSP increased by 150% ± 46 % and 229% ± 50% respectively. The increase in Ca^{2+} signals associated with the CF-EPSP paired with 5 PF-EPSP delayed by 60 or 100 ms in the presence of U73122 was consistent with that in control conditions. Thus, this experiment rules out the hypothesis that the mGluR1-dependent supralinear Ca^{2+} transient associated with the CF-EPSP is due to Ca^{2+} release from stores via $InsP_3$ receptors.

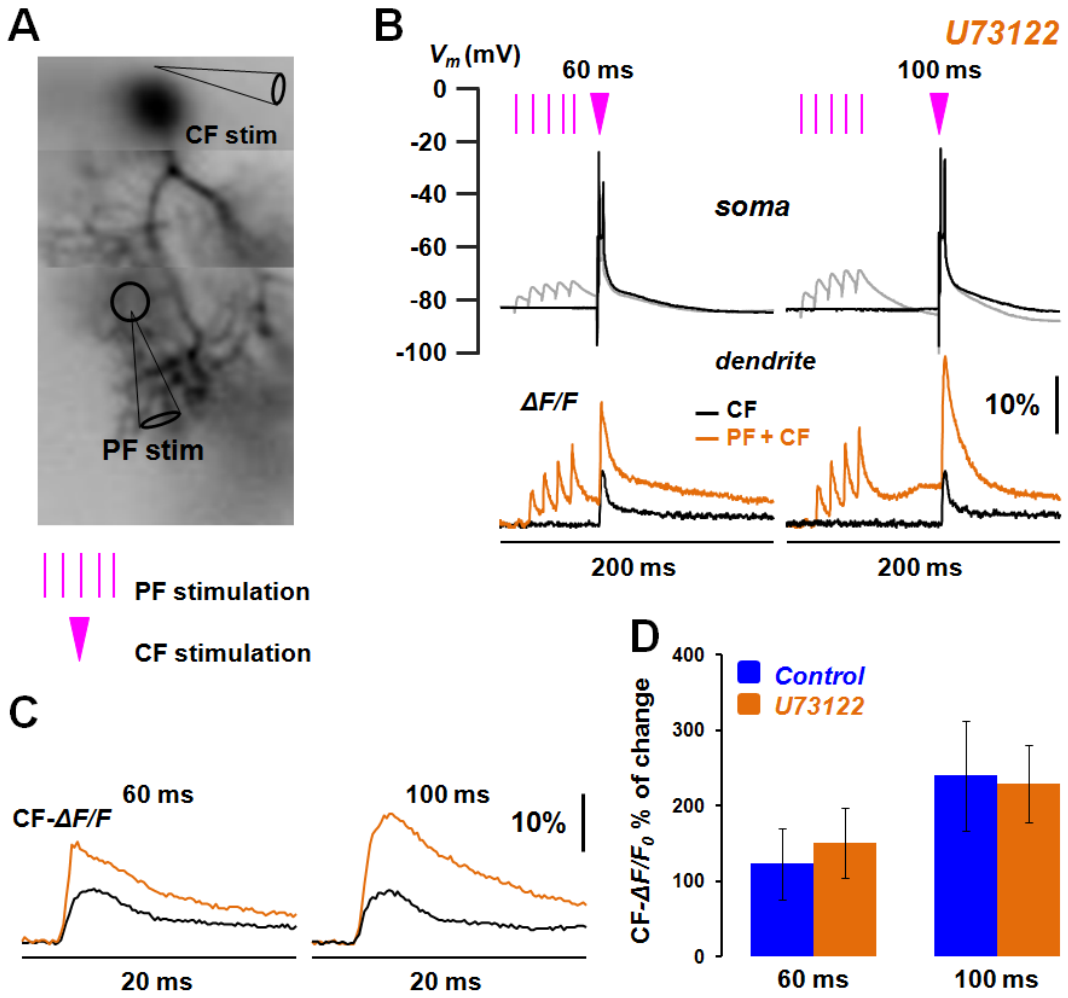

Figure 4.5. the effect of blocking $InsP_3$-mediated Ca^{2+} release on supralinear Ca^{2+} signal associated with PF-CF paired stimulation

A. Fluorescence reconstruction of a PN loaded with 2 mM of OG5N and 5 µM U73122 to block PLC and Ca^{2+} release from stores via InsP3 receptors. A region of interest and the position of the two PF stimulating pipette are indicated. **B.** On the top, somatic V_m following a CF-EPSP alone (black traces) and paired with 5 PF-EPSP with the CF-EPSP delayed by either 60 or 100 ms (gray traces) with respect to the first PF-EPSP, superimposed; on the bottom, the corresponding OG5N-$\Delta F/F_0$ signals. **C.** CF-$\Delta F/F_0$ associated with the CF-EPSP alone (black traces) and paired with 5 PF-EPSPs delayed by 60 or 100 ms (orange traces), superimposed. **D.** Statistics (mean ± sd) of the % of change in CF-$\Delta F/F_0$ signals produced by paired PF-CF stimulation with the CF-EPSP delayed by 60 or 100 ms relative to the CF-$\Delta F/F_0$ signals associated with the CF-EPSP alone in the absence (blue columns, 6 cells) and in the presence of U73122 (orange column, 6 cells).

4.6 The slow mGluR1-activated cation conductance is correlated with the physiological mGluR1-dependant supralinear Ca^{2+} transient

The glutamate release and its spillover from the synaptic clefts during strong PFs stimulation activates mGluR1 abundantly expressed by the dendrites of PN (Shigemoto *et al.*, 1992; Martin *et al.*, 1992) initiating two distinct signaling pathways and Ca^{2+} mobilization from internal and external space. We have demonstrated that PLC-dependent Ca^{2+} release from internal space does not contribute to the supralinear Ca^{2+} signals during paired PF-CF stimulation. Activation of mGluR1s, via the other signaling pathway, triggers a slow EPSP which is accompanied by Ca^{2+} influx from external space solely (Canepari *et al.*, 2004). Solid evidence indicates that this Ca^{2+} influx occurs through the transient receptor potential canonical channels (TRPC3) (Hartmann *et al.*, 2008, 2015). However, it was later shown that mGluR1 activates the orphan glutamate receptor δ2 (GluRδ2) that acts as non-selective cation channel permeable to Ca^{2+}, and the crosstalk between GluRδ2 and TRPC3 remains and open hypothesis (Ady *et al.*, 2014). TRPC3 belonging to TRPC subfamily of transient receptor potential (TRP) family of non selective cation channels is shown to be highly expressed in the cerebellum (Riccio et *al.*, 2002; Huang *et al.*, 2000) particularly at the somatodendrtic sites of PNs and it is pivotal for slow mGluR1-mediated synaptic transmission, synaptic plasticity and motor coordination (Hartmann et *al.*, 2008; Chae et *al.*, 2012). In fact, in TRPC3 knock-out mice, the sEPSC was suppressed and these animals showed walking behavior deficits (Hartmann *et al.*, 2008). Furthermore, mice with a TRPC gain-of-mutation exhibited cerebellar ataxia and their PNs showed abnormal development (Becker *et al.*, 2009). TRPC3 channels are Ca^{2+} permeable channels and, as a part of mGluR1 signaling cascade, should impact the Ca^{2+} signaling of PNs. Hence, the slow Ca^{2+} influx may contribute to the mGluR1-dependent supralinear Ca^{2+} transients in paired PF-CF activation. Additionally, TRPC3 mediated slow Ca^{2+} influx provides a more specific

and localized Ca^{2+} signaling at the PF-PN synapses in contrast to the widespread Ca^{2+} signaling mediated by VGCCs in response to CF activation. Therefore, investigating the possible contribution of mGluR1-mediated slow Ca^{2+} transients to the generation of to the mGluR1-dependent supralinear Ca^{2+} signal would provide the opportunity to elucidate the nature of the Ca^{2+} signal that triggers the coincident detection in PF-CF coactivation that underlies the induction cerebellar long term depression (Ito, 2000).

Thus, we examined the change in the supralinear Ca^{2+} signals associated with paired PF-CF activation produced by the non-selective channel blocker IEM-1460 (IEM, Magazanik *et al*., 1997). We loaded 7 PNs with 2 mM OG5N and left equilibrating as in previous experiments. After a first set of measurements in control conditions, 250 µM of IEM was bath applied and further measurements were performed after 10 minutes and every 5 minutes until 25-30 minutes in the presence of the drug. This procedure was designed to take into account the use-dependent mechanism of channel block that makes the action of IEM slower with respect to higher affinity inhibitors. Figure 4.5A illustrates a representative PN indicating the position of the two stimulating pipettes and a region of interest (black circle) where PFs were stimulated. In these experiments, after application of IEM, OG5N-$\Delta F/F_0$ signals were recorded at 3 different times. A train of 5 PF stimuli at 100 Hz were first delivered to the PF in the absence and in the presence of IEM and the corresponding OG5N-$\Delta F/F_0$ signals are reported in Figure 4.5B. The application of IEM decreased the mGluR1-dependent slow Ca^{2+} influx. We next stimulated the CF alone (CF-EPSP impaired) or after 5 PF-EPSPs with delays of 60 or 100 ms (Paired PF-CF stimulation) in the absence and in the presence of IEM and the corresponding OG5N-$\Delta F/F_0$ signals before (blue traces) and during IEM application (brown traces) are reported in Figure 4.5C.

Figure 4.4.1: The effect of blocking TRPC3 channels on the physiological mGluR1-dependent supralinear Ca^{2+} signals

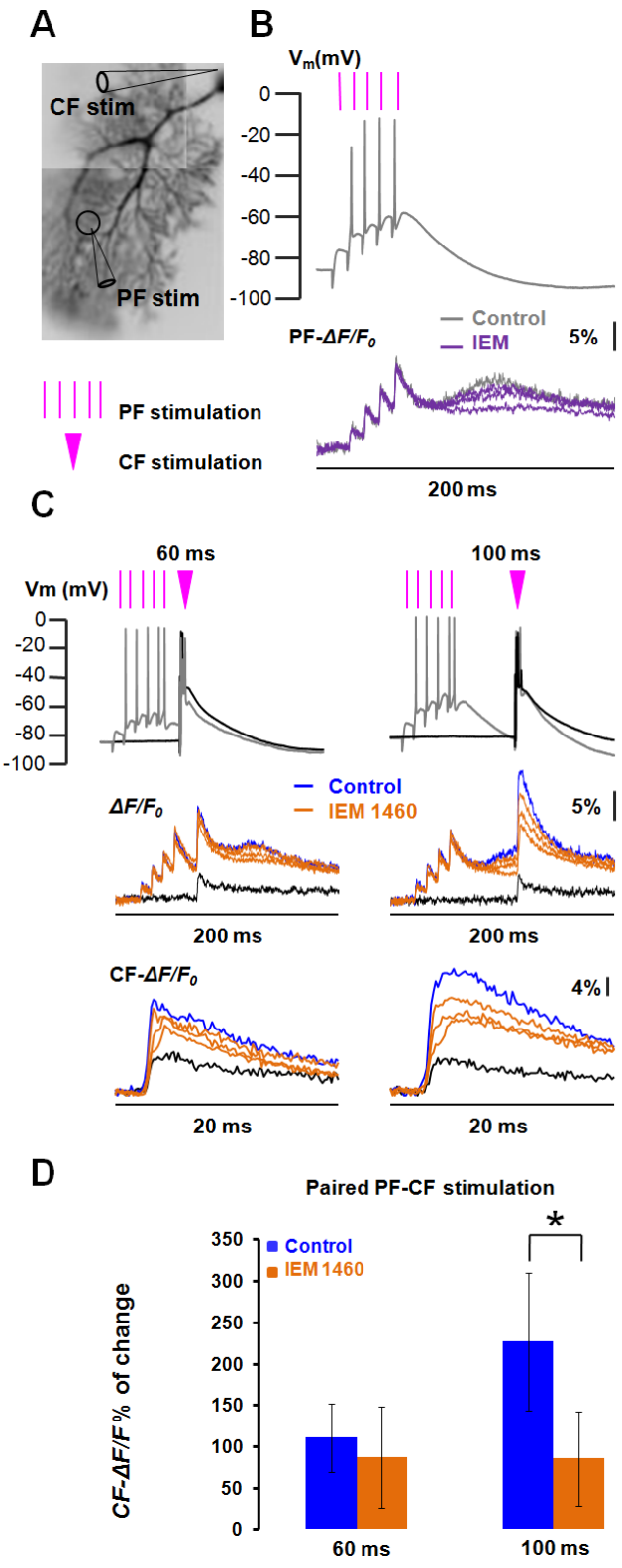

A. Florescence reconstruction of a PN filled with 2mM of OG5N indicating a region of interest next to the glass pipette used to stimulate the PFs. Another pipette is positioned above the soma to stimulate the CF input, 500 µM of the non selective open channel blocker IEM-1460 (IEM) was bath applied in order to block TRPC channels. **B.** On the top, the somatic V_m following a train of 5 PF stimuli delivered at 100 Hz; on the bottom, the corresponding OG5N-$\Delta F/F_0$ signals before (gray traces) and after bath application of IEM (3 recordings in time, pink traces), superimposed. **C.** On the top, the somatic V_m following CF-EPSP alone (black traces) and the somatic V_m following paired PF-CF stimulation with the CF-EPSP delayed by 60 or 100 ms (gray traces) with respect to the first PF-EPSP, superimposed; in the middle, OG5N-$\Delta F/F_0$ signals associated with the CF-EPSP alone (black traces) and the OG5N-$\Delta F/F_0$ signals associated with the paired PF-CF with the CF-EPSP delayed by 60 or 100 ms before (blue traces) and after bath application of IEM (3 recordings in time, brown traces) and on the bottom the corresponding CF-$\Delta F/F_0$ signals. **D.** statistic (mean ± sd, N = 7 cells) of the % of change in CF-$\Delta F/F_0$ signals produced by paired PF-CF stimulation with the CF-EPSP delayed by 60 or 100 ms relative to the CF-$\Delta F/F_0$ signals associated with the CF-EPSP alone in the absence (blue columns) and in the presence of IEM (brown column). The asterisk symbol "*" indicates the significant effect of the block of TRPC3 ($p < 0.001$, paired t-test).

The block produced by IEM decreased the supralinear Ca^{2+} signals progressively with time, as expected for a use-dependent blocker. We report in Figure 4.5D the statistics (mean ± sd, N = 7 cells) of the % of change in CF-$\Delta F/F_0$ signals associated with the CF-EPSP during paired PF-CF stimulation with the CF-EPSP delayed by 60 or 100 ms in the absence (blue column) or in the presence of IEM (brown columns) relative to CF-$\Delta F/F_0$ signals associated with the CF-EPSP impaired. While the block produced by IEM decreased the supralinear Ca^{2+} signals associated with the CF-EPSP paired with 5 PF-EPSPs occurring with 100 ms delay from 227% ± 83% to 86% ± 56%, it decreased the supralinear Ca^{2+} signal associated with the CF-EPSP paired with 5 PF-EPSP occurring with 60 ms delay non significantly from 111% ± 41 to 87% ± 61%. The significant effect is indicated by "*" ($p < 0.001$, paired t-test).

In order to block the channel mediating the slow mGluR1-dependent slow Ca^{2+} influx, we used IEM which is a non selective open channel blocker of non GluA2-containing AMPA receptors. The block of the channel decreased significantly the mGluR1-dependent slow Ca^{2+} influx and the supralinear Ca^{2+} transients associated with the CF-EPSPs occurring with 100 ms delay. In contrast, the same block had no considerable effect on the supralinear Ca^{2+} transient associated with the CF-EPSPs occurring with 60 ms delay. This result provides evidence that mGluR1-mediated slow conductance is correlated with the generation of the mGluR1-dependent supralinear Ca^{2+} transient which is in line with its importance in mGluR1-signaling and synaptic plasticity in PN. At this stage, it is however impossible to clearly correlate the activation of TRPC3 with the mGluR1-dependent supralinear Ca^{2+} transient. We also tested, in 6 cells, the more specific TRPC3 inhibitor pyr3 (Kiyonaka et *al*., 2009), but we obtained inconsistent results from cell to cell (data not shown).

4.7 Conclusions

The main goal of the experiments reported in this chapter was to investigate the Ca^{2+} signals in cerebellar Purkinje neurons associated with the coactivation of the two excitatory inputs (PFs and CFs) using the optical approaches developed in our laboratory. CF stimulation alone generates a complex spike signal in the soma and a dendritic signal that was described in the previous chapter. Repetitive PFs stimulation leads to glutamate release, activating AMPA receptors, and spillover that activates mGluR1 leading to a slow Ca^{2+} influx. Strong evidences were provided demonstrating that the slow Ca^{2+} influx is mediated by TRPC3 channels (Hartmman *et al.*, 2008). The coactivation of PF and CF produces a Ca^{2+} signal larger than the linear summation of the signals associated with the PFs and the CF separately activated (Wang *et al.*, 2000). It is well known that these large Ca^{2+} transients, strictly dependent on the timing between the PFs and CF activation, provide the signal that underlies the coincident detection between PFs and CF inputs (Wang *et al.*, 2000) which is associated with short-term (Brenowitz and Regehr, 2003) and long-term (Ito and Kano, 1996; Konnerth *et al*., 1992; Augustine et *al*., 2003) synaptic changes at PF-PN synapses. However, the molecular mechanisms leading to the supralinear Ca^{2+} signals and their nature are still poorly understood.

We sought to explore the supralinear Ca^{2+} signals at different delays between the train of five local PF-EPSPs and one CF-EPSP. We thereby performed experiments in which membrane potential (V_m) and Ca^{2+} imaging were carried out using a voltage sensitive dye and Ca^{2+} indicators of different affinities respectively. These experiments included pharmacological manipulations. The main finding was that the stimulation of CF after the train of five PF-EPSPs was associated with two different types of supralinear Ca^{2+} signals. The principal difference was determined by the timing delay between the PF and CF. In fact, when the CF-EPSP occurred with short delays (60 ms) after PF stimulation, the supralinear Ca^{2+} signals were

independent of the activation of mGluR1s whereas when the CF-EPSP occurred with longer delays (100-150 ms), the CF supralinear Ca^{2+} signals depended on mGluR1 activation. Other differences concerned the mechanisms underlying the generation of these two different signals. We demonstrated that the mGluR1-independent supralinear Ca^{2+} signals were generated through a combined effect of two mechanisms. First, the inactivation of A-type K^+ channels, that was mediated by PF-dependent depolarization, led to an increase in Ca^{2+} influx through P/Q-type VGCCs opening and second, a subsequent transient saturation of endogenous Ca^{2+} buffers which amplified Ca^{2+} concentration. We also demonstrated that the generation of mGluR1-supralinear Ca^{2+} signals, in contrast, did not involve any of these mechanisms. We however demonstrated that the generation of supralinear Ca^{2+} signals in this case was correlated with an increase in the slow Ca^{2+} influx via the activation of the cation conductance accompanying mGluR1 activation. Unexpectedly, we could not confirm that this conductance was the TRPC3 channel.

Chapter 5:
Discussion

5.1 Discussion of results in Chapter 3

The current results were obtained using recent optical methods which consist on combining voltage imaging with Ca^{2+} imaging recorded from multiple dendritic sites in Purkinje neurons at high temporal resolution (5 kHz). Using low affinity Ca^{2+} fluorescent indicators and a voltage sensitive dye, the available system allowed us monitoring Ca^{2+} transients and their correlation with the underlying membrane potential under physiological conditions, offering the opportunity to fully investigate and understand the occurrence of Ca^{2+}-dependent events and their voltage dependence following synaptic transmission. These achievements cannot be accomplished using electrophysiological tools given the fact that V_m recorded directly from the site of origin is different from that recorded at the site of the patch due to dendritic electrical filtering. Moreover, a series of technical aspects favor using our optical system in order to investigate Ca^{2+} dependent events. The dendritic tree of PNs is flat, their dendritic electrical responses are regulated by Ca^{2+} transients and the biophysical properties of these Ca^{2+} signals rely on the membrane depolarization (Tank *et al.,* 1988). One of the specific goals of my work was to investigate Ca^{2+} transients and V_m signals associated with the CF-EPSP.

CF activation transiently depolarizes the dendrites of PNs and the subsequent electrical signal plays a pivotal role in dendritic processing, integration and in shaping the final output of PNs. This electrical signal is mediated by Ca^{2+} and V_m dependent ion channels operating at the dendrites of PNs. Thus, understanding the functional role of these channels is crucial for understanding PN function. In the first set of the results, we reported the measurement of V_m and Ca^{2+} signals associated with the CF-EPSP at different initial states of the somatic membrane potential.

V_m calibration and correlation with Ca^{2+} signals

The correlation between dendritic Ca^{2+} transients and V_m signals associated with the CF-EPSP under physiological conditions facilitates the interpretation of the results obtained and provides critical information about dendritic Ca^{2+} dependent events and the underlying membrane potentials. Direct measurement of V_m and Ca^{2+} transient from multiple sites were achieved and signals were initially expressed as fractional changes of fluorescence (*$\Delta F/F_0$* signals). In order to correlate V_m signals with Ca^{2+} transient, two conditions must be satisfied. First, voltage $\Delta F/F_0$ must be expressed on an absolute scale (in mV), which was achieved by calibrating these signals in terms of membrane potential. In fact, in PNs, V_m $\Delta F/F$ signals can be calibrated in terms of membrane potential using long-lasting hyperpolarizing pulses that have approximately the same amplitude all over the dendritic arbor (Stuart and Häusser, 1994; Roth and Häusser, 2001). More importantly, the calibration of optical V_m signals on an absolute scale is important to compare ΔV_m from multiple dendritic sites. Second, Ca^{2+} optical signals must reflect Ca^{2+} influx into the cytosol in order to correlate with the corresponding V_m. While Ca^{2+} measurements using high-affinity indicators (with K_D < 1 µm) distort the physiological Ca^{2+} transients (Canepari & Mammano, 1999; Higley & Sabatini, 2008), the use of low-affinity indicators (with K_D > 10 µm), for instance FuraFF, allows physiological measurements of Ca^{2+} transients. Moreover, PNs have high dendritic buffering capacity estimated at ~2,000 (Fierro and Llano 1996). Therefore, the addition of a low affinity Ca^{2+} indicator does not significantly alter the physiological homeostasis of Ca^{2+}, and if needed Ca^{2+} signals can be quantified in terms of intracellular Ca^{2+} concentrations.

CF-EPSPs were evoked at a state of hyperpolarization (*hyp*, blue trace) around -80 mV, at an intermediate V_m (*int*, green trace) close to the resting V_m, and at a state of depolarization (*dep*, red trace). The associated dendritic V_m signals and Ca^{2+} transient were measured and correlated (see Materials and methods). The amplitudes of the dendritic Ca^{2+} transients associated with the CF-EPSP were

sensitive to variations in membrane potential. At hyperpolarized initial V_m, the associated dendritic V_m was below -10 mV and was associated with a moderate Ca^{2+} influx. As the initial V_m increases, both the dendritic V_m and Ca^{2+} influx increase. Additionally, dendritic spikes (typically two in the 18 ms after the stimulation) and correlated Ca^{2+} transients occur only when the dendrite is depolarized.

The activation of dendritic Ion channels during the CF-EPSP

The dendritic depolarization generated by the passive spread of the CF-EPSP from the site of origin activates voltage-gated Ca^{2+} channels (VGCCs). The block of individual VGCCs channels differently influences the kinetics and the amplitude of Ca^{2+} transients according to the obvious difference in the biophysical properties of activation and de-activation of these channels. In particular, we found that T-type VGCCs are mainly activated at hyperpolarized states, while P/Q-type VGCCs are mainly activated at depolarized states. Interestingly, we established a clear role for the A-type VGKCs in controlling the transition from the hyperpolarized state to the depolarized state.

Ion channels activated at hyperpolarized V_m

At initial hyperpolarized V_m (V_m ~ -80 mV), the dendritic transient depolarization associated with the CF-EPSP activates maximally T-type VGCCs. This is in agreement with the previous studies reporting that T-type channels are activated by subthreshold potential and that even small synaptic activation might generate a voltage-dependent Ca^{2+} current via T-type calcium channels (Isope & Murphy 2005; Isope *et al.*, 2012). Interestingly, the block of T-type channels did not suppress completely the Ca^{2+} transient and a fraction of P/Q channels was already activated at hyperpolarized V_m, albeit very weakly and not sufficiently enough to initiating Ca^{2+} spikes. In fact, at these state, A-type VGKC were fully activated and kept the V_m below ~-10 mV thus limiting the activation of P/Q channels (Sacco and Tempia,

2002). In these conditions, the Ca^{2+} provided by T-type channels opening activates SK channels which slightly contribute to V_m repolarization (Hosy *et al.*, 2011).

Ion channels activated at depolarized V_m

When the dendrite is depolarized (V_m ~ -50 mV), T-type channels and A-type VGKC fully inactivate bringing the dendritic V_m transient to supra-thresholds and therefore allowing maximal activation of P/Q channels and initiation of dendritic Ca^{2+} spikes (Usowicz *et al.*, 1992). Interestingly, P/Q-type VGCCs are active at all V_m state, this evidence reflects the fact that they conduct the big majority of PN Ca^{2+} current and their activation is very crucial in synaptic transmission (Llinas & Sugimori 1980; Konnerth *et al.*, 1992; Regehr *et al.*, 1994). In this condition, the V_m depolarization and the Ca^{2+} influx allow in conjunction BK channels to be activated (Womack & Khodakhah, 2002). BK channels activation accelerates the repolarization of V_m and therefore limits the number of Ca^{2+} spikes which appears to be a primary function of BK channels (Rancz and Hausser, 2006).

Functional coupling among VGCCs and K^+ channels during CF-EPSPs

We have shown how dendritic Ca^{2+} influx associated with a CF-EPSP activates VGCCs, VGKCs and Ca^{2+} activated K^+ channels (BK and SK). Using pharmacological tools, we reported a detailed analysis of the changes in the CF-mediated dendritic Ca^{2+} transient at the different initial V_m produced by local selective inhibition of different Ca^{2+} or K^+ channels. Remarkably, our results showed that the changes observed in Ca^{2+} signals associated with the CF-EPSP at different initial V_m produced by the block of the different dendritic channels were variables depending on the initial V_m, indicating that these channels are selectively and differentially activated at different initial V_m. Indeed, the CF-EPSP activates two distinct sets of channels according to whether the initial V_m was hyperpolarized or depolarized. While at hyperpolarized V_m Ca^{2+} influx through T-type VGCCs activates SK channels,

the V_m depolarization and the subsequent P/Q mediated Ca^{2+} influx activates BK channels. In the brain, BK and SK are reported to be coupled to specific types of VGCCs. This coupling is possibly mediated by the co-localization and molecular interaction with the VGCCs which facilitate BK and SK channels to sense rapidly the rise in Ca^{2+} influx through VGCCs (Davies *et al.*, 1996; Marrion and Tavalin, 1998; Prakriya and Lingle, 1999; Smith *et al.*, 2002; Wolfart and Roeper, 2002 Cueni *et al.*, 2008). In dendrites of hippocampal pyramidal cells, for instance, SK channels are activated by Ca^{2+} influx through L-type VGCC channels to control dendritic excitability (Marrion and Tavalin, 1998). When the dendrite is depolarized, P/Q channels activation provides the Ca^{2+} that activates BK channels which accelerates V_m repolarization and limits the number of Ca^{2+} spike. This evidence suggests a role of BK channels in controlling P/Q-type VGCCs activation. Indeed, a functional coupling between BK channels and P/Q-type VGCCs was previously reported (Womack *et al.*, 2004). BK channels provide negative feedback to limit the duration of depolarization and Ca^{2+} entry through voltage-gated calcium channels. In contrast, SK channels have been shown to be more implicated in the regulation of the frequency of firing and contribute to the slow after hyperpolarization (Sah, 1996; Pedarzani *et al.* 2001; Edgerton & Reinhart, 2003). Yet, a research reports a role in the repolarization of dendritic plateau potentials (Cai *et al.* 2004). The block of SK channels affects the Ca^{2+} transient when the dendrite is hyperpolarized indicating that the T-type channels provides Ca^{2+} influx at this V_m. Indeed, SK channels appear to be selectively linked to T-type channels, presumably by molecular coupling (Stocker, 2004; Cueni et *al.*, 2008). On the other hand, the block of SK channels did not have any apparent effect on the Ca^{2+} transient when the dendrite is depolarized. This is surprising if we consider the following facts: SK channels are exclusively activated by Ca^{2+} influx and their activation does not depend on the V_m. In addition, previous electrophysiological studies showed that SK channels are selectively coupled to P/Q-type calcium channels and that activation of SK2 channels is regulated by Ca^{2+}influx through $Ca_V2.1$ channels during spontaneous firing in PNs

(Womack *et al.*, 2004). Consequently, we cannot conclude that SK channels are not activated when the dendrites are depolarized. The most possible explanation is that SK channels might be active at depolarized V_m, but the current carried by SK channels was negligible with respect to the BK current. Thus, the block of SK channels doesn't affect Ca^{2+} transients associated with the CF-EPSP at depolarized V_m. Finally, SK and BK are activated by a transient Ca^{2+} elevation in the cytosol and their activation leads to V_m repolarization which in turn reduces the Ca^{2+} influx. They, in fact, serve as negative feedback that regulates the spatiotemporal pattern of Ca^{2+} dynamics and thus dendritic responsiveness to synaptic input activation.

Physiological role of A-type VGKCs and it is potential role in synaptic plasticity

Several studies have been reported emphasizing the physiological role of A-type VGKCs and their modulation. They reported their involvement in the regulation of many aspects of neuronal excitability and integration (Coetzee *et al,* 1999; Hille, 2001; Iohnston et *al.*, 2003; midtgaard, 1993). The physiological role of these channels relies on their biophysical and molecular properties, mainly the kinetics of activation and inactivation and the voltage dependence. In our experiments, we observed that at hyperpolarized initial V_m, A-type VGKCs limit the activation of P/Q-type VGCCs and prevent the activation of BK channels. However, they are rapidly inactivated after membrane depolarization leading to maximal activation of P/Q-type VGCCs and Ca^{2+} spike generation. Since they control the subthreshold dendritic excitability, the modulation of these channels by synaptic transmission may be an important aspect in Ca^{2+} signalling and synaptic plasticity induction. In pyramidal neurons, the transient subthreshold A-type K^+ current attenuates back-propagating action potentials and limits their propagation into distal regions of the dendritic tree (Hoffman et *al.*, 1997). However, when action potentials and Schaffer collateral EPSPs are coupled in CA1 pyramidal neurons, the subsequent depolarization inactivates A-type VGCCs (Johnston et *al.*, 2000, Migliore et *al.*, 1999) causing action potentials to be potentiated and unlocking NMDA receptors, increasing Ca^{2+}

influx that promotes synaptic plasticity. This interaction provided a coincident detection mechanism that plays an important role in Ca^{2+} signaling and synaptic plasticity. Additionally, several modelling studies further supported this hypothesis (Migliore et *al.*, 1999; Johnston et *al.*, 2000). In PNs, the CF-EPSP associated with dendritic depolarization increases the dendritic Ca^{2+} transient through P/Q-type VGCC activation. Furthermore, A-type VGKCs are modulated by mGluR1s (Otsu *et al.*, 2014). These evidences suggested an important role for A-type VGKC in the induction of synaptic plasticity mediated by the coactivation of PF and CF inputs and motivated the following experiments of my thesis.

5.1 Discussion of results in Chapter 4

The coincidence activity of multiple signals at a synaptic site is believed to trigger several forms of associative synaptic plasticity. A notable site where such a type of phenomenon occurs is the dendrite of PNs receiving two excitatory inputs, namely PFs and the CF. The activation of PFs triggers local Ca^{2+} influx confined to a small number of spiny branchlets being activated whereas the activation of the CF input produces a depolarization that spreads passively into the dendrite and activates a set of ion channels eliciting Ca^{2+} transients in PF input territory, as investigated in Chapter 3. Accordingly, the dendritic transient depolarization induced by the CF input act as a global signal regulating local PF signals and their plasticity at distal sites. Indeed, the concurrent activity of local PF and global CF inputs amplifies Ca^{2+} transient providing coincident signals leading to short and long term depression at PF-PN synapse associated with motor learning and crucial cerebellar functions. Here, we exploited our advanced imaging techniques based on V_m imaging and Ca^{2+} imaging, using principally low affinity Ca^{2+} indicators but also a high affinity Ca^{2+} indicator combined with pharmacological assays to explore the sequences of events that lead to local supralinear Ca^{2+} transients associated with the CF-EPSP after PF activity. The principal finding was that the activation CF paired with physiologically

realistic PF activity was associated with two different types of supralinear Ca^{2+} signals which were determined by the temporal delay between CF and PFs activity and, in each type, different mechanisms are determined by concomitant PF and CF activity.

Supralinear Ca^{2+} transients associated with concomitant PF and CF activity

Dendritic supralinear Ca^{2+} signals associated with coactivation of PFs and the CF are believed to trigger the induction of short and long term depression. This phenomenon strictly depends on the timing between these two inputs. In order to explore these supralinear Ca^{2+} signals, we defined a protocol for PF and CF stimulation similar to that utilized by Brenowitz and Regehr (2005), which was associated with short-term plasticity of PF activity. In order to best mimic the natural activity of PFs, we adjusted the intensity and the frequency of PF stimulation to a level that limited to the minimum the number of synapses activated, while producing a detectable Ca^{2+} signal at the first 1-2 PF-EPSPs of the train. Under this condition, PF-mediated depolarization and Ca^{2+} influx was confined to very small areas. The protocol consisted of a train of 5 PF-EPSP followed by one CF-EPSP. We varied the timing window between the start of the PF train and the CF stimulus (60, 100 or 150 ms). At all temporal windows, the coactivation of PF and FF evoked supralinear Ca^{2+} signals that were confined to the activated area. Bath application of CPCCOEt allowed us discrimining two types of supralinear Ca^{2+} signals. Indeed, when the CF occurs near the end of the PF-EPSP burst, the associated supralinear Ca^{2+} signal is insensitive to CPCCOEt application indicating an independence of mGluR1 activation. This signal is instead generated through a combined effect of two mechanisms. The PF-mediated membrane depolarization inactivates A-type VGKCs permitting P/Q-type VGCC activation and leading to a largee Ca^{2+} influx (see Chapter 3 and discussion above). In addition, the saturation of endogenous Ca^{2+} buffers during the PF-EPSP burst amplifies the free Ca^{2+}, therefore leading a supralinear OG5N signal without any additional Ca^{2+} influx. When instead the CF-EPSP occurs

at longer delays after the end of the PF burst, the associated supralinear Ca^{2+} signals were inhibited by CPCCOEt application indicating that mGluR1 was mediating these signals. In this case, the generation of supralinear Ca^{2+} signals did not involve the former mechanisms. Indeed, an entirely distinct mechanism is recruited and we demonstrated that the generation of supralinear Ca^{2+} signals was correlated with an increase in the slow Ca^{2+} influx via the activation of the cation conductance accompanying mGluR1 activation.

PF-mediated membrane depolarization, A-type inactivation and P/Q channels activation

The activation of PFs leads to the activation of AMPA receptors at the postsynaptic site and the consequent depolarization activates T-type VGCC channels. We demonstrated here that when the CF occurred near the end of the PF burst, the PF-dependent depolarization transient was long and large enough to inactivate A-type K+ channels increasing the CF-associated V_m peak to levels that enabled the activation of P/Q-type VGCCs. In fact, in Chapter 3, we showed that the activation of PF at depolarized initial V_m inactivates A-type channels leading to maximal activation of P/Q channels. Additionally, in a recent study, it has been shown that chemical stimulation of mGluR1s combined with depolarization shift the inactivation curve of A-type K^+ channels towards more hyperpolarized membrane potential decreasing their availability at resting membrane potential which led to Ca^{2+} spike initiation. In our experiments, chemical stimulation of mGluR1 by DHPG amplified the Ca^{2+} transient associated with the CF-EPSP. The kinetic quantification performed showed that the kinetics of the supralinear Ca^{2+} signals associated with CF occurring at short delays after the end of the PF burst were comparable with those associated with CF after chemical stimulation of CF. But, they were different with those associated with CF stimulation at longer delays (100-150 ms) after PF stimulation. Thus, this result confirmed that mGluR1-independent supralinear Ca^{2+} transients are mediated by A-type K^+ inactivation and P/Q-type VGCCs activation.

Transient saturation of endogenous Ca^{2+} buffers

The Ca^{2+} influx through P/Q-type VGCCs does not fully explain the supralinearity of Ca^{2+} transient associated with CF activity occurring near the end of the PF suggesting that another mechanism could be involved. In fact, supralinearity can be observed with low affinity indicators while high-affinity Ca^{2+} buffers reach saturation. PNs express a high level of mobile endogenous Ca^{2+} buffers (ECB) including calbindin-D28K (CB) and parvalbumin. CB displays high and medium Ca^{2+} affinity and it is characterized by relatively fast kinetics. Furthermore, the degree of the saturation also is determined by the time course of the Ca^{2+} signals. Indeed, fast occurring episodes of local Ca^{2+} signals do not give the time for ECBs to equilibrate and, as a consequence, ECBs saturate. In contrast, slow and persistent Ca^{2+} influx binds more slowly to ECBs allowing equilibration of these proteins and preventing their saturation. Canepari & Vogt (2008) demonstrated that bursts PF-EPSPs can locally saturate the endogenous calcium buffer leading to supralinear summation of intracellular free Ca^{2+}. In our experiments, in addition to the low affinity indicator OG5N, we introduced a high-affinity indicator Fura-2 at a concentration comparable to that of CB. Thus, Fura-2 competing with Calbindin would saturate in similar proportion. Hence, the observed reduction in Fura-2 fluorescent signals amplitude associated with the CF-EPSP shortly after PF burst was the result of the transient Fura-2 saturation by fast Ca^{2+} elevation induced by PF activity. Thus, when Fura-2 is not present, the transient saturation of the endogenous buffer contributes to the supralinear Ca^{2+} signal during the pairing protocol when the CF is stimulated near the end of the PF burst.

Physiological mGluR1 activation

More recently, it has been shown that mGluR1s activation with DHPG combined with depolarization promotes A-type VGKC inactivation unlocking local dendritic Ca^{2+} spikes during the CF-EPSP (Otsu *et al.*, 2014). The analysis of the kinetics

performed from our data showed that the supralinear Ca^{2+} signals associated with CF-EPSP after mGluR1 stimulation with DHPG and those associated with CF activity occurring at the same time with physiological activation of mGluR1 displayed different features, indicating that the mechanisms involved in the generation of these Ca^{2+} transients are different. In fact, the mGluR1-depandent slow depolarization is counteracted by the K^+ channels-dependant afterhyperpolarization following PF-EPSPs preventing A-type K^+ inactivation and P/Q channels activation. Since the activation of mGluR1s in PN dendrites is associated with distinct Ca^{2+} entry through a non selective cation conductance (Canepari *et al.*, 2004) and Ca^{2+} release from stores via $InsP_3$ receptors (Canepari and Ogden, 2006), it has been suggested that the triggering supralinear Ca^{2+} signal during coincident PF-CF activity may be one from these two pathways. mGluR1s activate PLCβ leading to Ca^{2+} release from stores via InsP3 receptors. Selective inhibition of PLCβ by dialysis with the antagonist U73122 did not affect the CF-associated Ca^{2+} signal during the pairing protocol, ruling out the involvement of Ca^{2+} release from internal stores in the triggering of supralinear Ca^{2+} transients. On the other hand, mGluR1-dependent slow depolarization is associated with slow Ca^{2+} influx via non selective cation conductance. Interestingly, the block of this conductance substantially reduced the supralinear Ca^{2+} signals associated with CF-EPSPs occurring at long delays after PF activity, indicating that mGluR1-mediated slow conductance is correlated with the generation of the mGluR1-dependent supralinear Ca^{2+} transient. It has been shown that this ion conductance is TRPC3 (Hartmann *et al.,* 2008). In our experiment, we were not able to provide solid evidence regarding the implication of TRPC3 in the generation of the supralinear Ca^{2+} transients, since a test using the selective TRPC3 inhibitor pyr3 gave inconclusive results (data not reported). Remarkably, a more recent study has however provided indications that the orphan GluD2 receptor forms functional channels that are triggered by mGluR1 activation in PNs indicating that the origin of the mGluR1-dediated slow EPSP may be more complex (Ady *et al*., 2014). Both TRPC3 and GluD2 have been found to be crucial in PN function.

Physiological relevance for synaptic plasticity

Supralinear Ca^{2+} signals mediated by the concomitant PF and CF activity provide the pivotal signal that triggers short term and long term depression that underlie motor learning and coordination. Both forms of plasticity appear to be homosynaptic and to require the activation of mGluR1 pathways which are involved in crucial cerebellar functions. This view is supported by the observation that mice lacking mGluR1 have deficient cerebellar synaptic plasticity and displayed severe impairment in motor learning and coordination (Aiba *et al.*, 1994, Conquet *et al.*, 1994). Interestingly, we demonstrated that concomitant PF and CF activity are able to generate supralinear Ca^{2+} signals that are either dependent or independent of the activation of mGluR1 signaling pathways and are mediated by entirely different mechanisms. Whether the mGluR1-independent signal has physiological significance is not clear, although supralinear Ca^{2+} signals associated with PF stimulation only have been shown to be associated with induction of PF long-term potentiation (Canepari and Vogt, 2008). PF synapses lack postsynaptic NMDA receptors and it is the physiological signaling pathway mediated by mGluR1s that leads to mechanisms of synaptic plasticity at PF-PN synapses which are crucial for cerebellar function. It has been shown that induction of PF-LTD required activation of metabotropic glutamate receptors (Linden *et al.*, 1991). The contribution of mGluR1s to PF-LTD was further confirmed and extended by studies in mGluR1-knockout mice (Aiba *et al.*, 1994, Conquet *et al.*, 1994). Furthermore, mGluR1 activation is an important step for the generation of endocannabinoids that rapidly act as retrograde messengers by activating CB1 receptors expressed on boutons of PF inputs (Maejima *et al.*, 2001; Brown *et al.*, 2003), reducing glutamate release and therefore leading to short-term depression of PF-PN synapses (Brenowits and Regehr, 2005). The endocannabinoid signaling is also required for the induction of LTD of at PF-PN synapses, since it was demonstrated that mGluR1-dependent LTD was inhibited by the block of CB1 receptors (Safo & Regehr 2005).

5.3 Future perspectives

The results reported here advanced our important understanding of supralinear Ca^{2+} signals associated with concomitant PF and CF activation. In particular, we were able to rule out several hypotheses that have been thus far proposed in the recent literature. Nevertheless, we were not able yet to answer a crucial question: what is the Ca^{2+} source mediating the mGluR1-dependent supralinear Ca^{2+} signal? Our data suggest that this signal originates from a Ca^{2+} signal through the plasma membrane, although our membrane potential imaging experiments have shown that no addition depolarization occurs during the paired CF-EPSP with respect to the CF-EPSP alone. An interesting possibility is that this conductance is the same mediating the slow mGluR1 Ca^{2+} influx possibly boosted by the CF depolarization. Indeed, both signals are inhibited by the channel blocker IEM1460. Another possibility is a local boosting of permeability of T-type VGCCs, that are equally activated by the CF-EPSP, but that might mediate more or less Ca^{2+} influx under paired or unpaired conditions. These two possibilities must be further investigated in future experiments.

References

-A-

Adrian E. D. (1943). Afferent areas in the cerebellum connected with the limbs. Brain. 66: 289–315.

Ady V., Perroy J., Tricoire L., Piochon C., Dadak S., Chen X., Dusart I., Fagni L., Lambolez B. & Levenes C. (2014). Type 1 metabotropic glutamate receptors (mGlu1) trigger the gating of GluD2 delta glutamate receptors. EMBO. Rep. 15: 103–109.

Afshari F.S., Ptak K., Khaliq Z. M., Grieco T. M., Slater N. T., McCrimmon D.R., Raman I. M. (2004). Resurgent Na currents in four classes of neurons of the cerebellum. J. Neurophysiol. 92: 2831–2843.

Aiba A., Kano M., Chen C., Stanton M.E., Fox G.D., Herrup K., Zwingman T.A., Tonegawa S. (1994). Deficient cerebellar long-term depression and impaired motor learning in mGluR1 mutant mice. Cell. 79: 377–388.

Airaksinen M. S., Eilers J., Garaschuk O., Thoenen H., Konnerth A., Meyer M. (1997). Ataxia and altered dendritic calcium signaling in mice carrying a targeted null mutation of the calbindin D28k gene. Proc. Natl. Acad. Sci. U S A. 94: 1488–1493.

Ait Ouares K., Jaafari N. and Canepari M. (2016). A generalised method to estimate the kinetics of fast Ca(2+) currents from Ca(2+) imaging experiments. J. Neurosci. Methods 268: 66 -77.

Akemann W., Knöpfel T. (2006). Interaction of Kv3 potassium channels and resurgent sodium current influences the rate of spontaneous firing of Purkinje neurons. J. Neurosci. 26: 4602–4612.

Albus J. S. (1971). A theory of cerebellar function. Mathematical Biosciences, 10: 25–61.

Allbritton A., Meyer T., Stryer L. (1992). Range of messenger action of calcium ion and inositol 1,4,5 trisphosphate. Science. 258: 1812–1815.

Aman T.K., Raman I.M. (2007). Subunit dependence of Na channel slow inactivation and open channel block in cerebellar neurons. Biophysical. J. 92(6): 1938–1951.

Andersson G. and Oscarsson O. (1978). Climbing fiber microzones in cerebellar vermis and their projection to different groups of cells in the lateral vestibular nucleus. Exp. Brain Res. 32: 565–579.

Annoura H., Fukunaga A., Uesugi M., Tatsuaka T., and Horikawa Y. (1996). A novel class of antagonists for metabotropic glutamate receptors, 7-(hydroxyimino)cyclopropa[b]chromen-1a-carboxylates. Bioorg. Med. Chem. Lett. 6: 763–766.

Anwar H., Hong S., and De Schutter E. (2010). Controlling Ca2+-activated K+ channels with models of Ca2+ buffering in Purkinje cells. Cerebellum 11: 1–13.

Apps R., Garwicz M. (2005). Anatomical and physiological foundations of cerebellar information processing. Nat. Rev. Neuroscience 6(4): 297 - 311.

Armstrong D. M., Harvey R. J., and Schild R. F. (1973). Branching of inferior olivary axons to terminate in different folia, lobules or lobes of the cerebellum. *Brain* Res. 54: 365–371.

Armstrong D. M., Rawson J. A. (1979). Activity patterns of cerebellar cortical neurones and climbing fibre afferents in the awake cat. J. Physiol. 289: 425–448.

Augustine G.J., Santamaria F., and Tanaka K. (2003). Local calcium signaling in neurons. Neuron. 40: 331–346.

-B-

Babinski J. (1902). Sur le rôle du cervelet dans les actes volitionnels necessitant une succession rapide de mouvements (diadococinésie). Rev Neurol 10:1013–1015.

Baimbridge K., Celio M., Rogers J. (1992). Calcium-binding proteins in the nervous system. Trends in Neurosciences. 15: 303–308.

Baldwin T. J., Tsaur M. L., Lopez G. A., Jan Y. N., Jan L. Y. (1991). Characterization of a mammalian cDNA for an inactivating voltage-sensitive K 1 channel. Neuron 7: 471–483.

Ballesteros-Merino C., Martínez-Hernández J., Aguado C., Watanabe M., Adelman, J. P., and Luján R. (2014a). Localization of SK2 channels relative to excitatory synaptic sites in the mouse developing Purkinje cells. Front. Neuroanat. 8: 154.

Barski J. J., Hartmann J., Rose C. R., Hoebeek F., Morl K, Noll-Hussong M., De Zeeuw C. I., Konnerth A., Meyer M. (2003). Calbindin in cerebellar Purkinje cells is a critical determinant of the precision of motor coordination. J. Neurosci. 23: 3469–3477.

Bastianelli E. (2003). Distribution of calcium-binding proteins in the cerebellum.

Cerebellum. 2:242–262.

Batchelor A. M., Garthwaite J. (1997). Frequency detection and temporally dispersed synaptic signal association through a metabotropic glutamate receptor pathway. Nature. 385: 74–77.

Baude A., Nusser Z., Roberts J. D. B., Mulvihill E., McIlhinney R. A. J., Somogyi P., (1993). The metabotropic glutamate receptor (mGluR1K) is concentrated at perisynaptic membrane of neuronal subpopulations as detected by immunogold reaction. Neuron 11: 771-787.

Becker E B, Oliver P L, Glitsch M D, Banks G T, Achilli F, Hardy A, Nolan PM, Fisher EM, Davies KE. (2009). A point mutation in TRPC3 causes abnormal purkinje cell development and cerebellar ataxia in moonwalker mice. PNAS. 106: 6706–6711.

Benton M. D., Lewis A. H., Bant J. S., Raman I. M. (2013). Iberiotoxin-sensitive and -insensitive BK currents in Purkinje neuron somata. J. Neurophysiol. 109: 1–38.

Blatow M., Caputi A., Burnashev N., Monyer H., Rozov A.. (2003). Ca^{2+} buffer saturation underlies paired pulse facilitation in calbindin-D28k-containing terminals. Neuron. 38:79–88.

Bossu J. L., Fagni L. & Feltz A. (1989). Voltage-activated calcium channels in rat Purkinje cells maintained in culture. Pflügers. Arch. 414: 92–94.

Bourinet E., T. W. Soong, K. Sutton, S. Slaymaker, E. Mathews, A. Monteil, G. W. Zamponi, J. Nargeot, and T. P. Snutch. (1999). Splicing of 1A subunit gene generates phenotypic variants of P- and Q-type calcium channels. Nat. Neurosci. 2: 407– 415.

Brenowitz S. D., Regehr W. G. (2003). Calcium dependence of retrograde inhibition by endocannabinoids at synapses onto Purkinje cells. J. Neurosci. 23: 6373–6384.

Brenowitz S. D. and Regehr W. G. (2005). Associative short-term synaptic plasticity mediated by endocannabinoids. Neuron. 45: 419–431.

Brodal A. (1954). Afferent cerebellar connections. In *Aspects of Cerebellar Anatomy*, ed. JANSEN, J. and BRODAL, A. ch. II, 82–188.

Buckner R. L., Krienen FM., Castellanos A., Diaz JC., Yeo BT. (2011). The organization of the human cerebellum estimated by intrinsic functional connectivity. Journal of neurophysiology. 106:2 322- 2345.

Butler A. B., Hodos W., 2005. Comparative Vertebrate Neuroanatomy: Evolution and

Adaptation. Wiley-Liss, New York.

-C-

Canepari M., Auger C., Ogden D. (2004). Ca2+ ion permeability and single-channel properties of the metabotropic slow EPSC of rat Purkinje neurons. J. Neurosci. 24: 3563–3573.

Canepari M., Mammano F. (1999). Imaging neuronal calcium fluorescence at high spatio-temporal resolution. J Neurosci. Methods 87: 1 -11.

Canepari M., Ogden D. (2003). Evidence for protein tyrosine phosphatase, tyrosine kinase, and G-protein regulation of the parallel fiber metabotropic slow EPSC of rat cerebellar Purkinje neurons. J. Neurosci. 23: 4066–4071.

Canepari M., Ogden D. (2006). Kinetic, pharmacological and activity-dependent separation of two Ca2+ signalling pathways mediated by type 1 metabotropic glutamate receptors in rat Purkinje neurons. J. Physiol. 573: 65–82.

Canepari M., Papageorgiou G., Corrie J. E., Watkins C., Ogden D. (2001b). The conductance underlying the parallel fibre slow EPSP in rat cerebellar Pur-kinje neurones studied with photolytic release of L-glutamate. J. Physiol. (Lond). 533: 765–772.

Canepari M., Vogt K. E. (2008). Dendritic Spike Saturation of Endogenous Calcium Buffer and Induction of Postsynaptic Cerebellar LTP. PLoS ONE 3: e4011.

Canepari M., Vogt K., Zecevic D. (2008). Combining voltage and calcium imaging from neuronal dendrites. Cell Mol Neurobiol 58: 1079-1093.

Canepari M., Willadt S., Zecevic D., Vogt K.E. (2010). Imaging Inhibitory Synaptic Potentials Using Voltage Sensitive Dyes. Biophys. J. 98: 2032-2040.

Catterall W. A. (2000). From ionic currents to molecular mechanisms: the structure and function of voltage-gated sodium channels. Neuron. 26: 13–25.

Catterall W. A. (2000). Structure and regulation of voltage-gated Ca^{2+} channels. Annu. Rev. Cell. Dev. Biol. 16: 521–555.

Catterall W. A., Perez-Reyes E., Snutch T. P., Striessnig J. (2005). International Union of Pharmacology. XLVIII. Nomenclature and structure-function relationships of voltage-gated calcium channels. Pharmacol. Rev. 57: 411–425.

Cavelier P., Lohof A. M., Lonchamp E., Beekenkamp H., Mariani J., Bossu J. L. (2008). Participation of low-threshold Ca2+ spike in the Purkinje cells complex spike. Neuroreport.19: 299–303.

Cavelier P., Pouille F., Desplantez T., Beekenkamp H., Bossu J. L. (2002). Control of the propagation of dendritic low-threshold Ca(2) spikes in Purkinje cells from rat cerebellar slice cultures. J. Physiol. 540: 57–72.

Chadderton P., Margrie T.W., Häusser M. (2004). Integration of quanta in cerebellar granule cells during sensory processing.428: 856–860.

Chae H. G., Ahn S. J., Hong Y. H., Chang W. S., Kim J. & Kim S. J. (2012). Transient receptor potential canonical channels regulate the induction of cerebellar long-term depression. J. Neurosci. 32: 12909–12914.

Chan-Palay V. (1977). Cerebellar Dentate Nucleus, Organization, Cytology and Transmitters. Berlin, Heidelberg, New York: Springer Verlag.

Chan C. Y., Hounsgaard J. and Nicholson C**.** (1988). Effects of electric fields on transmembrane potential and excitability of turtle cerebellar Purkinje cells in vitro. J. Physiol. 402: 751 -771.

Chen Y., Yu F.H., Sharp E. M., Beacham D., Scheuer T., Catterall W. A. (2008). Functional properties and differential neuromodulation of Na(v)1.6 channels. Molecular and Cellular Neurosciences. 38: 607–615.

Cheron G., Sausbier M., Sausbier U., Neuhuber W., Ruth P., Dan B., Servais L. (2009). BK channels control cerebellar Purkinje and Golgi cell rhythmicity in vivo. PloS One. 4(11): e7991.

Cingolani L. A., Gymnopoulos M., Boccaccio A., Stocker M., and Pedarzani, P. (2002). Developmental regulation of small-conductance Ca2+-activated K+ channel expression and function in rat Purkinje neurons. J. Neurosci. 22: 4456–44.

Coesmans M., Smitt P. A., Linden D. J., Shigemoto R., Hirano T., Yamakawa Y., et al. (2003). Mechanisms underlying cerebellar motor deficits due to mGluR1-autoantibodies. Ann. Neurol. 53: 325–336.

Coetzee W. A., Amarillo Y., Chiu J., Chow A., Lau D., McCormack T., Moreno H., Nadal M.S., Ozaita A., Pountney D., Saganich M, Vega-Saenz De Miera .E, Rudy B. (1999). Molecular diversity of K^+ channels. Ann. N. Y. Acad. Sci. 868: 233–285.

Coffman K. A., Dum R. P., and Strick P. L. (2011). Cerebellar vermis is a target of projections from the motor areas in the cerebral cortex. Proc. Natl. Acad. Sci. U.S.A. 108, 16068–16073.

Conn P.J, Pin J.P. (1997). Pharmacology and functions of metabotropic glutamate

receptors. Annu. Rev. Pharmacol. Toxicol. 37: 205–237.

Conquet F., Bashir Z. I., Davies C. H., Daniel H., Ferraguti F., Bordi F., Franz-Bacon K., Reggiani A., Matarese V., Conde F., Collingridge G.L., Crepel F. (1994). Motor deficit and impairment of synaptic plasticity in mice lacking mGluR1. Nature. 372: 237–243.

Curtis D. R., Phillis J. W., Watkins J. C. (1959). Chemical excitation of spinal neurones. Nature. 183: 611–612.

-D-

Davie J. T., Clark B. A., Häusser M. (2008). The origin of the complex spike in cerebellar Purkinje cells. J. Neurosci. 28: 7599–7609.

de Ruiter M. M., De Zeeuw C.I., Hansel C. (2006). Voltage-gated sodium channels in cerebellar Purkinje cells of mormyrid fish. J Neurophysiol. 96: 378–390.

de Schutter E., and J. M. Bower. (1994). An active membrane model of the cerebellar Purkinje cell. I. Simulation of current clamps in slice. J. Neurophysiol. 71: 375–400.

Dingledine R., Borges K., Bowie D., and Traynelis S.F. (1999). The endogenous synaptic modulator: localization to astrocytes and glu- glutamate receptor ion channels. Pharmacol. Rev. 51: 7–61.

Djurisic M., Antic S., Chen W. R., and Zecevic D. (2004). Voltage imaging from dendrites of mitral cells: EPSP attenuation and spike trigger zones. J. Neurosci. 24: 6703-6714.

-E-

Eccles J. C. (1967). Circuits in the cerebellar control of movement. Proc. Natn. Acad. Sci. U.S.A. 58: 336-343.

Eccles J.C., Ito M., Szentagothai J. (1967a). The cerebellum as a neural machine. Springer-Verlag, Berlin, Heidelberg, New York.

Eccles J. C., Llinás R., Sasaki K. (1966). The excitatory synaptic action of climbing fibers on the Purkinje cells of the cerebellum. J. Physiol 182 : 268–296.

Eccles J. C., Llinas R., Sasaki K. (1966). Intracellularly recorded responses of the cerebellar Purkinje cells. Exp Brain Res 1: 161–183.

Edgerton J. R., Reinhart P.H. (2003). Distinct contributions of small and large conductance Ca2+-activated K^+ channels to rat Purkinje neuron function. J.

Physiol. 548: 53–69.

Engbers J. D., Zamponi G. W., Turner R. W. (2013). Modeling interactions between voltage-gated Ca2+ channels and KCa1.1 channels. Channels (Austin) 7: 24–25.

Ertel E. A., Campbell K. P., Harpold M. M., Hofmann F., Mori Y., Perez-Reyes E. Schwartz A., Snutch T.P., Tanabe T., Birnbaumer L., et al. (2000). Nomenclature of voltage-gated calcium channels. Neuron. 25: 533–535.

-F-

Fakler B. and Adelman J. P. (2008). Control of KCa channels by calcium nano/microdomains. Neuron 59: 873–881.

Farre-Castany M. A., Schwaller B., Gregory P., Barski J., Mariethoz C., Eriksson J.L., Tetko I. V., Wolfer D., Celio M. R., Schmutz I., Albrecht U., Villa A.E. (2007). Differences in locomotor behavior revealed in mice deficient for the calcium-binding proteins parvalbumin, calbindin D-28k or both. Behav. Brain. Res. 178: 250–261.

Felts P.A., Yokoyama S., Dib-Hajj S., Black J.A., Waxman S. G. (1997). Sodium channel alpha-subunit mRNAs I, II, III, NaG, Na6 and hNE (PN1): different expression patterns in developing rat nervous system. Brain. Res. Mol. Brain. Res. 45: 71–82.

Fierro L., Llano I. (1996). High endogenous calcium buffering in Purkinje cells from rat cerebellar slices. J. Physiol. 496: 617–625.

Finch E. A. and Augustine G. J. (1998). Local calcium signalling by inositol-1,4,5-trisphosphate in Purkinje cell dendrites. Nature. 396: 753–756.

Finch E. A., Tanaka K. & Augustine G. J. (2012). Calcium as a trigger for cerebellar long-term synaptic depression. Cerebellum 11: 706–717.

Flourens P. (1824). Rechérches expérimentales sur les propriétés et les fonctions du système nerveux dans les animaux vertébrés. Paris: Crevot.

Fotuhi M., Sharp A. H., Glatt C. E., Hwang P. M., von Krosigk M., Snyder S. H., Dawson T. M. (1993). Differential localization of phosphoinositide-linked metabotropic glutamate receptor (mGluR1) and the inositol 1,4,5-triphosphate receptor in rat brain. J. Neurosci.13: 2001–2012.

Fry M. (2006). Developmental expression of Na+ currents in mouse Purkinje

neurons. Eur. J. Neurosci. 24: 2557-2566.

-G-

Gahwiler B. H., Llano I. (1989). Sodium and potassium conductances in somatic membranes of rat Purkinje cells from organotypic cerebellar cultures. J. Physiol. 417: 105–122.

Galvez A., Gimenez-Gallego G., Reuben J. P., Roy-Contacin L., Feigenbaum P., Kaczorowski G. J., Garcia M. L.(1990). Purification and characterization of a unique, potent, peptidyl probe for the high conductance calcium-activated potassium channel from venom of the scorpion *Buthus tamulus*. Journal of Biological Chemistry. 265: 11083–11090.

Gao Z., van Beugen B. J. & De Zeeuw C. I. (2012). Distributed synergistic plasticity and cerebellar learning. Nat Rev Neurosci 13: 619–635.

Gerrits N. M., Voogd J., Magras I. N. (1985). Vestibular afferents of the inferior olive and the vestibulo-olivo-cerebellar climbing fiber pathway to the flocculus in the cat. Brain. Res. 332: 325–336.

Glickstein M., Sultan F., Voogd J. (2011). Functional localisation in the cerebellum. Cortex 47: 59–8.

Goldin A. L. (2001). Resurgence of sodium channel research. Annu. Rev. Physiol. 63: 871–894.

Goldman-Wohl D. S., Chan E., Baird D., Heintz N. (1994). Kv3.3b: a novel Shaw type potassium channel expressed in terminally differentiated cerebellar Purkinje cells and deep cerebellar nuclei. J. Neurosci. 14: 511–522.

Goldstein S. S., Rall W. (1974). Changes of action potential shape and velocity for changing core conductor geometry. Biophys. J. 14: 731–757.

Golgi C. (1874). Sulla fine anatomia del cervelletto umano: Archivio Italiano per le Malattie Nervose, 2, pp. 90–107.

Granit R., Phillips C. G. (1956). Excitatory and inhibitory processes acting upon individual Purkinje cells of the cerebellum in cats. J. Physiol. 133 :520–547.

Gravel C., Hawkes R. (1990). Parasagittal organization of the rat cerebellar cortex: direct comparison of Purkinje cell compartments and the organization of the spinocerebellar projection. J. Comp. Neurol. 291: 79–102.

Gravius A., Pietraszek M., Dekundy A., Danysz W. (2010). Metabotropic glutamate receptors as therapeutic targets for cognitive disorders. Curr. Top. Med.

Chem. 10: 187–206.

Grodd W., Hulsmann E., Lotze M. et al,. (2001). Sensorimotor mapping of the human cerebellum: fMRI evidence of somatotopic organization. Hum Brain Mapp 13:55–73.

Groenewegen H. J., Voogd J., Freedman SL. (1979). The parasagittal zonation within the olivocerebellar projection. II. Climbing fiber distribution in the intermediate and hemispheric parts of cat cerebellum. J Comp Neurol.183: 551–601.

Groenewegen H. J., Voogd J. (1977). The parasagittal zonation within the olivocerebellar projection. I. Climbing fiber distribution in the vermis of the cat cerebellum. J Comp Neurol 174: 417–488.

Gruol D. L. (1984). Single channel analysis of voltage-sensitive K^+ channels in cultured Purkinje neurons. Biophys J. 1984;45:53–55.

Guergueltcheva V., Azmanov D. N., Angelicheva D., Smith K. R., Chamova T., Florez L., Bynevelt M., Nguyen T, Cherninkova S. & Bojinova V. (2012). Autosomal-recessive congenital cerebellar ataxia is caused by mutations in metabotropic glutamate receptor 1. Am. J. Hum. Genet. 91: 553–564.

-H-

Haghdoost-Yazdi H., Janahmadi M., and Behzadi G. (2008). Iberiotoxiin-sensitive large conductance Ca2+-dependent K+ (BK) channels regulate the spike configuration in the burst firing of cerebellar Purkinje neurons. Brain. Res. 121: 1–8.

Hartmann J., Blum R., Kovalchuk Y., Adelsberger H., Kuner R., Durand G. M., Miyata M., Kano M., Offermanns S., Konnerth A. (2004). Distinct roles of galpha(q) and Galpha11 for Purkinje cell signaling and motor behavior. Journal of Neuroscience. 24: 5119–5130.

Hartmann J., Dragicevic E., Adelsberger H., Henning H. A., Sumser M., Abramowitz J., Blum R., Dietrich A., Freichel M., Flockerzi V., Birnbaumer L. & Konnerth A. (2008). TRPC3 channels are required for synaptic transmission and motor coordination. Neuron. 59: 392–398.

Hartmann J., Henning H. A., Konnerth A. (2011). mGluR1/TRPC3-mediated synaptic transmission and calcium signaling in mammalian central neurons. Cold Spring Harbor Perspectives in Biology. 3: a006726.

Hartmann J., Karl R. M., Alexander R. P., Adelsberger H., Brill M. S., Rühlmann C.,

et al. (2014). STIM1 controls neuronal Ca^{2+} signaling, mGluR1-dependent synaptic transmission and cerebellar motor behavior. Neuron. 82: 635–644.

Harvey R. J., Napper R. M. (1991). Quantitative studies on the mammalian cerebellum. Prog. Neurobiol. 36: 437–463.

Hashimoto K., Tsujita M., Miyazaki T., Kitamura K., Yamazaki M., Shin H. S., Watanabe M., Sakimura K., Kano M. (2011). Postynaptic P/Q-type Ca 2 channel in Purkinje cell mediates synaptic competition and elimination in developing cerebellum. Proc. Natl. Acad. Sci. 108: 9987–9992.

Hausser M., Clark B.A. (1997). Tonic synaptic inhibition modulates neuronal output pattern and spatiotemporal synaptic integration. Neuron. 19: 665–678.

Herculano-Houzel S. (2010). Coordinated scaling of cortical and cerebellar numbers of neurons. Front Neuroanat 4:12.

Hildebrand M. E., Isope P., Miyazaki T., Nakaya T., Garcia E., Feltz A., Schneider T., Hescheler J., Kano M., Sakimura K., Watanabe M., Dieudonne S & Snutch T. P. (2009). Functional coupling between mGluR1 and Cav3.1 T-type calcium channels contributes to parallel fiber-induced fast calcium signaling within Purkinje cell dendritic spines. J. Neurosci. 29: 9668–9682.

Hille B., (2001). Ion Channels of Excitable Membranes. Mass, Sunderland, MA, USA.

Hillman D., Chen S., Aung T. T, Cherksey B Sugimori M Llinas R. (1991). Localization of P-type calcium channels in the central nervous system. Proc Natl Acad Sci USA 88:7076–7080.

Hirono M., Konishi S., Yoshioka T. (1998). Phospholipase C-independent group I metabotropic glutamate receptor-mediated inward current in mouse Purkinje cells. Biochem. Biophys. Res. Commun. 251: 753–758.

Holmes G. (1917). The symptoms of acute cerebellar injuries due to gunshot injuries. Brain 4:461–535.

Horrigan F.T., and R.W. Aldrich. (2002). Coupling between voltage sensor activation, Ca2+ binding, and channel opening in large conductance (BK) potassium channels. J. Gen. Physiol. 120: 267–305.

Hosy E., Piochon C., Teuling E., Rinaldo L., and Hansel, C. (2011). SK2 channel expression and function in cerebellar Purkinje cells. J. Physiol. 589: 3433–3440.

Hu W., Tian C., Li T., Yang M., Hou H., Shu Y. (2009). Distinct contributions of $Na_v1.6$ and $Na_v1.2$ in action potential initiation and backpropagation. Nat. Neurosci. 12: 996–1002.

Huang W. C., Young J.S., Glitsch M. D. (2007). Changes in TRPC channel expression during postnatal development of cerebellar neurons. Cell. Calcium. 42: 1–10.

-I-

Ichikawa R., Hashimoto K., Miyazaki T., Uchigashima M., Yamasaki M., Aiba A., Kano M., and Watanabe M. (2016). Territories of heterologous inputs onto Purkinje cell dendrites are segregated by mGluR1-dependent parallel fiber synapse elimination. Proc. Natl. Acad. Sci. USA 113: 2282–2287.

Ichise T., Kano M., Hashimoto K., Yanagihara D., Nakao K., Shigemoto R., Katsuki M. & Aiba A. (2000). mGluR1 in cerebellar Purkinje cells essential for long-term depression, synapse elimination, and motor coordination. Science 288: 1832–1835.

Indriati D. W., Kamasawa N., Matsui K., Meredith A. L., Watanabe M., and Shigemoto R. (2013). Quantitative localization of $Ca_v2.1$ (P/Q-type) voltage-dependent calcium channels in Purkinje cells: somatodendritic gradient and distinct somatic coclustering with calcium-activated potassium channels. J. Neurosci. 33: 3668–7368.

Inoue T., Kato K., Kohda K., Mikoshiba K. (1998). Type 1 inositol 1,4,5-trisphosphate receptor is required for induction of long-term depression in cerebellar Purkinje neurons. J. Neurosci. 18: 5366–5373.

Isope P., Franconville R., Barbour B., Ascher P. (2004). Repetitive firing of rat cerebellar parallel fibres after a single stimulation. J Physiol 554: 829 –839.

Isope P. and Murphy T.H. (2005). Low threshold calcium currents in rat cerebellar Purkinje cell dendritic spines are mediated by T-type calcium channels. J. Physiol., 562: 257–269.

Ito M. (1982). Cerebellar control of the vestibulo-ocular reflex—around the flocculus hypothesis. Annu Rev Neurosci 5: 275–296.

Ito M. (1978). Recent advances in cerebellar physiology and pathology. Adv. Neurol. 21, 59–84.

Ito M. (1984). The Cerebellum and Neural Control. Raven Press, New York.

Ito M. (1993). Movement and thought: identical control mechanisms by the cerebellum. Trends. Neurosci. 16: 448–450.

Ito M. (2000). Mechanisms of motor learning in the cerebellum. Brain. Res. 886: 237–

245.

Ito M. (2006). Cerebellar circuitry as a neuronal machine. Prog. Neurobiol. 78: 272–303.

Ito M. (2008). Control of mental activities by internal models in the cerebellum. Nat. Rev. Neurosci. 9: 304–313.

Ito M. and Kano M. (1982). Long-lasting depression of parallel fiber-Purkinje cell transmission induced by conjunctive stimulation of parallel fibers and climbing fibers in the cerebellar cortex. Neurosci. Lett. 33: 253–258.

-J-

Jaafari N., Canepari M. (2016). Functional coupling of diverse voltage-gated Ca(2+) channels underlies high fidelity of fast dendritic Ca(2+) signals during burst firing. J. Physiol. 594: 967-983.

Jaafari N., De Waard M., Canepari M. (2014). Imaging Fast Calcium Currents beyond the Limitations of Electrode Techniques. Biophys. J. 107.1280-1288.

Jacquin T. D., Gruol D. L. (1992). Ca2+ regulation of a large conductance K+ channel in cultured rat cerebellar Purkinje neurons. Eur. J. Neurosci. 11:735–739.

Jan L. Y., Jan Y. N.. (2012). Voltage-gated potassium channels and the diversity of electrical signalling. J. Physiol. 590: 2591–2599.

Jerng H. H., Pfaffinger P. J., Covarrubias M. (2004a). Molecular physiology and modulation of somatodendritic A-type potassium channels. Mol. Cell. Neurosci. 27: 343–369.

Johnston D., Hoffman D. A., Magee .J C., Poolos N. P., Watanabe S., Colbert C. M., Migliore M. (2000). Dendritic potassium channels in hippocampal pyramidal neurons. J. Physiol. (Lond). 525: 75–81.

-K-

Kalume F., Yu F. H., Westenbroek R. E., Scheuer T., Catterall W. A. (2007). Reduced sodium current in Purkinje neurons from Nav1.1 mutant mice: implications for ataxia in severe myoclonic epilepsy in infancy. J Neurosci. 27: 11065–11074.

Kaneda M., Wakamori M., Ito C., Akaike N. (1990). Low-threshold calcium current in isolated Purkinje cell bodies of rat cerebellum. J. Neurophysiol. 63: 1046–1051.

Kano M., Hashimoto K. & Tabata T. (2008). Type-1 metabotropic glutamate receptor

in cerebellar Purkinje cells: a key molecule responsible for long-term depression, endocannabinoid signalling and synapse elimination. Philos. Trans. R. Soc. Lond. 363: 2173–2186.

Kano M., Hashimoto K., Kurihara H., Watanabe M., Inoue Y., Aiba A., Tonegawa S. (1997). Persistent multiple climbing fiber innervation of cerebellar Purkinje cells in mice lacking mGluR1. Neuron. 18: 71–79.

Kaplan M. R., Cho M. H., Ullian E. M., Isom L. L., Levinson S.R., Barres B. A. (2001). Differential control of clustering of the sodium channels $Na_v1.2$ and $Na_v1.6$ at developing CNS nodes of Ranvier. Neuron. 30: 105–119.

Kasumu A.W., Hougaard C., Rode F., Jacobsen T.A., Sabatier J.M., Eriksen B.L., Strøbæk D., Liang X., Egorova P., Vorontsova D., Christophersen P., Rønn L. C. B., Bezprozvanny I., (2012a). Selective positive modulator of calcium-activated potassium channels exerts beneficial effects in a mouse model of spinocerebellar ataxia type 2. Chem. Biol. 19: 1340–1353.

Kato A. S., Knierman M. D., Siuda E. R., Isaac J. T., Nisenbaum E. S. & Bredt D. S. (2012). Glutamate receptor δ2 associates with metabotropic glutamate receptor 1 (mGluR1), protein kinase Cγ, and canonical transient receptor potential 3 and regulates mGluR1-mediated synaptic transmission in cerebellar Purkinje neurons. J. Neurosci. 32: 15296–15308.

Khaliq Z. M., Gouwens N. W., Raman I. M. (2003). The contribution of resurgent sodium current to high-frequency firing in Purkinje neurons: an experimental and modeling study. J. Neurosci. 23: 4899-4912.

Khodakhah K. & Ogden D. (1993). Functional heterogeneity of calcium release by inositol trisphosphate in single Purkinje neurones, cultured cerebellar astrocytes, and peripheral tissues. Proc. Natl. Acad. Sci. USA. 90: 4976–4980.

Knaus H. G., Schwarzer C., Koch R., Eberhart A., Kaczorowski G., Glossman H., Wunder F., Pongs O., Garcia M., Sperk G. (1996). Distribution of high-conductance Ca^{2+}-activated K^+ channels in rat brain: targeting to axons and nerve terminals. J. Neurosci. 16: 955–963.

Kodama T., Itsukaichi-Nishida Y., Fukazawa Y., Wakamori M., Miyata M., Molnar E., Mori Y., Shigemoto R., Imoto K. (2006). A CaV2.1 calcium channel mutation rocker reduces the number of postsynaptic AMPA receptors in parallel fiber-Purkinje cell synapses. Eur. J. Neurosci. 24: 2993–3007.

Köhler M., Hirschberg B., Bond C. T., Kinzie J. M., Marrion N. V., Maylie J., Adelman J. P. (1996). Small-conductance, calcium-activated potassium channels from

mammalian brain. Science. 273:1709–1714.

Kohrman D.C., Harris J.B., and Meisler, M.H. (1996a). Mutation detection in the med and medJ alleles of the sodium channel Scn8a: unusual patterns of exon skipping are influenced by a minor class AT-AC intron. J. Biol. Chem. 271: 17576–17581.

Konnerth A., Dreessen J., Augustine G. J. (1992). Brief dendritic calcium signals initiate long-lasting synaptic depression in cerebellar Purkinje cells. Proc. Natl. Acad. Sci. U.S.A. 89: 7051–705510.

Konnerth A., Llano I., Armstrong C. M. (1990). Synaptic currents in cerebellar Purkinje cells. Proc Natl Acad Sci U S A. 87: 2662–2665.

-L-

Lange W. (1975). Cell number and cell density in the cerebellar cortex of man and some other mammals. Cell Tissue Res. 157: 115–12510.

Larsell, O. (1937). The cerebellum. A review and interpretation. Arch. Neurol. Psychiatry (Chirago) 38t580-607.

Larsell O. (1952). The morphogenesis and adult pattern of the lobules and fissures of the cerebellum of the white rat. J. Comp. Neurol. 97: 281–356.

Latorre R., Oberhauser A., Labarca P., Alvarez O. (1989). Varieties of calcium-activated potassium channels. Ann. Rev. Physiol 51: 385–399.

Lein E. S., Hawrylycz M. J., Ao N., Ayres M., Bensinger A., Bernard A., Boe A. F., Boguski M. S., Brockway K. S., Byrnes E. J., et al. (2007). Genome-wide atlas of gene expression in the adult mouse brain. Nature 445: 168–176.

Levenes C., Daniel, H., Jaillard D., Conquet F., Crepel, F. (1997). Incomplete regression of multiple climbing fibre innervation of cerebellar Purkinje cells in mGluR1 mutant mice. Neuro. Report. 8: 571-574.

Levin S. I., Khaliq Z. M., Aman T. K., Grieco T. M., Kearney J. A., Raman I. M., Meisler M. H. (2006). Impaired motor function in mice with cell-specific knockout of sodium channel Scn8a (Nav1.6) in cerebellar Purkinje neurons and granule cells. J. Neurophysiol. 96: 785–793.

Liljelund P., Netzeband J. G. & Gruol D. L. (2000). L-type calcium channels mediate calcium oscillations in early postnatal Purkinje neurons. J. Neurosci. 20: 7394–7403.

Litschig S., Gasparini F., Rueegg D., Stoehr N., Flor P.J., Vranesic I., Prezeau L., Pin

J.P., Thomsen C., Kuhn R. (1999). CPCCOEt, a Noncompetitive Metabotropic Glutamate Receptor 1 Antagonist, Inhibits Receptor Signaling Without Affecting Glutamate Binding. Mol. Pharmacol. 55: 453–61.

Liu S., Friel D. D. (2008). Impact of the leaner P/Q-type Ca2+ channel mutation on excitatory synaptic transmission in cerebellar Purkinje cells. J. Physiol. 586: 4501–4515.

Llano I., Marty A., Armstrong C. M., Konnerth A. (1991). Synaptic- and agonist-induced excitatory currents of Purkinje cells in rat cerebellar slices. J. Physiol. 434: 183–213.

Llinás R., Nicholson C., Freeman J. A., Hillman D. E. (1968). Dendritic spikes and their inhibition in alligator Purkinje cells. Science. 160: 1132–1135.

Llinas R., Sugimori M. (1980a). Electrophysiological properties of in vitro Purkinje cell dendrites in mammalian cerebellar slices. Journal of Physiology. 305: 197–213.

Llinas R., Sugimori M. (1980b). Electrophysiological properties of in vitro Purkinje cell somata in mammalian cerebellar slices. Journal of Physiology. 305: 171–195.

Llnas R., Sugimori M., Hillman D.E., Cherksey B. (1992). Distribution and functional significance of the P-type, voltage-dependent Ca^{2+} channels in the mammalian central nervous system. Trends Neurosci. 15: 351–355.

Loew L. M., Cohen L. B., Dix J., Fluhler E. N., Montana V., Salama G., Wu J. Y. (1992). A naphthyl analog of the aminostyryl pyridinium class of potentiometric membrane dyes shows consistent sensitivity in a variety of tissue, cell, and model membrane preparations. J. Membr. Biol. 130: 1–10.

Loew L. M., Simpson L. L. (1981). Charge-shift probes of membrane potential: a probable electrochromic mechanism for p-aminostyrylpyridinium probes on a hemispherical lipid bilayer. Biophys. J. 34: 353–365.

Loewenstein Y., Mahon S., Chadderton P., Kitamura K., Sompolinsky H., Yarom Y., and Hausser M. (2005). Bistability of cerebellar Purkinje cells modulated by sensory stimulation. Nature Neuroscience. 8: 202–211.

Lu X., Miyachi S., Ito Y., Nambu A., Takada M. (2007). Topographic distribution of output neurons in cerebellar nuclei and cortex to somatotopic map of primary motor cortex. Eur. J. Neurosci. 25: 2374–2382.

Luciani L. (1891). Il cervelletto: nuovi studi di fisiologia normale e pathological. Firenze : Le Monnier.

Lujan R. Nusser Z., Roberts J.D., Shigemoto R., Somogyi P. (1996). Perisynaptic location of metabotropic glutamate receptors mGluR1 and mGluR5 on dendrites and dendritic spines in the rat hippocampus. Eur. J. Neurosci. 8: 1488–1500.

Luscher, C., and Huber, K.M. (2010). Group 1 mGluR-dependent synaptic € long-term depression: mechanisms and implications for circuitry and disease. Neuron 65: 445–459.

Ly R., Bouvier G., Schonewille M., Arabo A., Rondi-Reig L., Lena C., Casado M., De Zeeuw C. I. and Feltz A. (2013). T-type channel blockade impairs long-term potentiation at the parallel fiber-Purkinje cell synapse and cerebellar learning. Proc. Natl. Acad. Sci. 110: 20302–20307.

-M-

Maejima T., Hashimoto K., Yoshida T., Aiba A., Kano M. (2001). Presynaptic inhibition caused by retrograde signal from metabotropic glutamate to cannabinoid receptors. Neuron. 31: 463–475.

Maffie J. K., Dvoretskova E., Bougis P. E., Martin-Eauclaire M. F., Rudy B. (2013). Dipeptidyl-peptidase-like-proteins confer high sensitivity to the scorpion toxin AmmTX3 to Kv4-mediated A-type Kþ channels. J. Physiol. 591: 2419-2427.

Maltecca F., Baseggio E., Consolato F., Mazza D., Podini P., Young SM J. r., Drago I., Bahr B. A., Puliti A., Codazzi F., Quattrini A. & Casari. G. (2015). Purkinje neuron Ca2+ influx reduction rescues ataxia in SCA28 model. J. Clin. Invest. 125: 263–274.

Mark M. D., Maejima T., Kuckelsberg D., Yoo J. W., Hyde R. A., Shah V., et al. (2011). Delayed postnatal loss of P/Q-type calcium channels recapitulates the absence epilepsy, dyskinesia, and ataxia phenotypes of genomic *Cacna1a* mutations. J. Neurosci. 31: 4311–4326.

Markram H., Hel, P.J., and Sakmann B. (1995). Dendritic calcium transients evoked by single back-propagating action potentials in neocortical pyramidal neurons. J. Physiol. 485: 1–20.

Marr D. (1969). A theory of cerebellar function. J Physiol 202: 437–470.

Marrion N. V., Tavalin S. J. (1998). Selective activation of Ca+-activated K+ channels by co-localized Ca+ channels in hippocampal neurons. Nature. 395: 900–905.

Martin L.J., Backstone C. D., Huganir R. L., Price D. L., (1992). Cellular localization of a metabotropic glutamate receptor in rat brain. Neuron. 9: 259-270.

Martina M., Yao G. L., and Bean B. P. (2003). Properties and functional role of voltage-dependent potassium channels in dendrites of rat cerebellar Purkinje neurons. J. Neurosci. 23: 5698–5707.

Mateos J. M., Benitez R., Elezgarai I., Azkue J. J., Lazaro E., Osorio A., Bilbao A., Donate F., Sarria R., Conquet F., Ferraguti F., Kuhn R., Knopfel T. & Grandes P. (2000). Immunolocalization of the mGluR1b splice variant of the metabotropic glutamate receptor 1 at parallel fiber-Purkinje cell synapses in the rat cerebellar cortex. J. Neurochem. 74: 1301–1309.

Matsushita K., Wakamori M., Rhyu I. J., Arii T., Oda S., Mori Y., Imoto K. (2002). Bidirectional alterations in cerebellar synaptic transmission of tottering and rolling Ca2+ channel mutant mice. J. Neurosci. 22: 4388–4398.

McKay B. E, McRory J. E., Molineux M. L, Hamid J., Snutch T. P., Zamponi G. W. & Turner R. W. (2006). Ca(V)3 T-type calcium channel isoforms differentially distribute to somatic and dendritic compartments in rat central neurons. Eur. J. Neurosci 24: 2581–2594.

McKay B. E., Turner R. W. (2005). Physiological and morphological development of the rat cerebellar Purkinje cell. J. Physiol. 567: 829–850.

Midtgaard J. (1995). Spatial synaptic integration in Purkinje cell dendrites. J. Physiol. 89: 23–32.

Midtgaard J., Lasser-ross N., and Ross W. (1993). Spatial distribution of Ca2influx in turtle Purkinje cell dendrites in vitro: role of a transient outward current. J. Neurophysiol. 70: 2455–2469.

Migliore M., Hoffman D. A., Magee J. C., Johnston D. (1999). Role of an A-type K+ conductance in the back-propagation of action potentials in the dendrites of hippocampal pyramidal neurons. J. Comput. Neurosci.7:5–15.

Mintz I. M., Venema V. J., Swiderek K. M., Lee T. D., Bean B. P., Adams M. E. (1992). P-type calcium channels blocked by the spider toxin omegaAga-Iva. Nature. 355: 827–829.

Miyakawa H., Lev-Ram V., Lasser-Ross N., and Ross W. N. (1992). Calcium transients evoked by climbing fiber and parallel fiber synaptic inputs in guinea pig cerebellar Purkinje neurons. J. Neurophysiol. 68: 1178–1189.

Miyata M., Finch E. A., Khiroug L., Hashimoto K., Hayasaka S., Oda S. I., Inouye M., Takagishi Y., Augustine G. J., Kano M. (2000). Local calcium release in dendritic spines required for long-term synaptic depression. Neuron. 28: 233–244.

Miyazaki T., Hashimoto K., Shin H. S., Kano M., Watanabe M. (2004). P/Q type Ca 2 channel a1A regulates synaptic competition on developing cerebellar Purkinje cells. J. Neurosci. 24: 1734 –1743.

Moczydlowski E., Lucchesi K. and Ravindran A. (1988). An emerging pharmacology of peptide toxins targeted against potassium channels. J. Memb. Biol. 105: 95-111.

Monaghan D.T., Bridges R.J., Cotman C.W. (1989).The excitatory amino acid receptors: their classes, pharmacology and distinct properties in the function of the central nervous system. Ann. Rev. Pharmacol. Toxicol. 29:365–402.

Mouginot D., Bossu J. L., Gahwiler B. H. (1997). Low-threshold Ca^{2+} currents in dendritic recordings from Purkinje cells in rat cerebellar slice cultures. J. Neurosci. 17: 160–170.

-N-

Nakamura M., Sato K., Fukaya M., Araishi K., Aiba A., Kano M., Watanabe M. (2004). Signaling complex formation of phospholipase Cbeta4 with metabotropic glutamate receptor type 1alpha and 1,4,5-trisphosphate receptor at the perisynapse and endoplasmic reticulum in the mouse brain. Eur. J. Neurosci. 20: 2929–2944.

Nakanishi S. (1992). Molecular diversity of glutamate receptors and implications for brain function. Science. 258: 597-603.

Niswender C.M., and Conn P.J. (2010). Metabotropic glutamate receptors: physiology, pharmacology, and disease. Annu. Rev. Pharmacol. Toxicol. 50: 295–322.

Nusser .Z, Mulvihill E., Streit P., Somogyi P. (1994). Subsynaptic segregation of metabotropic and ionotropic glutamate receptors as revealed by immunogold localization. Neuroscience. 61: 421–427.

-P-

Patel, A. J., Honore, E., Maingret, F., Lesage, F., Fink, M., Duprat, F., Lazdunski, M., (1998). A mammalian two pore domain mechanogated S-like K+ channel. EMBO. Journal. 17: 4283–4290.

Pedarzani P., Mosbacher J., Rivard A., Cingolani L.A., Oliver D., Stocker M., Adelman JP, Fakler B. (2001). Control of electrical activity in central neurons by modulating the gating of small conductance Ca2+-activated K+ channels. J.

Biol. Chem. 276: 9762–9769.

Pietrobon D. (2002). Calcium channels and channelopathies of the central nervous system. Mol. Neurobiol. 25: 31–50.

Pouille F., Cavelier P., Desplantez T., Beekenkamp H., Craig P. J., Beattie R. E., Volsen S. G., Bossu J. L. (2000). Dendro-somatic distribution of calciummediated electrogenesis in purkinje cells from rat cerebellar slice cultures. J Physiol (Lond). 527: 265–282.

Prakriya M. and Lingle C. J. (2000). Activation of BK channels in rat chromaffin cells requires summation of Ca2+ influx from multiple Ca2+ channels. J. Neurophysiol. 84: 1123-1135.

Purkinje J. (1838). Über Neuesten Untersuchungen aus der Nerven- und HirnAnatomie. Prague: Gottlieb Haase.

-O-

Offermanns S., Hashimoto K., Watanabe M., Sun W., Kurihara H., Thompson R. F., Inoue Y., Kano M., Simon M. I. (1997). Impaired motor coordination and persistent multiple climbing fiber innervation of cerebellar purkinje cells in mice lacking galphaq. PNAS. 94:14089–14094.

Oldfield C. S., Marty A., & Stell B. M. (2010). Interneurons of the cerebellar cortex toggle Purkinje cells between up and down states. Proceedings of the National Academy of Sciences. 107: 13153–13158.

Olivera B. M., Miljanich G. P., Ramachandran J., Adams M. E. (1994). Calcium channel diversity and neurotransmitter release: The omega-conotoxins and omega-agatoxins. Annu. Rev. Biochem. 63: 823–867.

Otsu Y., Marcaggi P., Feltz A., Isope P., Kollo M., Nusser Z., Mathieu B., Kano M., Tsujita M., Sakimura K., Dieudonne S., (2014). Activity-dependent gating of calcium spikes by A-type Kþ channels controls climbing fiber signaling in Purkinje cell dendrites. Neuron. 84: 137e151.

-R-

Raman I. M., and Bean B. P. (1997). Resurgent sodium current and action potential formation in dissociated cerebellar Purkinje neurons. J. Neurosci. 17: 4517–4526.

Raman I. M., and Bean B. P. (1999a). Ionic currents underlying spontaneous action potentials in isolated cerebellar Purkinje neurons. J Neurosci. 19: 1663–1674.

Raman I. M., and Bean B. P. (1999b). Properties of sodium currents and action potential firing in isolated cerebellar Purkinje neurons. Ann. N.Y. Acad. Sci. 868: 93–96.

Raman I. M., Bean B. P. (2001). Inactivation and recovery of sodium currents in cerebellar Purkinje neurons: evidence for two mechanisms. Biophys. J. 80: 729-737.

Ramón y Cajal S. (1888). Sobre las fibras nerviosas de la capa molecular del cerebelo. Rev. Trim. Histol. Norm. Patol. 1: 33–42.

Ramón y Cajal S. (1889a). Sur l'origine et la direction des prolongations nerveuses de la couche molèculaire du cervelet. Internat. Mschr. Anat. Physiol. 7, 12–31.

Ramón y Cajal S. (1889b). Sobre las fibras nerviosas de la capa granulosa del cerebelo. Rev. Trim. Histol. Norm. Patol. 1: 107–118.

Ramón y Cajal S. (1909). Histologie du sistéme nerveux de l'homme et des vertebras (transl. L. Azoulay). Paris: Maloine.

Ramón y Cajal S. (1911). Histologie du sistéme nerveux de l'homme et des vertebras (Transl, L. Azoulay). Paris: Maloine.

Ramón y Cajal S. (1967). The Structure and Connections of Neurons. (1901–1921): Elsevier Publishing Company, Amsterdam, 220–253.

Ramón y Cajal S. (1995). Histology of the Nervous System of Man and Vertebrates (Transl. N. Swanson and L. Swanson). New York: Oxford University Press.

Rancz E. A., Häusser M. (2006). Dendritic calcium spikes are tunable triggers of cannabinoid release and short-term synaptic plasticity in cerebellar Purkinje neurons. J. Neurosci. 26:5428–5437.

Rancz E. A., and Hausser M. (2010). Dendritic spikes mediate negative synaptic gain control in cerebellar Purkinje cells. Proc. Natl. Acad. Sci. 107: 22284–22289.

Randall A., Tsien R. W. (1995). Pharmacological dissection of multiple types of calcium channel currents in rat cerebellar granule neurons. J. Neurosci. 15: 2995–3012.

Rapp M., Segev I., Yarom Y. (1994). Physiology, morphology and detailed passive models of cerebellar Purkinje cells. J. Physiol. 471: 87-99.

Regan L. J. (1991). Voltage-dependent calcium currents in Purkinje cells from rat cerebellar vermis. J. Neurosci. 11: 2259-2269.

Regehr W. G., Mintz I. M. (1994). Participation of multiple calcium channel types in transmission at single climbing fiber to Purkinje cell synapses. Neuron. 12: 605–

613.

Riccio A., Medhurst A.D., Mattei C., Kelsell R.E., Calver A.R., Randall A.D., Benham C.D., Pangalos M.N. (2002). mRNA distribution analysis of human TRPC family in CNS and peripheral tissues. Brain Res. Mol. Brain Res. 109: 95–104.

Robitaille R., Garcia M. L., Kaczorowski G. J., Charlton M. P. (1993). Functional colocalization of calcium and calcium-gated potassium channels in control of transmitter release. Neuron. 11: 645–655.

Rolando, L. (1809). Saggio sopra le vera struttura del cervello dell'uomo e degli nimali e sopra le funzioni del sistema nervoso. Sassari:Stamperia da S.S.R.M.

Romano C., van den Pool A. N., O'Malley K. L. (1996). Enhanced early developmental expression of the metabotropic glutamate receptor mGluR5 in rat brain: protein, mRNA splice variants and regional distribution. J Comp Neurol. 367: 403–412.

Roth A., Hausser M. (2001). Compartmental models of rat cerebellar Purkinje cells based on simultaneous somatic and dendritic patch-clamp recordings. J. Physiol. 535: 445–472.

Royeck M., Horstmann M. T., Remy S, Reitze M., Yaari Y., Beck H. (2008). Role of axonal Nav1.6 sodium channels in action potential initiation of CA1 Pyramidal neurons. J Neurophysiol. 100: 2361–2380.

Rudy B. (1988). Diversity and ubiquity of K channels. Neuroscience 25: 729—749.

Rudy B., Sen K., Vega-Saenz de Meira E. C., Lau E, Reid T., Ward D. (1991). Cloning of a human cDNA expressing a high voltage-activating TEA-sensitive, type A K+ channel which maps to human chromosome 1 band p21. J. Neurosci. Res. 29: 401–412.

Ryo Y., Miyawaki A., Furuichi T., Mikoshiba K., (1993). Expression of the metabotropic glutamate receptor mGluR1a and the ionotropic glutamate receptor GluR1 in the brain during the postnatal development of normal mouse and in the cerebellum from mutant mice. J. Neurosci. Res. 36: 19-32.

-S-

Sacco T., Tempia F. (2002). A-type potassium currents active at subthreshold potentials in mouse cerebellar Purkinje cells. J. Physiol. 543: 505-520.

Sah P., Faber E.S.L. (2002). Channels underlying neuronal calcium-activated potassium currents. Prog. Neurobiol. 66: 345-353.

Sailer C. A., Kaufmann, W. A., Marksteiner J., and Knaus H. G. (2004). Comparative immunohistochemical distribution of three small-conductance Ca2+-activated potassium channel subunits, SK1, SK2 and SK3 in mouse brain. Mol. Cell. Neurosci. 26: 458–469.

Sailer C. A., Hu, H., Kaufmann W. A., Trieb M., Schwarzer C., Storm J. F., et al. (2002). Regional differences in distribution and functional expression of small-conductance Ca2+-activated K+ channels in rat brain. J. Neurosci. 22: 9698–9707.

Salkoff L. and Wyman R. (1981). Genetic modification of potassium channels in Drosophila Shaker mutants. Nature. 293: 228–230.

Sausbier M., Hu H., Arntz C., Feil S., Kamm S., Adelsberger H., …Ruth P. (2004). Cerebellar ataxia and Purkinje cell dysfunction caused by Ca2+-activated K+ channel deficiency. Proceedings of the National Academy of Sciences of the United States of America. 101(25): 9474–9478.

Schaller K. L., Caldwell J. H. (2003). Expression and distribution of voltage gated sodium channels in the cerebellum. Cerebellum. 2: 2–9.

Schmahmann J. (1991). An emerging concept. The cerebellar contribution to higher function. Archives of Neurology, 48, 1178-1187.

Schmidt H., Brown E. B., Schwaller B., Eilers J. (2003a). Diffusional mobility of parvalbumin in spiny dendrites of cerebellar purkinje neurons quantified by fluorescence recovery after photobleaching. Biophys. J. 84: 2599–2608.

Schmidt H., Eilers J. (2009). Spine neck geometry determines spino-dendritic cross-talk in the presence of mobile endogenous calcium binding proteins. J. Comput. Neurosci. 27: 229–243.

Schoepp D. D., Goldsworthy J., Johnson B. G., Salhoff C. R., Baker S. R. (1994). 3,5-Dihydroxyphenylglycine is a highly selective agonist for phosphoinositide-linked metabotropic glutamate receptors in the rat hippocampus. J. Neurochem. 63: 769 –772.

Schwaller B., Tetko I. V., Tandon P., Silveira D. C., Vreugdenhil M., Henzi T., Potier M C, Celio M. R., Villa A. E. (2004). Parvalbumin deficiency affects network properties resulting in increased susceptibility to epileptic seizures. Mol. Cell. Neurosci. 25: 650–663.

Serodio P., Kentros C., Rudy B. (1994). Identification of molecular components of A-type channels activating at subthreshold potentials. Journal of Neurophysiology. 72: 1516–1529.

Serodio P., Vega-Saenz D. M., Rudy B. (1996). Cloning of a novel component of A-type K+ channels operating at subthreshold potentials with unique expression in heart and brain. Journal of Neurophysiology. 75: 2174–2179.

Servais L., Bearzatto B., Schwaller B., Dumont M., De Saedeleer C., Dan B., Barski J. J., Schiffmann S. N., Cheron G. (2005). Mono- and dual-frequency fast cerebellar oscillation in mice lacking parvalbumin and/or calbindin D-28k. Eur. J. Neurosci. 22: 861–870.

Shah B. S., Stevens E. B., Pinnock R. D., Dixon A. K., Lee K. (2001). Developmental expression of the novel voltage-gated sodium channel auxiliary subunit β3, in rat CNS. J. Physiol. 534: 763–77610.

Sheng M., Tsaur M. L., Jan Y. N., and Jan L. Y. (1992). Subcellular segregation of two A-type K^+ channel proteins in rat central neurons. Neuron. 9: 271–284.

Shigemoto R., Abe T., Nomura S., Nakanishi S., Hirano T. (1994). Antibodies inactivating mGluR1 metabotropic glutamate receptor block long-term depression in cultured Purkinje cells. Neuron.12: 1245–1255.

Shigemoto R., Nakanishi S., Mizuno N. (1992). Distribution of the mRNA for a metabotropic glutamate receptor (mGluR1) in the central nervous system: an in situ hybridization study in adult and developing rat. J. Comp. Neurol. 322: 121–135.

Shin J. H., Linden D. J. (2005). An NMDA receptor/nitric oxide cascade is involved in cerebellar LTD but is not localized to the parallel fiber terminal. J. Neurophysiol. 94: 4281–4289.

Sillevis-Smitt P., Kinoshita A., De Leeuw B., Moll W., Coesmans M., Jaarsma D., Henzen-Logmans S., Vecht C., De Zeeuw C., Sekiyama N., Nakanishi S., Shigemoto R. (2000). Paraneoplastic cerebellar ataxia due to autoantibodies against a glutamate receptor. New England Journal of Medicine 342: 21–27.

Silver R. A., Momiyama A., and Cull-Candy S.G. (1998). Locus of frequency-dependent depression identified with multiple-probability fluctuation analysis at rat climbing fibre-Purkinje cell synapses. J. Physiol. 510: 881–902.

Stocker M. (2004). Ca2+-activated K+ channels: molecular determinants and function of the SK family. Nat Rev Neurosci. 5: 758–770.

Stocker M., Krause M., Pedarzani P. (1999). An apamin-sensitive Ca2+-activated K+ current in hippocampal pyramidal neurons. Proc. Natl. Acad. Sci. U S A. 96: 4662–4667.

Stocker M., Pedarzani P. (2000). Differential distribution of three Ca^{2+}-activated K+

channel subunits, SK1, SK2, and SK3, in the adult rat central nervous system. Mol. Cell. Neurosci. 15: 476–493.

Stuart G., Häusser M. (1994). Initiation and spread of sodium action potentials in cerebellar Purkinje cells. Neuron. 13:703–712.

Sultan F., Glickstein M. (2007). The cerebellum: comparative and animal studies. Cerebellum 6, 168–17610.

Sugiyama H., Ito .I, Hirono C. (1987). A new type of glutamate receptor linked to inositol phospholipid metabolism. Nature. 325: 531–533.

Swensen A. M., Bean B.P. (2003). Ionic mechanisms of burst firing in dissociated Purkinje neurons. J. Neurosci. 23: 9650-9663.

Szapiro G., Barbour B. (2007). Multiple climbing fibers signal to molecular layer interneurons exclusively via glutamate spillover. Nat. Neurosci. 10: 735-42.

Szentágothai J., Rajkovits K. (1959). Uber den Ursprung der Kletterfasern Des Kleinhirns. Z Anat Entwickl Gesch 121:130–141.

-T-

Taddese A., Bean B.P. (2002). Subthreshold sodium current from rapidly inactivating sodium channels drives spontaneous firing of tuberomammillary neurons. Neuron. 33: 587–600.

Takechi H., Eilers J. & Konnerth A. (1998). A new class of synaptic response involving calcium release in dendritic spines. Nature. 396: 757–760.

Talley E. M., Cribbs L. L., Lee J. H., Daud A., Perez-Reyes E. & Bayliss D. A. (1999). Differential distribution of three members of a gene family encoding low voltage-activated (T-type) calcium channels. J. Neurosci. 19: 1895–1911.

Tanabe T., Takeshima H., Mikami A., Flockerzi V., Takahashi H., Kangawa K., Kojima M., Matsuo H., Hirose T., Numa S. (1987). Primary structure of the receptor for calcium channel blockers from skeletal muscle. Nature. 328: 313–318.

Tank D. W., Sugimori M., Connor J. A., Llinás R. R. (1988). Spatially resolved calcium dynamics of mammalian Purkinje cells in cerebellar slice. Science 242: 773–777.

Tempia F., Alojado M. E., Strata P. & Knopfel T. (2001). Characterization of the mGluR1-mediated electrical and calcium signaling in Purkinje cells of mouse cerebellar slices. J Neurophysiol 86: 1389–1397.

Tempia F., Miniaci M. C., Anchisi D., Strata P. (1998). Postsynaptic current mediated by metabotropic glutamate receptors in cerebellar Purkinje cells. J. Neurophysiol. 80: 520–528.

Thach WT J.r. (1967). Somatosensory receptive fields of single units in cat cerebellar cortex. J Neurophysiol 30: 675–696.

Thach W.T., Goodkin H.P., Keating J.G. (1992). The cerebellum and the adaptive coordination of movement. Annu. Rev. Neurosci 15: 403-442.

Trimmer J.S., Rhodes K. J. (2004). Localization of voltage-gated ion channels in mammalian brain. Annu. Rev. Physiol. 66: 477–519.

Tsien R. W., Lipscombe D., Madison D. V., Bley K.R., Fox. A. P. (1988). Multiple types of neuronal calcium channels and their selective modulation. Trends Neurosci 11: 431-438.

Tsunoda S., Salkoff L. (1995a). Genetic analysis of Drosophila neurons: Shal, Shaw, and Shab encode most embryonic potassium currents. J. Neurosci. 15: 1741–1754.

Tu J. C., Xiao B., Naisbitt S., Yuan J. P., Petralia R. S., Brakeman P., Doan A., Aakalu V. K., Lanahan A. A, Sheng M., Worley P. F. (1999). Coupling of mGluR/Homer and PSD-95 complexes by the Shank family of postsynaptic density proteins. Neuron. 23: 583–592.

Tu J. C., Xiao B., Yuan J. P., Lanahan A. A., Leoffert K., Li M., Linden D. J., Worley P.F. (1998). Homer binds a novel proline-rich motif and links group 1 metabotropic glutamate receptors with IP3 receptors. Neuron. 21: 717–726.

Turner R. W. and Zamponi G.W., (2014). T-type channels buddy up. Pflugers. Arch. 466: 661–675.

-U-

Usowicz M. M., Sugimori M., Cherksey B., Llinás R. (1992). P-type calcium channels in the somata and dendrites of adult cerebellar Purkinje cells. Neuron 9: 1185-1199.

-V-

van der Staay F. J., Fanelli R. J., Blokland A., Schmidt B. H. (1999). Behavioral effects of apamin, a selective inhibitor of the SK_{Ca}-channel, in mice and rats. Neurosc. i Biobehav. Rev. 23: 1087–1110.

Vecellio M., Schwaller B., Meyer M., Hunziker W., Celio M.R. (2000). Alterations in Purkinje cell spines of calbindin D-28 k and parvalbumin knock-out mice. Eur. J. Neurosci. 12: 945–954.

Vega-Saenz de Miera E., B. Rudy M., Sugimori and R. Llinas. (1997). Molecular characterization of the sodium channel subunits expressed in mammalian cerebellar Purkinje cells. Proc. Natl. Acad. Sci. 94: 7059 –7064.

Vergara C., Latorre R., Marrion N. V., Adelman J. P. (1998). Calcium-activated potassium channels. Curr. Opin. Neurobiol. 8: 321–329.

Vetter P., Roth A., Hausser M. (2001). Propagation of action potentials in dendrites depends on dendritic morphology. J. Neurophysiol. 85: 926 –937.

Veys K., Snyders D. & De Schutter E. (2013). Kv3.3b expression defines the shape of the complex spike in the Purkinje cell. Front Cell Neurosci 7: 205.

Voogd J., Glickstein M. (1998). The anatomy of the cerebellum. Trends Neurosci 21:370–375.

Voogd J., Hess D., Marani E. (1987). The parasagittal zonation of the cerebellar cortex in cat and monkey: topography, distribution of acetylcholinesterase, and development. In New Concepts in Cerebellar Neurobiology,ed. JS King, 22: 183–220.

Voogd J., Ruigrok T.J., (2004). The organization of the corticonuclear and olivocerebellar climbing fiber projections to the rat cerebellar vermis: the congruence of projection zones and the zebrin pattern. J. Neurocytol. 33(1): 5–21.

-W-

Walter J. T., Alvina K., Womack M. D., Chevez C., Khodakhah K. (2006). Decreases in the precision of Purkinje cell pacemaking cause cerebellar dysfunction and ataxia. Nat. Neurosci. 9: 389–397.

Wang D. and Schreurs B. G. (2006). Characteristics of IA currents in adult rabbit cerebellar Purkinje cells. Brain. Res. 1096: 85-96.

Wang F., Xu Q., Wang W., Takano T., and Nedergaard M. (2012). Bergmann glia

modulate cerebellar Purkinje cell bistability via Ca2+-dependent K+ uptake. Proc. Natl. Acad. Sci 109: 7911–7916.

Wang SS-H., Denk W, Häusser M. (2000). Coincidence detection in single dendritic spines mediated by calcium release. Nature Neuroscience. 3: 1266–1273.

Wang Y. W., Strahlendof J. C., and StrahlendorF H. K. (1991). A transient voltage dependent outward potassium current in mammalian cerebellar Purkinje cells. Brain. Res. 567: 153–158.

Watanabe S., Takagi H., Miyasho T., Inoue M., Kirino Y., Kudo Y., Miyakawa H. (1998). Differential roles of two types of voltage-gated Ca^{2+} channels in the dendrites of rat cerebellar Purkinje neurons. Brain. Res. 791: 43–55.

Watson T.C., Becker N., Apps R., Jones M.W. (2014). Back to front: cerebellar connections and interactions with the prefrontal cortex. Front Syst Neurosci 8: 1–11.

Watt C., Mihailoff G. (1983). The cerebellopontine system in the rat. I. Autoradiographic studies. J. Comp. Neurol. 215: 312–330.

Waxman S. G., Quick D. C. (1978). Functional architecture of the initial segment. In: Waxman SG, editor. Physiology and Pathobiology of Axons. 125–130.

Widmer H. A., Rowe I. C., Shipston M. J. (2003). Conditional protein phosphorylation regulates BK channel activity in rat cerebellar Purkinje neurons. J. Physiol. 552: 379–391.

Williams S. R., Christensen S. R., Stuart G. J., Häusser M., (2002). Membrane potential bistability is controlled by the hyperpolarization-activated current I(H) in rat cerebellar Purkinje neurons in vitro. J. Physiol. 539: 469-483.

Womack M. D., Chevez C., Khodakhah K. (2004). Calcium-activated potassium channels are selectively coupled to P/Q-type calcium channels in cerebellar Purkinje neurons. J. Neurosci. 24: 8818–8822.

Womack M. D., Khodakhah K. (2002a). Characterization of large conductance Ca 2-activated K channels in cerebellar Purkinje neurons. Eur. J. Neurosci. 16: 1214–1222.

Womack M. D., Khodakhah K. (2002b). Active contribution of dendrites to the tonic and trimodal patterns of activity in cerebellar Purkinje neurons. J Neurosci 22: 10603–10612.

Womack M. D., Khodakhah K. (2003). Somatic and dendritic smallconductance calcium-activated potassium channels regulate the output of cerebellar Purkinje

neurons. J. Neurosci. 23: 2600–2607.

Womack M. D., Khodakhah K. (2004). Dendritic control of spontaneous bursting in cerebellar Purkinje cells. J. Neurosci. 24: 3511–3521.

-X-

Xia X. M., Fakler B., Rivard A., Wayman G., Johnson-Pais T., Keen J. E., Ishii T., Hischberg B., Bond C. T., Lutsenko S., Maylie J., Adelman J. P... Mechanism of calcium gating in small-conductance calcium-activated potassium channels. Nature. 395: 503–507.

-Y-

Yartsev M. M., Givon-Mayo R., Maller M., & Donchin O. (2009). Pausing purkinje cells in the cerebellum of the awake cat. Frontiers in System Neuroscience. 3: 2.

Yokoyama C. T., Westenbroek R. E., Hell J. W., Soong T. W., Snutch T. P., Catterall W. A. (1995). Biochemical properties and subcellular distribution of the neuronal class E calcium channel 1 subunit. J. Neurosci. 15: 6419–6432.

-Z-

Zagha E., Manita S., Ross W.N. & Rudy B. (2010). Dendritic Kv3.3 potassium channels in cerebellar Purkinje cells regulate generation and spatial dynamics of dendritic Ca^{2+} spikes. J. Neurophysiol. 103: 3516–3525.

Zamponi G. W., Bourinet E., Snutch T. P. (1996). Nickel block of a family of neuronal calcium channels: subtype- and subunit-dependent action at multiple sites. J. Membr. Biol. 151: 77–9010.

Zhou Y. D., Turner T. J., Dunlap K. (2003). Enhanced G protein-dependent modulation of excitatory synaptic transmission in the cerebellum of the Ca2+ channel-mutant mouse, tottering. J. Physiol. 547: 497–507.

Annex

The results reported in Chapter 3 are under publication in the following accepted Manuscript:

Ait Ouares K, Filipis K, Tzilivaki A, Poirazi P, Canepari M (2019) Two distinct sets of Ca^{2+} and K^+ channels are activated at different membrane potentials by the climbing fibre synaptic potential in Purkinje neuron dendrites. *J Neurosci*, in press (doi: 10.1523/JNEUROSCI.2155-18.2018).

While the results reported in Chapter 4 are still not yet submitted for publication, the work carried out during my PhD contributed to other five published or accepted publications, which are not strictly related to the present thesis. The list below reports these references with the indication of my specific contribution. These publications, in published or accepted version, are fully included in the following pages.

Ait Ouares K, Jaafari N, Canepari M (2016). A generalised method to estimate the kinetics of fast Ca^{2+} currents from Ca^{2+} imaging experiments. *J Neurosci Methods*, 268: 66-77.
In this work, I terminated the experiments started by Nadia Jaafari to extend the technique of Ca^{2+} current imaging to PNs. This method, however, was not used in my thesis.

Filipis L, **Ait Ouares K**, Moreau P, Tanese D, Zampini V, Latini A, Bleau C, Bleau C, Graham J, Canepari M (2018). A novel multisite confocal system for rapid Ca^{2+} imaging from submicron structures in brain slices. *J Biophoton*, 11(3).
In this work, I participated to the experiments performed in PNs.

Zoukimian C, Meudal H, De Waard S, **Ait Ouares K**, Nicolas S, Canepari M, Béroud R, Landon C, De Waard M, Boturyn D (2019). Synthesis by native chemical ligation and characterization of the scorpion toxin AmmTx3. *Bioorg Med Chem*, 27: 247-253.
In this work, I provided evidence of the effect of the toxin AmmTx3 on PNs.

Ait Ouares K, Beurrier C, Canepari M, Laverne G, Kuczewski N (2019). Opto nongenetics inhibition of neuronal firing. *Eur J Neurosci*, 49:6-26.
In this work, I performed all experiments in PNs.

Ait Ouares K, Jaafari N, Kuczewski N, Canepari M (2019). Imaging Native Calcium Currents in Brain Slices. *Advs Exp Med Biol*, in press.
In this review, I contributed data in PNs.

The results reported in Chapter 3 are under publication in the following accepted Manuscript:

Ait Ouares K, Filipis K, Tzilivaki A, Poirazi P, Canepari M (2019) Two distinct sets of Ca^{2+} and K^{+} channels are activated at different membrane potentials by the climbing fibre synaptic potential in Purkinje neuron dendrites. *J Neurosci*, in press.

While the results reported in Chapter 4 are still not yet submitted for publication, the work carried out during my PhD contributed to other five published or accepted publications, which are not strictly related to the present thesis. The list below reports these references with the indication of my specific contribution. These publications, in published or accepted version, are fully included in the following pages.

Ait Ouares K, Jaafari N, Canepari M (2016) A generalised method to estimate the kinetics of fast Ca^{2+} currents from Ca^{2+} imaging experiments. *J Neurosci Methods*, 268: 66-77.

In this work, I terminated the experiments started by Nadia Jaafari to extend the technique of Ca^{2+} current imaging to PNs. This method, however, was not used in my thesis.

Filipis L, **Ait Ouares K**, Moreau P, Tanese D, Zampini V, Latini A, Bleau C, Bleau C, Graham J, Canepari M (2018) A novel multisite confocal system for rapid Ca^{2+} imaging from submicron structures in brain slices. *J Biophoton*, 11(3).

In this work, I participated to the experiments performed in PNs.

Zoukimian C, Meudal H, De Waard S, **Ait Ouares K**, Nicolas S, Canepari M, Béroud R, Landon C, De Waard M, Boturyn D (2019) Synthesis by native chemical ligation and characterization of the scorpion toxin AmmTx3. *Bioorg Med Chem*, 27: 247-253.

In this work, I provided evidence of the effect of the toxin AmmTx3 in PNs.

Ait Ouares K, Beurrier C, Canepari M, Laverne G, Kuczewski N (2019) Opto nongenetics inhibition of neuronal firing. *Eur J Neurosci*, 49:6-26.

In this work, I performed all experiments in PNs.

Ait Ouares K, Jaafari N, Kuczewski N, Canepari M (2019) Imaging Native Calcium Currents in Brain Slices. *Advs Exp Med Biol*, in press.

In this review, I contributed data in PNs.

Journal of Neuroscience Methods 268 (2016) 66–77

Contents lists available at ScienceDirect

Journal of Neuroscience Methods

journal homepage: www.elsevier.com/locate/jneumeth

A generalised method to estimate the kinetics of fast Ca^{2+} currents from Ca^{2+} imaging experiments

Karima Ait Ouares[a,b], Nadia Jaafari[a,b], Marco Canepari[a,b,c,*]

[a] Laboratory for Interdisciplinary Physics, UMR 5588, Université Grenoble Alpes and CNRS, 38402 Saint Martin d'Hères, France
[b] Laboratories of Excellence, Ion Channel Science and Therapeutics, France
[c] Institut National de la Santé et Recherche Médicale (INSERM), France

HIGHLIGHTS

- Imaging Ca^{2+} fluorescence at high temporal resolution.
- Estimate the kinetics of Ca^{2+} currents.
- Study the physiological function of neuronal Ca^{2+} channels.

ARTICLE INFO

Article history:
Received 18 March 2016
Received in revised form 4 May 2016
Accepted 5 May 2016
Available online 6 May 2016

Keywords:
Calcium currents
Calcium imaging
CA1 hippocampal pyramidal neuron
Purkinje neuron
Calcium binding proteins

ABSTRACT

Background: Fast Ca^{2+} imaging using low-affinity fluorescent indicators allows tracking Ca^{2+} neuronal influx at high temporal resolution. In some systems, where the Ca^{2+}-bound indicator is linear with Ca^{2+} entering the cell, the Ca^{2+} current has same kinetics of the fluorescence time derivative. In other systems, like cerebellar Purkinje neuron dendrites, the time derivative strategy fails since fluorescence kinetics is affected by Ca^{2+} binding proteins sequestering Ca^{2+} from the indicator.
New method: Our novel method estimates the kinetics of the Ca^{2+} current in cells where the time course of fluorescence is not linear with Ca^{2+} influx. The method is based on a two-buffer and two-indicator model, with three free parameters, where Ca^{2+} sequestration from the indicator is mimicked by Ca^{2+}-binding to the slower buffer. We developed a semi-automatic protocol to optimise the free parameters and the kinetics of the input current to match the experimental fluorescence change with the simulated curve of the Ca^{2+}-bound indicator.
Results: We show that the optimised input current is a good estimate of the real Ca^{2+} current by validating the method both using computer simulations and data from real neurons. We report the first estimates of Ca^{2+} currents associated with climbing fibre excitatory postsynaptic potentials in Purkinje neurons.
Comparison with existing methods: The present method extends the possibility of studying Ca^{2+} currents in systems where the existing time derivative approach fails.
Conclusions: The information available from our technique allows investigating the physiological behaviour of Ca^{2+} channels under all possible conditions.

1. Introduction

The possibility of measuring the kinetics of Ca^{2+} currents from fluorescence transients of a Ca^{2+} indicator allows studying the local activation and de-activation of Ca^{2+} channels during physiological activity. The founding principle of this measurement is that the fractional change of Ca^{2+} fluorescence ($\Delta F/F_0$) following a transmembrane Ca^{2+} influx is proportional to the Ca^{2+} bound to the indicator if the dye-Ca^{2+} binding reaction has reached its equilibrium and if the indicator is not saturated (Sabatini and Regehr, 1998). Under this condition, the $\Delta F/F_0$ signal will be proportional to the integral of the Ca^{2+} current if two further conditions are met: (*A*) that the dye-Ca^{2+} binding reaction equilibration is faster than the kinetics of the Ca^{2+} current; and (*B*) that the Ca^{2+} binding reactions with the endogenous molecules of the cell are either also faster than the kinetics of the Ca^{2+} current or slower but negligible with

* Corresponding author at: Laboratoire Interdisciplinaire de Physique (UMR 5588), Bat. E45, 140 Avenue de la Physique, Domaine Univ., 38402 St. Martin d'Hères Cedex, France.
E-mail address: marco.canepari@univ-grenoble-alpes.fr (M. Canepari).

http://dx.doi.org/10.1016/j.jneumeth.2016.05.005
0165-0270/

respect to the dye-Ca^{2+} binding reaction during the time-window of the measurement.

We have previously demonstrated that both conditions are fulfilled by the Ca^{2+} indicator Oregon Green BAPTA-5N (OG5N) in the case of dendritic Ca^{2+} currents associated with back-propagating action potentials in CA1 hippocampal pyramidal neurons (Jaafari et al., 2014, 2015). OG5N is a low-affinity indicator (K_D = 35 μM, Canepari and Odgen, 2006) that equilibrates in <200 μs according to the Kao and Tsien theoretical estimate of the relaxation time (Kao and Tsien, 1988). Its ability to track the kinetics of voltage-gated Ca^{2+} channels (VGCCs) can be therefore considered universal in all cellular systems. The second condition, i.e. the linearity with the endogenous Ca^{2+} binding reactions, is however not universal. In the dendrites of CA1 hippocampal pyramidal neurons, where the endogenous buffer capacity (Canepari et al., 2008) is relatively low (~100, Helmchen et al., 1996; Maravall et al., 2000), the Ca^{2+}-$\Delta F/F_0$ signal associated with an action potential is essentially constant for the first 10 ms after the peak and decays only later in ~100 ms. Fig. 1A shows a representative example of dendritic Ca^{2+} transient associated with a back-propagating action potential from a cell filled with 2 mM OG5N. The $\Delta F/F_0$ signal starts rising near the peak of the action potential reaching a plateau for a few milliseconds after the end of the action potential. The flat behaviour of the $\Delta F/F_0$ signal after the end of the current indicates that not only the dye-Ca^{2+} binding, but also the Ca^{2+} binding to the endogenous buffer, have reached the equilibrium during this short time window (Jaafari et al., 2014). Hence, the time derivative of the $\Delta F/F_0$ signal has the same kinetics of the Ca^{2+} current. The CA1 hippocampal pyramidal neuron of Fig. 1B was filled with 2 mM OG5N and 100 μM BAPTA, a high-affinity Ca^{2+} buffer (K_D = 160 nM, Pethig et al., 1989). In contrast to the OG5N-Ca^{2+} binding reaction, the BAPTA-Ca^{2+} binding reaction equilibrates in the millisecond range. As BAPTA sequestrates Ca^{2+} from OG5N, the slope of the $\Delta F/F_0$ signal becomes negative after the end of the current deviating from the linear behaviour with the Ca^{2+} influx. In this case, the time derivative of the OG5N-$\Delta F/F_0$ signal does not match the kinetics of the Ca^{2+} current. Fig. 1C shows an example of dendritic Ca^{2+} transient associated with a climbing fibre excitatory postsynaptic potential (EPSP) from a cerebellar Purkinje neuron (PN) filled with 2 mM OG5N. In this cell type, where the endogenous buffer capacity is high (~2000, Fierro and Llano, 1996), the dendritic Ca^{2+}-$\Delta F/F_0$ signal associated with climbing fibre EPSPs decays more rapidly (Miyakawa et al., 1992) following the Ca^{2+} binding to slow endogenous buffers. Thus, the OG5N-$\Delta F/F_0$ time derivative in Fig. 1C has a negative component and does not reproduce the kinetics of the Ca^{2+} current. Since the theoretical ability of Ca^{2+} imaging experiments for tracking a fast Ca^{2+} influx depends exclusively on the equilibration time of the indicator, a way to extract the kinetics of the Ca^{2+} current can be still developed if the kinetics of Ca^{2+} sequestration is taken into account. This is clearly a difficult task since the kinetics of Ca^{2+} binding proteins, measured with flash photolysis techniques (Faas and Mody, 2012), is very complex and depends on many parameters that vary from cell to cell. In contrast, a useful method should utilise a simple model with only a small number of degrees of freedom, allowing the development of a semi-automatic procedure to standardise the extraction of the Ca^{2+} current kinetics. In this report, we present a novel method to estimate the kinetics of the Ca^{2+} current based on this principle. The method applies a simple two-buffer and two-indicator model to the hypothetical current input to match the experimental time course of the OG5N-$\Delta F/F_0$ signal. The parameters of the model are set, initially, using the rising phase of the OG5N-$\Delta F/F_0$ time derivative as initial approximation of the current. The full kinetics of the current is then extrapolated by maximising the similarity between the experimental OG5N-$\Delta F/F_0$ signal and the equivalent curve obtained by computer simulation.

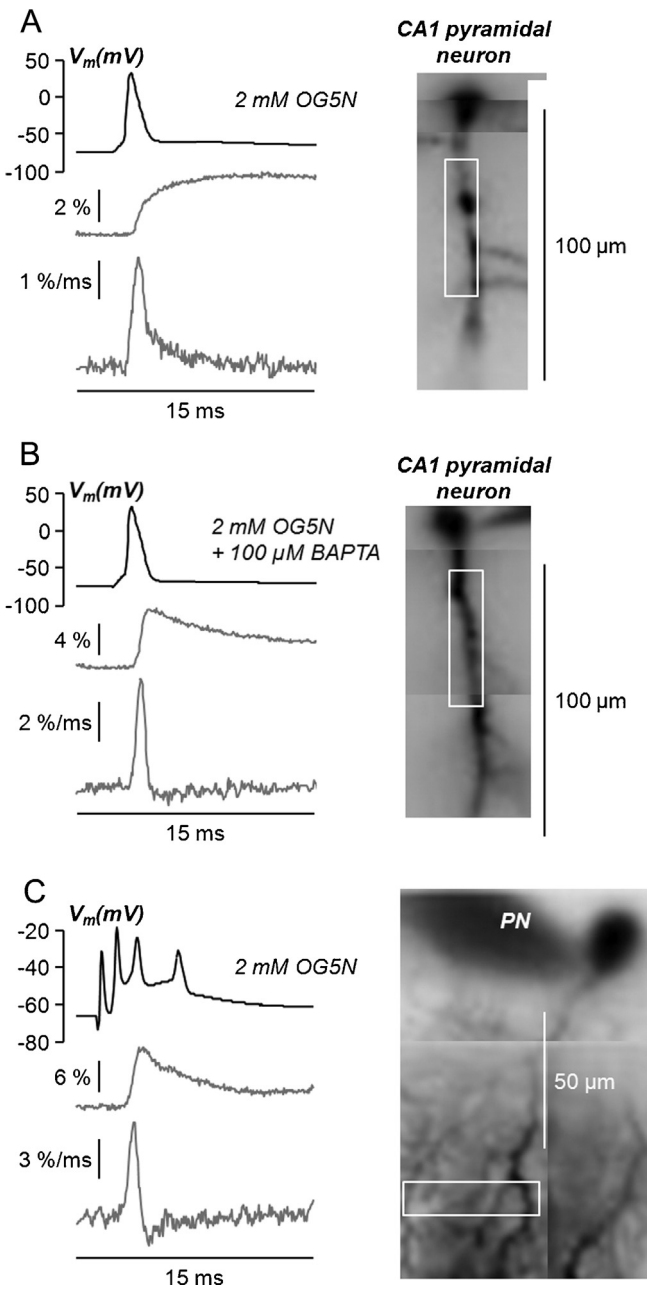

Fig. 1. OG5N-$\Delta F/F_0$ signals in CA1 hippocampal pyramidal neurons and in PNs. (A) OG5N-$\Delta F/F_0$ signal (2nd trace from the top) and its time derivative (3rd trace from the top) associated with an action potential (top trace) from the dendritic region of a CA1 hippocampal pyramidal neuron indicated on the right. The cell was filled with 2 mM OG5N. (B) Same as A but in another CA1 hippocampal pyramidal neuron filled with 2 mM OG5N and 100 μM BAPTA. (C) OG5N-$\Delta F/F_0$ signal (2nd trace from the top) and its time derivative (3rd trace from the top) associated with a climbing fibre EPSP (top trace) from the dendritic region of a PN indicated on the right. The cell was filled with 2 mM OG5N. All data, recorded at 20 kHz, were from averages of 16 trials.

To validate the method, we used combined fluorescence measurements from OG5N and Fura-2. In particular, since the time scale of Fura-2 equilibration is similar to that of endogenous Ca^{2+} binding proteins (Kao and Tsien, 1988), the measurement of Fura-2 $\Delta F/F_0$ (Fura-$\Delta F/F_0$) signal provided a direct estimate of Ca^{2+} sequestration. The usefulness and limitations of the estimate of the Ca^{2+} current kinetics, obtained with this approach, are discussed at the end of the paper.

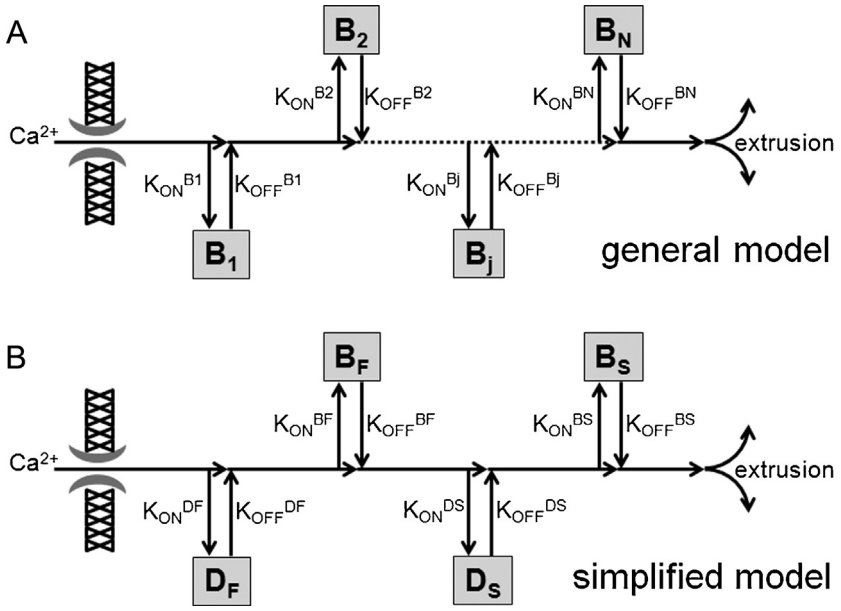

Fig. 2. Models of cellular Ca^{2+} binding kinetics. (A) General model of Ca^{2+} cellular influx and reaction with N buffers followed by extrusion. (B) Simplified version of the model in A, used in our method, with a fast and a slow endogenous buffer (B_F and B_S) and with a fast and a slow Ca^{2+} indicator (D_F and D_S).

2. Materials and methods

2.1. Slice preparation, solutions and electrophysiology

Experiments, performed at the Laboratoire Interdisciplinaire de Physique, were approved by the Isere prefecture (authorisation no. 38 12 01). Transversal hippocampal slices and sagittal cerebellar slices (250 μm thick) were prepared from 24 to 35 postnatal days old C57Bl6 mice following published procedures (Vogt et al., 2011a, 2011b) using a Leica VT1200 (Leica, Wetzlar, Germany). Slices were cut in iced extracellular solution and incubated at 37 °C for 1 h before use. The extracellular solution contained (in mM): 125 NaCl, 26 $NaHCO_3$, 1 $MgSO_4$, 3 KCl, 1 NaH_2PO_4, 2$CaCl_2$ and 20 glucose, bubbled with 95% O_2 and 5% CO_2. The intracellular solution contained (in mM): 125 $KMeSO_4$, 5 KCl, 8 $MgSO_4$, 5 Na_2-ATP, 0.3 Tris-GTP, 12 Tris-phosphocreatine, 20 HEPES, adjusted to pH 7.35 with KOH. The Ca^{2+} indicator Oregon Green 488 BAPTA-5N (OG5N, Invitrogen, Carlsbad, CA) was added at the concentration of 2 mM. In some experiments, the Ca^{2+} indicator Fura-2 (Invitrogen) was added at 400 μM. Chemicals were purchased from Sigma–Aldrich (St. Louis, MO). Experiments were performed at 32–34 °C using an Olympus BX51 microscope equipped with a 60X/1.0 NA Nikon objective. Patch-clamp recordings were made using a Multiclamp amplifier 700A (Molecular Devices, Sunnyvale, CA) and recorded with the A/D board of the CCD camera. The membrane potential, measured with the patch pipette, was corrected for the junction potential (−11 mV) as previously estimated (Canepari et al., 2010). In PNs, climbing fibre EPSPs were elicited by current pulses, of 5–20 μA amplitude and 100 μs duration, which were delivered by a pipette placed in granule cell layer near the recording cell. In CA1 hippocampal pyramidal neurons, somatic action potentials were elicited by 2 ms depolarising current injections through the patch pipette.

2.2. Optical recordings and analysis

OG5N and Fura-2 fluorescence were excited at 470 nm and 385 nm respectively with an OptoLED (CAIRN Research Ltd., Faversham, UK). Both fluorescence signals, filtered at 510 ± 42 nm, were recorded using a NeuroCCD-SMQ camera (RedShirtimaging, Decatur, GA). Images, de-magnified by ~0.25× to visualise ~150 μm, were acquired at 5 kHz with a resolution of 26 × 26 pixels, except in the case of Fig. 1 in which the sampling frequency was 20 kHz and the resolution of 26 × 4. All recordings were performed at least 35 min after establishing the whole cell configuration to allow equilibration of the indicators. To average multiple trials, consistency was verified by checking the somatic electrical signal. Fluorescence averages were corrected for bleaching using filtered trials without signal. All data were analysed with Matlab (The Mathworks, Natick, MA). $\Delta F/F_0$ signals were calculated after subtraction of the autofluorescence background.

2.3. Models and simulations

A general model for Ca^{2+} dynamics in a cell cytoplasm after an influx is illustrated in Fig. 2A and described by the set of 2N +1 equations:

$$\frac{d\left[Ca^{2+}\right]}{dt} = \xi_{Ca} - \sum_{j=1}^{N}\left(K_{ON}^{Bj} \times [Bj] \times \left[Ca^{2+}\right] - K_{OFF}^{Bj} \times \left[BjCa^{2+}\right]\right) - \varepsilon \times \frac{\left[Ca^{2+}\right]}{\left[Ca^{2+}\right] + \theta_M}$$

$$\frac{d\left[BjCa^{2+}\right]}{dt} = K_{ON}^{Bj} \times \left[Ca^{2+}\right] \times [Bj] - K_{OFF}^{Bj} \times \left[B_FCa^{2+}\right]$$

$$\frac{d[Bj]}{dt} = -\frac{d\left[BjCa^{2+}\right]}{dt}$$

This model comprises N buffers, with association and dissociation constants K_{ON}^{Bj} and K_{OFF}^{Bj} respectively, which represent the different binding sites of Ca^{2+} binding proteins and possibly to exogenous Ca^{2+} chelators such as the indicators. The model also includes Ca^{2+} extrusion with Michaelis–Menten kinetics, where ε is a factor that depends on the pumps velocity and θ_M is the Michaelis–Menten constant. The input ξ_{Ca} is the Ca^{2+} current to volume ratio, i.e. the curve that we are aiming at estimating. A simplified version of the general model is the two-buffer model (Nowycky and Pinter, 1993; Canepari and Mammano, 1999). Here, as shown in Fig. 2B, the two buffers are a fast buffer (B_F) and a slow buffer (B_S). The presence of a fast dye (D_F), representing OG5N, and possibly of a slow dye (D_S), representing Fura-2, complete the simplified model leading to nine

or seven differential equations, depending on whether or not Fura-2 is added in the experiment. We used this simplified model to fit the experimental OG5N-$\Delta F/F_0$ signal with the $[D_F Ca^{2+}]$ resulting from computer simulations using the function "ode45" in Matlab. In all simulations, the ξ_{Ca} input was expressed as sum of four Gaussian functions:

$$\xi_{Ca}(t) = \sum_{k=1}^{4} \xi_{Ca}^{k} \times e^{-\left(\frac{t-\alpha k}{\beta k}\right)^2}$$

For both dyes, the diffusion-limited association constant ($K_{ON}{}^{DF}$ and $K_{ON}{}^{DS}$) was set to 570 $\mu M^{-1}\,s^{-1}$ as in a previous study (Canepari and Mammano, 1999), the total concentrations were those of the patch pipette and the equilibrium constant ($K_D = K_{OFF}/K_{ON}$) was set to 35 μM for OG5N (Canepari and Odgen, 2006) and 0.24 μM for Fura-2 (Shuttleworth and Thompson, 1991). We arbitrarily set the equilibrium constants of the fast and slow buffers to 10 μM and 0.2 μM respectively, and the association constant of the fast buffer ($K_{ON}{}^{BF}$) equal to that of the dyes. The concentrations of the fast and slow buffers and the association constant of the slow buffer were varied to optimise the similarity between the experimental OG5N-$\Delta F/F_0$ signal and the simulated $[D_F Ca^{2+}]$. Finally, the extrusion constants ε and and θ_M were set to 1000 $\mu M\,s^{-1}$ and 3 μM respectively. To fit experimental data, we associated the Ca^{2+}-bound concentrations of OG5N and Fura-2 ($[D_F Ca^{2+}]$ and $[D_S Ca^{2+}]$) with their respective fluorescence (F) signals using the two equations:

$$\left[D_F Ca^{2+}\right] = [D_F]_{TOT} \times \frac{F^{DF} - F_{zero}^{DF}}{F_{sat}^{DF} - F_{zero}^{DF}}$$

$$\left[D_S Ca^{2+}\right] = [D_S]_{TOT} \times \frac{F^{DS} - F_{zero}^{DS}}{F_{sat}^{DS} - F_{zero}^{DS}}$$

where F_{zero} and F_{sat} are the fluorescence values at zero and saturating Ca^{2+} respectively and $[D_F]_{TOT}$ and $[D_S]_{TOT}$ are the total concentrations of OG5N (2 mM) and Fura (400 μM) respectively. Assuming the initial fluorescence (F_0) equal to F_{zero}, the variable $[D_F Ca^{2+}]$ and $[D_S Ca^{2+}]$ can be obtained from the OG5N-$\Delta F/F_0$ signal and the $\Delta F/F_0$ signal from Fura-2 (Fura-$\Delta F/F_0$) by using the two equations:

$$\left[D_F Ca^{2+}\right] = [D_F]_{TOT} \times \frac{OG5N - \Delta F/F_0}{\sigma^{DF}}$$

$$\left[D_S Ca^{2+}\right] = [D_S]_{TOT} \times \frac{Fura\text{-}\Delta F/F_0}{\sigma^{DS}}$$

where σ^{DF} and σ^{DS} are the *dynamic range factors* defined as $(F_{sat} - F_0)/F_0$. To measure σ^{DF} and σ^{DS}, we filled 9 CA1 pyramidal neurons with 0.5 mM OG5N and, 4 of them, also with 0.1 mM Fura-2. In these cells, in the presence of 4 mM extracellular $CaCl_2$, the somatic membrane was made permeable to Ca^{2+} by applying a 30 s step of −500 mV in voltage clamp, is this way saturating the indicators. σ^{DF}, which did not depend on the presence of Fura-2 concentration, was globally 15 ± 2 (N = 9 cells). σ^{DS} was −0.44 ± 0.07 (N = 4 cells). The simulation of $[D_F Ca^{2+}]$ was divided by the mean value of σ^{DF}(15) to match the corresponding experimental $\Delta F/F_0$ signal. The simulation of $[D_S Ca^{2+}]$ was divided by a value ranging between −0.37 to −0.48 value to match the corresponding experimental $\Delta F/F_0$ signal.

2.4. Quantification of the similarity between two curves

To quantify the similarity between the curves from computer simulations and the experimental $\Delta F/F_0$ signals, we found that the simple comparison of the signals gave ambiguous results. We therefore used a classical approach based on the estimate of the correlation between the two curves in the frequency (ν) domain. In detail, defining ΔG as $\sigma \times [DCa^{2+}]/[D]_{TOT}$, where D is the dye (either OG5N or Fura-2) and σ its dynamic range factor, the similarity between ΔG and $\Delta F/F_0$ was estimated by calculating their *magnitude squared coherence* $\Gamma_{\Delta F/F0}$:

$$\Gamma_{\Delta F/F0}(\nu) = \frac{|\Pi_{\Delta F \Delta G}(\nu)|^2}{\Pi_{\Delta F \Delta F}(\nu) \times \Pi_{\Delta G \Delta G}(\nu)}$$

where $\Pi_{\Delta F \Delta F}(\nu)$ and $\Pi_{\Delta G \Delta G}(\nu)$ are the *power spectral densities* of $\Delta F/F_0$ (ΔF in the equations below) and ΔG respectively, and $\Pi_{\Delta F \Delta G}(\nu)$ is their *cross power spectral density*. $\Gamma_{\Delta F/F0}(\nu)$ is the fractional part of ΔG that matches ΔF at the frequency ν and, therefore, $\Gamma_{\Delta F/F0}(\underline{\nu}) = 1$ if ΔF and ΔG are identical at $\nu = \underline{\nu}$. The frequency functions $\Pi_{\Delta F \Delta F}(\nu)$, $\Pi_{\Delta G \Delta G}(\nu)$ and $\Pi_{\Delta F \Delta G}(\nu)$ (see for example Oppenheim and Schafer, 1999) are normally computed with the equations:

$$\Pi_{\Delta F \Delta F}(\nu) = \frac{\Delta t}{N} \times \left|\sum_{k=1}^{N} \Delta F_k \times e^{-i\nu k}\right|^2$$

$$\Pi_{\Delta G \Delta G}(\nu) = \frac{\Delta t}{N} \times \left|\sum_{k=1}^{N} \Delta G_k \times e^{-i\nu k}\right|^2$$

$$\Pi_{\Delta F \Delta G}(\nu) = \frac{\Delta t}{N} \times \sum_{k=1}^{N} \left(\sum_{h=1}^{N} \Delta F_h \times \Delta G_{h+k}\right) \times e^{-i\nu k}$$

where Δt is sampling time and N is the number of samples. In our method, however, we found convenient to calculate $\Gamma_{\Delta F/F0}$ in Matlab (Signal Processing Toolbox) using the function "mscohere" that uses the Welch's averaged modified periodogram method (Welch, 1967) to compute $\Pi_{\Delta F \Delta F}(\nu)$, $\Pi_{\Delta G \Delta G}(\nu)$ and $\Pi_{\Delta F \Delta G}(\nu)$ with minimal effect of the noise. In particular, since the precise frequency information is irrelevant for the purpose of our method, the segments used for the calculation of Welch $\Gamma_{\Delta F/F0}$ were windowed with a two-point *Hamming window* to obtain a nearly uniform $\Gamma_{\Delta F/F0}$ over ν range of 0–1 kHz. This quantification was found efficient as $\Gamma_{\Delta F/F0}$ approached 1 when the curve from computer simulation matched the experimental $\Delta F/F_0$ signal. Thus, in the optimisation protocol described in the results, the parameters of the current input and of the models were set to maximise the mean $\Gamma_{\Delta F/F0}$ over the range $0 < \nu < 1$ kHz ($<\Gamma_{\Delta F/F0}>$). Empirically, we considered the optimisation process satisfactory if $<\Gamma_{\Delta F/F0}>$ was >0.96.

3. Results

3.1. Limitations of extracting the Ca^{2+} current kinetics by using a simple time derivative

The method of extracting the Ca^{2+} current kinetics by calculating the time derivative of the OG5N-$\Delta F/F_0$ signal is based on the assumption that the kinetics of the OG5N-Ca^{2+} binding reaction is linear with the kinetics of Ca^{2+} binding to the endogenous buffers. This assumption is realistic if the slope of the $\Delta F/F_0$ signal is zero after the end of the current for a time window as long as the duration of the current (Jaafari et al., 2014). If a buffer with higher affinity but slower equilibrium constant with respect to OG5N is present, this will sequestrate Ca^{2+} from OG5N producing an early decay phase and a negative component in the OG5N-$\Delta F/F_0$ time derivative. To illustrate this general concept, we show in Fig. 3 the results of computer simulations from a two-buffer model at increasing slow buffer concentrations. The model includes a

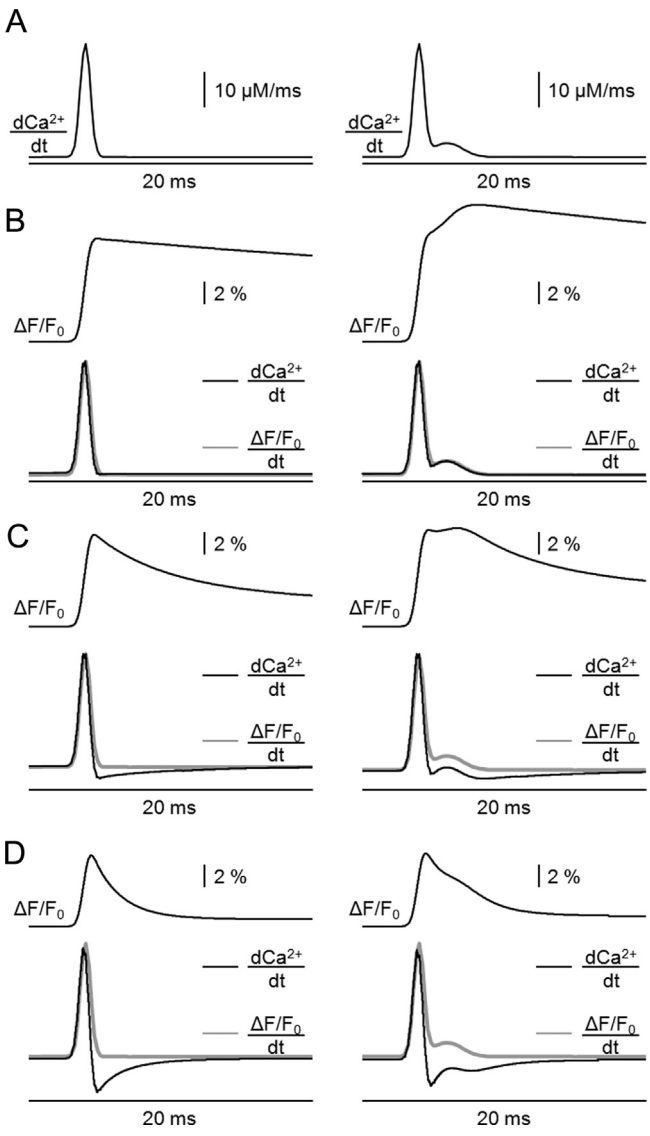

Fig. 3. Theoretical examples of distortions of Ca^{2+} currents calculated as OG5N-$\Delta F/F_0$ time derivative. (A) Model Ca^{2+} currents used for computer simulations. Left: $dCa^{2+}/dt = (40\,\mu M/ms) \times \exp(-[(t-4\,ms)/0.5\,ms)]^2)$. Right: $dCa^{2+}/dt = (40\,\mu M/ms) \times \exp(-[(t-4\,ms)/0.5\,ms)]^2) + (5\,\mu M/ms) \times \exp(-[(t-6\,ms)/1.5\,ms)]^2)$. (B) Results of computer simulations of OG5N (2 mM) kinetics with 1 mM of a fast buffer with $K_D = 10\,\mu M$; the black traces are the expected $\Delta F/F_0$ signal (top) and its time derivative (bottom); the superimposed bottom greytraces are the input Ca^{2+} currents reported in panel A. (C) Same as B with additional 100 μM of a slow buffer with $K_D = 0.2\,\mu M$. (D) Same as B with additional 400 μM of a slow buffer with $K_D = 0.2\,\mu M$.

realistic slow extrusion mechanism which is capable of re-establishing the initial Ca^{2+} conditions, as described in Section 2. To visualise the difference between the real current and the time derivative of the $\Delta F/F_0$ signal, we used two input currents illustrated in Fig. 3(A). The first current on the left is a simple Gaussian function with a time constant of 0.5 ms. The second current on the right is the summation of the same fast current plus a smaller and slower current which is also a Gaussian function. Fig. 3(B) (top) shows the OG5N-$\Delta F/F_0$ signals in simulations where the cell has only 1 mM of a fast buffer with $K_D = 10\,\mu M$. The traces on the bottom show the kinetics of the time derivative of the OG5N-$\Delta F/F_0$ signal. In this case, as expected, the time derivatives of the OG5N-$\Delta F/F_0$ signal and the input currents have the same kinetics. Thus, the slow decay of the OG5N-$\Delta F/F_0$ signals produced by the Ca^{2+} extrusion has negligible effect on the time derivatives of the OG5N-$\Delta F/F_0$ signal and does not produce negative components in its time derivative. Fig. 3(C) and (D) (top traces) shows the OG5N-$\Delta F/F_0$ signals in two simulations where the model includes an additional slow buffer with $K_{ON} = 200\,\mu M^{-1}\,s^{-1}$ and $K_D = 0.2\,\mu M$ at concentrations of 100 and 400 μM respectively. In these cases, the faster decay of the OG5N-$\Delta F/F_0$ signal results in a difference between the time derivative of the OG5N-$\Delta F/F_0$ signal and the input current. This difference is however minimal for the rising phase of the fast current. Therefore, the time derivative of the OG5N-$\Delta F/F_0$ signal can be still considered an approximation of the real current in its initial phase. The goal is to develop a strategy to obtain a curve that approaches the kinetics of the real current, starting from the time derivative of the OG5N-$\Delta F/F_0$ signal as first approximation. This is done by optimising the parameters of a simplified kinetic model to reach a simulated OG5N-$\Delta F/F_0$ signal matching the experimental one. The parameters are determined by those characteristics of the experimental signal that depend only weakly on the full kinetics of the current input.

3.2. Correcting the time derivative to account for a slow buffer using a semi-automatic protocol

To address the problem introduced at the end of the previous paragraph we used computer simulations corresponding to three more complex scenarios that may occur in real cells. In detail, we produce three "experimental" OG5N-$\Delta F/F_0$ signals from models that comprise four progressively slower and stronger buffers: a low-affinity buffer ($K_{ON} = 570\,\mu M^{-1}\,s^{-1}$ and $K_D = 10\,\mu M$); a medium-affinity buffer ($K_{ON} = 570\,\mu M^{-1}\,s^{-1}$ and $K_D = 1\,\mu M$); a fast high-affinity buffer ($K_{ON} = 400\,\mu M^{-1}\,s^{-1}$ and $K_D = 0.4\,\mu M$); and a slow and high-affinity buffer ($K_{ON} = 200\,\mu M^{-1}\,s^{-1}$ and $K_D = 0.1\,\mu M$); The parameters of the three particular scenarios are reported in Table 1. In the first scenario, the model contains 250 μM of the low-affinity buffer and 100 μM of each high-affinity buffer. In this scenario, fast buffering is small and most of the Ca^{2+} is sequestrated by the slow high-affinity buffer. In the second scenario, the model contains 1 mM of the low-affinity buffer, 500 μM of the fast high-affinity buffer and only 50 μM of the slow high-affinity buffer. In this case, fast buffering is more prominent and later buffering more rapid. Finally, in the third scenario, the model contains 2000 μM of the low-affinity buffer, 400 μM of the medium-affinity buffer, 100 μM of the fast high-affinity buffer and 20 μM of the slow high-affinity buffer. In this last scenario, faster buffering is prevailing with respect to slow buffering. To generate the three $\Delta F/F_0$ signals, we used the same two-component current of the previous paragraph. We added white noise to these curves to mimic experimental scenarios. The $\Delta F/F_0$ signals are reported in Fig. 4(A) (top). The peak of the $\Delta F/F_0$ signal varies in the three cases and it is larger in the first scenario, where fast buffering is weaker. The slope of the faster component of the decay depends on the quantity and speed of the high-affinity buffers. As shown by the time derivatives of the $\Delta F/F_0$ signal reported below (grey traces), the negative peak of the curve, relative to the positive peak, is larger in the second scenario where high-affinity buffering is strong, with respect to low-affinity buffering, but relatively rapid. The slower component of $\Delta F/F_0$ signal decay, after the end of the current, depends on the speed and on the amount of the high-affinity buffers and it is slower in the first scenario. Finally, in the third scenario involving the intermediate (fast) buffer, the time derivative of the $\Delta F/F_0$ signal has a small negative component and it approaches the fast Gaussian component of the current while the slow component is lost (see the right traces in Fig. 4(A)). In the development of a generalised method to estimate the Ca^{2+} current kinetics, the idea is not to precisely predict the kinetics of Ca^{2+} buffering, but to correct for the distortion in the $\Delta F/F_0$ time derivative due to Ca^{2+} sequestration from the indicator. As shown in Fig. 4(A), the time derivative of the $\Delta F/F_0$ signal is

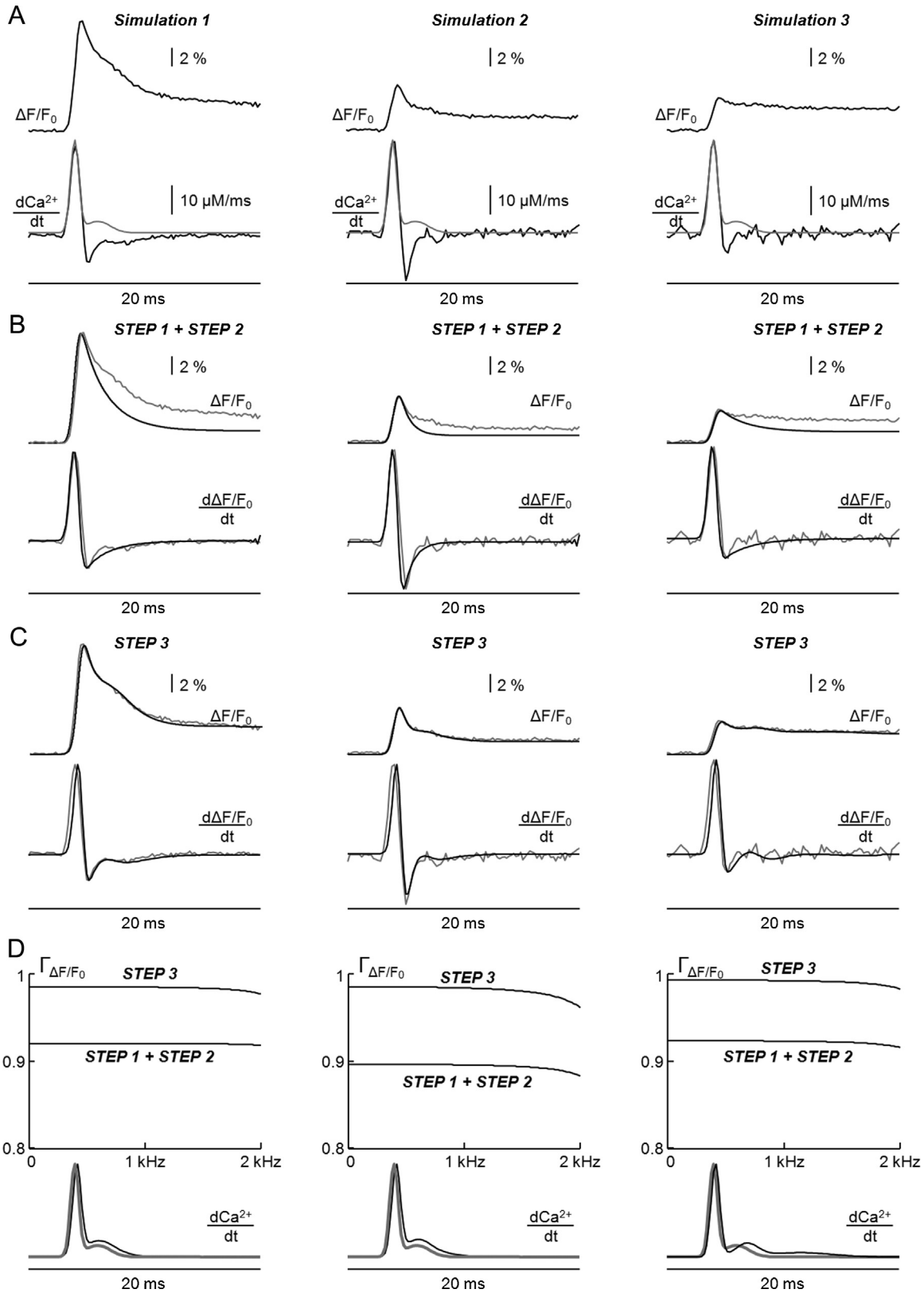

Fig. 4. Assessment of the protocol from simulated complex cellular scenarios. (A) Using a model Ca^{2+} current for computer simulations the second current of Fig. 3, the results of 3 computer simulations of OG5N (2 mM) kinetics from complex models with 3 or 4 buffers (see Table 1); the top and bottom black traces are the expected $\Delta F/F_0$ signals and their time derivatives respectively; bottom grey trace is the superimposed current; white noise is added to mimic putative experimental scenarios. (B) Using as input current the single Gaussian function fitting the time derivative rising phase, and optimising the two-buffer parameters of the model (*STEP* 1 +*STEP* 2), the results of computer simulations (black traces) superimposed to the original signals (grey traces) shown in panel A. (C) With the model parameters established in STEP 2, after optimising the input current (STEP 3), the results of computer simulations (black traces) superimposed to the original signals (grey traces) shown in panel A. (D) Top: $\Gamma_{\Delta F/F0}$, defined in Section 2, to quantify the similarity of the curves obtained after *STEP* 1 +*STEP* 2 and after *STEP* 3; in all cases, the mean $\Gamma_{\Delta F/F0}$ over 0–1 kHz increases to >0.96 after *STEP* 3. Bottom: the obtained Ca^{2+} currents (black traces) normalised to the peak and superimposed to the original currents.

Table 1
Values of the parameters of the four buffers used in the three simulations of Fig. 4.

	Conc. buffer 1 (μM) K_{on} = 570 μM^{-1} s^{-1} K_D = 10 μM	Conc. buffer 2 (μM) K_{on} = 570 μM^{-1} s^{-1} K_D = 1 μM	Conc. buffer 3 (μM) K_{on} = 400 μM^{-1} s^{-1} K_D = 0.4 μM	Conc. buffer 4 (μM) K_{on} = 200 μM^{-1} s^{-1} K_D = 0.1 μM
Simulation 1	250	0	100	100
Simulation 2	1000	0	500	50
Simulation 3	2000	400	100	20

always matching the rising phase of the current. Therefore, "*STEP* 1" of the protocol is the fit of the rising phase of the $\Delta F/F_0$ time derivative with one Gaussian function. This curve can be considered the first approximation of the current kinetics to be used in "*STEP* 2" of the protocol. Given this current, the ratio between the positive and the negative peak of the $\Delta F/F_0$ time derivative and the slower decay phase of the signal are two independent conditions that depend on the ratio between the low-affinity (fast) buffer and the high-affinity (slow) buffer, and on the speed of the high-affinity buffer. The positive/negative peak ratio, however, also depends on the slower components of the current and it is expected that the protocol will be less effective when this negative component is small, like in the case of the third scenario in Fig. 4(A). By using a simple model with 1 mM of a low-affinity buffer (K_{ON} = 570 μM^{-1} s^{-1} and K_D = 10 μM) and a high-affinity buffer of K_D = 0.2 with K_{ON} = varying from 100 to 570 μM^{-1} s^{-1} and concentration varying from 0 to 500 μM, the two variables can be determined by matching the ratio between the positive and the negative peak of the $\Delta F/F_0$ time derivative and the slower decay phases of the signal obtained experimentally and by computer simulation. If the experimental ratio is still larger than that obtained by computer simulation, the concentration of the low-affinity buffer is decreased until a match is obtained. Once the "optimal" simple model is obtained in *STEP* 2, the current input is optimised by adding three additional Gaussian components to optimise the match between the experimental and the expected $\Delta F/F_0$ signal in *STEP* 3. At this stage, the parameter of the model can be refined, with corrections of up to ~20% from their original values, to optimise the curve. The optimisation process can go on to maximally increase the mean magnitude squared coherence and it is considered satisfactory if the similarity between the $\Delta F/F_0$ signal and the optimised curve, quantified by the $\Gamma_{\Delta F/F0}$ averaged over the range 0–1 kHz, is >0.96 (see Section 2 for details).

The results of applying this semi-automatic protocol to the three scenarios of Fig. 4(A) are shown in (B–C). In Fig. 4(B), the expected $\Delta F/F_0$ signal and its time derivative, produced by a single fast Gaussian input (*STEP* 1) with the "optimal" simple parameters of the model (*STEP* 2), are plotted and superimposed to the corresponding traces of the real $\Delta F/F_0$ signal. Remarkably, but as expected from the previous observations, the $\Delta F/F_0$ time derivatives are similar despite the signals are substantially different. In Fig. 4(C), the expected $\Delta F/F_0$ signal and its time derivative, produced after correcting the input with three additional Gaussian components (*STEP 3*), are again plotted and superimposed to the corresponding traces of the real $\Delta F/F_0$ signal. This correction, performed to improve the similarity between the experimental and simulated signals, increased the mean $\Gamma_{\Delta F/F0}$ at 0–1 kHz from ~0.9 to >0.98 in all three cases as shown in Fig. 4(D). In all three scenarios, a slower current component was necessary to match the experimental $\Delta F/F_0$ signal. In the first two scenarios, where the $\Delta F/F_0$ time derivative negative component is large, the slow component of the current obtained with the protocol was only ~20% larger and delayed by a few hundred microseconds with respect to the real one.

The current obtained by applying our protocol is not a faithful reproduction of the real current, but can be considered a satisfactory estimate of its kinetics. The protocol performs better in the first two scenarios where the fast negative component of the $\Delta F/F_0$ time derivative is less dependent on the slower component of the current. Thus, the Gaussian function that matches the rising phase of the time derivative allowed the determination of the optimal model parameters since the negative component of the $\Delta F/F_0$ time derivative depended only weakly on the slower current component. In contrast, in the third scenario, the smaller negative component of the $\Delta F/F_0$ time derivative depended more strongly on the slow component of the current affecting the determination of the model parameters from the fast component of the current. In the previous method applicable to CA1 hippocampal pyramidal neurons, it was convenient to oversample signals at 20 kHz and then applying a smoothing algorithm to reduce the noise and to obtain a faithful calculation of the time derivative (Jaafari et al., 2014). Here, where the initial estimate of the time derivative is based on the fit of the rising phase with a Gaussian function, applying a filter is less critical and recordings can be done at 5 kHz increasing the number of points sampled. We can, in this way, extrapolate a realistic kinetic curve for the Ca^{2+} current where the fidelity in reproducing the real current depends on how large and fast the negative component of the $\Delta F/F_0$ time derivative is. The proper assessment of this new method required the validation through biological experiments presented in the next two paragraphs.

3.3. Experimental validation of the protocol in CA1 hippocampal pyramidal neurons

The dendrites of CA1 hippocampal pyramidal neurons do not have any slow endogenous buffer that significantly affects the fast OG5N-$\Delta F/F_0$ kinetics (Jaafari et al., 2014). Therefore, as shown in the example cell of Fig. 5(A), the OG5N-$\Delta F/F_0$ signal associated with an action potential (Fig. 5(B), top trace) had slope equal to zero after the end of its rising phase (Fig. 5(B), middle trace). When applying *STEP* 2 of our protocol to this signal, the optimal concentration of the slow buffer was obviously zero and the multivariate Gaussian function optimised on the OG5N-$\Delta F/F_0$ signal matched the OG5N-$\Delta F/F_0$ time derivative (Fig. 5(B), bottom traces). If we add to the internal solution 400 μM Fura-2, i.e. an exogenous buffer of known kinetics (K_{ON} = 570 μM^{-1} s^{-1} as in Canepari and Mammano, 1999 and K_D = 0.24 μM at 33 °C as in Shuttleworth and Thompson, 1991), the OG5N-$\Delta F/F_0$ signal is artificially changed by the slower binding to Fura-2 that can be directly measured since this indicator is excited at a different wavelength (385 nm) with respect to OG5N (470 nm). Therefore, the match of the Fura-$\Delta F/F_0$ signal with the time course of the slow buffer in the model can be used to validate the protocol as predictor of the real current. In the cell of Fig. 5(C), filled with 400 μM Fura-2, the OG5N-$\Delta F/F_0$ signal associated with an action potential (Fig. 5(D), top two traces) had negative slope (Fig. 5(D), third trace from the top). The OG5N-$\Delta F/F_0$ signal and its time derivative were used to set the optimal parameters in the model and the current that matched the experimental traces (Fig. 5(D), fourth trace from the top), as described in the previous paragraph. As expected, the optimal concentration of the slow buffer was ~400 μM, i.e. the concentration of Fura-2 in the pipette. The time course of the bound slow buffer from the computer sim-

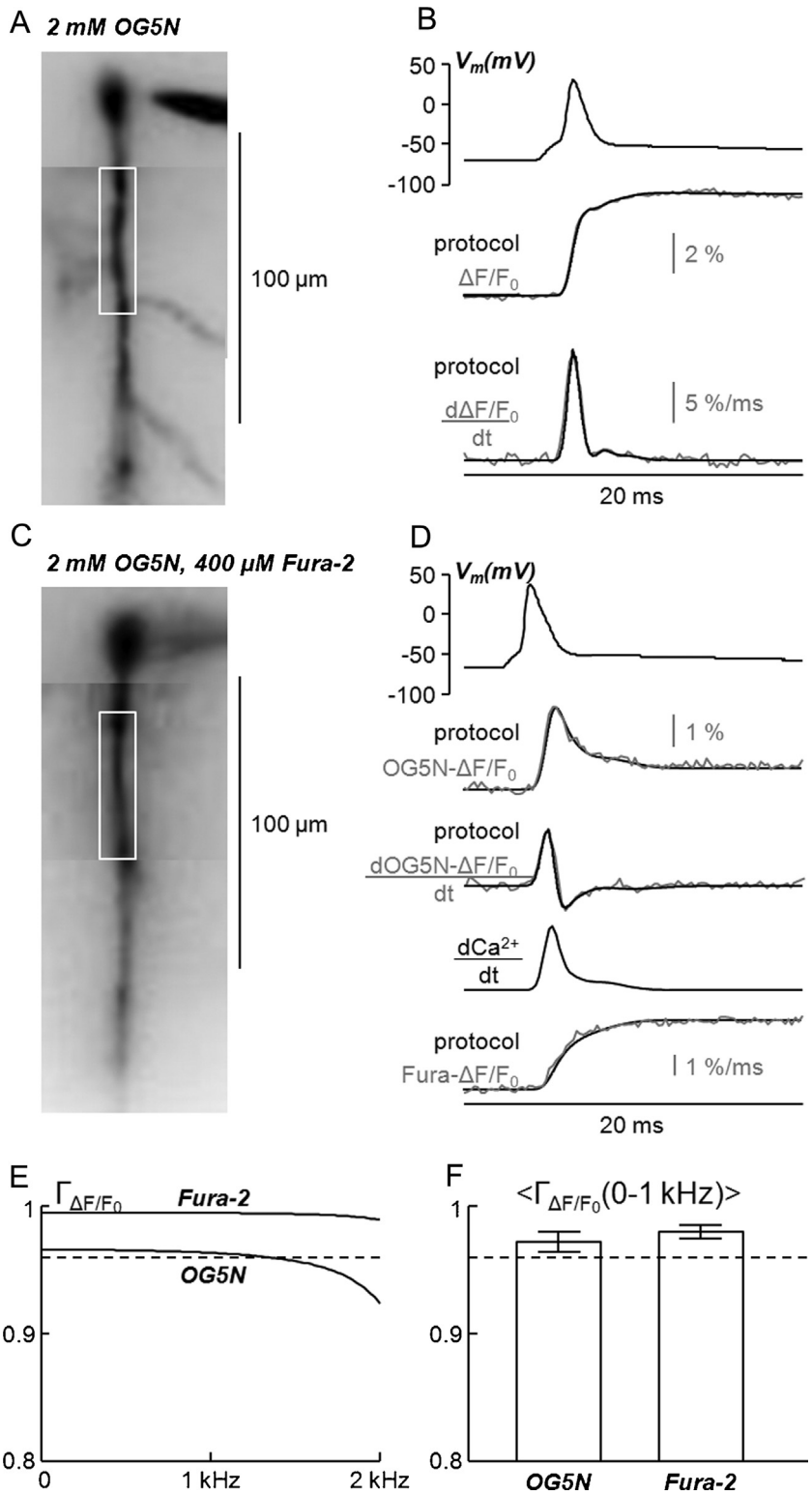

Fig. 5. Validation of the protocol in CA1 hippocampal pyramidal neurons. (A) CA1 hippocampal pyramidal neuron filled with 2 mM OG5N with a region of interest indicated. (B) Top trace: action potential. Middle traces: associated OG5N-$\Delta F/F_0$ signal; grey trace is the experiment; black trace is the optimal curve from computer simulation. Bottom traces: the extracted Ca^{2+} current kinetics leading to the optimal curves (black trace) superimposed to the OG5N-$\Delta F/F_0$ time derivative (grey trace). (C) CA1 hippocampal pyramidal neuron filled with 2 mM OG5N and 400 µM Fura-2 with a region of interest indicated. (D) From the top, 1st trace: action potential. From the top, 2nd and 3rd traces: associated OG5N-$\Delta F/F_0$ signal and its time derivative in the region of interest; grey traces are the experiments; black traces are the optimal curves from computer simulation. From the top, 4th trace: the extracted Ca^{2+} current kinetics leading to the optimal curves. From the top, 5th traces: the associated Fura-$\Delta F/F_0$ signal in the region of interest; grey trace is the experiment; black trace is the curve from computer simulation. (C) $\Gamma_{\Delta F/F0}$ calculated for both the OG5N-$\Delta F/F_0$ signal and the Fura-$\Delta F/F_0$ signal reported in panel B. (D) Mean ± SD of the mean $\Gamma_{\Delta F/F0}$ ($<\Gamma_{\Delta F/F0}>$) averaged over 0–1 kHz from five cells for OG5N-$\Delta F/F_0$ signals and Fura-$\Delta F/F_0$ signals. In C and D, the dotted lines indicate the 0.96 minimal value of $<\Gamma_{\Delta F/F0}>$ for the experimental and simulated curves to be similar. All data were from averages of 16 trials.

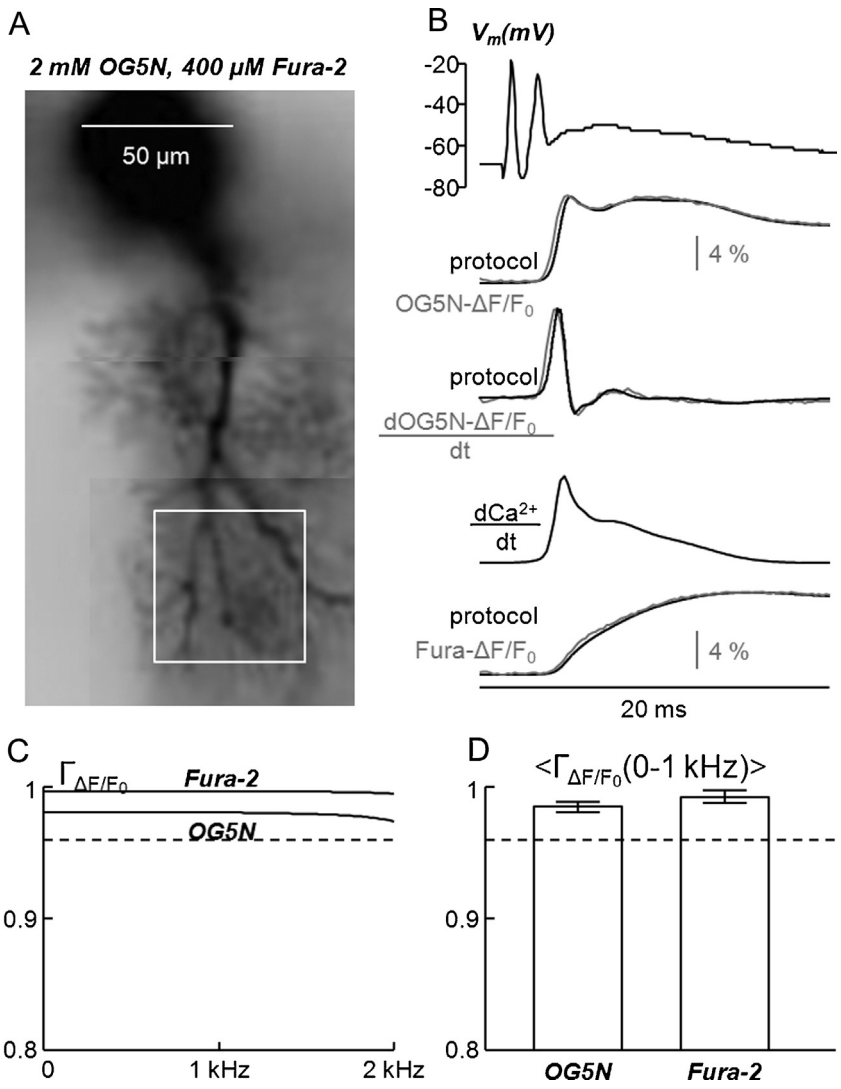

Fig. 6. Validation of the protocol in PNs. (A) PN filled with 2 mM OG5N and 400 µM Fura-2 with a dendritic region of interest indicated. (B) From the top, 1st trace: climbing fibre EPSP. From the top, 2nd and 3rd traces: the associated OG5N-$\Delta F/F_0$ signal and its time derivative in the region of interest; grey traces are the experiments; black traces are the optimal curves from computer simulation. From the top, 4th trace: the extracted Ca^{2+} current kinetics leading to the optimal curves. From the top, 5th traces: the associated Fura-$\Delta F/F_0$ signal in the region of interest; grey trace is the experiment; black trace is the curve from computer simulation. (C) $\Gamma_{\Delta F/F0}$ calculated for both the OG5N-$\Delta F/F_0$ signal and the Fura-$\Delta F/F_0$ signal reported in panel B. (D) Mean ± SD of $<\Gamma_{\Delta F/F0}>$ from six cells for OG5N-$\Delta F/F_0$ signals and Fura-$\Delta F/F_0$ signals. In C and D, the dotted lines indicate the 0.96 minimal value of $<\Gamma_{\Delta F/F0}>$ for the experimental and simulated curves to be similar. All data were from averages of 9 trials.

ulation was then superimposed to the measured Fura-$\Delta F/F_0$ signal (Fig. 5(D), bottom traces). The two curves had the same kinetics. In this particular cell, the mean $\Gamma_{\Delta F/F0}$ at 0–1 kHz ($<\Gamma_{\Delta F/F0}>$) was 0.97 for the OG5N-$\Delta F/F_0$ signal and >0.98 for the Fura-$\Delta F/F_0$ signal (Fig. 5(E)). The same experiment was performed in five cells altogether, always obtaining a satisfactory similarity between the experimental and the simulated curve for both indicators. Hence, in $N = 5$ cells, $<\Gamma_{\Delta F/F0}>$ was 0.972 ± 0.008 for OG5N and 0.990 ± 0.005 for Fura-2 (Fig. 5(F)). The experimental validation of the method in CA1 hippocampal pyramidal neurons was meaningful since, in this cell, the slow buffering was artificially caused by a single relatively simple buffer (Fura-2) with known characteristics. The fact that CA1 hippocampal pyramidal neurons have negligible slow buffers may however explain why the protocol was efficient in finding a Ca^{2+} current producing signals that matched the $\Delta F/F_0$ signal of both indicators. Next, we report the same type of experimental validation in PNs where slow buffering is naturally produced by multiple proteins with more complex kinetics.

3.4. Experimental validation of the protocol in cerebellar Purkinje neurons

In contrast to CA1 hippocampal pyramidal neurons, the negative slope of OG5N-$\Delta F/F_0$ signals is due to complex binding to several proteins that cannot be directly monitored. Nevertheless, Fura-2 can be added to the internal solution and its binding to Ca^{2+} can be monitored to assess whether our protocol finds a current for which a satisfactory match between the experimental $\Delta F/F_0$ signals and the simulated curves can be found. This experiment would provide a validation that the method works also in more complex experimental scenarios. The cell of Fig. 6(A) was filled with 400 µM Fura-2 and 2 mM OG5N. In this set of analysis, the model included Fura-2 as fixed buffer at concentration of 400 µM, $K_{ON} = 570\ \mu M^{-1}\ s^{-1}$ and $K_D = 0.24\ \mu M$. The optimisation of the parameters of the endogenous buffer (*STEP* 2) was performed exclusively on the OG5N-$\Delta F/F_0$ signal and its time derivative, as in the previous cases. The fast Ca^{2+} transient was associated with an evoked climbing fibre EPSP (Fig. 6(B), top trace). The time course of the OG5N-$\Delta F/F_0$ signal was biphasic (Fig. 6(B), second traces from the top), but the time

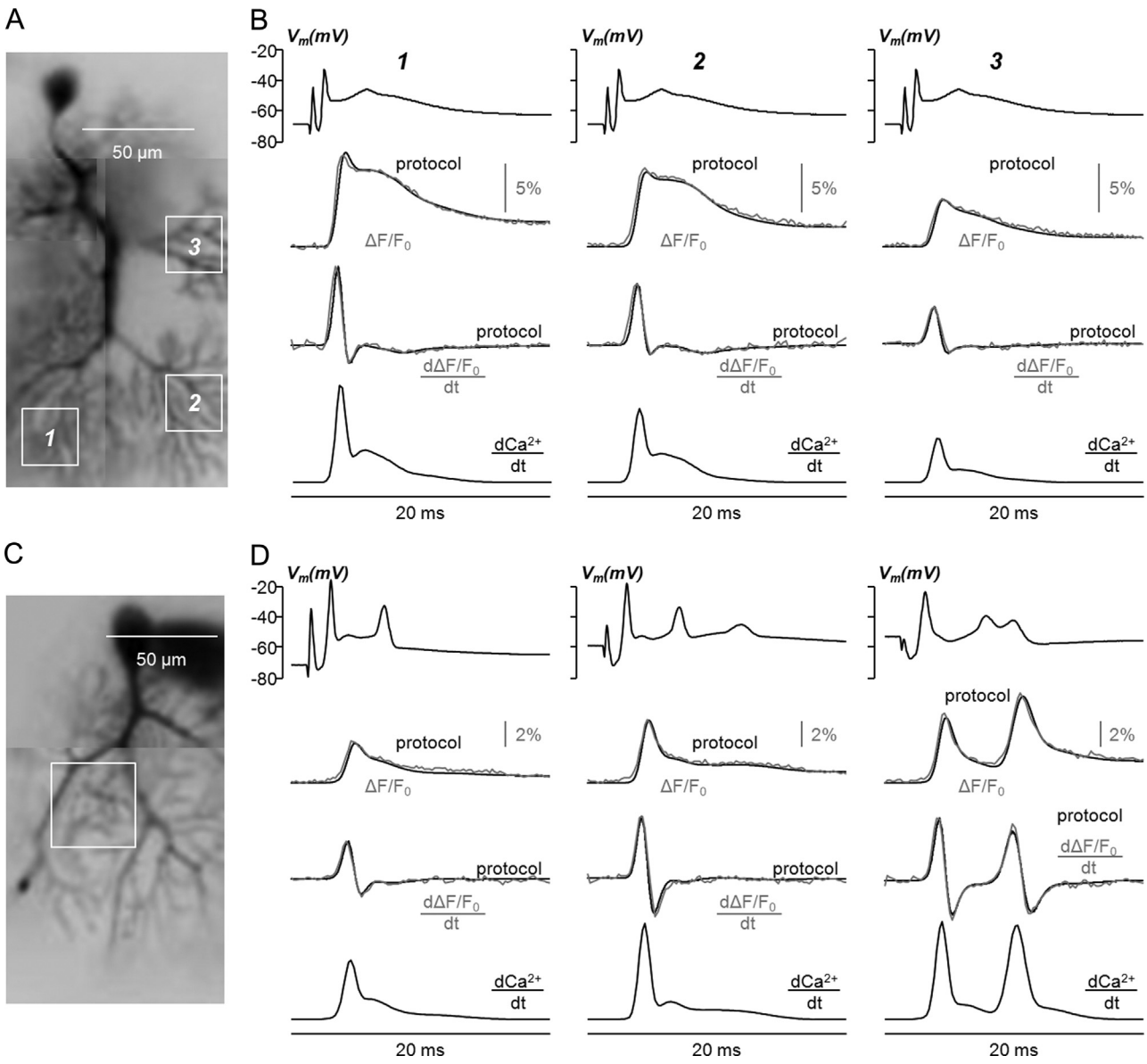

Fig. 7. Examples of extraction of Ca^{2+} current kinetics in PNs. (A) PN filled with 2 mM OG5N and three numbered regions of interest indicated. (B) Top traces: a climbing fibre EPSP. Middle traces: the associated OG5N-$\Delta F/F_0$ signals and the time derivatives in the three regions of interest; grey traces are the experimental data; black traces are the optimal curves from computer simulation. Bottom traces: the extracted Ca^{2+} current kinetics leading to the above optimal curves. (C) Another PN filled with 2 mM OG5N and one dendritic region of interest indicated. (D) Top traces: climbing fibre EPSPs at different initial membrane potential. Middle traces: the associated OG5N-$\Delta F/F_0$ signals and the time derivatives in the region of interest; grey traces are the experimental data; black traces are the optimal curves from computer simulation. Bottom traces: the extracted Ca^{2+} current kinetics leading to the above optimal curves. All data were from averages of 4 trials.

Table 2
Values of the model parameters obtained by analysing OG5N-$\Delta F/F_0$ signals associated with climbing fibre EPSPs in six cells. The first two cells are those of Fig. 7.

	Conc. fast buffer (µM) K_{ON} = 570 µM^{-1} s^{-1} K_D = 10 µM	Conc. slow buffer (µM) K_D = 0.2 µM	K_{ON} slow buffer (µM^{-1} s^{-1})	$<\Gamma_{\Delta F/F0}>$
Cell 1	400	400	230	0.987
Cell 2	180	490	300	0.975
Cell 3	680	400	280	0.992
Cell 4	290	350	210	0.988
Cell 5	300	500	260	0.974
Cell 6	500	430	200	0.994

derivative had still a fast negative peak (Fig. 6(B), third traces from the top). The experimental traces were matched by the curves obtained with the protocol where the input current had a fast and a slow distinct component (Fig. 6(B), fourth trace from the top). Remarkably, the kinetics of the expected Ca^{2+} bound to Fura-2 matches, as in the case of CA1 hippocampal pyramidal neurons, the time course of the Fura-$\Delta F/F_0$ signal (Fig. 6(B), bottom traces). In this particular cell, $<\Gamma_{\Delta F/F0}>$ was 0.98 for the OG5N-$\Delta F/F_0$ signal and >0.99 for the Fura-$\Delta F/F_0$ signal (Fig. 6(C)). The same experiment was performed in six cells altogether, always obtaining an excellent

match between the experimental and the simulated curve for both indicators. In $N = 6$ cells, $<\Gamma_{\Delta F/F0}>$ was 0.985 ± 0.004 for OG5N and 0.993 ± 0.005 for Fura-2 (Fig. 6(D)). We concluded that our protocol is also capable of reproducing the time course of both OG5N-$\Delta F/F_0$ and Fura-$\Delta F/F_0$ signals in PNs, suggesting that the generating Ca^{2+} current input is kinetically a realistic approximation of the real current associated with the climbing fibre EPSP.

3.5. Measurement of Ca^{2+} current kinetics in cerebellar Purkinje neurons

In the previous paragraphs, our novel method to extract the Ca^{2+} current kinetics from OG5N-$\Delta F/F_0$ signals was first assessed using simulated artificial scenarios and then validated in CA1 hippocampal pyramidal neurons and PNs using combined fluorescence measurements of the added exogenous buffer Fura-2. In this last paragraph of the Results, we eventually report the first measurements of physiological Ca^{2+} currents associated with climbing fibre EPSPs in PNs using our new protocol. In the cell of Fig. 7(A), filled with 2 mM OG5N (and no Fura-2), we analysed the $\Delta F/F_0$ signals associated with a climbing fibre EPSP (Fig. 7(B), top traces) in three sample regions indicated on the image. As in all previous cases, in all the three regions the protocol was capable to find realistic currents (Fig. 7(B), bottom traces) that produced optimal curves matching the $\Delta F/F_0$ signal and its time derivative (Fig. 7(B), middle traces). Notably, although the $\Delta F/F_0$ signals were quite different in the three regions, the optimal match was found using the same parameters of the model, while only the current changed from a region to another. In this experiment, $<\Gamma_{\Delta F/F0}>$ was >0.98 in all three regions. In the cell of Fig. 7(C), we analysed the $\Delta F/F_0$ signals associated with climbing fibre EPSPs elicited at different initial membrane potential (Fig. 7(D), top traces) in a larger region. Interestingly, the $\Delta F/F_0$ signal increased at increasing initial membrane potential and exhibited two peaks for the less negative initial membrane potential (Fig. 7(D), middle traces). The protocol was capable to find realistic currents (Fig. 7(D), bottom traces) for the three different cases using, again, only one set of parameters. In this experiment, $<\Gamma_{\Delta F/F0}>$ was >0.97 in all three cases. We performed this analysis in six cells altogether, either focussing different dendritic regions or on climbing fibre EPSPs elicited at different initial membrane potentials. The values of the optimal model parameters found in each cell, as well as the averaged $<\Gamma_{\Delta F/F0}>$ values (always >0.97), are reported in Table 2. From these values, it is possible to estimate the buffer capacity as the summation of the fast and slow buffer concentrations divided by their respective K_Ds. In this group of six cells, this was 2181 ± 282, in agreement with the mean value of 2129 reported by Fierro and Llano in PNs from rats older than 15 days (Fierro and Llano, 1996). Thus, we concluded that the parameters of the model leading to the extraction of the optimal Ca^{2+} current kinetics are consistent with the measured buffer capacity of this cell type.

4. Discussion

In this article, we presented a novel strategy to extrapolate the kinetics of Ca^{2+} currents from fluorescence Ca^{2+} measurements using OG5N, or other low-affinity indicators, in cases where the method based on the simple calculation of the time derivative fails. A low-affinity Ca^{2+} indicator, which equilibrates in less than 200 μs, has the intrinsic ability of tracking fast neuronal Ca^{2+} currents. In many cases, the time course of the Ca^{2+} current is matched by the time derivative of the fractional change of fluorescence (Sabatini and Regehr, 1998; Jaafari et al., 2014). This method fails when Ca^{2+} unbinds from the indicator over a time scale that is longer than the current duration, but sufficiently short to distort the estimate of Ca^{2+} influx dynamics by fluorescence measurement. In other words, this method fails when the $\Delta F/F_0$ signal decays rapidly generating a negative component in its time derivative.

The Ca^{2+} sequestration responsible for the rapid decay of the $\Delta F/F_0$ signal is due, in reality, to what we define "slow buffer", where slow is referred to the faster buffer equilibrating over a time scale shorter than the current duration and similar to the equilibration time of low-affinity indicators. In cells, slow buffers typically correspond to calcium binding proteins such as Calmodulin (Faas et al., 2011), Calretinin (Faas et al., 2007), Parvalbumin (Lee et al., 2000) and Calbindin (Nägerl et al., 2000). In the case of PNs, the fast decay time of the OG5N-$\Delta F/F_0$ signal, preventing the measurement of the Ca^{2+} current, is due to Calbindin-D28k (Airaksinen et al., 1997) and Parvalbumin (Schmidt et al., 2003). Modelling the kinetics of a Ca^{2+} transient is a complex task since Calbindin-D28k and Parvalbumin have multiple binding sites with different kinetic parameters (Schmidt and Eilers, 2009; Canepari and Vogt, 2008) and the diffusion of these Ca^{2+} binding proteins also plays an important role (Schmidt et al., 2012). Thus, the extraction of the precise Ca^{2+} current kinetics is limited by the absence of detailed information on slow buffering that is different from cell to cell and, in general, from site to site in the same cell. While the effect of diffusion can be neglected in recordings from relatively large dendritic portions, like in this case, our method is based on a simplified model with only one slow buffer and three free parameters. Reducing the degrees of freedom to three allowed the development of a semi-automatic protocol in which the optimisation of the model parameters and of the current kinetics, leading to the fit of the OG5N-$\Delta F/F_0$ signal, is done in two distinct steps. The condition permitting the separation between the model parameters setting and the current reconstruction is that the fast rising phase of the current can be reliably approximated with the time derivative of the OG5N-$\Delta F/F_0$ signal. The consistency of the curve obtained with this protocol in reproducing the kinetics of the real buffering depends on the characteristics of the buffer and of the current. In the cases of the first two simulations in Fig. 4, or in the case of PNs (Fig. 7), the model parameters can be reliably obtained from the fast current component (i.e. the initial OG5N-$\Delta F/F_0$ time derivative) and the method extracts a curve that approaches the kinetics of the Ca^{2+} current, also for the slower components. In the putative case of a buffer with intermediate behaviour between a "fast" and a "slow" buffer, (see the third simulation in Fig. 4), the analysis of the time course of the OG5N-$\Delta F/F_0$ signal is more complicated and may lead to unreliable determination of the model parameter and a more distorted estimation of the current kinetics. This observation points out the limits of this method, which, in contrast to the straightforward time derivative method, can only produce an estimate and not a direct measurement of the Ca^{2+} current kinetics. Yet, the information extracted by this curve is very important. The extrapolation of diverse current components may be associated to the activation and de-activation of different types of HVA-VGCCs and LVA-VGCCs (see as an example Jaafari and Canepari, 2016). In the dendrites of PNs, for instance, the fast and the slow component of the Ca^{2+} current associated with a climbing fibre EPSP (Fig. 7) are likely associated with the activation of P/Q-type VGCCs (Usowicz et al., 1992) and T-type Ca^{2+} channels (Isope et al., 2012). Thus, the extrapolation of a curve that approaches the kinetics of the Ca^{2+} current can be used to quantitatively investigate the variability of channels activation at different dendritic sites, the modulation of channel activation due to physiological activity or to pharmacological action or the variability in channel activation in different animals (for instance during development).

The ability to perform the measurement of fast Ca^{2+} currents relies on the recent availability of cameras capable of acquiring frames, at relatively high spatial resolution and sensitivity, in the

kHz range (Davies et al., 2013). If the $\Delta F/F_0$ signal is recorded for a longer period (>200 ms), its kinetics is dominated, over this time scale, by a slower decay time due to Ca^{2+} extrusion (see for instance Majewska et al., 2000). We included Ca^{2+} extrusion in our model with simple Michaelis–Menten kinetics. As shown in Fig. 3, Ca^{2+} extrusion does not affect the OG5N-$\Delta F/F_0$ time derivative associated with a fast Ca^{2+} transient. We can however imagine measuring $\Delta F/F_0$ signals associated with currents with a duration that is longer than the equilibration time of the slow buffer. In this case, this buffer behaves as a fast buffer, but there will be a negative component of the $\Delta F/F_0$ time derivative due to Ca^{2+} extrusion. Under this condition, the method presented in this article can be modified by considering only one "fast" buffer and by optimising the parameters of Ca^{2+} extrusion on the $\Delta F/F_0$ signal to extrapolate the Ca^{2+} current. Thus, the approach we developed can be considered a generalised method to estimate the full kinetics of all types of physiological Ca^{2+} currents.

Conflict of interest

The authors have no conflict of interest to disclose.

Author contributions

K.A.-O., N.J. and M.C. performed the experiments. M.C. designed the study, developed the method, analysed the data and wrote the paper.

Acknowledgements

This work was supported by the *Agence Nationale de la Recherche* through three grants: (1) Grant *WaveFrontImag*, program number ANR-14-CE17-0006-01; (2) Labex *Ion Channels Science and Therapeutics*, program number ANR-11-LABX-0015; (3) National Infrastructure France Life Imaging "Noeud Grenoblois"; and by the *Federation pour la Recherche sur le Cerveau* (FRC) through the grant *Espoir en tête* (in partnership with Rotary France). We thank Joseph Gallagher and Bertrand Fourcade for reading the manuscript before submission.

References

Airaksinen, M.S., Eilers, J., Garaschuk, O., Thoenen, H., Konnerth, A., Meyer, M., 1997. Ataxia and altered dendritic calcium signalling in mice carrying a targeted nullmutation of the calbindin D_{28k} gene. Proc. Natl. Acad. Sci. U. S. A. 94, 1488–1493.

Canepari, M., Mammano, F., 1999. Imaging neuronal calcium fluorescence at high spatio-temporal resolution. J. Neurosci. Methods 87, 1–11.

Canepari, M., Odgen, D., 2006. Kinetic pharmacological and activity-dependent separation of two Ca^{2+} signalling pathways mediated by type 1 metabotropic glutamate receptors in rat Purkinje neurons. J. Physiol. 573, 65–82.

Canepari, M., Vogt, K.E., 2008. Dendritic spike saturation of endogenous calcium buffer and induction of postsynaptic cerebellar LTP. PLoS One 3, e4011.

Canepari, M., Vogt, K., Zecevic, D., 2008. Combining voltage and calcium imaging from neuronal dendrites. Cell. Mol. Neurobiol. 58, 1079–1093.

Canepari, M., Willadt, S., Zecevic, D., Vogt, K.E., 2010. Imaging inhibitory synaptic potentials using voltage sensitive dyes. Biophys. J., 2032–2040.

Davies, R., Graham, J., Canepari, M., 2013. Light sources and cameras for standard in vitro membrane potential and high-speed ion imaging. J. Microsc. 251, 5–13.

Faas, G.C., Mody, I., 2012. Measuring the kinetics of calcium binding proteins with flash photolysis. Biochim. Biophys. Acta 1820, 1195–1204.

Faas, G.C., Schwaller, B., Vergara, J.L., Mody, I., 2007. Resolving the fast kinetics of cooperative binding: Ca^{2+} buffering by calretinin. PLoS Biol. 5, e311.

Faas, G.C., Raghavachari, S., Lisman, J.E., Mody, I., 2011. Calmodulin as a direct detector of Ca^{2+} signals. Nat. Neurosci. 14, 301–304.

Fierro, L., Llano, I., 1996. High endogenous calcium buffering in Purkinje cells from rat cerebellar slices. J. Physiol. 496, 617–625.

Helmchen, F., Imoto, K., Sakmann, B., 1996. Ca^{2+} buffering and action potential-evoked Ca^{2+} signaling in dendrites of pyramidal neurons. Biophys. J. 70, 1069–1081.

Isope, P., Hildebrand, M.E., Snutch, T.P., 2012. Contributions of T-type voltage-gated calcium channels to postsynaptic calcium signaling within Purkinje neurons. Cerebellum 11, 651–665.

Jaafari, N., Canepari, M., 2016. Functional coupling of diverse voltage-gated Ca(2+) channels underlies high fidelity of fast dendritic Ca(2+) signals during burst firing. J. Physiol. 549, 967–983.

Jaafari, N., De Waard, M., Canepari, M., 2014. Imaging fast calcium currents beyond the limitations of electrode techniques. Biophys. J. 107, 1280–1288.

Jaafari, N., Marret, E., Canepari, M., 2015. Using simultaneous voltage and calcium imaging to study fast Ca^{2+} channels. Neurophotonics 2, 021010.

Kao, J.P., Tsien, R.Y., 1988. Ca^{2+} binding kinetics of fura-2 and azo-1 from temperature-jump relaxation measurements. Biophys. J. 53, 635–639.

Lee, S.H., Schwaller, B., Neher, E., 2000. Kinetics of Ca^{2+} binding to parvalbumin in bovine chromaffin cells: implications for $[Ca^{2+}]$ transients of neuronal dendrites. J. Physiol. 525, 419–432.

Majewska, A., Brown, E., Ross, J., Yuste, R., 2000. Mechanisms of calcium decay kinetics in hippocampal spines: role of spine calcium pumps and calcium diffusion through the spine neck in biochemical compartmentalization. J. Neurosci. 20, 1722–1734.

Maravall, M., Mainen, Z.F., Sabatini, B.L., Svoboda, K., 2000. Estimating intracellular calcium concentrations and buffering without wavelength ratioing. Biophys. J. 78, 2655–2667.

Miyakawa, H., Lev-Ram, V., Lasser-Ross, N., Ross, W.N., 1992. Calcium transients evoked by climbing fiber and parallel fiber synaptic inputs in guinea pig cerebellar Purkinje neurons. J. Neurophysiol. 68, 1178–1189.

Nägerl, U.V., Novo, D., Mody, I., Vergara, J.L., 2000. Binding kinetics of calbindin-D(28k) determined by flash photolysis of caged Ca(2+). Biophys. J. 79, 3009–3018.

Nowycky, M.C., Pinter, M.J., 1993. Time courses of calcium and calcium-bound buffers following calcium influx in a model cell. Biophys. J. 64, 77–91.

Oppenheim, A.V., Schafer, R.W., 1999. Discrete-Time Signal Processing. Prentice-Hall, Upper Saddle River, NJ.

Pethig, R., Kuhn, M., Payne, R., Adler, E., Chen, T.H., Jaffe, L.F., 1989. On the dissociation constants of BAPTA-type calcium buffers. Cell Calcium 10, 491–498.

Sabatini, B.L., Regehr, W.G., 1998. Optical measurement of presynaptic calcium currents. Biophys. J. 74, 1549–1563.

Schmidt, H., Eilers, J., 2009. Spine neck geometry determines spino-dendritic cross-talk in the presence of mobile endogenous calcium binding proteins. J. Comput. Neurosci. 27, 229–243.

Schmidt, H., Stiefel, K.M., Racay, P., Schwaller, B., Eilers, J., 2003. Mutational analysis of dendritic Ca^{2+} kinetics in rodent Purkinje cells: role of parvalbumin and calbindin D_{28k}. J. Physiol. 551, 13–32.

Schmidt, H., Arendt, O., Eilers, J., 2012. Diffusion and extrusion shape standing calcium gradients during ongoing parallel fiber activity in dendrites of Purkinje neurons. Cerebellum 11, 694–705.

Shuttleworth, T.J., Thompson, J.L., 1991. Effect of temperature on receptor-activated changes in $[Ca^{2+}]i$ and their determination using fluorescent probes. J. Biol. Chem. 266, 1410–1414.

Usowicz, M.M., Sugimori, M., Cherksey, B., Llinás, R., 1992. P-type calcium channels in the somata and dendrites of adult cerebellar Purkinje cells. Neuron 9, 1185–1199.

Vogt, K.E., Gerharz, S., Graham, J., Canepari, M., 2011a. High-resolution simultaneous voltage and Ca^{2+} imaging. J. Physiol. 589, 489–494.

Vogt, K.E., Gerharz, S., Graham, J., Canepari, M., 2011b. Combining membrane potential imaging with L-glutamate or GABA photorelease. PLoS One 6, e24911.

Welch, P.D., 1967. The use of fast Fourier transform for the estimation of power spectra: a method based on time averaging over short, modified periodograms. IEEE Trans. Audio Electroacoust. AU-15, 70–73.

Received: 29 July 2017 | Accepted: 13 November 2017

DOI: 10.1002/jbio.201700197

Journal of BIOPHOTONICS

FULL ARTICLE

A novel multisite confocal system for rapid Ca^{2+} imaging from submicron structures in brain slices

Luiza Filipis[1,2] | Karima Ait Ouares[1,2] | Philippe Moreau[1] | Dimitrii Tanese[3] | Valeria Zampini[3] | Andrea Latini[4] | Chun Bleau[5] | Charlie Bleau[6] | Jeremy Graham[7] | Marco Canepari[1,2,8*]

[1]Laboratory for Interdisciplinary Physics, UMR 5588 CNRS and Université Grenoble Alpes, Saint Martin d'Hères Cedex, France

[2]Laboratories of Excellence, Ion Channel Science and Therapeutics, France

[3]Wavefront-Engineering Microscopy Group, Neurophotonics Laboratory, UMR8250 CNRS and Paris Descartes University, Paris, France

[4]CrestOptics Spa, Rome, Italy

[5]RedshirtImaging LLC, Decatur, Georgia

[6]SciMeasure Analytical Systems Inc, Decatur, Georgia

[7]Cairn Research Ltd, Faversham, UK

[8]Institut National de la Santé et Recherche Médicale (INSERM), France

***Correspondence**
Marco Canepari, Laboratory for Interdisciplinary Physics, UMR 5588 CNRS and Université Grenoble Alpes, 38402 Saint Martin d'Hères Cedex, France.
Email: marco.canepari@univ-grenoble-alpes.fr

Funding information
Agence Nationale de la Recherche, Grant/Award numbers: ANR-14-CE17-0006-01, ANR-11-LABX-0015; Federation pour la Recherche sur le Cerveau, Grant/Award number: Espoir en tete

In brain slices, resolving fast Ca^{2+} fluorescence signals from submicron structures is typically achieved using 2-photon or confocal scanning microscopy, an approach that limits the number of scanned points. The novel multiplexing confocal system presented here overcomes this limitation. This system is based on a fast spinning disk, a multimode diode laser and a novel high-resolution CMOS camera. The spinning disk, running at 20 000 rpm, has custom-designed spiral pattern that maximises light collection, while rejecting out-of-focus fluorescence to resolve signals from small neuronal compartments. Using a 60× objective, the camera permits acquisitions of tens of thousands of pixels at resolutions of ~250 nm per pixel in the kHz range with 14 bits of digital depth. The system can resolve physiological Ca^{2+} transients from submicron structures at 20 to 40 μm below the slice surface, using the low-affinity Ca^{2+} indicator Oregon Green BAPTA-5N. In particular, signals at 0.25 to 1.25 kHz were resolved in single trials, or through averages of a few recordings, from dendritic spines and small parent dendrites in cerebellar Purkinje neurons. Thanks to an unprecedented combination of temporal and spatial resolution with relatively simple implementation, it is expected that this system will be widely adopted for multisite monitoring of Ca^{2+} signals.

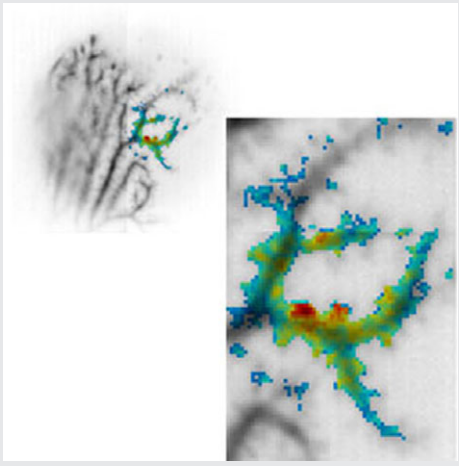

KEYWORDS
brain slices, calcium imaging, confocal microscopy, neurons

1 | INTRODUCTION

Ca^{2+} fluorescence imaging allows the detailed investigation of biochemical processes that are triggered by transient elevation of intracellular Ca^{2+}. In particular, Ca^{2+} transients can be recorded from individual neurons in brain slices to investigate local mechanisms of physiological importance [1]. In these recordings, the number of detected photons necessary to resolve fluorescence changes with adequate signal-to-noise ratio (*S/N*) determines the dimension of emitting sites or the duration of exposure time window [2]. Hence, at a given acquisition rate, the

smallest useful detection element is the one from which the number of emitted photons allows the signal to be above the photon (shot) noise. Detection of fluorescence changes from structures ≤1 μm at temporal resolution of ~ 1 ms is satisfactory for investigating many physiological signals from relevant neuronal compartments in dendrites and axons. In addition, it is also crucial to monitor Ca^{2+} signals from many sites simultaneously. The most straightforward methodology involves uniformly illuminating the whole area of interest and recording Ca^{2+} fluorescence with a fast camera (widefield imaging). In widefield imaging, the lateral resolution limit is theoretically given by $1.22\lambda_{em}$/NA, where NA is the numerical aperture of the objective used and λ_{em} is the fluorescence emission wavelength [3]. Thus, objectives with NA ≥ 1 can ideally resolve signals from structures ≤1 μm at all visible wavelengths. This theoretical resolution limit is however compromised for fluorescence signals originating from structures in brain slices that are tens of microns below the slice surface. In this case, the tissue between the fluorescence-emitting structure and the slice surface scatters light decreasing spatial resolution and preventing the possibility of resolving signals from submicron structures [4]. A way to recover the original spatial resolution is to reject tissue-scattered photons by means of confocal microscopy [5]. Conventional confocal microscopy, performed by scanning a pinhole and recording fluorescence with a photomultiplier, can work at high acquisition rates by limiting the capture to line scans or random access scans [6]. In this approach, however, the exposure time and therefore the number of photons recorded in each point is inversely proportional to the number of scanned points. Thus, the number of photons necessary to provide the adequate *S/N* limits the number of scanned points or the sampling rate. One way to overcome these limitations is to use a spinning disk [7]. A rapidly spinning disk is positioned conjugate with the focal plane in both illumination and detection pathways to scan a series of transparent pinholes over the field of view of a digital camera. This fast parallel-scan approach significantly reduces the instantaneous photon dose required and increases the acquisition rate. Using this approach, several systems were recently implemented for Ca^{2+} imaging in various preparations [7–10]. In this article, we report the design and the assessment of a novel confocal system, based on a spinning disk specifically designed for rapid Ca^{2+} imaging from submicron structures in brain slices. The pinhole array pattern was replaced with a spiral pattern that maximises emitted light detection while preserving the resolution in the order of the diffraction limit (see section 2). The high fluorescence excitation is obtained using a 1.2-W laser coupled to the spinning disk, with light detection at high spatial and temporal resolution achieved using a fast CMOS camera.

2 | MATERIALS AND METHODS

2.1 | Slice preparation, solutions and electrophysiology

Experiments were ethically carried out in accordance with European Directives 2010/63/UE on the care, welfare and treatment of animals. Procedures were reviewed by the ethics committee affiliated to the animal facility of the university (D3842110001). Transversal hippocampal and cerebellar sagittal slices (250-μm thick) were prepared from 21 to 35 postnatal-days-old mice (C57Bl6) following established procedures [11, 12] with a Leica VT1200 (Leica, Wetzlar, Germany) and incubated at 37°C for 1 hour before use. The extracellular solution contained (in mM): 125 NaCl, 26 $NaHCO_3$, 1 $MgSO_4$, 3 KCl, 1 NaH_2PO_4, 2 $CaCl_2$ and 20 glucose, bubbled with 95% O_2 and 5% CO_2. The intracellular solution contained (in mM): 125 $KMeSO_4$, 5 KCl, 8 $MgSO_4$, 5 Na_2-ATP, 0.3 Tris-GTP, 12 Tris-Phosphocreatine, 20 HEPES, adjusted to pH 7.35 with KOH. The Ca^{2+} indicator Oregon Green BAPTA-5N (OG5N, K_D = 35 μM) was added to the internal solution at 2 mM. Patch-clamp recordings were made at 32°C to 34°C using a Multiclamp amplifier 700A (Molecular Devices, Sunnyvale, California) and signals acquired at 20 kHz using a USB-6221 board (National Instruments, Austin, Texas). The measured membrane potential was corrected for junction potential (−11 mV) as previously estimated [13]. In experiments on cerebellar Purkinje neurons (PNs), either climbing fibre (CF) or parallel fibre (PF) excitatory postsynaptic potentials (EPSPs) were elicited by current pulses, of 5 to 20 μA amplitude and 100-μs duration delivered by a pipette. In experiments on CA1 hippocampal pyramidal neurons, action potentials were elicited by 2-ms current pulses through the patch pipette.

2.2 | Detailed description of the confocal system

The system was mounted on a SliceScope microscope (Scientifica, Uckfield, UK) equipped with motorised XY translation stage, PatchStar manipulators and 60× Olympus water immersion objective (NA = 1). The motorised *Z* translation allowed estimation of the depth of the recording plane from the slice surface. The microscope incorporated an OptoLED unit (Cairn Research, Faversham, UK) mounted on the Olympus epifluorescence unit to provide widefield illumination at 470 nm independent of the spinning disk. The system, illustrated in the scheme of Figure 1A, is based on 2 units: (1) the spinning disk unit and (2) the CMOS camera.

2.2.1 | Spinning disk unit

The spinning disk is a customised version of the X-Light, developed by CrestOptics Spa (Rome, Italy). This incorporates a disk which, instead of pinholes, has multiple sets of continuous spirals with the following structure: (1) 36 spirals;

(2) spiral thickness of 90 μm; (3) spiral step of 16.2 mm; (4) spiral-to-spiral radial distance of 450 μm (Figure 1B). The disk was installed in the primary image plane of the microscope. The spiral pattern was projected to the sample to scan the entire field of view 36 times per disk revolution. The modified disk unit was run at 20 000 rpm (333.33 revolution per second). Finally, the spinning disk was automated to move in and out of the light path to enable both confocal and widefield imaging in the same experiment. The spinning disk was coupled to a TriLine LaserBank (Cairn Research) through a Ø550 μm, 0.22NA, SMA-SMA Fiber patch cable (Thorlabs, Newton, New Jersey). The laser head used was a multimode diode 465 nm/1.2 W (Ushio Opto semiconductors, Tokyo, Japan). A custom 25-mm focal length aspheric condenser (Cairn Research) was used at the output of the fibre to generate a concentrated and homogeneous illumination field of ~60 μm at the sample (Figure 1C). The fibre was stressed and vibrated to mix modes to reduce laser speckle and improve homogeneity. Finally, the whole confocal system was tested for optical sectioning performance against widefield illumination using 500-nm fluorescent beads attached to a coverslip (Figure 1D) and taking images at different depths below the focal plane of the bead with steps of 250 nm (comparable to the pixel dimension). In $N = 16$ beads, fluorescence normalised to the value in the focal plane was 0.68 ± 0.09, 0.28 ± 0.09 and 0.10 ± 0.02 at 1, 2 and 3 μm, respectively, in confocal imaging. These values were significantly different from 0.86 ± 0.04, 0.51 ± 0.10 and 0.22 ± 0.12 obtained in widefield imaging ($P < 0.01$, paired t-test), indicating a clear improvement in optical sectioning in confocal imaging.

2.2.2 | CMOS camera

The camera is a DaVinci-2K (SciMeasure, Decatur, Georgia) which uses a low-noise 2 k × 2 k pixel CMOS sensor with traditional readout architecture and true on-chip binning. The flexible sensor and camera design allows low read-noise performance (<2.8e−) using either correlated double sampling (CDS) or non-destructive read (NDR) to subtract the reset voltage. The large pixel size of 15 μm × 15 μm gives a relatively high fill factor and hence a native quantum efficiency of 65% without requiring microlenses. A single 14-bit A/D per readout channel is used to achieve high bit depth without the dual-amplifier stitching required in sCMOS cameras. Sixteen parallel readout channels are implemented to achieve high frame rates without compromising noise. This is the first use of this novel camera in CDS mode for high–speed, live-cell imaging, although an alternative configuration has been used for stochastic super resolution of fixed samples using NDR [14]. Within the present configuration, each pixel is mapped to collect light from a square of ~250 nm side. Data were acquired using Turbo-SM written in C by RedShirtImaging (Decatur, Georgia).

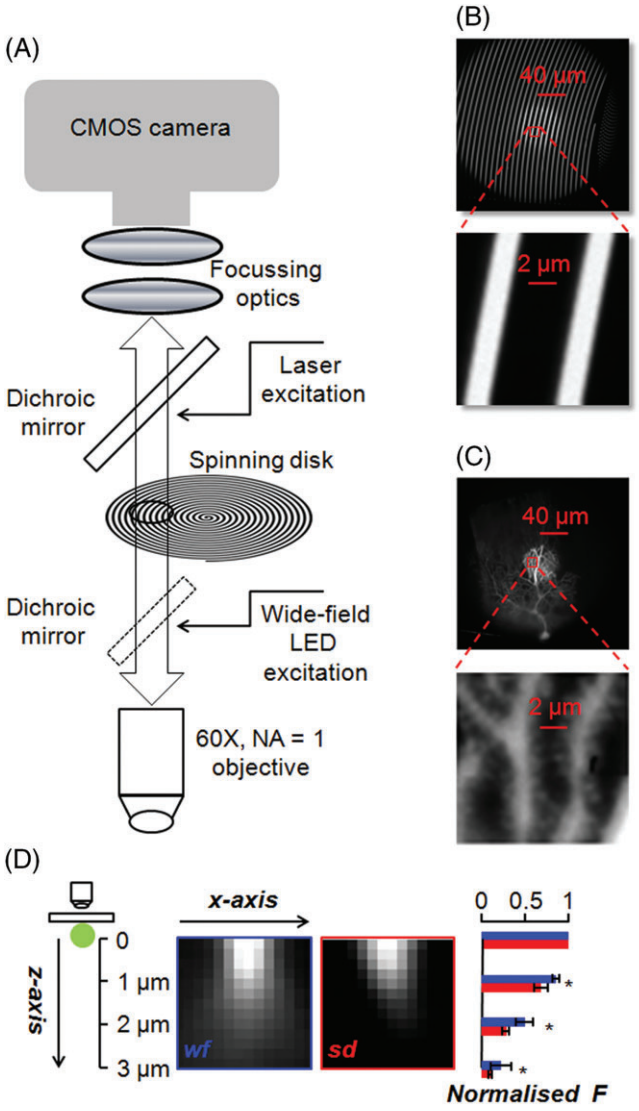

FIGURE 1 Description of the confocal system. (A) Schematic showing a fast (20 000 rpm) spiral pattern spinning disk, coupled to a 465-nm multimode laser and fast CMOS camera. The configuration includes widefield LED illumination at 470 nm independent of the spinning disk. (B) Top: image of the disk obtained using a uniform fluorescence slide with the 60× objective. A frame obtained with whole-field LED illumination is superimposed to a frame with ~60 μm laser spot. Bottom: enlargement of the red square region on the top to appreciate the fine structure of the disk. (C) Top: image of a PN filled with OG5N showing the detailed confocal region acquired with laser and spinning disk superimposed over a full frame taken with widefield LED illumination. Bottom: enlargement of the red square region on the top to appreciate the resolution of dendrites and synaptic spines. (D) A 500-nm fluorescent bead attached to a coverslip is imaged at different depths with 250-nm steps from its focal plane in widefield (*wf*) or with the spinning disk (*sd*); the 2 images are in the *xz* plane; on the right the mean ± SD from $N = 16$ beads of the fluorescence normalised to that in the focal plane at 1, 2 and 3 μm from the focal plane; * indicates that the difference between *sd* and *wf* imaging was significantly different ($P < 0.01$, paired t-test)

2.3 | Optical recordings and analysis

Laser or light emitting diode (LED) fluorescence excitation was band-passed filtered at 469 ± 17 nm (Semrock, Rochester, New York) and reflected toward the objective by a

495-nm long-pass dichroic mirror (Chroma, Bellows Falls, Vermont). Emitted OG5N fluorescence was filtered at 525 ± 25 nm (Chroma) before detection. Synchronisation of the camera with laser and LED illumination and with the electrophysiology was provided by a Master 9 (A.M.P.I., Jerusalem, Israel). The timing of synaptic stimulation or action potentials was set during the acquisition window to prevent jittering when averaging over 3 to 9 trials. Fluorescence signals were sometimes corrected for bleaching by subtraction of filtered trials without signal. Fluorescence signals were expressed as fractional changes of fluorescence ($\Delta F/F_0$).

3 | RESULTS

In this section, we describe the temporal and the spatial performances of the system and we present 2 examples of measurements that can be achieved.

3.1 | Temporal performance of the system

The temporal performance of the system relies on the characteristics of the CMOS, illustrated in the picture of Figure 2A. The sensor (~3 cm × 3 cm) is composed of 2048 × 2048 pixels. As depicted in Figure 2A, the full-frame image array is divided into 16 rectangular 256 × 1024 pixel arrays processed in parallel. In our configuration, however, the field of view of the image covers around half of the sensor length, reducing the size of the acquired array to 1024 × 1024 pixels. The left image of Figure 2B shows the dendrite of a PN filled with 2 mM OG5N. This image was collected without the spinning disk in place using widefield LED illumination. The image on the right was recorded using laser illumination with the spinning disk. The maximal acquisition rate of the camera depends on the vertical dimension of the acquired pixel array. In the right image of Figure 2B, several acquired arrays are outlined by coloured rectangles: 1024 × 1024 pixels (blue, maximal rate 200 frames per second); 1024 × 512 pixels (green, maximal rate 400 frames per second); 1024 × 256 pixels (red, maximal rate 800 frames per second); 1024 × 160 pixels (purple, maximal rate 1250 frames per second). Figure 2C shows a portion of the dendrite captured with the LED (left) or with the laser and the spinning disk (right). The coloured traces on the bottom of Figure 2C are the $\Delta F/F_0$ signals, averaged over the 40 × 40 pixels region shown with a yellow square on the right image of Figure 2C, acquired at the maximal acquisition rates in single trials. These signals associated with a CF-EPSP illustrate generically the excellent quality of the signal at acquisition rates up to more than 1 kHz. The images in Figure 2D show a portion of the dendrite in (C). Three regions of 2 × 2 pixels (~0.25 μm^2) from where fluorescence was averaged are indicated: *1* and *3* corresponding to

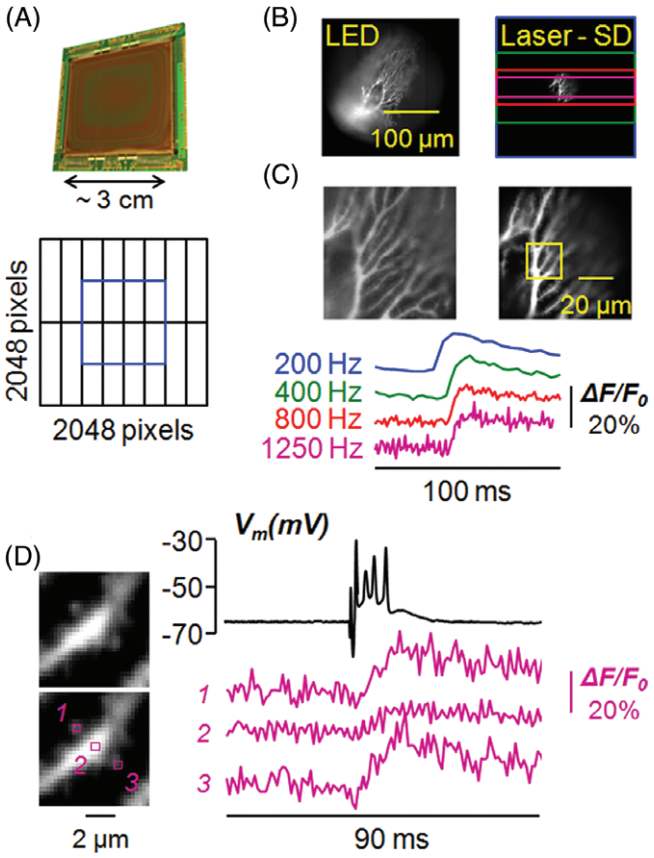

FIGURE 2 Speed performance of the system. (A) Top: picture of the full CMOS sensor composed of 2048 × 2048 pixels of 15 μm × 15 μm (~3 cm length). Bottom: scheme of the 16 parallel processed sectors with blue square indicating the actual field of view. (B) Images of a PN filled with OG5N obtained with widefield LED illumination (left) and laser and spinning disk (right); in the image on the right, the blue, green, red and purple rectangles are CMOS areas, where acquisitions can be achieved at maximal speeds of 200, 400, 800 and 1250 frames per second. (C) Top: image detail (160 × 160 pixels) obtained with widefield LED illumination (left) and laser and spinning disk (right); bottom: Ca^{2+} signals (single trials) associated with a CF-EPSP at the maximal speeds of the 4 rectangles in the yellow region on the top-right image. (D) Left: detail of the image in (C) with regions (2 × 2 pixels, ~0.25 μm^2) *1* and *3* corresponding to synaptic spines and *2* in the parent dendrite. Right: Ca^{2+} signals (average of 3 trials) associated with a CF-EPSP in regions *1-3*; somatic patch recording on the top

2 individual synaptic spines and *2* corresponding to the bulk of the parent dendrite. Traces on the right report the corresponding $\Delta F/F_0$ signals at 1250 Hz, associated with a CF-EPSP, obtained by averaging 3 trials. In summary, these recordings demonstrate that our confocal system is capable of recording Ca^{2+} signals, from structures <1 μm, at frame intervals <1 ms.

3.2 | Spatial performance of the system

The spatial performance was assessed by analysing fluorescence profiles and transients in sequential recordings without or with the spinning disk (widefield vs confocal imaging). A first assessment was carried out in the initial

part of apical dendrites from CA1 hippocampal pyramidal neurons, an approximately cylindrical structure. In Figure 3A, images of 3 dendrites at 23, 37 and 50 μm depth from the slice surface (δ) were obtained in widefield (*wf*) or confocal (*sd*) imaging. The *X* line is positioned on the site of the dendrite in focus and the absolute intensity profile in Figure 3B was calculated by averaging fluorescence from 2 × 4 pixels regions and normalising the values to the maximum at $X = 0$. The profile was fitted with a Lorentzian function.

$$\frac{1}{\pi}\cdot\frac{\Gamma/2}{X^2+\left(\frac{\Gamma}{2}\right)^2}.$$

The parameter Γ specifies the width of the intensity profile that depends on the dendrite thickness but also on light scattering [15], and it is systematically larger in widefield imaging (Γ_{wf}) with respect to spinning disk imaging (Γ_{sd}), as shown in Figure 3B. We then computed $\Delta F/F_0$ associated with 4 action potentials at $X = \pm\Gamma_{sd}$ for widefield and confocal imaging and normalised the signals to those at $X = 0$. As shown in the plots on the right of (B), the $\Delta F/F_0$ at $\pm\Gamma_{sd}$ was systematically smaller in confocal imaging. Figure 3C reports the analysis of intensity profiles from 8 dendrites in 5 cells. Γ values in widefield and confocal imaging, as well as their difference ($\Gamma_{wf}-\Gamma_{sd}$), increase with δ, whereas Γ_{wf} and Γ_{sd} also depend on the dendrite thickness, $\Gamma_{wf}-\Gamma_{sd}$ is expected to depend only on tissue scattering, providing an estimate of the improvement produced by the spinning disk. Thus, at $\pm\Gamma_{sd}$, the normalised $\Delta F/F_0$ peak assesses the ability of the system to resolve Ca^{2+} transients free of scattered light. Figure 3D reports the mean ± SD of normalised $\Delta F/F_0$ peak at $\pm\Gamma_{sd}$, that was 0.27 ± 0.07 in confocal imaging, significantly smaller than 0.55 ± 0.17 in widefield imaging ($P < .001$, paired *t*-test). In summary, within 40 μm from the surface, the gain in spatial resolution quantified by $\Gamma_{wf}-\Gamma_{sd}$ was between 200 and 600 nm. This result can be interpreted as an indication that, within 40 μm from the slice surface, our system can de-blur images to restore spatial resolution closer to the diffraction limit. Hence, in this δ range, we assessed the ability of the system to resolve signals from submicron structures by measuring $\Delta F/F_0$ associated with CF-EPSPs from PN synaptic spines. Figure 4A shows widefield (*wf*) and confocal images (*sd*) of a PN dendrite at $\delta = 25$ μm. Fluorescence was averaged over 2 regions of 2 × 2 pixels centred onto 2 spines in focus, and on regions at ~0.5 μm and ~1 μm from the edge of the spine-centred regions outside the cell. Figure 4B shows that, in widefield imaging, $\Delta F/F_0$ signals are comparable in size in spines and in the adjacent regions outside the cell. In contrast, in confocal imaging, the $\Delta F/F_0$ signals were progressively smaller with the distance from the spine, indicating scattered light elimination by the spinning disk. The same analysis was done in 48 spines in focus from 6 cells, with varying δ from 18 to 30 μm. Figure 4C reports the mean ± SD of $\Delta F/F_0$ peaks at ~0.5 and ~1 μm

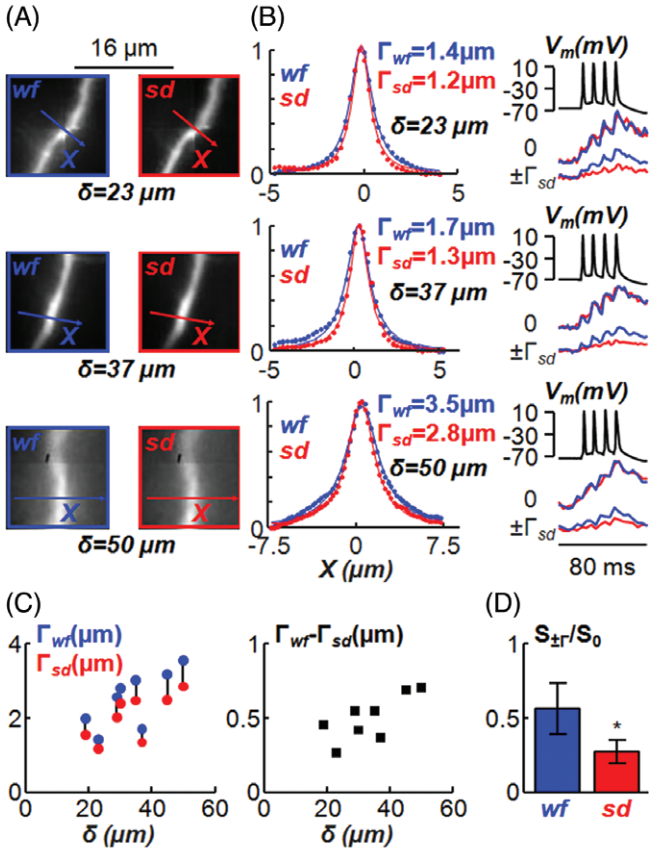

FIGURE 3 Improvement of spinning disk (*sd*) imaging with respect of widefield (*wf*) imaging at different depths from the slice surface (δ). (A) Images of 3 apical dendrites from CA1 hippocampal pyramidal neurons at $\delta = 23$, 37 or 50 μm with *wf* imaging (blue, left) or with *sd* imaging (red, right); the *X* axes of analysis are positioned on the dendritic part in focus. (B) Left: fluorescence normalised to the maximum (at $X = 0$) along the *X* axes (points) fitted with a Lorentzian functions (lines) in the 3 cases with *wf* and *sd* imaging; each spot was calculated by averaging fluorescence of 2 × 4 pixels; Γ values are indicated. Right: Ca^{2+} signals (average of 4 trials) associated with 4 action potentials at 10-ms interval at $X = 0$ and $X = \pm\Gamma_{sd}$; since the *sd* is removing scattered light, the Ca^{2+} $\Delta F/F_0$ signal drops away more rapidly with distance from the dendritic centre making confocal imaging significantly better is resolving the origin of a Ca^{2+} signal. (C) Γ values with *wf* and *sd* imaging (left plot) and their difference (right plot) vs δ in 8 *X* lines from 5 cells. (D) Mean ± SD of Ca^{2+} $\Delta F/F_0$ signal associated with 4 action potentials at $X = \pm\Gamma$, normalised to the signal at $X = 0$, in 8 *X* lines from 5 cells; * indicates that the *sd* signal was significantly smaller than the *wf* signal ($P < .001$, paired *t*-test)

distance from the cell, normalised to the peaks on the spine centres, in widefield and confocal imaging. In confocal imaging, the normalised peaks at ~0.5 and ~1 μm distance were 0.62 ± 0.11 and 0.29 ± 0.08, respectively, significantly smaller than 0.90 ± 0.13 and 0.86 ± 0.16, respectively, in widefield imaging ($P < .001$, paired *t*-test). In particular, the ~0.3 value at ~1 μm distance in confocal imaging is within our ability to discriminate the signal from noise as shown in the examples of Figure 4B. This indicates that we can resolve Ca^{2+} signals from submicron structures in this δ range where this task cannot be accomplished by widefield imaging. Another advantage of confocal imaging,

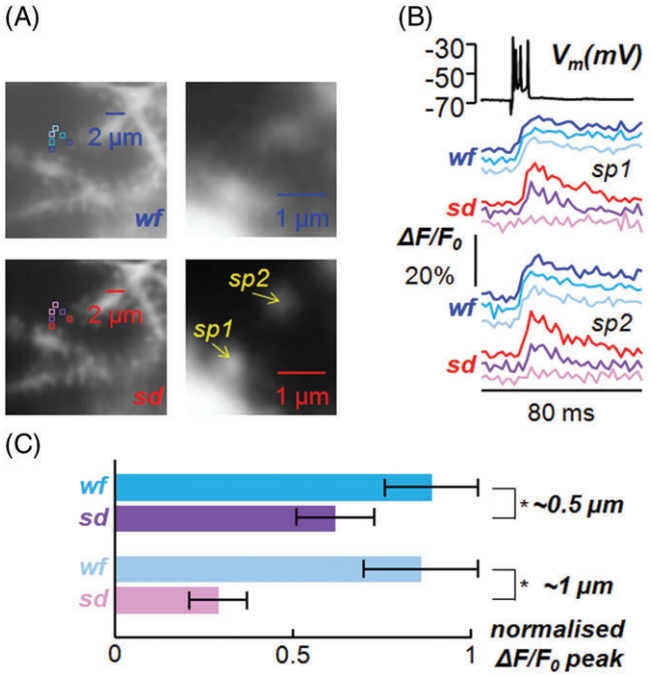

FIGURE 4 Ability of the system to resolve Ca^{2+} transients from synaptic spines. (A) Images of a PN dendrite at $\delta = 25$ µm with widefield illumination (*wf*, top) or with the spinning disk (*sd*, bottom); 2 spines in focus (*sp1* and *sp2*) are indicated on the right; 2 × 2 pixels regions centred on *sp1* and *sp2*, at ~0.5 µm from the spine or at ~1 µm from the spine are shown on the left. (B) Ca^{2+} signals (average of 8 trials) associated with a CF-EPSP at 500 Hz in the regions in (A) shown in the same colour code; somatic patch recording on the top; the Ca^{2+} $\Delta F/F_0$ signal decreases with distance in *sd* imaging but not in *wf* imaging. (C) Mean ± SD of Ca^{2+} $\Delta F/F_0$ signal associated with a CF-EPSP, normalised to the signal in the spines, from 2 × 2 pixels regions at ~0.5 µm from the spine or at ~1 µm from the spine calculated over 48 spines in focus in 6 cells with δ ranging from 18 to 30 µm; * indicates that both at ~0.5 µm and at ~1 µm the difference between *sd* and *wf* imaging was significantly different ($P < .001$, paired *t*-test)

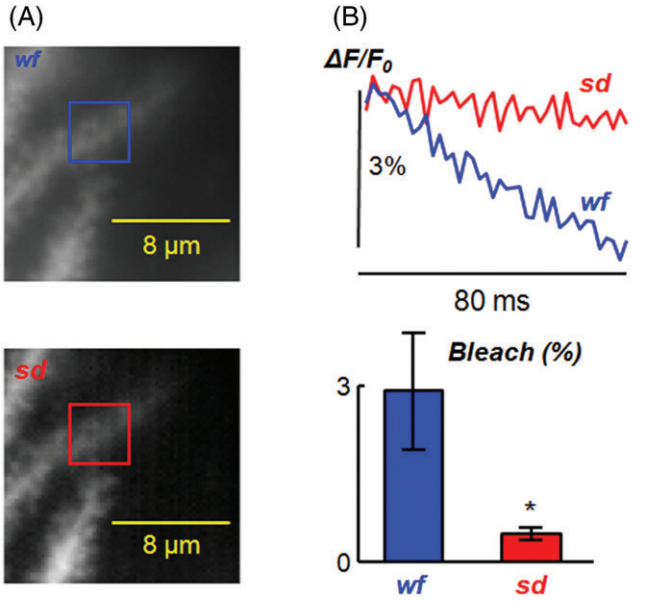

FIGURE 5 Bleach improvement of the system. (A) Images of a PN dendrite detail with widefield illumination (*wf*, top) or with the spinning disk (*sd*, bottom); a region of interest is indicated. (B) Top: $\Delta F/F_0$ from the region of interest in (a) in *wf* (blue trace) and *sd* (red trace) mode following 80-ms light application; light intensity was the maximum for the *sd*, whereas it was decreased in *wf* in order to obtain comparable photon noise. Bottom: mean ± SD of the $\Delta F/F_0$ in *wf* and *sd* (red trace) mode following 80-ms light application, calculated from $N = 7$ cells; * indicates that the difference between *sd* and *wf* imaging was significantly different ($P < .001$, paired *t*-test)

with respect to widefield imaging, is the reduced bleaching. Dendrite of Figure 5A was exposed to laser illumination for 80 ms with the spinning disk at the maximal intensity, or without the spinning disk at reduced intensity to obtain a similar photon noise. As shown in the plots of Figure 5B, dye bleaching reduced fluorescence by ~3% in widefield imaging, but only by ~0.5% in confocal imaging. In 7 cells tested, bleaching was 2.9 ± 1.0% in widefield imaging, significantly larger than in spinning disk imaging (0.5 ± 0.1%, $P < .001$ paired *t*-test).

3.3 | Examples

After evaluating the system, we describe 2 examples of the type of information accessible with this approach. In the cell of Figure 6A, the Ca^{2+} signal associated with the CF-EPSP was recorded at 500 Hz in 2 areas containing several dendritic branches and many spines. Such recordings permit exhaustive analysis of the amplitude and kinetics of Ca^{2+} transients in synaptic spines with respect to those in parent dendrites. Figure 6B shows Ca^{2+} signals in 4 spines and 4 locations of the parent dendrites in the red and blue regions indicated in (A). These representative $\Delta F/F_0$ signals indicate that the kinetics of the Ca^{2+} transient is systematically different in spines and parent dendrites. In particular, Ca^{2+} signals in spines are larger and decay more rapidly with respect to those in parent dendrites. This phenomenon may be due to the different surface-to-volume ratio of the 2 types of structure [16], as well as to different distributions of Ca^{2+} channels [17] or to Ca^{2+}-binding proteins [18, 19]. In the example of Figure 7A, we monitored the Ca^{2+} signal associated with PF-EPSPs. For this signal, produced by activation of synaptic spines, the size and the extent of the Ca^{2+} transient depends on the number and spatial distribution of activated PFs. [20] In this example, the train of 5 EPSPs produced a Ca^{2+} transient in the dendrites and spines over a region of ~100 µm^2. As shown in Figure 7B, the Ca^{2+} signal had 2 components: a fast component nearly synchronous with the EPSPs recorded in the somatic patch mediated by voltage-gated Ca^{2+} channels [20] and a slower component mediated by metabotropic glutamate receptors. [21] The false-colour scale images in Figure 7C illustrate the spatial profile of the signal at different time windows of the recording; in particular images *b* and *d* correspond to the peak of the fast and slow components. As shown by these images and by the traces in (B), the 2 signals do not spatially overlap. In some dendrites or spines, the fast component was larger than the slow component and in other

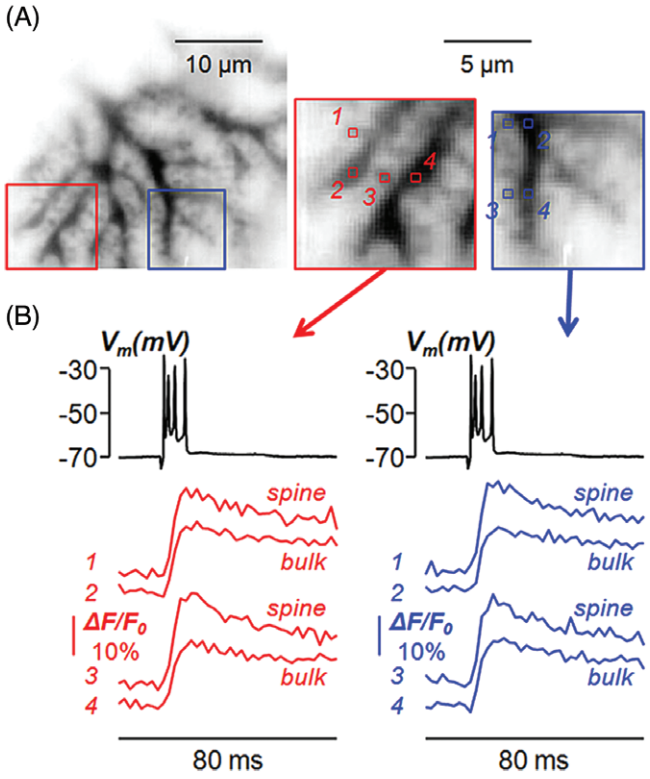

FIGURE 6 Example 1: analysis of Ca^{2+} transients associated with a CF-EPSP. (A) Left: intensity inverted confocal image of a PN filled with OG5N. Right: enlargements of the red and blue square regions of the left with 4 spine regions (*1* and *3*) and 4 regions of the parent dendrites (*2* and *4*). (B) Ca^{2+} signals (average of 8 trials) associated with a CF-EPSP at 500 Hz in the spines and dendritic regions in (A); somatic patch recording on the top. For this experiment, see also Movie S1

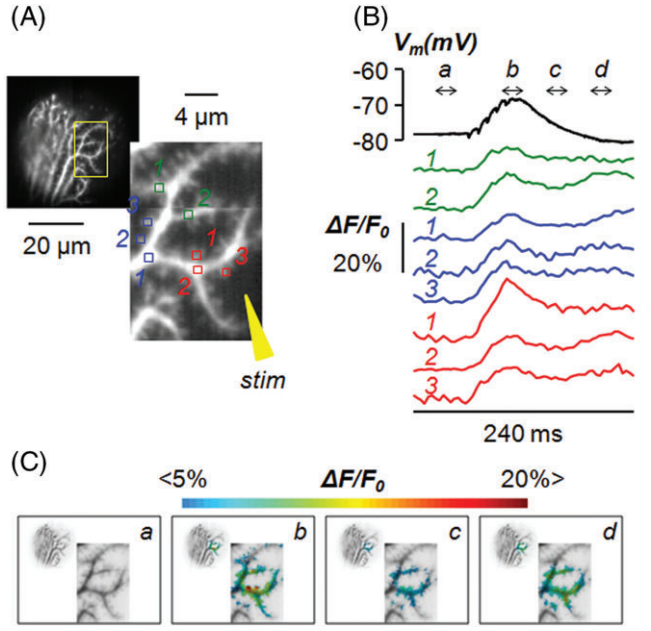

FIGURE 7 Example 2: Analysis of Ca^{2+} transients associated with parallel fibre (PF) EPSPs. (A) Left: confocal image of a PN filled with OG5N. Right: enlargements of the activated dendritic region with 8 spine or dendritic regions indicated. (B) Ca^{2+} signals (average of 8 trials) associated with a train of 5 PF EPSPs at 250 Hz in the spines and dendritic regions in (a); somatic patch recording on the top. (C) Colour scaled signals of the experiment in (B) superimposed on the inverted fluorescence image of the dendrite. Signal profiles are obtained by averaging 6 frames in the time windows *a*, *b*, *c* and *d* indicated in (B). Signal *b* corresponds to the peak of the fast component of the Ca^{2+} transient, mediated by voltage-gated Ca^{2+} channels. Signal *d* corresponds to the peak of the slow component of the Ca^{2+} transient, mediated by metabotropic glutamate receptors. For this experiment, see also Movie S2

sites it was the opposite. This result suggests that activation of metabotropic glutamate receptors does not spatially coincide with activation of voltage-gated Ca^{2+} channels, that is, that PF-EPSPs may trigger different signalling pathways at different sites of the dendrite. The 2 examples in Figures 6 and 7 demonstrate the advantages of our system with respect to scanning systems, where only limited numbers of selected submicron sites can be simultaneously analysed. Movies of these experiments are available online (Movie S1 and Movie S2).

4 | DISCUSSION AND CONCLUSIONS

The understanding of fast Ca^{2+} signalling in small axonal or dendritic compartments and in synaptic spines is crucial in neurobiology [22]. In this article, we report a novel fast confocal system based on a spinning disk specifically designed to investigate Ca^{2+} signals in submicron neuronal compartments in brain slices, in combination with patch clamp recordings [23]. To this purpose, other confocal solutions have been proposed in the past few years. A scanning confocal imaging system developed for this application and based on pinholes and digital micromirror devices could operate in the kHz range, but it was limited in the number of recording points [24]. Similarly, the number of recording points could be effectively increased by using fixed pinhole arrays [25], but this approach limits the exact selection of recording sites. The confocal system described in this report overcomes these limitations allowing recording of Ca^{2+} transients from continuous structures in tens of thousands of pixels simultaneously. The system performs optimally in the common situation of structures at 20 to 40 µm below the slice surface, where widefield illumination fails discriminating signals with submicron resolution. Under these conditions, we achieved recordings at 250 to 1250 Hz from submicron structures. This was possible thanks to the combination of a fast custom-patterned disk, an efficient powerful laser and a fast and sensitive CMOS camera. The acquisition rate of these recordings is sufficient to detect fast Ca^{2+} transients associated with action potentials or synaptic activity, although still insufficient to measure the kinetics of fast Ca^{2+} channels [26–29]. The limitation of confocal imaging in acquisition speed is mainly set by the number of detected photons, which is reduced by light rejection. The way to obtain submicron resolution without rejection of emitted light is to use 2-photon imaging that also allows axial confinement of fluorescence excitation

[30]. Two-photon imaging without scanning microscopy is achievable by patterning the light shape to match the imaged structures, that is, by performing 2-photon holographic illumination [31]. In voltage imaging, signals have been recorded at several kHz from small neuronal compartments using 1-photon holographic illumination [32, 33]. In contrast, 2-photon holographic illumination has been set for Ca^{2+} imaging in brain slices and in vivo, but without achieving recordings from submicron structures in the kHz range [34–37]. Yet, it appears possible to achieve this resolution in the near future.

Whereas holographic 2-photon imaging is potentially more powerful, the present confocal system has several advantages. It can be easily coupled to existing microscopes equipped for electrophysiology; it requires moderate knowledge of optics to implement measurements; it is economic requiring minimal maintenance. In particular, the multimode laser box allows other wavelengths for excitation of different indicators and is 5 to 10 times cheaper than lasers used in the conventional confocal microscopes for equivalent power. Thus, this system offers an easy solution to measure fast Ca^{2+} transients in brain slices with submicron resolution.

ACKNOWLEDGMENTS

This work was supported by the *Agence Nationale de la Recherche* through: (1) Grant *WaveFrontImag*, program number ANR-14-CE17-0006-01; (2) Labex *Ion Channels Science and Therapeutics*, program number ANR-11-LABX-0015; (3) National Infrastructure France Life Imaging "Noeud Grenoblois"; and by the *Federation pour la recherché sur le Cerveau* (FRC) through the grant *Espoir en tête* (in partnership with Rotary France). We thank Hanen Ziri for starting development of the software, Vanni Petrolli for preparing the beads and Irène Wang for useful discussions.

AUTHOR BIOGRAPHIES

Please see Supporting Information online.

REFERENCES

[1] F. Helmchen, K. Imoto, B. Sakmann, *Biophys. J.* **1996**, *70*, 1069.
[2] R. Davies, J. Graham, M. Canepari, *J. Microsc.* **2013**, *251*, 5.
[3] G. H. Patterson, *Semin. Cell Dev. Biol.* **2009**, *20*, 886.
[4] Z. F. Mainen, M. Maletic-Savatic, S. H. Shi, Y. Hayashi, R. Malinow, K. Svoboda, *Methods* **1999**, *18*, 231.
[5] A. Fine, W. B. Amos, R. M. Durbin, P. A. McNaughton, *Trends Neurosci.* **1988**, *11*, 346.
[6] P. Saggau, *Curr. Opin. Neurobiol.* **2006**, *16*, 543.
[7] C. G. Coates, D. J. Denvir, N. G. McHale, K. D. Thornbury, M. A. Hollywood, *J. Biomed. Opt.* **2004**, *9*, 1244.
[8] Y. Takahara, N. Matsuki, Y. Ikegaya, *J. Integr. Neurosci.* **2011**, *10*, 121.
[9] F. Ceriani, C. D. Ciubotaru, M. Bortolozzi, F. Mammano, *Methods Mol. Biol.* **2016**, *1427*, 223.
[10] J. P. Nguyen, F. B. Shipley, A. N. Linder, G. S. Plummer, M. Liu, S. U. Setru, J. W. Shaevitz, A. M. Leifer, *Proc. Natl. Acad. Sci. U. S. A.* **2016**, *113*, E1074.
[11] K. E. Vogt, S. Gerharz, J. Graham, M. Canepari, *J. Physiol.* **2011**, *589*, 489.
[12] K. E. Vogt, S. Gerharz, J. Graham, M. Canepari, *PLoS One* **2011**, *6*, e24911.
[13] M. Canepari, S. Willadt, D. Zecevic, K. E. Vogt, *Biophys. J.* **2010**, *98*, 2032.
[14] S. F. Barnett, M. Snape, C. N. Hunter, M. A. Juárez, A. J. Cadby, *Sci. Rep.* **2017**, *7*, 42313.
[15] T. R. Corle, C. H. Chou, G. S. Kino, *Opt. Lett.* **1986**, *11*, 770.
[16] M. Canepari, F. Mammano, *J. Neurosci. Methods* **1999**, *87*, 1.
[17] P. Isope, M. E. Hildebrand, T. P. Snutch, *Cerebellum* **2012**, *11*, 651.
[18] H. Schmidt, K. M. Stiefel, P. Racay, B. Schwaller, J. Eilers, *J. Physiol.* **2003**, *551*, 13.
[19] K. Vogt, M. Canepari, *Cerebellum* **2010**, *9*, 284.
[20] M. Canepari, K. Vogt, *PLoS One* **2008**, *3*, e4011.
[21] M. Canepari, D. Ogden, *J. Physiol.* **2006**, *573*, 65.
[22] C. Grienberger, A. Konnerth, *Neuron* **2012**, *73*, 862.
[23] G. J. Augustine, *J. Neurosci. Methods* **1994**, *54*, 163.
[24] V. Bansal, S. Patel, P. Saggau, *J. Biomed. Opt.* **2006**, *11*, 34003.
[25] T. Tominaga, Y. Tominaga, *J. Neurophysiol.* **2013**, *110*, 553.
[26] N. Jaafari, M. De Waard, M. Canepari, *Biophys. J.* **2014**, *107*, 1280.
[27] N. Jaafari, E. Marret, M. Canepari, *Neurophotonics* **2015**, *2*, 021010.
[28] N. Jaafari, M. Canepari, *J. Physiol.* **2016**, *594*, 967.
[29] K. Ait Ouares, N. Jaafari, M. Canepari, *J. Neurosci. Methods* **2016**, *268*, 66.
[30] T. G. Oertner, *Exp. Physiol.* **2002**, *87*, 733.
[31] E. Papagiakoumou, A. Bégue, B. Leshem, O. Schwartz, B. M. Stell, J. Bradley, D. Oron, V. Emiliani, *Nat. Photon.* **2013**, 2013, *7*, 274.
[32] A. J. Foust, V. Zampini, D. Tanese, E. Papagiakoumou, V. Emiliani, *Neurophotonics* **2015**, *2*, 021007.
[33] D. Tanese, J. Y. Weng, V. Zampini, V. De Sars, M. Canepari, B. Rozsa, V. Emiliani, D. Zecevic, *Neurophotonics* **2017**, *4*, 031211.
[34] V. Nikolenko, B. O. Watson, R. Araya, A. Woodruff, D. S. Peterka, R. Yuste, *Front. Neural Circuits* **2008**, *2*, 5.
[35] P. Pozzi, D. Gandolfi, M. Tognolina, G. J. E. Chirico, Mapelli, E. D'Angelo, *Neurophotonics* **2015**, *2*, 015005.
[36] W. Yang, J. E. Miller, L. Carrillo-Reid, E. Pnevmatikakis, L. Paninski, R. Yuste, D. S. Peterka, *Neuron* **2016**, *89*, 269.
[37] S. Bovetti, C. Moretti, S. Zucca, M. Dal Maschio, P. Bonifazi, T. Fellin, *Sci. Rep.* **2017**, *7*, 40041.

SUPPORTING INFORMATION

Additional Supporting Information may be found online in the supporting information tab for this article.

Movie S1. Example of spatial profile of Ca^{2+} signal associated with 1 CF-EPSP.

Movie S2. Example of spatial profile of Ca^{2+} signal associated with a train of PF-EPSPs.

How to cite this article: Filipis L, Ait Ouares K, Moreau P, et al. A novel multisite confocal system for rapid Ca^{2+} imaging from submicron structures in brain slices. *J. Biophotonics*. 2018;11:e201700197. https://doi.org/10.1002/jbio.201700197

Bioorganic & Medicinal Chemistry 27 (2019) 247–253

Contents lists available at ScienceDirect

Bioorganic & Medicinal Chemistry

journal homepage: www.elsevier.com/locate/bmc

Synthesis by native chemical ligation and characterization of the scorpion toxin AmmTx3

Claude Zoukimian[a,b], Hervé Meudal[c], Stephan De Waard[d], Karima Ait Ouares[e], Sébastien Nicolas[d], Marco Canepari[e], Rémy Béroud[b], Céline Landon[c], Michel De Waard[d], Didier Boturyn[a,*]

[a] Department of Molecular Chemistry, Univ. Grenoble Alpes, CNRS, 570 rue de la chimie, CS 40700, Grenoble 38000, France
[b] Smartox Biotechnology, 6 rue des platanes, Saint Egrève 38120, France
[c] Center for Molecular Biophysics, CNRS, rue Charles Sadron, CS 80054, Orléans 45071, France
[d] Institut du Thorax, INSERM, CNRS, Univ. Nantes, 8 quai Moncousu, BP 70721, Nantes 44007, France
[e] Laboratory for Interdisciplinary Physics, Univ. Grenoble Alpes, CNRS, 140 Avenue de la Physique, BP 87, Saint-Martin d'Hères 38402, France

ARTICLE INFO

Keywords:
Toxin
AmmTx3
Potassium channel
Native chemical ligation
NMR

ABSTRACT

The scorpion toxin AmmTx3 is a specific blocker of K_v4 channels. It was shown to have interesting potential for neurological disorders. In this study, we report the first chemical synthesis of AmmTx3 by using the native chemical ligation strategy and validate its biological activity. We determined its 3D structure by nuclear magnetic resonance spectroscopy, and pointed out that AmmTx3 possesses the well-known CSαβ structural motif, which is found in a large number of scorpion toxins. Overall, this study establishes an easy synthetic access to biologically active AmmTx3 toxin.

1. Introduction

An increasing number of toxins are isolated from various animal venoms and become key molecular compounds for biomedical applications such as cardiovascular diseases,[1] treatment of pain,[2] multiple sclerosis.[3] and diabetes.[4] These toxins are mainly produced by microorganisms, such as bacteria and fungi. Interestingly, the discovery of specific blockers has significantly contributed to the understanding of the involvement of distinct ion channels to cellular and tissue function and pathology. In particular, several potassium channels have been identified as promising therapeutic targets.[5]

In this context, the AmmTx3 toxin identified from the venom of the scorpion *Androctonus mauretanicus*, is a specific blocker of K_v4 channels and was found to reduce Parkinsonian-like motor symptoms and, emotional and cognitive symptoms.[6] Curiously, it was less active on recombinant K_v4 channels and it was explained that auxiliary subunits may contribute to the pharmacological action of the peptide.[7] This toxin protein has a polypeptide chain of 37 amino acid residues with 6 cysteines that forms 3 disulfide bonds. Initially AmmTx3 was isolated from the venom.[8] In order to better characterize this toxin, chemical synthesis was preferred as it avoids venom extraction and purification from natural sources, and provides much larger amounts of toxins. In addition, it paves the way for the production of interesting analogues. As solid phase peptide synthesis (SPPS) presents limitations in the production of peptides of more than 50 amino acids or containing "difficult sequences", convergent synthetic strategies such as the native chemical ligation (NCL) of short fragments are usually used.[9] Additionally, this strategy allows the introduction of segmental isotopic or fluorescent labeling of proteins.[10] To date, recent methods of NCL were developed.[11,12] The use of crypto-thioesters remains a convenient strategy as Fmoc-based SPPS can be exploited to prepare peptide fragments avoiding the handling of strong acids such as hydrogen fluoride used during the Boc strategy.

We herein report the first chemical synthesis of biologically active AmmTx3 by using peptide hydrazide as crypto-thioester.[13] As its structure was not determined to date, we also report the 3D structure of AmmTx3 by using homo- and heteronuclear 2D nuclear magnetic resonance (NMR) spectroscopy.

2. Results and discussion

2.1. Synthesis of AmmTx3

To our knowledge, AmmTx3 was mainly produced by

* Corresponding author.
E-mail address: didier.boturyn@univ-grenoble-alpes.fr (D. Boturyn).

https://doi.org/10.1016/j.bmc.2018.12.009
Received 26 September 2018; Received in revised form 28 November 2018; Accepted 5 December 2018
Available online 06 December 2018

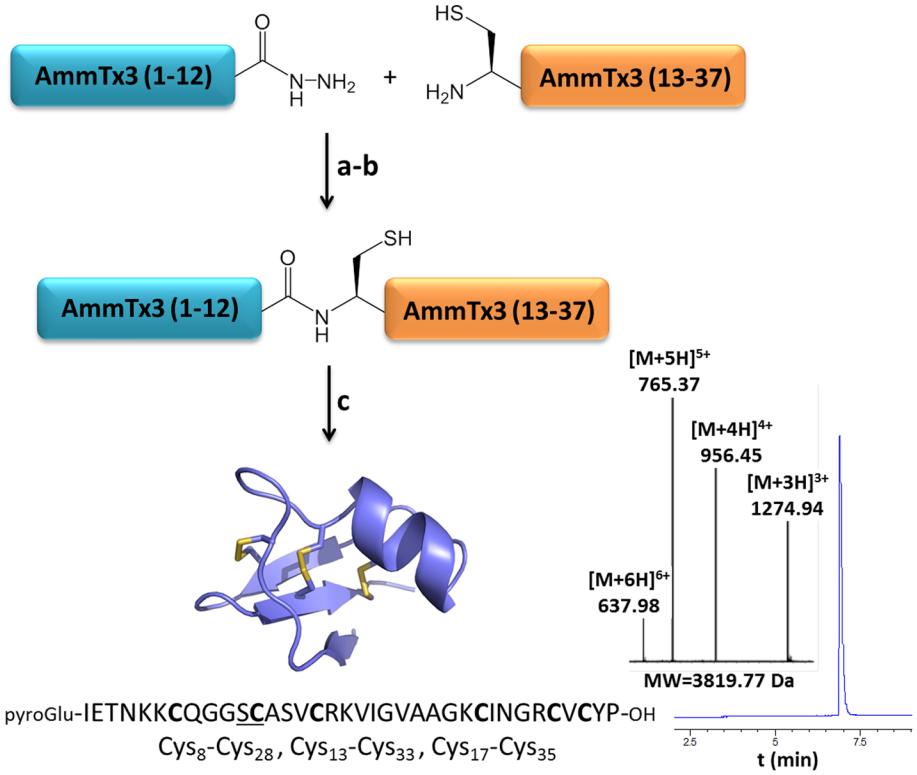

Scheme 1. Synthesis of AmmTx3 using NCL of two peptide segments. a) AmmTx3(1–12) activation: Gn-HCl (6 M), sodium phosphate (0.2 M, pH 3.0), $NaNO_2$ (10 equiv.), −15 °C ; b) Ligation : AmmTx3(13–37), MPAA (100 equiv.), pH 6.5, room temperature ; c) Folding and disulfide formation: Tris (0.2 M, pH 8.2). Analytical RP-HPLC (λ = 214 nm) and ES-MS for the final purified AmmTx3 toxin were performed. Observed mass 3819.77 Da *vs* calculated mass 3819.87 Da. MPAA = 4-Mercaptophenylacetic acid; Tris = Tris(hydroxymethyl)aminomethane.

biotechnology. To enable structural studies, chemical synthesis may be used to obtain enough amounts of pure toxin. As predicted, first attempt using standard Fmoc-based SPPS to produce the toxin gave very low yield (See the Supporting Information).[14] We then decided to use the NCL of two short peptide fragments (scheme 1). AmmTx3 contains six cysteine residues that could serve as potential sites for ligation. As the ligation rate between Val and Cys is known to be very low,[12,15] we preferred to carry out the ligation at the Ser-Cys site by using the hydrazide-based NCL.[12]

In this context, AmmTx3(1–12) peptide was first prepared starting with hydrazine resin using standard Fmoc protocols.[16] The pure fragment was obtained in an excellent 90% overall yield. In parallel, thiol containing-AmmTx3(13–37) peptide was produced using the SPPS in a moderate 30% overall yield. Prior to the NCL, sodium nitrite was used to produce AmmTx3(1–12) peptide azide at low pH and low temperature.[17] The thiol containing-AmmTx3(13–37) peptide segment was then added and the pH value was adjusted to 6.5 to initiate the native chemical ligation at room temperature. The reaction was monitored by RP-HPLC (Fig. 1A).[18] This methodology is relatively simple to operate, and the overall isolated yield based on resin loading is higher (15% from C-term fragment) than the previous linear SPPS (4%).

Finally, folding and disulphide formation was carried out under alkaline conditions (Tris buffer, pH 8.2). Peptide folding was monitored by RP-HPLC (Fig. 1B).[19] and purification by RP-HPLC gave AmmTx3 toxin that was characterized by ES-MS analysis (Scheme 1, see also the Supporting Information). Experimentally determined molecular weight (MW = 3819.77) was found in excellent agreement with the calculated value (MW = 3819.87).

2.2. Structural determination of AmmTx3

The AmmTx3 in hand, a nuclear magnetic resonance (NMR) study was performed to determine AmmTx3 3D structure. The dispersion of the resonances is good, illustrating that AmmTx3 was well-folded, and all the NH groups are visible on homonuclear spectra except for Asn[5] (see also the Supporting Information). All.^{15}N resonances could be assigned from the ^{1}H-^{15}N heteronuclear multiple-quantum correlation (HMQC).[20] except for Asn[5] and Gly[10]. ^{1}H and.^{15}N chemical shifts have been deposited in the BioMagResBank (http://www.brmb.wisc.edu) under the entry code 34268. Two sets of NMR spectra were recorded for AmmTx3 prepared from the NCL (AmmTx3-NCL) in comparison with AmmTx3 prepared from classical SPPS (AmmTx3). Chemical shifts of both samples are identical, as highlighted by the superimposition of their HMQC spectra (Fig. 2), signifying that the synthetic route does not interfere with the 3D structure of the molecule.

The NOE (nuclear overhauser effect) data set used in the final ARIA (ambiguous restraints for iterative assignment) run includes 994 distance restraints (Table 1), with an average of about 28 restraints per residue. Among these restraints, 748 are non-ambiguous. Moreover, during the iterative ARIA procedure, additional constraints were introduced: covalent bonds between sulphur atoms involved in each defined bridge (C8-C28, C13-C33, C17-C35), and 10*H*-bond constraints observed within the β-strands.

The 10 selected structures representative of the solution structure of AmmTx3 display small potential energy values, respect all the experimental data and are in agreement with standard covalent geometry (Table 1). The root mean square deviations (RMSD) are low, no experimental distance constraint violation greater than 0.3 Å is observed and the Ramachandran plot exhibits 100% of the (ϕ,ψ) angles in the most favoured regions. The coordinates of this ensemble of structures have been deposited in the Protein Data Bank (http://www.pdb.org) with the entry code 6GGZ.

Fig. 3 represents the overall fold of AmmTx3. As attested by the pairwise RMSD on the backbone atoms, the structure is very well defined and composed of an α-helix (14–20) and a 3-stranded β-sheet (2–4, 26–29, 32–35) (Table 1), organized into the well-known CSαβ motif [21] that is typical of this family of scorpion toxins.[22]

2.3. Biological activity of AmmTx3

We next assessed whether AmmTx3-NCL was functional and showed identical activity to AmmTx3 that was prepared by classical SPPS. This

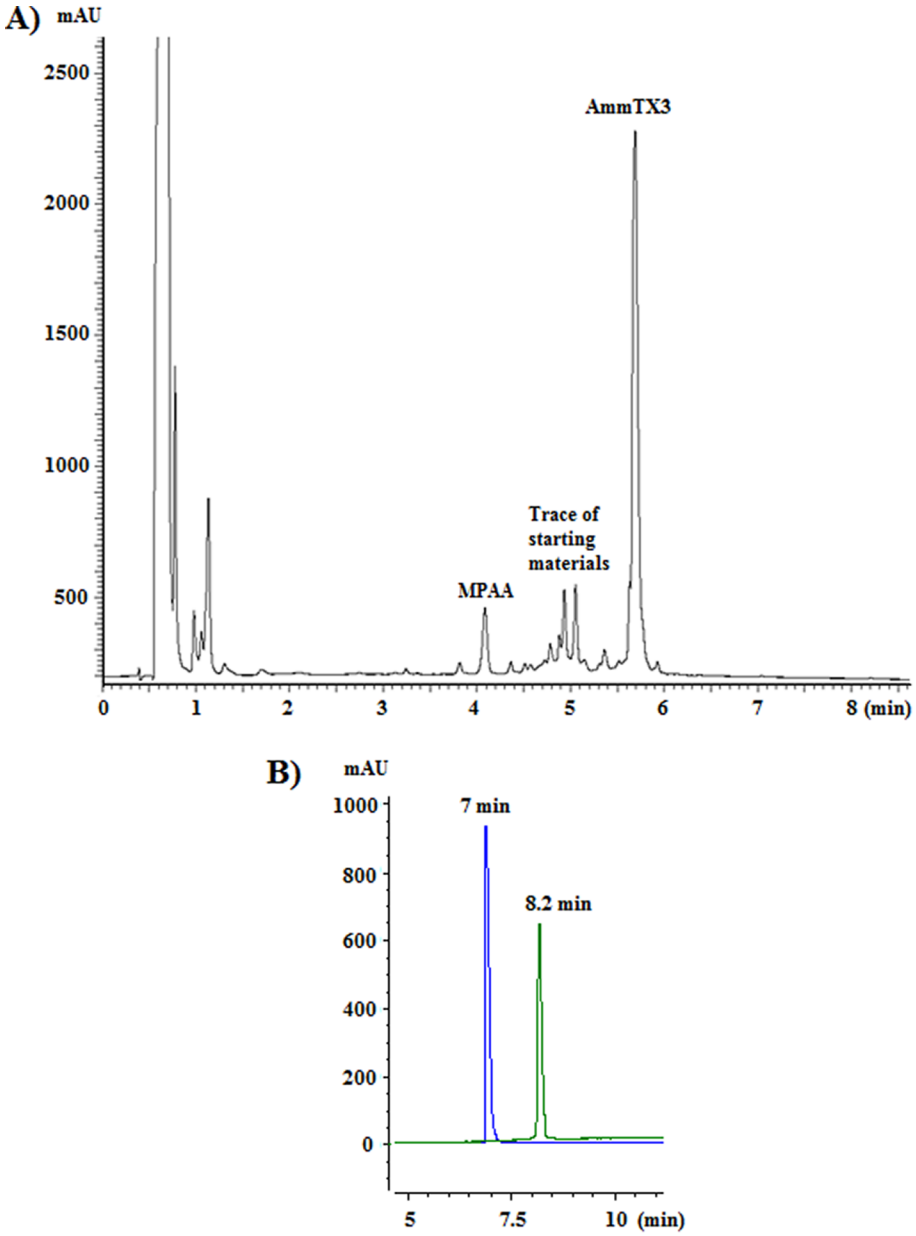

Fig. 1. A) HPLC trace at t = 18 h of the NCL reaction; B) Overlapping of unfolded AmmTx3 (green) and folded AmmTx3 (blue) HPLC traces. The absorbance was measured at 214 nm.

would be expected as both peptides had similar HMQC spectra. K_v4.2 channels were co-expressed with DDP6S and KCHIP1 subunits in Cos-7 cells, as they were shown to contribute to AmmTx3 pharmacology,[7] and recorded using the automated synchropatch 384PE patch clamp system (Fig. 4).

As shown, classical SPPS-prepared AmmTx3 and NCL-prepared AmmTx3 display very similar average K_v4.2 inhibition time courses, indicating that both peptides block with similar kinetics (Fig. 4A). Within 10 min K_v4.2 currents are almost completely blocked by the application of either 333 nM AmmTx3 or 333 nM AmmTx3-NCL (Fig. 4A and B). No statistical differences were found for the degree of maximum inhibition at 333 nM (90 ± 4% and 85 ± 5% for AmmTx3 produced by SPPS and NCL, respectively. P = 0.5421 Mann Whitney test). The effect of a lower peptide concentration on K_v4.2 activation properties was also investigated (Fig. 4C and D). None of the two toxins induced a shift in voltage-dependence of activation on partially blocked K_v4.2 currents at 33 nM AmmTx3 compared to control recordings in the absence of toxins (Fig. 4C). We concluded that both peptides were functional and identical in properties.

Finally, to demonstrate that our NCL-prepared AmmTx3 was also functional on native potassium channels, we tested the block of A-type K + channels in a native living neuron in a brain slice using functional combined V_m and Ca^{2+} imaging as described in the experimental section. In the Purkinje neuron (PN) reported in Fig. 5, the dendritic V_m and Ca^{2+} signals associated with a climbing fibre (CF) synaptic potential were recorded in control conditions and after local application of 1 μM AmmTx3-NCL. It has been shown that inactivation of A-type K + channels enhances dendritic excitability and Ca^{2+} signals associated with CF synaptic potentials.[23] In agreement with this observation, application of AmmTx3-NCL substantially increased the dendritic V_m and Ca^{2+} signals associated with this stimulation protocol.

As expected, the biological activity of folded AmmTx3 prepared by NCL is coherent with expectations of channel block in native tissues.

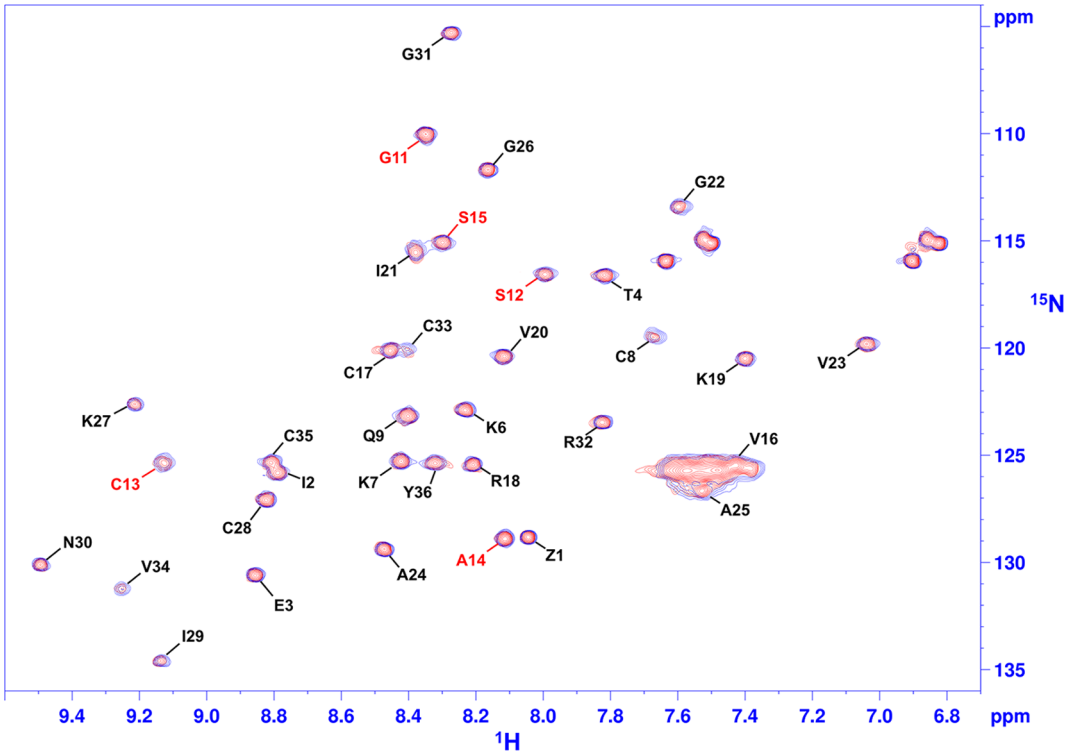

Fig. 2. Superimposition of the ^{1}H-^{15}N SoFast-HMQC (natural abundance, 700 MHz with cryoprobe) of AmmTx3-NCL (red) and AmmTx3 (blue). The assignment of each residue is depicted (for clarity side-chain assignments are not indicated). Residues G11 to S15 corresponding to the area of ligation are annotated in red.

Table 1
Experimental NMR data used for the calculations, and final structural statistics for the ten models representative of the solution structure of AmmTx3.

NMR constraints	
Distance restraints	
Total NOE	994
Unnambiguous	748
Hydrogen bonds	10
Disulfide bridges[a]	C8-C28, C13-C33, C17-C35
Structural statistics (PDB code 6GGZ)	
Average violations per structure	
NOEs ≥ 0.3 Å	0
Hydrogen bonds ≥ 0.5 Å	0
RMSD[b] *on backbone atoms (pairwise, Å)*	
Global	0.27
Ramachandran analysis	
Most favoured region	77.3%
Allowed region	22.7%
Generously allowed	0%
Disallowed	0%
Energies (kcal.mol^{-1})[c]	
Electrostatics	−1211 ± 10
Van der Waals	−280 ± 4
Total energy	−1243 ± 16
Residual NOE energy	10 ± 2

[a] Introduced as covalent bonds after convergence of the first runs of calculations.
[b] Calculated with CCpNMR.
[c] Calculated with the standard parameters of ARIA and given as mean ± standard deviation.

3. Conclusions

In summary, AmmTx3 toxin was chemically produced via the NCL technique using peptide hydrazide as crypto-thioester. This approach provides an easy access to multi-milligram quantities of protein. We then determined the structure of AmmTx3 by using the NMR spectroscopy. The structural signature of this toxin is defined by the presence CSαβ motif that is typical of a family of scorpion toxins.[22] In parallel, complementary studies have shown biological activities of chemically-prepared AmmTx3 to be fully identical to the SPPS-mediated AmmTx3 synthetic peptide.

This methodology may be useful in order to carry out further biological studies as toxins represent potential therapeutic reagents but also for the production of interesting analogues.

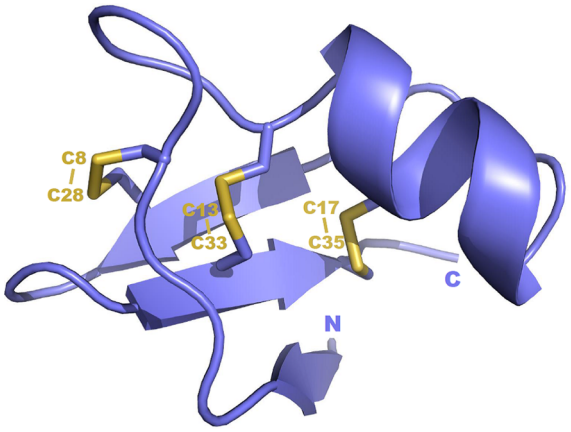

Fig. 3. Schematic representation of AmmTx3 backbone, drawn with the PyMOL software (The PyMOL Molecular Graphics System, Version 2.0 Schrödinger, LLC). Disulfide bridges are represented in yellow, and cysteine residues are numbered to clearly identify the three disulfide bridges.

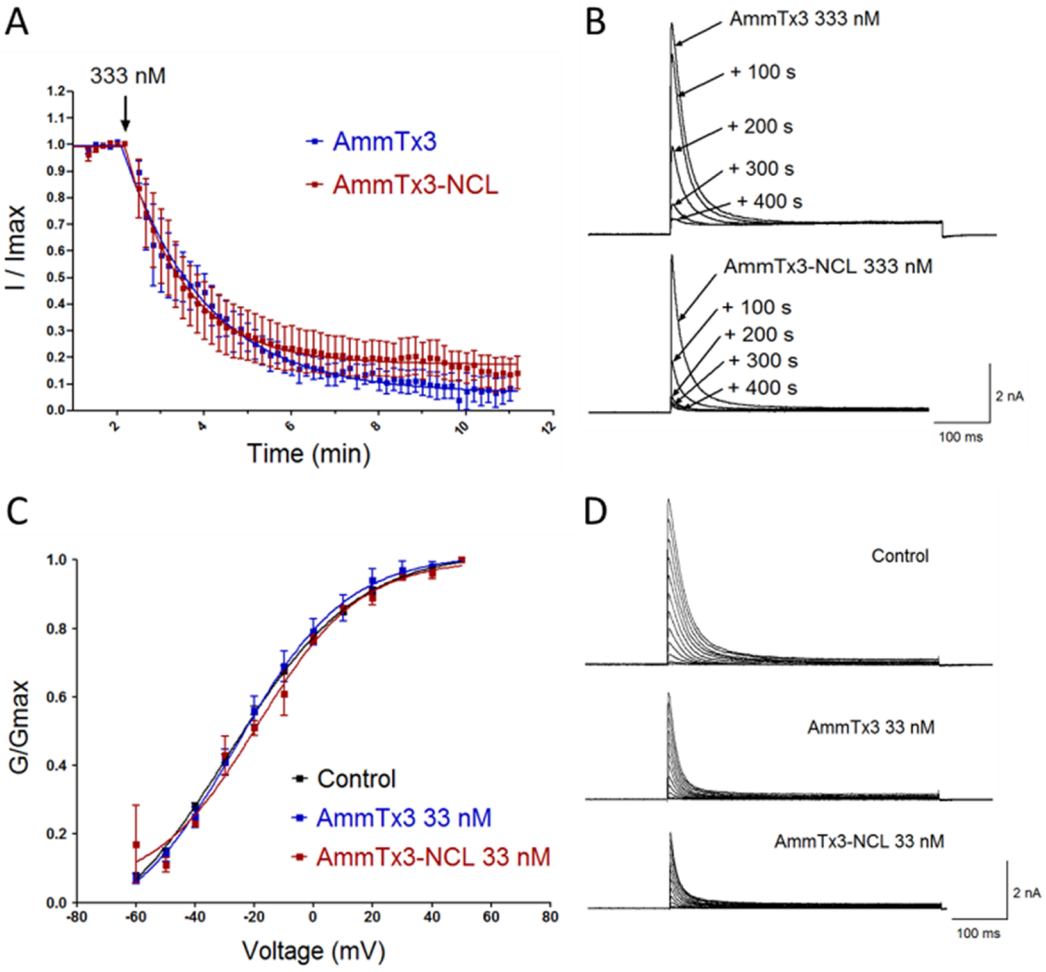

Fig. 4. AmmTx3-NCL and AmmTx3 (produced by SPPS) equally block $K_v4.2$ channels. A) Average time course of $K_v4.2$ channel outward current block recorded at 70 mV following addition of either 333 nM AmmTx3 (blue trace, n = 6) or AmmTx3-NCL (red trace, n = 9). Error bars are SEM. B) Current traces from representative cells for $K_v4.2$ channel block recorded at different time points (100 s, 200 s, 300 s and 400 s) following addition of AmmTx3 (top) or AmmTx3-NCL (bottom). C) Kv4.2 activation curve (conductance-voltage relation G/Gmax) fitted with Boltzmann functions for control currents (black trace, n = 81), and following addition of 33 nM AmmTx3 (blue trace, n = 7) or AmmTx3-NCL (red trace, n = 2). Error bars are SEM. D) Representative traces in response to voltage clamp activation protocol recorded for control currents (top) and in the presence of 33 nM AmmTx3 (middle) or AmmTx3-NCL (bottom).

4. Experimental section

4.1. Synthesis of AmmTx3 via NCL

20 mg of AmmTx3(1-12)-$NHNH_2$ (1 equiv., 12.3 µmol) was dissolved in 2.4 mL of 6 M Gn-HCl, 200 mM NaH_2PO_4 buffer at pH 3.0 and cooled in an ice/salt bath at −15 °C for 5 min. 245 µL of 0.5 M aqueous $NaNO_2$ solution (10 equiv.) were added and the mixture was agitated for 15 min at −15 °C. 29.6 mg of AmmTx3(13-37) (0.77 equiv.) and 206 mg of MPAA (100 equiv.) were dissolved in 2.4 mL of 6 M Gn-HCl, 200 mM Na_2HPO_4 buffer at pH 6.5 and added to the reaction mixture. The pH was adjusted to 6.8 and the reaction was mixed overnight under inert atmosphere at room temperature. 350 mg of tris(2-carboxyethyl) phosphine (TCEP) (100 equiv.) were dissolved in 15 mL of 6 M Gn-HCl solution, the pH was adjusted to 5.0, this solution was added to the reaction mixture and mixed during 30 min. The pH was lowered with 500 µL of TFA and the mixture was washed 4 times with 20 mL of Et_2O and purified by preparative RP-HPLC. After lyophilization, 20.1 mg of pure linear AmmTx3 were obtained. Yield 46%. MS calculated 3825.91; found 3825.83.

4.2. Folding of AmmTx3

6.8 mg of linear AmmTx3 obtained by NCL was dissolved in 2 mL of a solution containing 0.1% formic acid in H_2O and added dropwise to 35 mL of 0.2 M Tris.HCl buffer at pH 8.2 while stirring. The mixture was mixed gently for 48 h at room temperature, acidified with formic acid and purified by semi-preparative RP-HPLC. After lyophilization 3.2 mg of pure folded AmmTx3 were obtained. Yield 48%. Purity 96%. MS calculated 3819.87; found 3819.77.

4.3. NMR Experiments

Samples of 1.2 $mmol.l^{-1}$ of AmmTx3 produced by NCL (1.0 mg dissolved in 220 µL of H_2O/D_2O (90/10) solution, pH = 4.5) and 0.6 mmol.l−1 of AmmTx3 produced by SPPS (0.5 mg dissolved in 220 µL of H_2O/D_2O (90/10) solution, pH = 4.5) were used for NMR experiments. All NMR spectra were recorded in 3 mm tubes on a BRUKER 700 Mhz NMR spectrometer equipped with a TCI cryoprobe, at 298 K: homonuclear 2D-COSY, -TOCSY (80 ms) and -NOESY (160 ms), and heteronuclear 1H − 15 N SoFast-HMQC with natural

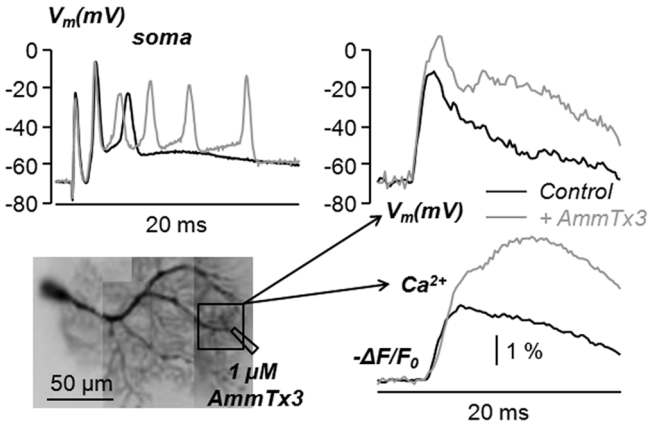

Fig. 5. Specific effect of AmmTx3-NCL on the V_m and Ca^{2+} signals associated with the CF synaptic potential. Top-Left. CF synaptic potentials recorded with a patch electrode from the soma. Bottom-Left. Image of the PN with a dendritic recording region of interest outlined; the position of the pipette delivering 1 µM AmmTx3 is also indicated. Top-Right. Dendritic V_m associated with the CF input. Bottom-Right. $-\Delta F/F0$ Ca^{2+} signals associated with the CF input. Black traces are in control conditions. Grey traces are after local application of AmmTx3-NCL.

abundancy (4096 scans). All spectra were processed with Bruker's TopSpin3.2 software and analysed with CcpNMR software.[24]

4.4. Structure calculations of AmmTx3-NCL

Sequential assignments of AmmTx3 produced *via* NCL were carried out following classical procedure; distance constraints were deduced from the volume integration of NOE correlations and introduced into the standard iterative calculation process of the Aria2.3 software.[25] For each Aria run, 500 structures per iteration were calculated, and 250 structures were performed in the final iteration in water. For the two first runs, ambiguous intersulfur constraints were introduced, an option assuming that a given half-cystine is part of a bridge without supposing a particular partner, then allowing all combinations of pairing. In the further Aria runs, after convergence of the calculation, covalent bonds between sulphur atoms involved in each defined bridge were introduced. Moreover, constraints corresponding to the H-bonds observed within the β-sheet were added. Finally, ten of the final structures in agreement with all the experimental data and with standard covalent geometry were selected. The quality of the structures was evaluated using the PROCHECK3.5 software.[26]

4.5. Constructs and transfections

The mouse pCMV-Script-Kv4.2 cDNA (NM_019697) was a generous gift from Dr. Jeanne M. Nerbonne (Washington University School of Medicine, St. Louis) and was previously described.[27] The human pCMV6-Entry-KCNIP1 (NM_014592) construct was purchased from Origene (Origene Technologies, Rockville, USA). The human pRC/RSV-DPP6S construct was a generous gift from Dr. Keiji Wada. The pEGFP-N1 plasmid was from Clontech Laboratories.

10xCOS-7 cells were transiently transfected using the OC-100 processing assemblies from the Maxcyte STX electroporation system (MaxCyte, Gaithersburg, MD) and used following the manufacturer's instructions. Co-transfections were performed as follows: 2 µg $K_v4.2$ plasmid, 6 µg DPP6S plasmid, 1 µg KCHIP1 plasmid and 1 µg eGFP plasmid. Transfected cells were plated onto P100 dishes and grown in DMEM supplemented with 10% FBS, 1% L-glutamine, 1% penicillin/streptomycin, at 37 °C with 5% CO_2. Cells were used for recordings 48 h after transfection.

4.6. Automated patch-clamp recording

Automated patch-clamp recordings were performed using the SynchroPatch 384PE (Nanion Technologies GmbH, Munich, Germany). Single-hole high-resistance chips (~10 MΩ) were used for the experiments. Before experiments, cells were washed with PBS and detached with trypsin-EDTA for 3 min. Trypsin was blocked with complete medium containing 10% FBS serum. Cells were then centrifuged 5 min at 900 rpm, and resuspended in patch-clamp extra-fill solution (composition in mM: NaCl 140, KCl 4, glucose 5, HEPES 10 (pH 7.4, NaOH)) for a 2×10^5 cells/mL final density. The cell suspension was maintained at 10 °C and shaked in a hotel reservoir prior to patch-clamp experiment. Whole-cell recordings were carried out at room temperature. Pulse generation and data collection were performed with PatchController384 V1.5.2 and DataController384 V1.5.0. Recordings were performed using an extracellular solution containing (in mM): NaCl 80, NMDG 60, KCl 40, $CaCl_2$ 2, $MgCl_2$ 1, glucose 5, HEPES 10 (pH 7.4, NaOH). Intracellular solution contained (in mM): KF 60, K-gluconate 50, KCl 30, NaCl 10, HEPES 10, HEDTA 10 (pH 7.2, KOH). For pharmacological experiments, compounds were first resuspended in milliQ water at a 1 mM stock concentration and then diluted in extracellular solution to different experimental concentrations.

For pharmacological investigation, currents were triggered with single step protocols. Holding potential was set at −90 mV and a 70 mV step was applied during 500 ms. Currents were recorded until they became stable. Sweep to sweep interval was 10 s. For voltage-dependent activation, holding potential was set at −90 mV and a series of test pulses from −60 mV to + 50 mV was applied in 10 mV increments with a 7 s sweep to sweep interval.

4.7. Data analyses and statistics

Electrophysiological data were analysed using the synchropatch 384PE datacontrol software version 1.5.0 and represented and statistically analysed using GraphPad Prism 5.02.

4.8. Evaluation of AmmTx3 effects on living neurons

The Cerebellar slice from a 25 postnatal days old C57Bl6 mouse was prepared as described in a recent report [28] with procedures approved by the Isere prefecture (Authorisation n. 38 12 01). The solutions and the equipment utilized were those described in other previous reports.[29] The patch clamp recording from a Purkinje neuron (PN) was performed to load the cell with the voltage-sensitive dye was JPW1114 and with 1 mM of the low-affinity Ca^{2+} indicator FuraFF, to combine dendritic membrane potential (V_m) and Ca^{2+} fluorescence recordings.[30] In particular, V_m fluorescence was calibrated in absolute values (in mV) using an established procedure,[31] and corrected for the junction potential (−11 mV) as previously estimated.[32] Ca^{2+} signals were expressed as negative fractional change of fluorescence (-ΔF/F0). Climbing fibre (CF) synaptic potentials were elicited by brief current pulses, of 5–20 µA amplitude and 100 µs duration delivered by a pipette placed near the recording cell. AmmTx3 was locally applied by pressure using a pipette placed near a distal dendritic region.

Acknowledgements

This work was supported by the Agence Nationale de la Recherche (ANR) LabEx "Arcane" support (ANR-11-LABX-0003-01) and LabEx "Ion Channels, Science and Therapeutics" (ANR-11-LABX-0015). MDW acknowledges financial support from Fondation Leducq, Région Pays de la Loire and FEDER. CZ acknowledges the Association Nationale de la Recherche et de la Technologie (ANRT) for its PhD financial support.

Appendix A. Supplementary data

Supplementary data to this article can be found online at https://doi.org/10.1016/j.bmc.2018.12.009.

References

1. Koh CY, Kini RM. *Toxicon.* 2012;56:497–506.
2. Willians JA, Days M, Heavners JE. *Expert Opin Pharmacother.* 2008;9:1575–1583.
3. Norton RS, Pennington MW, Wulff H. *Curr Med Chem.* 2004;11:3041–3052.
4. (a) Ahrén B. *Curr Diab Rep.* 2003;5:365–372
   (b) Holz GG, Chepurny OG. *Curr Med Chem.* 2003;10:2471–2483.
5. (a) Barrese V, Stott JB, Greenwood IA. *Annu Rev Pharmacol Toxicol.* 2018;58:625–648
   (b) Zhao W, Chen Y. *Curr Top Med Chem.* 2016;16:1877–1885
   (c) Mathie A, Veale EL. *Pflugers Atch.* 2015;467:931–943.
6. Aidi-knani S, Regaya I, Amalric M, Mourre C. *Behav Pharmacol.* 2015;26:91–100.
7. Maffie JK, Dvoretskova E, Bougis PE, Martin-Eauclaire M-F, Rudy B. *J Physiol.* 2013;591:2419–2427.
8. Vacher H, Alami M, Crest M, Possani LD, Bougis PE, Martin-Eauclaire M-F. *Eur J Biochem.* 2002;269:6037–6041.
9. (a) Raibaut L, Ollivier N, Melnyk O. *Chem Soc Rev.* 2012;41:7001–7015
   (b) Dawson PE, Kent SBH. *Annu Rev Biochem.* 2000;69:923–960.
10. De Rosa L, Russomanno A, Romanelli A, Domenico D'Andrea L. *Molecules.* 2013;18:440–465.
11. (a) Ollivier N, Dheur J, Mhidia R, Blanpain A, Melnyk O. *Org Lett.* 2010;12:5238–5241
    (b) Pattabiraman VR, Ogunkoya AO, Bode JW. *Angew Chem Int Ed.* 2012;51:5114–5118
    (c) Wang J-X, Fang G-M, He Y, et al. *Angew Chem Int Ed.* 2015;54:2194–2198
    (d) Terrier VP, Adihou H, Arnould M, Delmas AF, Aucagne V. *Chem Sci.* 2016;7:339–345.
12. Fang G-M, Li Y-M, Shen F, et al. *Angew Chem Int Ed.* 2011;50:7645–7649.
13. Huang Y-C, Fang G-M, Liu L. *Natl Sci Rev.* 2016;3:107–116.
14. Mlayah-Bellalouna S, Dufour M, Mabrouk K, et al. *Toxicon.* 2014;92:14–23.
15. Hackeng TM, Griffin JH, Dawson PE. *Proc Natl Acad Sci USA.* 1999;96:10068–10073.
16. Isidro-Llobet A, lvarez MA, Albericio F. *Chem Rev.* 2009;109:2455–2504.
17. Zheng J-S, Tang S, Qi Y-K, Wang Z-P, Liu L. *Nat Protoc.* 2013;8:2483–2495.
18. HPLC conditions: peptide elution was performed at a flow rate of 3 mL/min with a 5-65 % gradient of solvent B over 10 min with a Chromolith® High Resolution column (RP-18e, 150 Å, 10 x 4.6 mm). Solvents A and B were respectively 0.1% TFA in H2O and 0.1% TFA in MeCN.
19. HPLC conditions: peptide elution was performed at a flow rate of 1 mL/min with a 5-65% gradient of solvent B over 12 min with a Agilent AdvanceBio Peptide column (120 Å, 2.7 µm, 100 × 2.1 mm).
20. Schanda P, Brutscher B. *J Am Chem Soc.* 2005;127:8014–8015.
21. Cornet B, Bonmatin JM, Hetru C, Hoffmann JA, Ptak M, Vovelle F. *Structure.* 1995;3:435–448.
22. de la Vega CRR, Possani LD. *Toxicon.* 2004;43:865–875.
23. Otsu Y, Marcaggi P, Feltz A, et al. *J Neurosci.* 2014;84:137–151.
24. Vranken WF, Boucher W, Stevens TJ, et al. *Proteins.* 2005;59:687–696.
25. Rieping W, Habeck M, Bardiaux B, Bernard A, Malliavin TE, Nilges M. *Bioinformatics.* 2007;23:381–382.
26. Laskowski RA, MacArthur MW, Moss DS, Thornton JMJ. *Appl Cryst.* 1993;26:283–291.
27. Marionneau C, Carrasquillo Y, Norris AJ, et al. *J Neurosci.* 2012;32:5716–5727.
28. Ait Ouares K, Jaafari N, Canepari M. *J Neurosci Methods.* 2016;268:66–77.
29. Jaafari N, Canepari M. *J Physiol.* 2016;549:967–983.
30. Vogt KE, Gerharz S, Graham J, Canepari M. *J Physiol.* 2011;589:489–494.
31. Canepari M, Vogt KE. *PLoS ONE.* 2008;3 e4011.
32. Canepari M, Willadt S, Zecevic D, Vogt KE. *Biophys J.* 2010;98:2032–2040.

Received: 1 August 2018 | Revised: 7 September 2018 | Accepted: 14 September 2018

DOI: 10.1111/ejn.14251

REGISTERED REPORT (STAGE 2)

WILEY EJN European Journal of Neuroscience FENS

Opto nongenetics inhibition of neuronal firing

Karima Ait Ouares[1,2,‡] | **Corinne Beurrier**[3,‡] | **Marco Canepari**[1,2,4,‡] | **Gwenaelle Laverne**[3,‡] | **Nicola Kuczewski**[5,6,7,8]

[1]Univ. Grenoble Alpes, CNRS, LIPhy, Grenoble, France

[2]Laboratories of Excellence, Ion Channel Science and Therapeutics, Grenoble, France

[3]Aix Marseille University, CNRS, IBDM, Marseille, France

[4]Institut National de la Santé et Recherche Médicale, Paris, France

[5]CNRS, UMR 5292, INSERM, U1028, Lyon, France

[6]Lyon Neuroscience Research Center, Neuroplasticity and neuropathology of olfactory perception Team, Lyon, France

[7]University Lyon, Lyon, Franc

[8]University Lyon1, Villeurbanne, France

Correspondence
Nicola Kuczewski, Centre de Recherche en Neurosciences de Lyon, UMR CNRS 5292, INSERM 1028 Université Lyon1, Lyon, France.
Email:nicola.kuczewski@univ-lyon1.fr

Funding information
CNRS; Inserm; Lyon 1 University

Abstract

Optogenetics is based on the selective expression of exogenous opsins by neurons allowing experimental control of their electrical activity using visible light. The interpretation of the results of optogenetic experiments is based on the assumption that light stimulation selectively acts on those neurons expressing the exogenous opsins without perturbing the activity of naive ones. Here, we report that light stimulation, of wavelengths and power in the range of those normally used in optogenetic experiments, consistently reduces the firing activity of naive Mitral Cells (MCs) and Tufted Neurons in the olfactory bulb as well as in Medium Spiny Neurons (MSNs) in the striatum. No such effect was observed for cerebellar Purkinje and hippocampal CA1 neurons. The effects on MC firing appear to be mainly due to a light-induced increase in tissue temperature, between 0.1 and 0.4°C, associated with the generation of a hyperpolarizing current and a modification of action potential (AP) shape. Therefore, light in the visible range can affect neuronal physiology in a cell-specific manner. Beside the implications for optogenetic studies, our results pave the way to investigating the use of visible light for therapeutic purposes in pathologies associated with neuronal hyperexcitability.

KEYWORDS

cerebellum, hippocampus, mice, olfactory bulb, optogenetics, striatum

1 | INTRODUCTION

Since its conception and development at the beginning of this century, optogenetics have rapidly gained prominence in neuroscience research (Williams & Deisseroth, 2013) (Deisseroth, 2015). This technique uses genetic engineering to selectively express, in specific neuronal populations, light-sensitive proteins (opsins) initially obtained from nonmammalian species (Banghart, Borges, Isacoff, Trauner, & Kramer, 2004; Boyden, Zhang, Bamberg, Nagel, & Deisseroth, 2005). Exposure of the brain tissue to light at specific wavelengths activates these opsins and gates ionic flux through the cell membrane; it then modifies the membrane potential by activating or inhibiting the opsin-expressing neurons. The most widely used exogenous opsins in optogenetic experiments are channelrhodopsin 2 (ChR2) and halorhodopsin (NpHR). The first is a cation permeable channel that can be activated by visible light in the 350–550 nm range (experimentally activated mostly around 480 nm, blue light); stimulation of ChR2 produces membrane depolarization and neuronal

Abbreviations: AHP, afterhyperpolarization; AP, action potential; EPSP, excitatory postsynaptic potential; ES, effect size; MCs, mitral cells; MSNs, medium spiny neurons; R_m, membrane resistance; V_m, membrane potential; V_{rest}, resting membrane potential.

‡Equal contribution.

Edited by Chris Chambers. Reviewed by Quentin Gronau and D. Debanne. All peer review communications can be found with the online version of the article.

firing (Gradinaru et al., 2010). The second, NpHR, is a light-activated ionic pump selective for chloride ions that can be turned on by visible light in the 500–600 nm range (generally activated experimentally around 560 nm, yellow light); stimulation of NpHR produces membrane hyperpolarization and prevents neuronal firing (Gradinaru et al., 2010). Light-controlled firing of neuronal cells using optogenetics is therefore an extremely powerful tool to precisely determine the role of specific neuronal populations in brain physiology, brain pathology, and behavior (Deisseroth, 2015; Fenno, Yizhar, & Deisseroth, 2011). The interpretation of optogenetic experiments is based on the assumption that light stimulation selectively acts on those neurons expressing the exogenous opsins; however, several reports have shown that light can, in some cases, affect the physiology of naive neurons. While the action of infrared light (wavelength >700 nm) on neuronal physiology has been known since the early sixties (Arvanitaki & Chalazonitis, n.d.) and is well-documented (Deng, Goldys, Farnham, & Pilowsky, 2014; Shapiro, Priest, Siegel, & Bezanilla, 2013), few investigations have examined the effects of light in the visible spectrum on naive brain physiology. Christie et al., (2013) showed that blue laser light stimulation produces an fMRI signal in a rat cortex; an effect that has been attributed to direct vascular dilatation (Rungta, Osmanski, Boido, Tanter, & Charpak, 2017). Moreover, a recent report showed that in mice, laser stimulation at 532 nm increased the firing activity of prefrontal cortex neurons, in vivo (Stujenske, Spellman, & Gordon, 2015), depending on light power (~43% for 10 mW, ~31% for 5 mW and no modification for 1 mW). In both cases, the effect of the light appears to be due to an increase in brain tissue temperature. Such light-induced temperature increases depend on wavelength, power, and duration and could be attenuated by reducing the duty cycle of pulse light stimulation (Stujenske et al., 2015). Finally, our pilot experiments showed that LED stimulation (1 s stimulation with light in 470–570 nm range, with a power of 13 mW) consistently reduced the firing activity of Mitral Cells (MCs) recorded in vitro from olfactory bulb (OB) slices (see pilot data at https://osf.io/4fbpt/). Hence, light in the wavelength and power ranges used for optogenetic experiments appears to affect neuronal activity even in the absence of exogenous opsins. Investigating this phenomenon is important for at least two reasons. First, characterization of the action of visible light on naive neurons is crucial for the interpretation of optogenetic experiments, in order to exclude nonspecific effects. Second, optogenetics requires gene transfection, limiting its potential therapeutic utilization in humans, for example to prevent or reduce epileptic seizures (Bentley, Chestek, Stacey, & Patil, 2013). This limitation would be avoided if the activity of naive neurons could be controlled using light and this would open the way to investigating using visible light for therapeutic purposes.

The goals of the proposed research were the following:

- Reproduce the results reported in the pilot experiment
- Investigate whether and how light-induced inhibition of MC firing is affected by the light's power, wavelength, and duration in in vitro conditions.
- Determine the extent of any temperature modifications produced by light stimulation and so get information on potential correlations between this parameter and light-induced modifications of firing activity.
- Get insights into the cellular mechanisms of light-induced inhibition of MC firing (role of inhibitory network activity, role of G-protein coupled receptors, modification of membrane potential [V_m], modification of membrane resistance [R_m]), under in vitro conditions.
- Determine the effects of visible light on the firing activity of neuronal types other than MCs (hippocampal CA1 pyramidal neurons, cerebellar Purkinje neurons and striatal medium spiny neurons) under in vitro conditions.

2 | METHODS

The experiments were performed in three different laboratories, each working on a different preparation; namely: C. Beurrier's IC2N team (IBDM URM7288, Marseille) working on striatal medium spiny neurons (Striatum); M. Canepari's MOTIV team (Laboratoire Interdisciplinare de Physique Grenoble) studying cerebellar Purkinje neurons (Cerebellum) and N. Kuczewski's NEUROPOP team (Lyon Neuroscience Research Center, Lyon) using MCs and tufted cells from the olfactory bulb (OB) as well as hippocampal CA1 pyramidal neurons (Hippocampus). One of the principal purposes of this project was to determine whether the effect observed in the preliminary experiments of light on firing activity, is a generalizable phenomenon and independent of specific experimental conditions; for this reason, each laboratory worked using its own protocol for slice preparation and cell recording. The protocols for electrical and optical stimulations (light wavelength and power) of the neurons were the same in all laboratories.

The team FORGETTING (Lyon Neuroscience Research Center, Lyon) that was supposed to carry out the experiment in the hippocampus retired from the project after the stage 1 in principle acceptance. The proposed experiments in the hippocampus were therefore performed by N. Kuczewski and M Canepari.

The detailed experimental procedure (registered protocol), approved in a stage I submission, is available at https://osf.io/sf3eb/.

2.1 | Animals

Forty-one male C57Bl6/J mice (Charles River Laboratories, France) aged between 30 and 90 days were used. Mice were housed in groups of five in standard laboratory cages and kept on a 12 h light/dark cycle (at a constant temperature of 22°C) with food and water ad libitum. Experimental procedures were in accordance with the European Community Council Directive of 22nd September 2010 (2010/63/UE) on the care, welfare and treatment of animals. Procedures were reviewed by the ethics committee affiliated to the animal facility of the Grenoble university (D3842110001) and Lyon1 university (C2EA).

2.2 | Electrophysiology

2.2.1 | Olfactory bulb

Animals were anesthetized with an intraperitoneal injection of ketamine (50 mg/ml) and decapitated. The head was immediately immersed in ice-cold (2–4°C) carbogenized artificial cerebrospinal fluid (cACSF; composition: 125 mM NaCl, 4 mM KCl, 25 mM NaHCO3, 0.5 mM CaCl2, 1.25 mM NaH2PO4, 7 mM MgCl2, and 5.5 mM glucose; pH = 7.4) oxygenated with 95% O 2/5% CO2. The osmolarity was adjusted to 320 mOsm with sucrose. The OB was sliced horizontally (400 µm thick) with a vibratome. Slices were incubated in a recovery chamber, at 30 ± 1°C in the dark, using an ACSF solution with a composition similar to the cACSF, except that the CaCl2 and MgCl2 concentrations were 2 and 1 mM respectively. Slices were transferred to a recording chamber mounted on an upright microscope and continuously perfused with oxygenated ACSF (4 ml/min) at 30 ± 1°C. Neurons were visualized using a microscope (Zeiss axioscope) with a 40x objective (Zeiss Plan-APOCHROMAT). Data were acquired with an RK 400 BioLogic amplifier at a sampling frequency of 20 kHz using a 12-bit A/D-D/A converter (Digidata 1440A, Axon Instruments) and PClamp10Axon Instruments acquisition software. Patch-clamp whole-cell recordings were done using borosilicate pipettes with a resistance of 4–8 MΩ. The recording pipette was filled with the following intracellular solution (in mM): 126 K-gluconate, 5 KCl, 10 HEPES, 1 EGTA, 1 MgCl2, 2 ATP-Na2, 0.3 GTP-Na3, and 10 phosphocreatine; pH = 7.3, 290 mOsm). The membrane potential, measured with the patch pipette, was corrected for the junction potential (−15 mV). Data analysis was performed using OpenElectrophy (Garcia & Fourcaud-Trocmé, 2009), SciPy, and MySql database software (open source licenses).

2.2.2 | Cerebellum

The Prefecture of Isere approved the experiments on cerebellar Purkinje neurons, performed at the Laboratoire Interdisciplinaire de Physique (Authorization n. 38 12 01). Sagittal cerebellar slices (250 µm thick) were prepared from 30–45-day-old C57Bl6 mice following published procedures (Ait Ouares, Jaafari, & Canepari, 2016; Vogt, Gerharz, Graham, & Canepari, 2011a,b) using a Leica VT1200 (Leica, Wetzlar, Germany). Slices were cut in iced extracellular solution and incubated at 37°C for 30 min before use. The extracellular solution contained (in mM): 125 NaCl, 26 NaHCO3, 1 MgSO4, 3 KCl, 1 NaH2PO4, 2 CaCl2 and 20 glucose, saturated with 95% O2 and 5% CO2. The intracellullar solution contained (in mM): 125 KMeSO4, 5 KCl, 8 MgSO4, 5 Na2-ATP, 0.3 Tris-GTP, 12 Tris-Phosphocreatine, 20 HEPES, adjusted to pH 7.35 with KOH. Experiments were performed at 32–34°C using an Olympus BX51 microscope equipped with a 60X/1.0 NA Nikon objective. Patch-clamp recordings were done using a Multiclamp amplifier 700A (Molecular Devices, Sunnyvale, CA). The membrane potential, measured with the patch pipette, was corrected for junction potential (−11 mV) as described by Canepari, Willadt, Zecevic, & Vogt, (2010).

2.2.3 | Striatum

The methodology for striatum slices preparation differ from what is proposed in the manuscript approved in stage 1. This deviation is due to the fact that the new method increase the cell quality and survival in slices prepared from juvenile/adult mice (Ting, Daigle, Chen, & Feng, 2014). 30–45-day-old C57Bl6 mice were anesthetized with an intraperitoneal injection of ketamine and xylazine (100 and 10 mg/kg, respectively) and transcardially perfused with an ice-cold N-methyl D-glucamine (NMDG)-based solution containing (in mM): 93 NMDG, 2.5 KCl, 1.2 NaH_2PO_4, 30 $NaHCO_3$, 20 HEPES, 20 glucose, 10 $MgCl_2$, 93 HCl, 2 Thiourea, 3 sodium pyruvate, 12 N-acetyl cysteine and 0.5 $CaCl_2$ (saturated with 95% O_2 and 5% CO_2, pH 7.2–7.4). Immediately after decapitation the brain was removed, chilled in ice-cold oxygenated NMDG-based solution before cutting coronal slices (250 µm) with a vibratome (Leica, VT1000S) at 4°C. Slices were immediately transferred to recover in NMDG-based solution at 35°C for 5 min and then stored for at least 1 h at room temperature in normal ACSF (composition [in mM]: 126 NaCl, 2.5 KCl, 1.2 MgCl2, 1.2 NaH2PO4, 2.4 CaCl2, 25 NaHCO3, and 11 glucose), to which 250 µM kynurenic acid and 1 mM sodium pyruvate had been added. For the recordings, slices were transferred one at a time to a submersion-type chamber and perfused continuously with warm ACSF (32–34°C) at a rate of 3 ml/min. All solutions are continuously equilibrated with 95% O2/5% CO2. Neurons were visualized using an upright microscope (Nikon Eclipse FN1) equipped with a DIC optic and using a 40x water-immersion objective. Electrophysiological recordings were made with a Multiclamp 700B amplifier and Clampex 10.6 software (Molecular Devices). Patch-clamp electrodes (4–6 MΩ) were filled with an intracellular solution

containing (in mM): 126 KMeSO4, 14 KCl, 3 MgCl2, 0.5 CaCl2, 5 EGTA, 10 HEPES, 2 NaATP and 0.5 mM NaGTP, 10 Na-Phosphocreatine, pH adjusted to 7.25 with NaOH and osmolarity adjusted to 270–280 mOsm/L.

2.2.4 | CA1 areas of the hippocampus

The equipment used for slice preparation differs from that presented in the manuscript approved in stage 1. Such divergence is due by the fact that these experiments were done in a different laboratory of that originally planned.

Coronal brain slices (350 μm) were cut from 8–10-week-old C57Bl6 mice with a vibratome (VT1000S, Leica) and incubated at 33°C for 30 min and then left for at least 30 min at room temperature in artificial cerebrospinal fluid (aCSF) containing (in mM): 124 NaCl, 10 glucose, 1.25 NaH2PO4, 2.5 KCl, 26 NaHCO3, 1.3 MgCl2, and 2.5 CaCl2 and superfused with a gaseous mixture (95% O2 and 5% CO2). Slices were transferred to a recording chamber maintained at 33°C. For whole-cell current-clamp recordings of CA1/CA3 pyramidal cells, the patch pipettes were made of borosilicate glass (~5 MΩ) filled with the following solution (in mM): 120 potassium methyl sulfate, 10 Na-phosphocreatine, 0.1 CaCl2, 2 MgCl2, 10 HEPES, 1 EGTA and 2 Na-ATP, 0.5 mM NaGTP(300 mOsm, pH = 7.2). Neurons were visualized using a microscope (Zeiss axioscope) with a 40x objective (Zeiss Plan-APOCHROMAT). The data were acquired with the RK 400 BioLogic amplifier at a sampling frequency of 20 kHz using a 12-bit A/D-D/A converter (Digidata 1440A, Axon Instruments) and PClamp10Axon Instruments acquisition software.

2.3 | Temperature measurement

Slice and bath temperature were measured and controlled using a ThermoClamp™ -1 from Atomate Scientific.

2.4 | Optical stimulation

2.4.1 | Olfactory bulb, cerebellum, and hippocampus

With the olfactory bulb two wavelength ranges were used: (a) 430–495 nm peaked at 470 nm (blue light) using a Dual Port OptoLED, CAIRN, UK, dichroic mirror 495 nm, Zeiss; (b) 470–570 nm peaked at 540 nm (green/yellow light) using a white LED Dual Port OptoLED, CAIRN, UK with excitation 470 nm high-pass filter and 570 nm dichroic mirror, Zeiss. Only blue light was used in the cerebellum and hippocampus experiments.

2.4.2 | Striatum

Controlled by the acquisition software, blue light (470 nm) was delivered from a Spectra Light Engine (Lumencor, Optoprim) and connected to the back aperture of the microscope through a 3 mm liquid-core fiber, producing a wide-field exposure around the recorded cell. Its power on leaving the microscope objective was measured using a PM100 power meter via a S130C probe (Thorlabs).

2.5 | Proposed experiments:

2.5.1 | Experimental procedure

The present project is divided into two stages:

Stage one is aimed at reproducing the results observed in the pilot experiment, namely a reduction in MC firing frequency produced by light illumination in 470–570 nm range (green/yellow) during whole-cell recordings (stage 1 manuscript: https://osf.io/sf3eb/, Figure 4), and determining if these results depend on light intensity and/or light wavelength.

Stage 1 experiment 1: to determine whether the effect on MC firing activity produced by light stimulation in 470–570 nm range (green/yellow) depends on light intensity, we will use three light intensities: 13, 5, and 1 mW (stage 1 manuscript: https://osf.io/sf3eb/, Figure 4a). The first is the power used in the pilot experiments; the second and the third that produced an increase or no modification of firing activity in cortical neurons in vivo respectively (Stujenske et al., 2015). All these light intensities are commonly used in optogenetic experiments.

Stage 1 experiment 2: to determine whether the light effect depends on light wavelength, we will use the same protocol as the one described in experiment 1 but with 430–495 nm light stimulation (blue).

Stage one analysis

For each recorded neuron and for each intensity (depicted in Figure 4a), the effect of light will be assessed by a statistical comparison between the number of spikes in NO LED and LED conditions, using a paired unilateral test. For each comparison, the results will be reported as shown in Figure 2b. The sample size for this experiment is based on the pilot experiments. As shown in stage 1 manuscript, Figure 2d, the estimated effect size of light on MC firing is ES = −0.9. Using this value as target effect size, we have chosen the sweep sample size, i.e., the number of traces acquired for each neuron recorded (see stage 1 manuscript: https://osf.io/sf3eb/ Figures 1a, 2a), to be $n = 30$. This value predicted a statistical power of 0.999. It should be noted that even if the real ES is closer to the lower limit of the 95% CI (ES = −0.6), the statistical power is still above 0.9 (ES = 0.94). The authenticity of the effect will also be assessed by assuming that the null hypothesis, i.e., "light has no effect", is true and by computing the probability to have observed by chance at least n statistically significant results

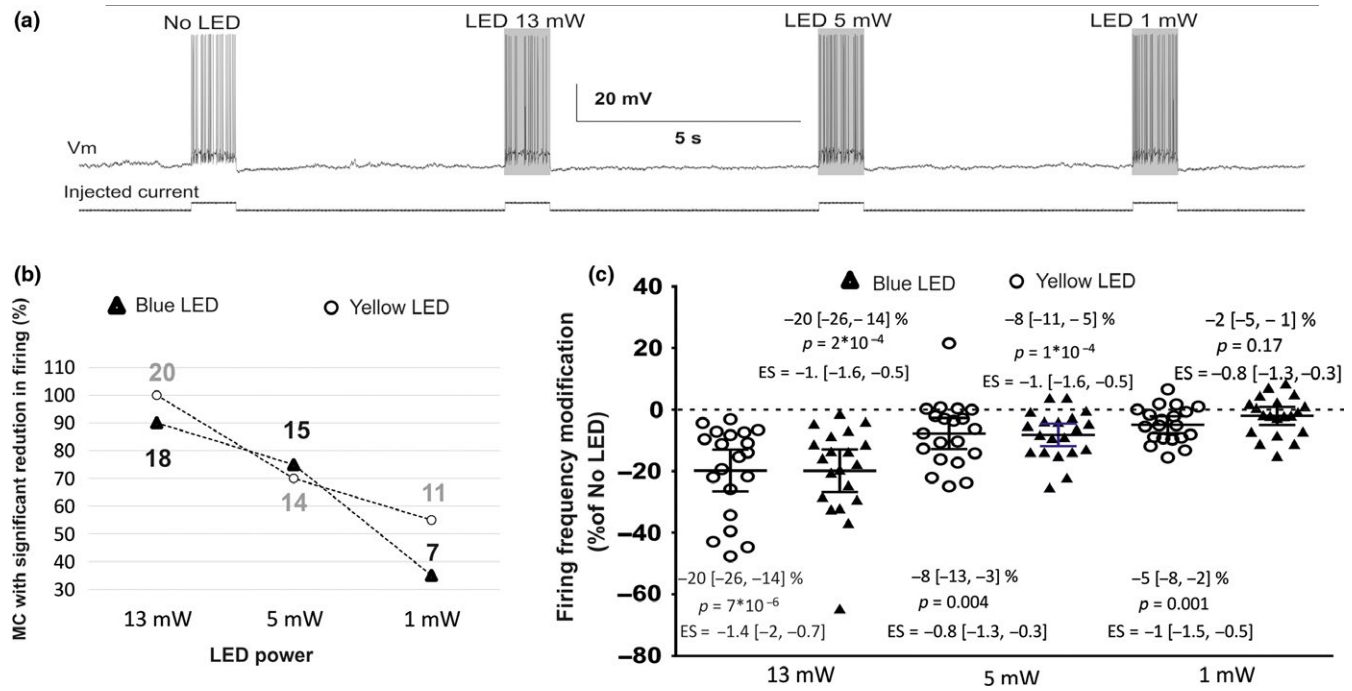

FIGURE 1 The reduction in the evoked mitral cells (MC) firing by LED stimulation depends on light power but not wavelength. (a) Representative example of LED effect on evoked MC firing. (b) Cell- by-cell analysis depicting the number and the percentage of neurons for which the LED stimulation (blue or yellow light) produce à significant ($p < 0.05$) reduction in MC firing, compared with no-LED condition. (c) Population analysis of the effect of blue and yellow LED stimulation on MC firing. Horizontal lines represent average. Error bars represent 95% CI. Gray bars in A depict the time of LED stimulation. $n = 20$ MC. ES: Effect Size

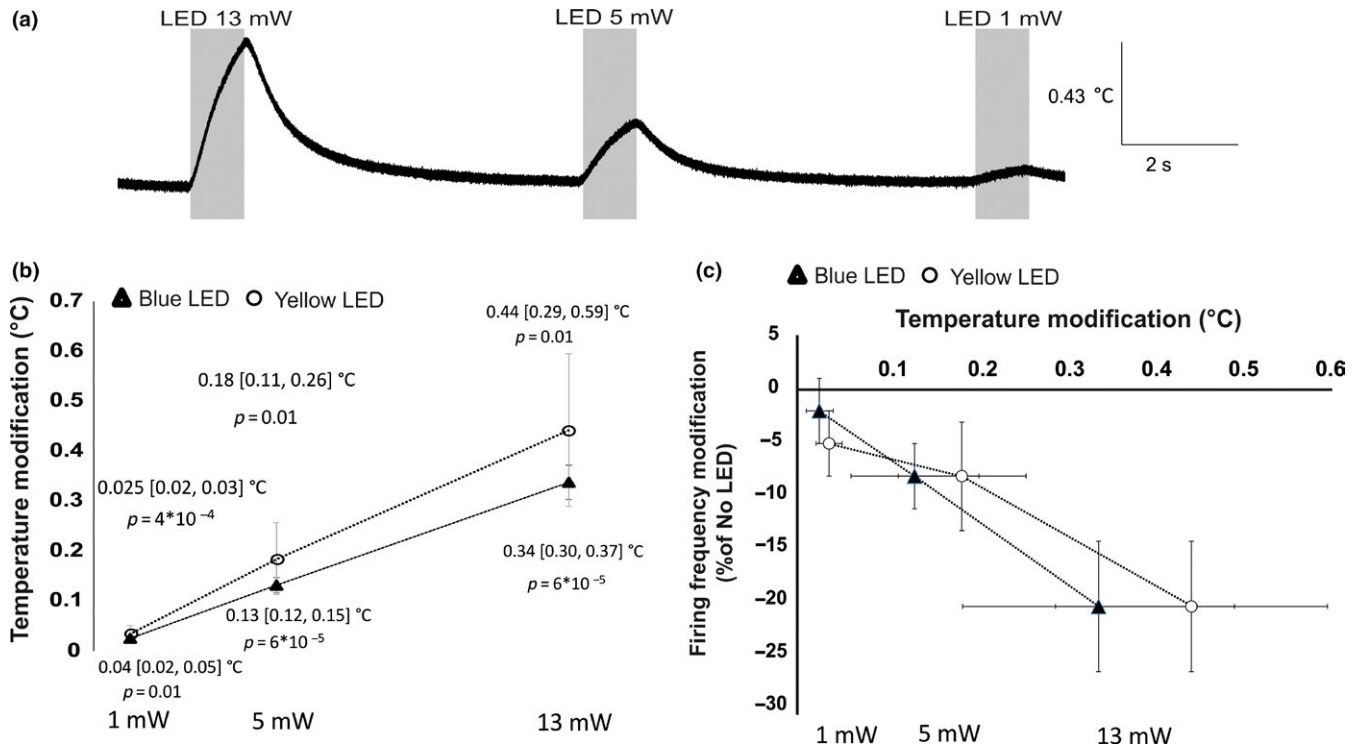

FIGURE 2 Tissue temperature modifications produced by LED stimulation at different powers and wavelengths. (a) Example of temperature modifications induced by blue LED stimulation. (b) Average temperature modification, compared with prelight temperature, during one-second stimulation with blue and yellow LEDs. *p*-values refer to comparisons between light and prelight temperatures. (c) Covariation of the effects of light on MC firing (data from Figure 1) and slice temperature. Error bars represent 95% CI. Blue light $n = 5$; yellow light $n = 4$

over N total comparisons. This probability value is obtained by the following equation:

$$P(h \geq n) = \sum_{h=n}^{N} C(N,h)\, p^h (1-p)^{N-h} \quad (1)$$

where $p = 0.05$, $N =$ the total number of recorded neurons and $n =$ the number of neurons for which the p-value is <0.05. For our pilot experiment, where $N = 11$ and $n = 7$ (see stage 1 manuscript: https://osf.io/sf3eb/, Figure 2b), this probability is equal to $2*10^{-7}$. In other words, the probability that the observed significant results are due exclusively to a repetition of type I error is $2*10^{-7}$. Three populations analyses, one for each intensity, will be made by comparing the average number of spikes of each recorded neuron in the NO LED condition to the average number of spikes in the LED condition. The result will be presented as % of modification, i.e., (average spike LED-average spike NO LED)/average spike NO LED, such as in Figure 2e).

The size effect of the population analysis showed in Figure 2e is ES = −1.07. Using this estimation as a target ES, a sample size of 20 neurons gives a predicted statistical power of 0.998.

It should be noted that we expect to reduce the effects of light on MC firing by decreasing light power and by increasing light wavelength (Stujenske et al., 2015; Senova et al., 2017); what would probably reduce the ES when using a light power lower than 13 mW (the one used in the pilot experiments). For $n = 30$ sweeps in the neuron by neuron analysis and $n = 20$ neurons in the population analysis, the statistical power becomes lower than 0.9 for ES < 0.54 and ES < 0.68 respectively. However, the utilization of equation 1 will still allow to reliably detect genuine light effects even for much lower effects size. For example, with an ES = 0.2 the statistical power on neuron by neuron analysis is 0.28. By repeating the experiment 20 times (20 recorded neurons) we should expect to observe ~ 5 neurons over 20 for which the p-value<0.05. Replacing these values in equation 1 give a probability of 0.002. Since this is the probability that the observed significant effects are due exclusively to a repetition of type I error, such value will constitute an argument to reject the null hypothesis.

Stage two will be performed only if stage one will reproduce the results of the pilot experiment. This stage is aimed to investigate: (a) the physical and physiological mechanisms of light effects on neuronal firing. (b) Whether light effect on MC firing is a phenomenon generalizable to other neuronal types. For stage two, light wavelength and power will be those that produced the maximum effect in stage 1 experiments. The sample size will be determined upon knowledge of stage 1 results as follows: the neuron analysis and population analysis ES's, observed in the experimental condition (light power and light wavelength) that produce the maximal effect in stage one, will be used to determine the number of sweeps and the number of neurons that give a statistical power equal to 0.95.

Experiment 4 bis, 6,7, and 8 should be considered exploratory. No statistical power is estimated a priori.

Stage 2 experiment 1–2: The goal is to determine whether the light-induced modification of MC firing is due to temperature changes.

Stage 2 Experiment 1: Determine the slice temperature modification produced by LED stimulus. The experiment will be performed by putting a temperature probe in the slice. The protocol is depicted in Figure 4b of stage 1 manuscript: https://osf.io/sf3eb/. Statistical effect will be assessed by paired unilateral test between the average slice temperature measured for one-second (T_{Ctr}) before light stimulation and the average slice temperature measured during one-second of light stimulation (T_{LED}). No electrophysiological recording will be made. For this experiment the two wavelengths of stage 1 will be used. This will allow to correlate an eventual difference between blue and yellow light effects, observed in stage 1, with an eventual difference in their hitting effects.

Stage 2 Experiment 2: Determine the impact of the slice temperature modification produced by LED stimulus (measured in experiment 1) on MC firing. The protocol is depicted in Figure 4c of stage 1 manuscript: https://osf.io/sf3eb/. The bath temperature in the recording chamber will be modified while performing CC recording on MC. Statistical effect will be assessed by umpired bilateral test between the number of action potentials elicited in T_{Ctr1} and the number of action potentials elicited in the condition T_{LED} spike. The number of action potentials elicited in the condition T_{Ctr2} will be evaluated to assess the reversibility of an eventual effect produced by the temperature modification. No LED stimulation will be made. MC will be recorded in the same dark ambient light condition used for the other experiments.

Stage 2 experiment 3: The goal is to determine whether the effect of light on MC firing depends on light duration. The protocol used is depicted in stage 1 manuscript, Figure 4d. The number of spikes in LED1, LED2, and LED3 condition will be compared using ANOVA (repeated measures) followed by post hoc paired test. Paired test comparisons between NO LED and LED1 conditions will be performed in order to make sure of the presence of the light effect. Unilateral test will be used.

Stage 2 experiment 3 bis: The goal is to determine the modification of slice temperature produced by increasing light duration. These results will be correlated with the eventual differences on MC firing activity produced by the modification of light duration (Stage 2 experiment 3). The protocol is similar to that described in *Stage 2 Experiment 1* and Figure 4b of stage 1 manuscript: https://osf.io/sf3eb/with T_{LED} measured in the last second of light stimulation.

Stage 2 experiment 4: The goal is to determine whether the effect of light on MC firing is a consequence of light-induced increase in inhibitory interneurons activity. The same protocol used in the pilot experiments (stage 1 manuscript: https://osf.io/sf3eb/, Figure 2a) will be used but with LED stimulation at the power and wavelength that produced the maximal effect in stage 1 experiments and in the presence, in the extracellular solution, of the GABAA receptors antagonist SR-95531 (Gabazine, 5 μM) and of the GABAB receptors antagonist CGP 55845 (10 μM). For each recorded neuron, light effect will be assessed by a statistical comparison between the number of spikes in the NO LED and LED conditions, using a paired unilateral test. Population analysis will be performed as previously described.

Stage 2 experiment 4 bis : This experiment will be performed only if, in Stage 2 experiment 4, Gabazine will prevent the light-induced reduction in MC firing. The same protocol described in stage 2 experiment 4 will be used but while recording from Granuler Cells (GC). For each recorded neuron, light effect will be assessed by a statistical comparison between the number of spikes in the NO LED and LED conditions, using a paired bilateral test. Population analysis will be performed as previously described.

Stage 2 experiment 5: The goal is to determine whether the effect of light on MC or GC firing is mediated by the activation of G-protein-coupled receptors. For this reason, the same protocol used in the pilot experiments (stage 1 manuscript: https://osf.io/sf3eb/, Figure 2a) will be used with LED stimulation at the power and wavelength that produced the maximal effect in stage 1 experiments. However, in order to block G protein activity, we will replace the GTP-Na3 in the intracellular solution with 2 mM of the nonhydrolyzable GDP analog Guanosine 5′-[β-thio]diphosphate trilithium salt (GDPβS), a G protein inhibitor. For each recorded neuron, light effect will be assessed by a statistical comparison between the number of spikes in the NO LED and LED conditions, using a paired unilateral test. The cellular type recorded in this experiment will depend on the outcome of stage 2 experiment 4. If GC is recorded, the sample size will be determined based on the effect size calculated from stage 2 experiment 4bis, to give a statistical power equal to 0.95.

Stage 2 experiment 6: The goal is to determine whether the light modifies neuronal membrane conductance and/or membrane resistance (R_m). The experiments will be performed in voltage-clamp configuration with neurons maintained at −60 mV. The protocol is depicted in Figure 4c. The effect of light on holding current will be quantified by comparing the average current in the control period with the average current during the one-second light stimulation (LED1). Light effect on R_m will be assessed comparing R_m in No LED to R_m in LED2. R_m is calculated according to Ohm's law R = V/I; where I is median current in the last 100 ms of hyperpolarizing step and $V = -5$ mV. Statistical effect will be assessed by paired bilateral test. The cellular type recorded in this experiment will depend on the outcome of stage 2 experiment 4. If GC is recorded, the sample size will be determined based on the effect size calculated from stage 2 experiment 4bis, to give a statistical power equal to 0.95.

Stage 2 experiment 7: The goal is to determine whether the light modifies the membrane potential (V_m) and/or the action potential (AP) parameters. The experiments will be performed in current-clamp configuration at resting membrane potential or after slight hyperpolarization to prevent spontaneous firing. The protocol is depicted in Figure 4e. Light effect on V_m will be assessed by comparing the average V_m in the control period (1 s before light stimulation) to the average V_m during 1 s of light stimulation (LED1). Statistical effect will be assessed by paired bilateral test. Light effect on AP will be assessed by generating a single action potential by a 5 ms positive current injection both in the absence (NO LED) and presence (LED) of light. Two AP parameters will be evaluated: AP amplitude, calculated as the difference between AP peak and the average V_m in the 100 ms that precedes the current step, and AP latency, calculated as the time between the beginning of the current step and AP peak (Duménieu, Fourcaud-Trocmé, Garcia, & Kuczewski, 2015). Statistical effect will be assessed by paired bilateral test. For the experiments on AP, the α risk, corrected for multiple comparison (2), will be $\alpha = 0.025$. The cellular type recorded in this experiment will depend on the outcome of stage 2 experiment 4. If GC will be recorded, the sample size will be determined based on the effect size calculated from stage 2 experiment 4bis, to give a statistical power equal to 0.95.

Stage 2 experiment 8: Determine the light effect on the firing activity of tufted cells in the OB, hippocampal CA3/CA1 pyramidal neurons, cerebellar purkinje neurons, and striatal medium spiny neurons. These experiments will be performed in three different laboratories. The same protocol used in the pilot experiments (stage 1 manuscript: https://osf.io/sf3eb/, Figure 2a) will be used but with LED stimulation at the power and wavelength that produced the maximal effect in stage 1 experiments. For each recorded neuron, light effect will be assessed by a statistical comparison between the number of spikes in the NO LED and LED conditions, using a paired unilateral test. Population analysis will be performed as previously described. For each of the cellular types investigated the results will be graphically presented as in Figure 2. For these experiments, the α risk, corrected for multiple comparison (4), will be $\alpha = 0.0125$ and the sample size will be adapted to keep the statistical power = 0.95.

2.6 | Statistics

Statistical comparisons will be performed using parametric or nonparametric tests depending on the normality of distributions, which will be assessed by D'Agostino Pearson

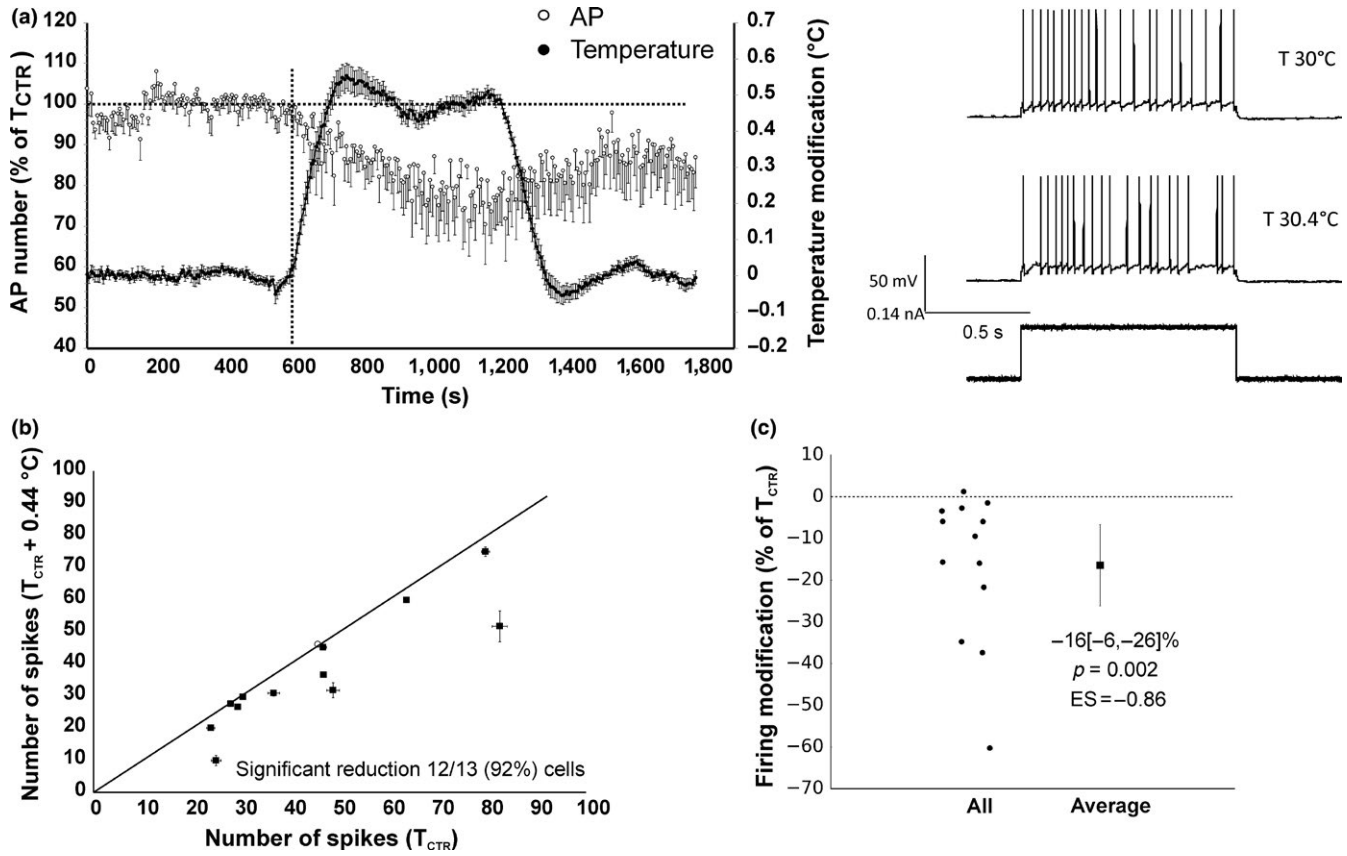

FIGURE 3 Mitral cells (MC) firing is reduced by temperature increase. (a) Time plot of the relative modification of the number of evoked APs produced by the increase in temperature in the recording chamber. The number of APs was normalized to the average number of APs in the first 600 s. Error bars represent sem. Vertical dashed line represents the start time for chamber warming. Right; representative traces. (b) Cell-by-cell analysis of temperature effect on MC firing. Empty dots depict MCs for which no significant difference was observed between the two conditions. Error bars represent 95% CI. (c) Population analysis of temperature effect on MC firing. Error bar represents 95% CI. $n = 13$ MC. ES: Effect size

test: a paired *t*-test or a Wilcoxon signed-rank test will be used for normal and nonnormal distributions respectively. As our working hypothesis is that light produces a decrease in neuronal firing, as shown by the pilot data, unilateral test will be used to compare the light effects on neuronal firing. Experiments in which no a priori hypothesis is made (light action on V_m, R_m, and AP parameters), data will be compared using a bilateral test. For normally distributed data the ES is calculated as Cohen's d effect size (the mean of the sample difference divided by the standard deviation of sample difference). For nonnormal data distributions, the effect size r is calculated using Kerby simple difference formula (Kerby, 2014) as follow: $r = (S\text{-}t)/S - t/S$, where $t =$ the test statistic, is the minimal rank sum; S is the total rank sum and $S\text{-}t$ is the maximal rank sum. The 95% CI for the Choen d ES is calculated using the ci.sm function of the R MBESS package. Statistical power and sample size are calculated by using G*Power 3.1.9.2 (Faul, Erdfelder, Lang, & Buchner, 2007) (Dusseldorf university). Results are presented using the following notation a[b,c] where a is the data average and b and c the lower and the higher limit of 95% CI respectively All data analysis will be graphically represented as shown in stage 1 manuscript: https://osf.io/sf3eb/, Figure 3. Bayesian statistics were performed using JASP SOFTWARE (JASP Team (2017). JASP (Version 0.8.5)[Computer software]).

2.7 | Exclusion criteria

Cells were excluded from experiments when (a) their resting membrane potential (V_{rest}) was above −50 mV, (b) when the step depolarization in the no-LED condition did not elicit at least 10 action potentials (AP), (c) when the starting V_m (calculated in the 100 ms preceding the depolarizing current step) in the no-LED condition differed by more than 5 mV from the starting V_m in the LED condition or iv) when the access resistance was higher than 50 MΩ. Cells were a priori excluded from the analysis when the defined sweep sample size was not reached due to a loss or degradation of neuronal whole-cell recording, that is, for experiments performed in the current-clamp configuration a depolarization of V_{rest} above 50 mV and for the voltage-clamp condition an access resistance greater than 50 MΩ.

TABLE 1 Bayesian statistic on light effect at different light power and wavelengths (bayesian one sample *t*-test, JASP software)

	Blue light			Yellow light		
	Prior ES	Posterior ES	BF	Prior ES	Posterior ES	BF
13 mW	1.07	1.27	5635	1.07	1.28	6579
5 mW	0.49	0.94	341	0.49	0.61	20
1 mW	0.18	0.19	1.57	0.12	0.63	24

Prior ES at 13 mW was estimated from the pilot experiment. Estimation of prior ES at 5 mW et 1 mW is calculated from the posterior ES observed, respectively, at 13 mW and 5 mW, supposing a linear modification of the ES whit the light power, i.e., prior $ES_{5mW} = ES_{13\ mW}/13 * 5$; prior $ES_{1\ mW} = ES_{5mW}/5$.

3 | RESULTS

All electrophysiological raw traces and data analysis are accessible on the Open Science Framework web site (https://osf.io/mrw93/).

3.1 | Changes in MC firing with light power (Stage 1 experiments 1–2)

In order to assess whether the light-induced reduction in MC firing activity observed in the preliminary data depends on light wavelength and/or power we applied the protocol depicted in Figure 1a for two different stimuli, 430–495 nm light (blue LED) and 470–570 nm light (green/yellow LED) ($n = 20$ MC for each type of stimulus, 5 animals). As shown in Figure 1 (see https://osf.io/ejh2u/, https://osf.io/fpd6y/for the experimental design and supplemental analysis), the reduction in firing frequency produced by LED-stimulation decreased at lower power intensities for both the wavelengths used (power effect: blue LED $p < 0.001$, $F = 33$; Yellow LED $p < 0.001$, $F = 17$, ANOVA). This decrease applied both to the percentage of neurons affected by the light (Figure 1b) as well as to the average effect of the light on the MC population (Figure 1c). While green/yellow light produced a significant reduction in firing at all powers tested, statistical comparison failed to show a significant reduction in MC firing when blue light was used at 1 mW ($p = 0.17$). It should, however, be noted that under this condition we still observed a significant decrease in firing in 35% of recorded neurons. Applying equation 1 shows that the probability of such a decrease being observed only by chance is $p = 3*10^{-5}$ suggesting that the absence of a significant effect in the population analysis is likely due to type II error consequent to a lower effect size at this light power. Comparison of the effect at different wavelengths did not show any difference between blue and green/yellow lights ($p = 0.75$, $F = 0.1$ ANOVA). The Bayesian statistics for this analysis are shown in Table 1. A decline in MC firing due to dialysis of intracellular components in whole-cell recordings could sometimes be observed in our experiments. To check whether this phenomenon contributed to reduction in MC firing when stimulated with light, we made a paired comparison between LED firing of trace acquisitions n and the no-LED firing of trace acquisitions $n + 1$ (shifted analysis). As shown in the exploratory analysis presented in Figure S1, the results produced by the shifted analysis do not qualitatively differ from those of a normal analysis, indicating that cell dialysis did not impact the quantification of the effect of light on firing activity.

3.2 | The increase in temperature produced by light is able to inhibit MC firing (Stage 2 experiments 1–2)

The parameter most likely affected by light is temperature. Temperature changes produced by LED stimulation were measured by approaching a temperature probe to the top of OB slices. As shown in Figure 2(a,b), a rapid and gradual increase in temperature was observed during a 1 s exposure to light. The mean temperature increased linearly with power for the two wavelengths tested (blue light $p < 0.0001$ $n = 5$, 1 animal; yellow light $p = 0.01$, $n = 4$, 1 animal; repeated measurement ANOVA). By plotting the effect of light on MC firing versus the effect of light on tissue temperature (Figure 2c), a linear covariation in these two parameters was observed, suggesting that light-induced temperature modification and firing reduction are correlated. To confirm this link between temperature and firing, we tested whether variations in temperature affected MC firing frequency by increasing the bath temperature in the recording chamber while monitoring firing activity induced by current pulses, in the absence of light. The average increase in bath temperature was 0.44 ± 0.04°C, that is, similar to that produced by 1 s LED stimulation at 13 mW. A gradual decrease in firing frequency was produced by heating the recording solution (Figure 3a, $n = 14$ MC, 5 animals). The effect of temperature was long-lasting and partially reversed 5 min after restoration of the initial bath temperature (Figure 3a). The decrease in firing was significant in 92% of the recorded MCs (Figure 3b). On average, the temperature increase modified MC firing by −16 [−6, −26] % (Figure 3c), similar to the decrease in firing activity produced by a 1 s LED stimulation at 13 mW (see Figure 1 and Figure 2c). All these data suggest that the effects of light on MC firing are mainly due to light-induced temperature increases. In the following

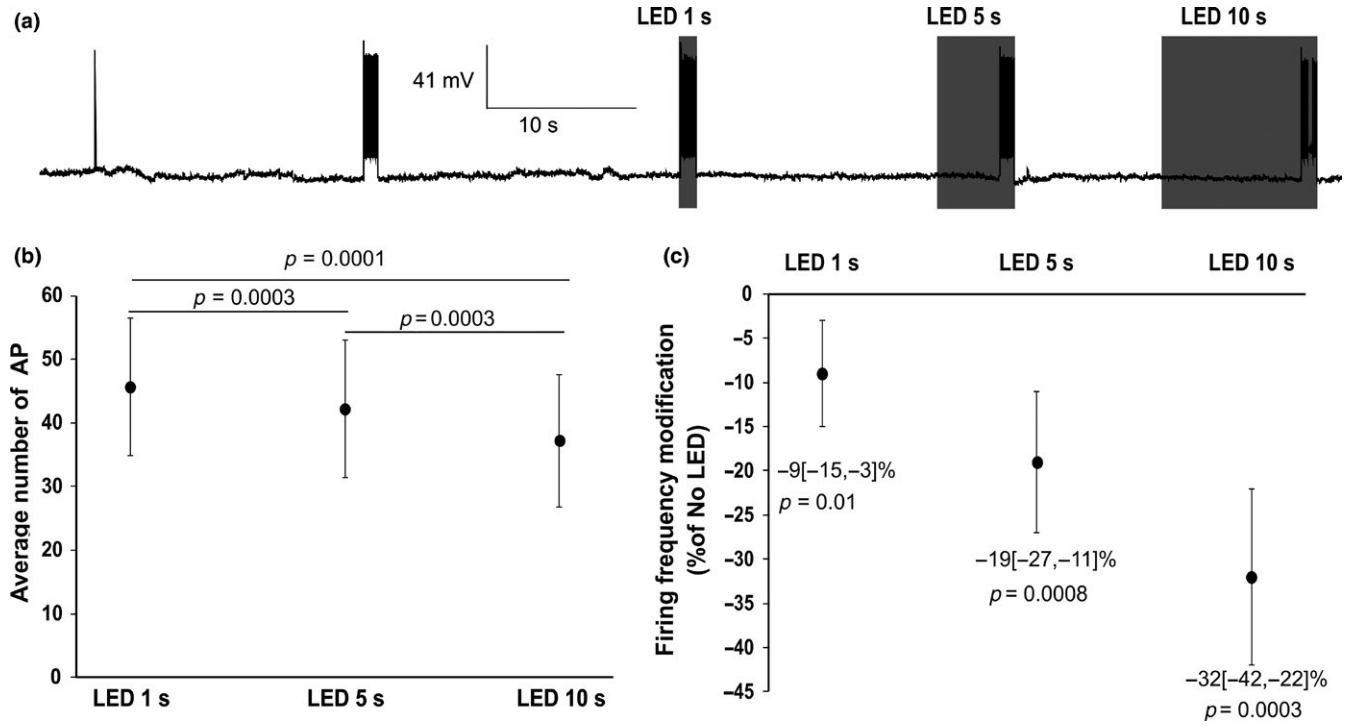

FIGURE 4 The effect of blue light (13 mW) on mitral cells (MC) firing increases with stimulus duration. (a) Example of the effect of blue light stimulations on evoked MC firing; depolarizing current steps inducing firing are omitted from the figure. (b) The average number of evoked action potentials decreases with increase in light duration. (c) Relative modification of firing frequencies produced by light stimulation at different durations; p-values refers to comparisons between no-LED and LED conditions. Error bars represent 95% CI. $n = 11$MC

experiments, only blue light at 13 mW was used and the sample size was determined from the results shown in Figure 1. As the effect size (ES) for the action of light on single MCs is −1 [−1.2 to 0.8] in cell-by-cell analysis, the number of sweep repetitions required to reach a statistical power = 0.95 is $n = 13$. The ES for population analysis is −1.07 [−1.62 to 0.51] and the number of recorded neurons to attain a statistical power of 0.95 is $n = 11$, except for experiments illustrated in Figure 12, where correction for multiple comparisons required $n = 16$ neurons to attain a power of 0.95.

3.3 | MC firing increases with duration of light stimulus (Stage 2 experiments 3-3bis)

To determine whether the impact of light stimulation on firing activity depends on its duration, we used the protocol depicted in Figure 4a. Unexpectedly, many neurons showed a hyperpolarization of V_{rest} associated with a strong decrease in evoked firing activity recorded in the no-LED condition when the procedure was repeated. This reduced firing could not be prevented by bringing V_{rest} to its initial value through steady current injection, or by increasing the depolarizing stimulus (for an individual example, see Figure S2). Both the V_m hyperpolarization and firing reduction persisted until the end of the recording session, suggesting that light can sustainably impact cellular physiology in addition to its acute effect on firing during light stimulation. Such long-lasting effects were not observed with short stimuli (1 s, Figure 1). These effects prevented us from using the number of repetitions compatibles with the exclusion criteria, that is, at least 10 action potentials in the no light stimulation condition. Consequently, we reduced the number of repetitions required for a cell to be accepted from $n = 13$ to $n = 10$, but thereby reducing the statistical power to detect the effect in cell-by-cell analysis to ~0.90. Applying these new criteria, we observed a significant decrease in evoked APs for all light durations (1, 5 and 10 s) but that was more pronounced at longer durations (Figure 4b,c, $n = 11$ MC, 4 animals). We used shifted analysis to assess whether the long-lasting effects of light (irreversible V_m hyperpolarization and firing reduction) impact the evaluation of its acute effects (reduction in firing during light pulses) (exploratory analysis, Figure S3). In this condition, a significant reduction in firing was only observed with 10 s light pulses showing that the long-lasting effects mask the acute effects of short pulses. It should, however, be noticed that, despite the decline in firing, the number of AP during 10-second light stimulation of acquisition trace n is significantly lower than that observed during the 1-second light stimulation of acquisition trace $n + 1$ (Figure S3b), suggesting that acute light effect increased with light duration. We next wondered whether the long-lasting effects of light

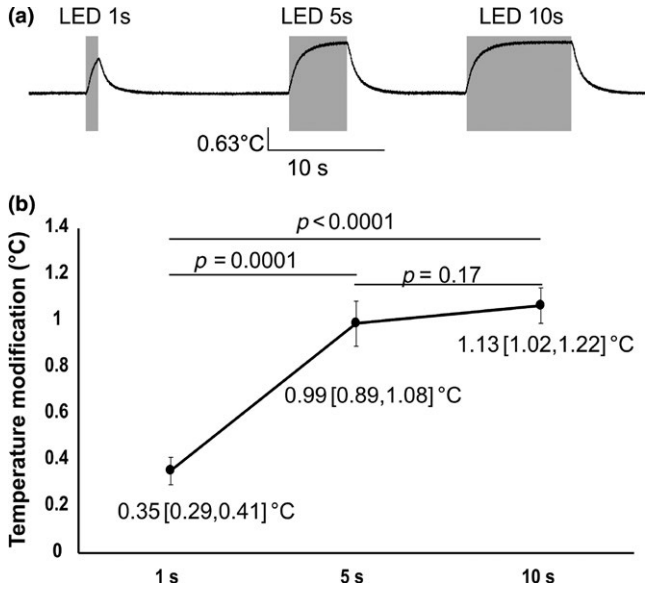

FIGURE 5 Modifications to slice temperatures vary with light duration.(a) Example of the modification of OB slice temperature produced by light stimulation (blue; 13 mW) of different durations. (b) Average temperature modification produced by the different durations ($n = 4$). Error bars represent 95% CI

were also related to temperature changes. Slice temperature increased with increasing light duration ($p < 0.0001$; ANOVA), but such an increase was not significant between 5 and 10 s LED stimulations (Figure 5a,b; Bayesian statistics for this analysis are shown in Table 2). The maximal light-induced temperature increase we observed (around 1°C) is in the range of the physiological fluctuations of the brain (Andersen & Moser, 1995) or of the bath temperature during in vitro slice experiments. It is therefore very unlikely that the long-term alterations of the physiological properties of MC by lengthy light stimuli are related to temperature modifications.

3.4 | The effect of light on MC firing does not depend on the inhibitory network and is partially reduced by blocking G protein activity (Stage 2 experiments 4–5)

Temperature can affect MC firing indirectly, for example, by increasing the inhibitory synaptic inputs projecting on these neurons. In agreement with this hypothesis, a light-induced increase in olfactory bulb temperature would be responsible for increasing inhibitory interneuron firing that, in turn, would reduce MC activity. This hypothesis is compatible with the differences in temperature sensitivity observed among different neuronal subtypes (Kim & Connors, 2012). We tested whether the reduction in MC firing when light-stimulated was due to a light-induced increase in inhibitory activity. This was explored in the presence of $GABA_A$ and $GABA_B$ receptors antagonists SR-95531 (Gabazine, 5 μM) and CGP 55845 (10 μM). Under this condition, light stimulation still reduced MC firing (Figure 6b, $n = 11$ MC, 1 animal), with an effect that was comparable to that observed when inhibitory network activity was intact (Figure 6d, Table 3). Hence, the inhibitory network is not involved in the light-induced decrease in MC firing. Extra-retinal photoreceptors expressed in mammal brain neurons (Blackshaw & Snyder, 1999; Fernandes, Fero, Driever, & Burgess, 2013; Kojima et al., 2011; Nissilä et al., 2012) may participate in this effect on MC firing. As these neuronal opsins are G-protein-coupled receptors, their possible involvement can be investigated by blocking G-protein signaling, the intracellular target of the photoreceptors. This was achieved by replacing GTP with the non-hydrolyzable GDP analog (GDPβS) in the patch pipette solution. As shown in Figure 6c, in this condition, light stimulation still produced a significant reduction in MC firing frequency ($n = 11$ MC, 2 animals), although we observed a slight reduction in the effect of light (Ctr vs. GDPβS ES = 0.68; $P = 0.032$, Man–Whitney test not corrected for

TABLE 2 Bayesian statistic of blue light effect at different light duration (bayesian repeated measurement ANOVA, JASP software)

Model comparison					
Models	**P(M)**	**P(M|data)**	**BF_M**	**BF_{10}**	**Error %**
Null model (incl. subject)	0.500	1.229e-6	1.229e-6	1.000	
Temperature modification	0.500	1.000	813869.418	813869.418	0.740
Post hoc comparisons – Temperature modification					
	Prior odds	**Posterior odds**		**$BF_{10, U}$**	**Error %**
1 s					
5 s	0.587	91.835		156.342	6.924e-4
10 s	0.587	139.777		237.958	0.001
5 s					
10 s	0.587	1.213		2.065	2.364e-4

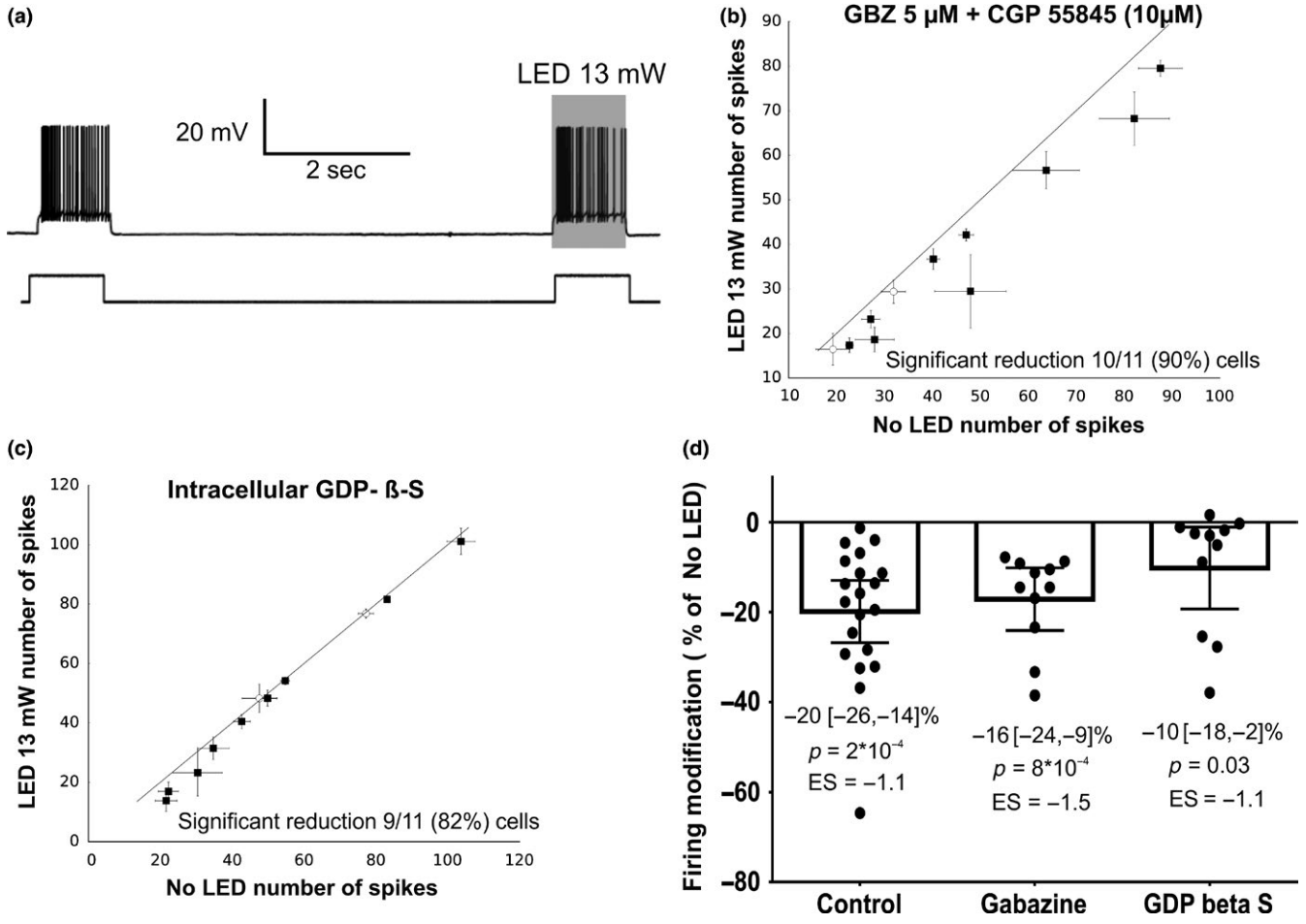

FIGURE 6 Activity in the inhibitory network or activation of extra-retinal photoreceptors are not required for light to modify mitral cells (MC) firing. (a) Representative example of the protocol used. (b) Cell-by-cell analysis of the effect produced by LED stimulation on MC firing in the presence of GABA receptor antagonists. (c) Cell-by-cell analysis of the effect produced by LED stimulation on MC firing in the presence of G-protein blockers GDPβS in the intracellular solution. (d) Population analysis of light-induced firing frequency modifications in the different conditions (control data are the same as Figure 1c). In b and c black squares depict MCs for which LED condition is significantly different compared with No-LED condition. Empty dots depict MCs for which no significant difference was observed between the two conditions. Error bars represent 95% CI. $n = 11$ MC. ES: Effect Size

TABLE 3 Bayesian statistic of the effect of GABAA antagonists (GBZ and CGP) and intracellular GDP-beta s) on blue light effect (bayesian ANOVA, JASP software)

Model comparison - Light effect					
Models	**P(M)**	**P(M|data)**	**BF_M**	**BF_{10}**	**Error %**
Null model	0.500	0.616	1.601	1.000	
Group	0.500	0.384	0.624	0.624	0.031
Post hoc tests : Post hoc comparisons - group					
	Prior odds	**Posterior odds**	**$BF_{10,U}$**	**Error %**	
Ctr					
GBZ + CGP	0.587	0.231	0.393	2.324e -4	
GDP-beta s	0.587	0.670	1.141	0.002	
GBZ + CGP					
GDP-beta s	0.587	0.429	0.731	0.008	

multiple comparisons; Figure 6d and Table 3 for Bayesian analysis). This result suggests that activation of encephalopsins could contribute to the reduction in MC firing caused by light, but further investigations are required to confirm this observation.

3.5 | Light stimulation generates an outward current associated with membrane hyperpolarization (Stage 2 experiments 6-7)

We next investigated the effect of short light stimulation on membrane currents and V_{rest}. As shown in Figure 7, LED stimulation (13 mW, 1 s) produced a small (4.8 [1.6, 8] pA) but consistent outward membrane current in MCs recorded at −60 mV in the voltage-clamp configuration (Figure 7a–c, $n = 11$ MC, 2 animals) and a small membrane hyperpolarization in the current-clamp configuration (−0.6[−0.8, −0.4] mV, Figure 7d–f, $n = 11$ MC, 2 animals). While performing these experiments, we noticed a decrease in spontaneous synaptic events during light stimulation in some MCs (Figure 7a,d and Figure S4). This synaptic activity is probably excitatory as the reversal potential of GABAergic transmission was −70 mV in our experimental conditions. One could imagine that the membrane potential modifications observed in the average traces lay behind the suppression of spontaneous excitatory activity by the light but this cannot hold true as the effects on membrane current and voltage were still observed in the presence of the antagonists of synaptic transmission NBQX and APV (unpublished data, but see https://osf.io/pwdjv/,https://osf.io/9k7xj/, and https://osf.io/vrm35/).

The effect of light on membrane resistance (R_m) was evaluated by quantifying the current modification produced by a 1-second hyperpolarizing step of 10 mV (Figure 8a; see https://osf.io/ejh2u/experiment 6). As illustrated in Figure 8b and c an apparent increase in R_m was observed during light stimulation. This result can be reconciled with the appearance of the outward current depicted in Figure 7 only by

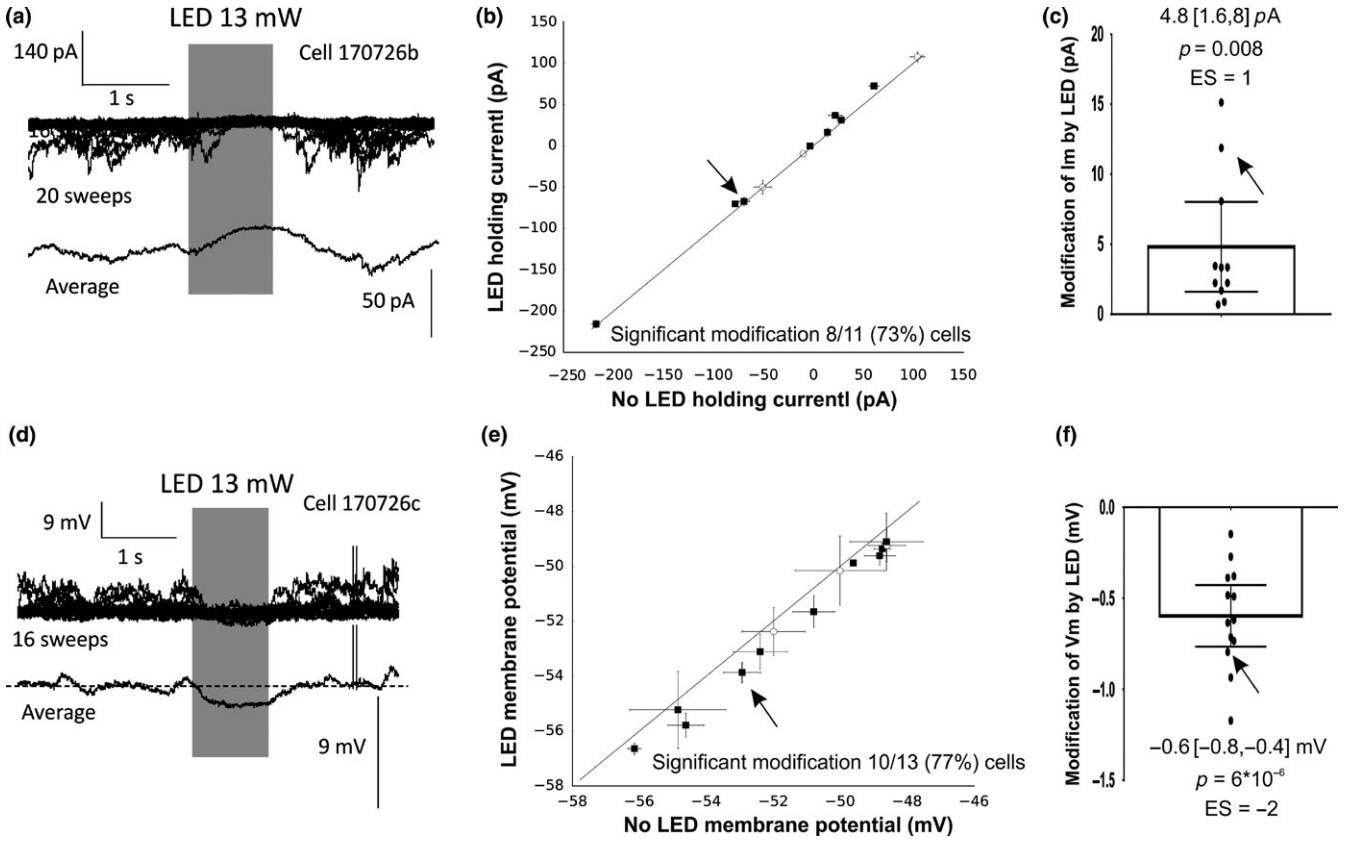

FIGURE 7 LED stimulation (blue light; 13 mW) generates an outward current and hyperpolarizes mitral cells (MCs). (a) Example of light-induced outward current in one neuron. Note the reduction in the spontaneous EPSC during stimulation. (b) Cell-by-cell analysis of the modification of the holding current by LED stimulation. (c) Population analysis on light-induced current modification. (d) Example of light-induced modification of membrane potential in one neuron. Note the reduction in the spontaneous EPSP during stimulation. (e) Cell-by-cell analysis of the modification of the membrane potential by LED stimulation. (f) Population analysis on light-induced modification of membrane potential. Arrows depict the analysis of the neurons represented in a and d. The black squares depict MCs for which LED condition is significantly different compared with No-LED condition. Empty dots depict MCs for which no significant difference is observed between the two conditions. Error bars represent 95% CI. $n = 11$ MC. ES: Effect Size

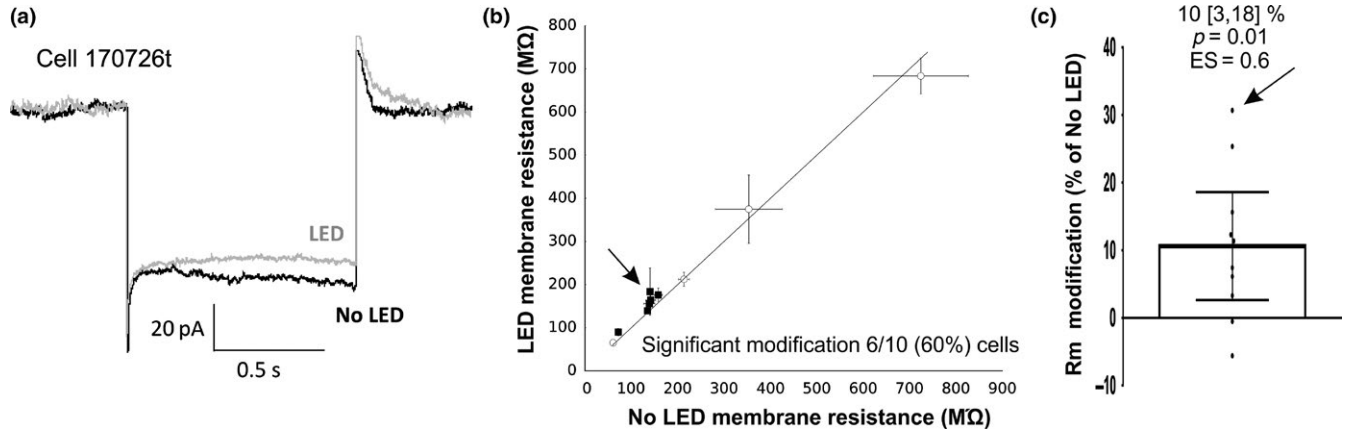

FIGURE 8 Light stimulation produces an apparent increase in membrane resistance in mitral cells (MC). (a) Example of the inward currents generated by a hyperpolarizing voltage step of 10 mV (not shown) in the presence and absence of LED stimulation (blue light; 13 mW). B) Cell by cell analysis of the modification of R_m by LED stimulation. The Black squares depict MCs for which LED condition is significantly different compared with No-LED condition. Empty dots depict MCs for which no significant difference is observed between the two conditions. C) Population analysis on light induced R_m modification. Arrows depict analysis of the neuron represented in A. Error bars represent 95% CI. $n = 11$ MC. ES: Effect Size

supposing that the light blocks an unknown steady depolarizing current. Moreover, an increase in R_m is likely to produce an increase in firing when stimulated, instead of the decrease we observed in MC. We therefore believe that the observed increase is likely due to the fact that our protocol is reliable only in a steady-state condition. As light stimulation activates an outward current, the latter needs to be subtracted from the current required to produce the voltage step (Figure 8d, blue traces) in order to obtain a correct estimation of R_m; this would otherwise be underestimated.

3.6 | Light stimulation increases AP latency and reduces AP amplitude (Stage 2 experiment 7)

To determine whether LED stimulation has a direct effect on the cellular mechanisms participating in AP generation, a single action potential was produced by a short (5 ms) injection of current in the absence of light and at the end of a 1 s LED stimulation. Analysis of the effect of light on a single AP showed a small reduction in both AP amplitude (−0.6[−0.9, −0.3] mV compared with the control condition; Figure 9a–c, $n = 11$ MC, two animals) and AP latency calculated from the beginning of current injection (0.16 [0.25, 07] ms compared with the control condition; Figure 9d–f, $n = 11$ MC, two animals). Additional exploratory analysis suggested that the AP threshold, rising slope, half-width, and after hyperpolarization (AHP) were also affected by light. Light shifted the AP threshold to more negative membrane potentials and triggered a small increase in the rising slope (Figure 10a,b). On the other hand, the half-width of the AP was reduced and the AHP increased (Figure 10c and d, $n = 11$ MC, 2 animals). As all these parameters mainly depend on sodium and/or potassium channel activation or inactivation (Bean, 2007; Hodgkin & Huxley, 1952; Platkiewicz & Brette, 2010; Sah & Faber, 2002), we can reasonably postulate that light affects AP generation through a modification of Na^+ and K^+ channels but further experiments are required to confirm such an interpretation.

3.7 | Effect of light on firing depends on neuronal types (Stage2 experiment 8)

Finally, we analyzed whether the firing reduction produced by blue light stimulation on MC was generalizable to other neuronal types using the protocol illustrated in Figure 6a with tufted cells in the OB, medium spiny neurons in the striatum, cerebellar Purkinje neurons and hippocampal CA1 pyramidal neurons. As shown in Figure 11, LED stimulation produced a significant reduction in firing activity in tufted cells ($n = 16$, 4 animals) and medium spiny neurons ($n = 16$, 8 animals) but not in cerebellar Purkinje ($n = 16$, 4 animals), or CA1 hippocampal neurons ($n = 16$, 3 animals). The possibility that the firing reduction observed in striatal medium spiny neurons was produced by a refractory period was investigated by applying two consecutive depolarizing steps in the absence of LED stimulation. In this condition, no firing reduction was observed ($n = 16$, unpublished results). We noticed that light stimulation produced, in some neuronal types, a modification of the AHP that follows the depolarizing step. To quantify the amplitude of the AHP we subtracted the average V_m in the 100 ms preceding the depolarizing step from the minimum value of V_m in the 500 ms that followed the depolarization. Exploratory analysis of this parameter showed a significant light-induced increase in AHP amplitude in tufted cells (no-LED −3.8 [−4.7, −2.7] mV; LED - 4.1 [−5.1, −3.1] mV, $n = 16$) and a reduction in hippocampal CA1 pyramidal neurons (no-LED

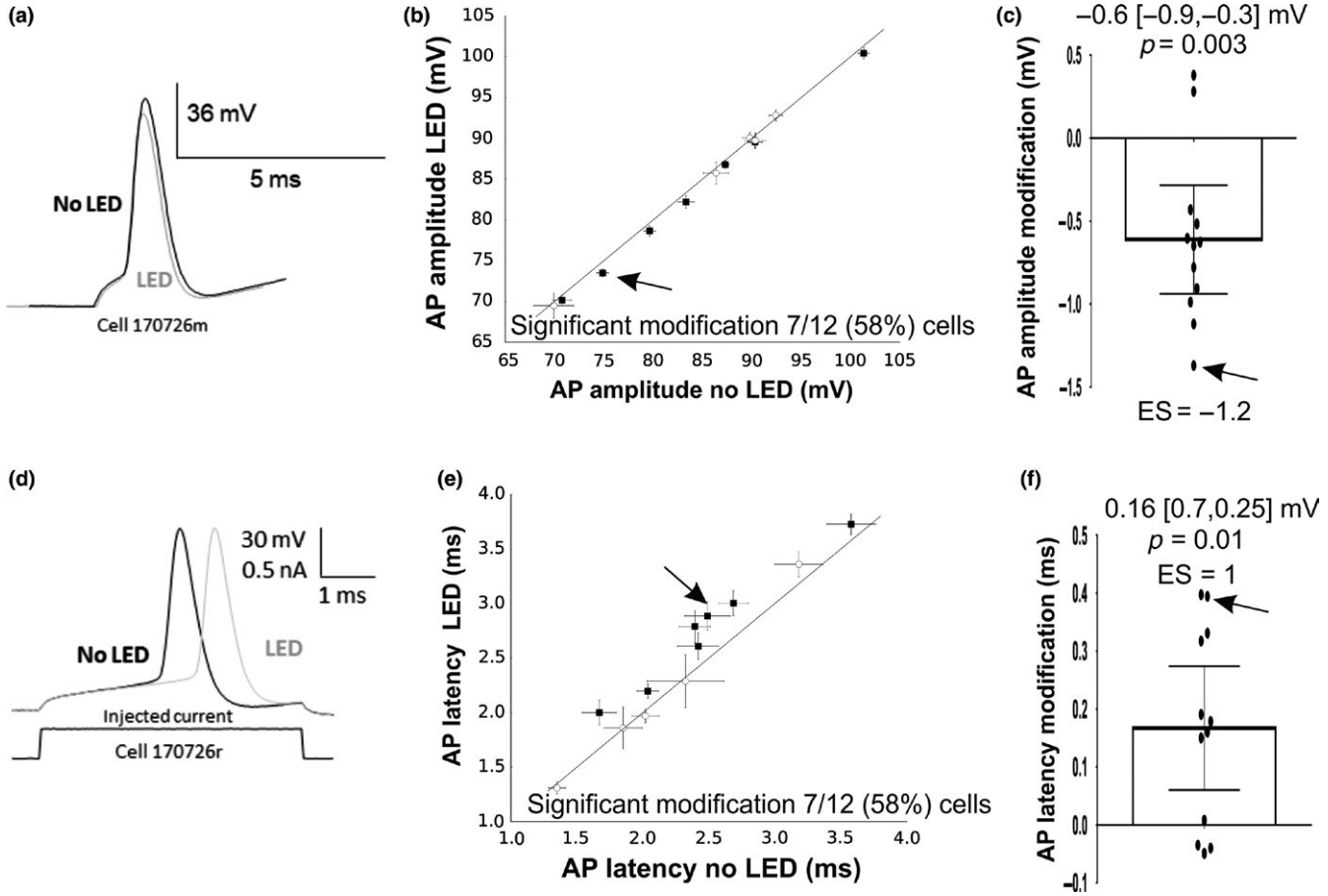

FIGURE 9 LED stimulation (blue light; 13 mW) modify action potential (AP) amplitude and latency. (a) Example of effect of light on AP amplitude. The traces are aligned on action potential threshold. (b) Cell-by-cell analysis of the modification of AP amplitude by LED stimulation. (c) Population analysis on light-induced amplitude modification. (d) Example of effect of light on AP latency. The traces are aligned vertically at the membrane potential preceding current injection. (e) Cell-by-cell analysis of the modification of AP latency by LED stimulation. (f) Population analysis on light-induced latency modification. In b and e the black squares depict MCs for which LED condition is significantly different compared with no-LED condition. Empty dots depict MCs for which no significant difference is observed between the two conditions. Arrows depict analysis of the neurons represented in a and d. Error bars represent 95% CI. The *p* values are corrected for multiple comparisons (2). $n = 12$ MC. The *p* values are corrected for multiple comparisons (2). ES: Effect Size

−4.9 [−5.5, −4.3] mV; LED −4.6 [−5.3, −3.9] mV, $n = 18$). No effect was observed in MC (no-LED −1.9 [−2.3, −1.5] mV; LED −2.0 [−2.4, −1.6] mV, $n = 20$) or Purkinje neurons (no-LED −1.9 [−2.3, −1.5] mV; LED −1.7 [−2.0, −1.4] mV, $n = 18$) (Figure 12). Although MSNs do not express AHP in normal conditions a significant negative shift of the membrane potential following the depolarizing step was observed after light stimulation (no-LED 0.17 [0.07, −0.27] mV; LED −0.39 [−0.53, −0.26] mV, $n = 17$; Figure 12). These results suggest that light can have opposite actions on membrane properties depending on the neuronal type.

4 | DISCUSSION

The results presented in this report show that light stimulation, in the wavelength and power ranges commonly used for optogenetic experiments, can modify neuronal firing activity depending on light power and cellular type. They suggest that such effects are mainly due to the increase in tissue temperature and they highlight some of the biophysical mechanisms that might be involved.

4.1 | Light's action on MC neuronal physiology is mainly due to a temperature modification

Three lines of evidence suggest that the main factor responsible for the light-induced reduction in MC firing is an increase in temperature of the brain tissue:

- The reduction in neuronal firing produced by light correlates with the light-induced modification of tissue temperature.

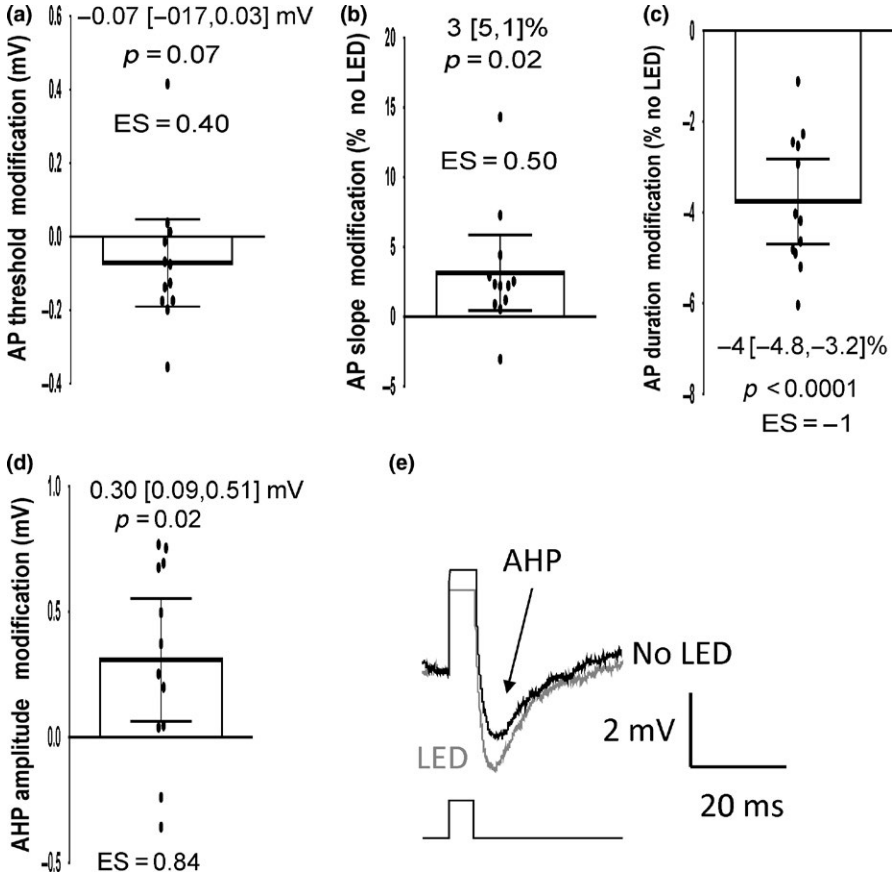

FIGURE 10 Exploratory analysis of LED stimulation (blue light; 13 mW) on action potential (AP) parameters. (a) A tendency toward a decrease in AP threshold was produced by light stimulation. (b) LED stimulation increases the rising slope of AP. (c) Half-width duration of AP is reduced by LED stimulation (d) LED stimulation produce an increase in the AHP amplitude that follows one AP; right example of the AHP in light and no-light condition. $n = 12$ MC. The p-values are not corrected for multiple comparisons. ES: Effect Size

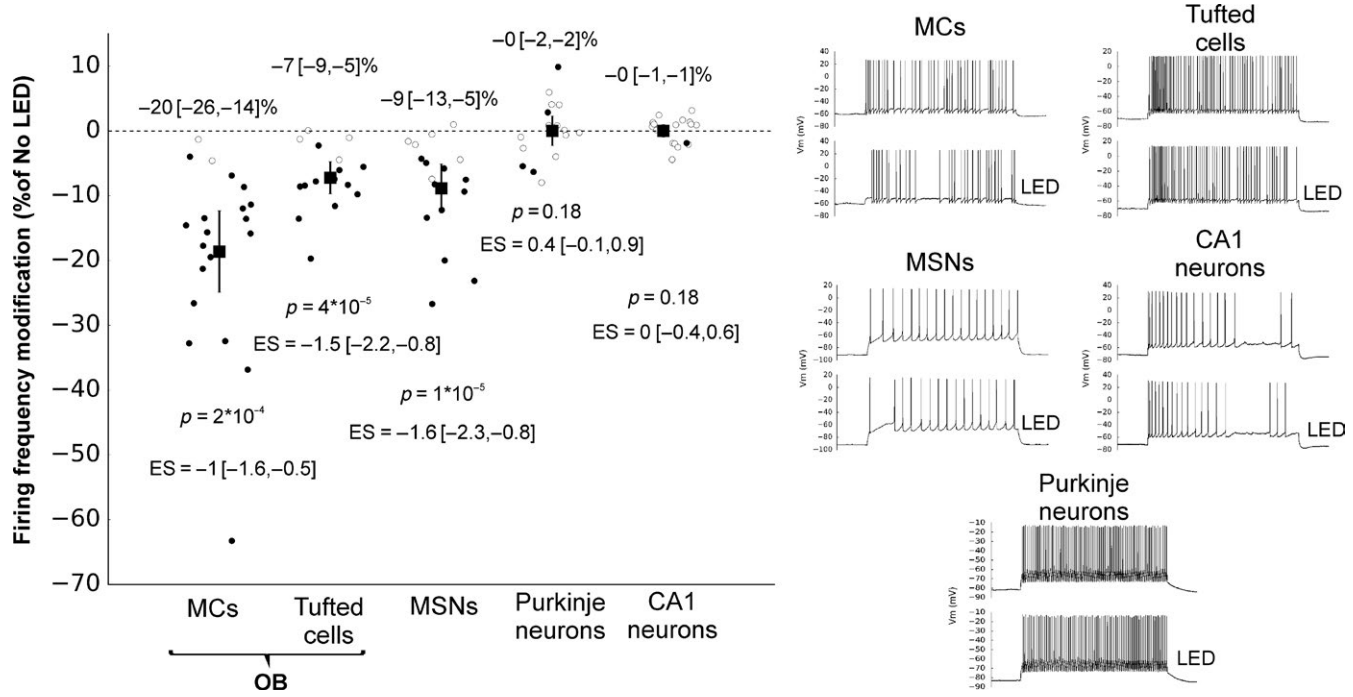

FIGURE 11 The effect of light on neuronal firing is dependent on neuronal type. The effect of LED stimulation (blue light; 1s starting from the beginning of the depolarizing step) on evoked firing activity is reported. MC: Mitral Cells; MS: medium spiny neurons. Empty dots represent effect of light on neurons for which no statistically significant modifications were observed, black dots represent effect of light on neurons for which statistically significant modifications were observed. MC data are the same as Figure 1c ($n = 20$). For tufted, MS, Purkinje and CA1 $n = 16$ and the p values are corrected for multiple comparisons (4). ES: Effect Size

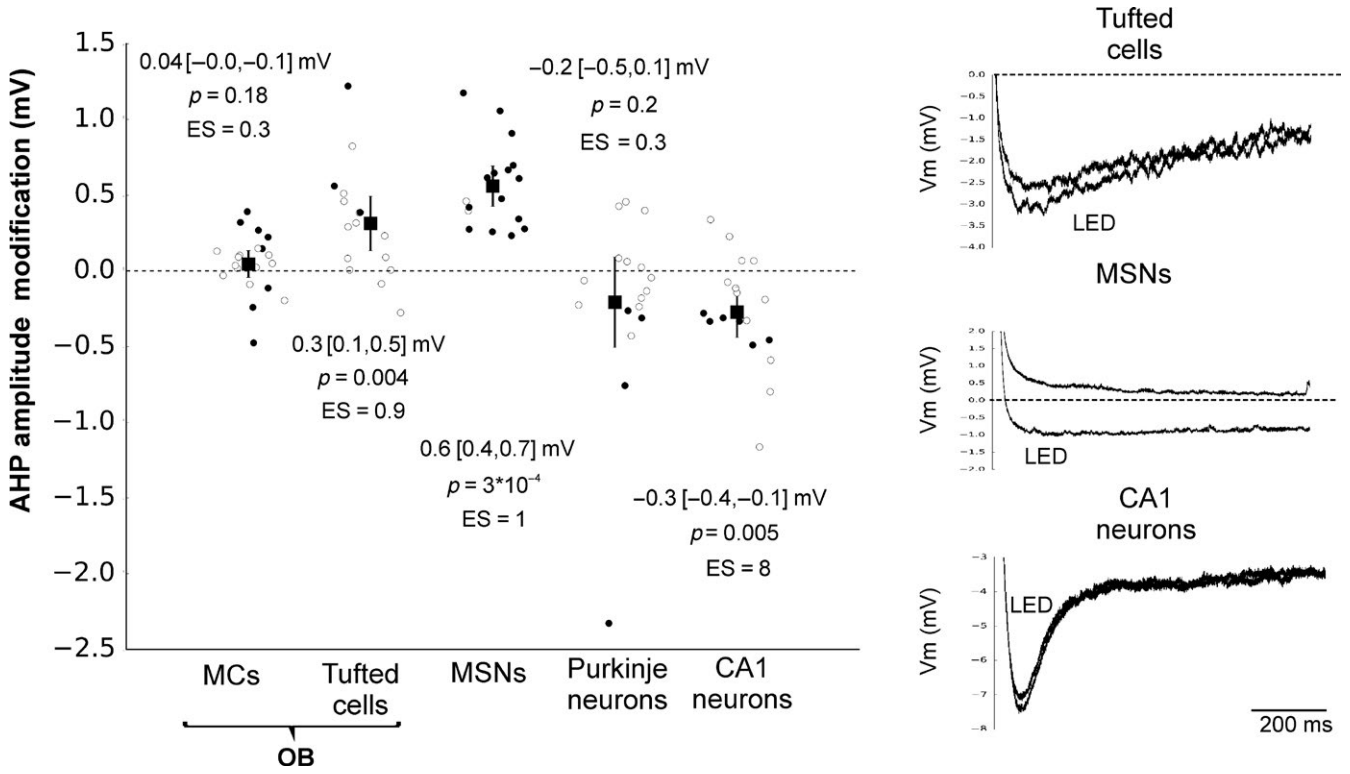

FIGURE 12 Exploratory analysis on effect of light on after hyperpolarization (AHP) amplitude. (a) The effect of LED stimulation (blue light; 1 s starting from the beginning of the depolarizing step) on the AHP amplitude observed at the end of the depolarization is reported. Empty dots represent effect of light on neurons for which no statistically significant modifications were observed, black dots represent effect of light on neurons for which statistically significant modifications were observed MC: Mitral Cells; MS: medium spiny neurons. Empty dots represent effect of light on single neurons. (b) Representative trace of observed AHP modification; blue traces under LED stimulation. MC $n = 20$; Tufted cells $n = 16$, MSNs $n = 17$, Purkinje neurons $n = 18$ and CA1 neurons $n = 18$. The p values are not corrected for multiple comparisons. ES: Effect Size

- The modification of tissue temperature produces a reduction in MC firing similar to that produced by light stimulation.
- The light-induced modifications of membrane potential and action potential parameters are compatible to those produced by temperature modifications reported in the literature.

We have shown that tissue temperature linearly increases with light power reaching an average value of 0.4°C at 13 mW. Such an increase is in the range predicted in the model proposed by Stunjenske et al. for the effect of light in in vitro preparations see (Figure 3c of Stujenske et al., 2015). When looking at the effect of light on MC firing, a significant reduction was observed even when using a power of 1 mW, a condition producing a temperature increase less than 0.03°C. The linear covariation between temperature and firing modifications with light power supports the hypothesis that even at this low light-intensity there is a reduction in firing with increasing temperature, suggesting that neuronal physiology can be affected by extremely small variations of brain temperature. A theoretical model predicts reduced warming with an increase in light wavelength in vivo (Stujenske et al., 2015); here no significant differences were found between the two wavelengths used. At least three factors could account for this discrepancy: (a) the partial overlapping of wavelength bandwidth used in the present study; (b) the difference in temperature absorption of in vitro versus in vivo tissue slices (Johansson, 2010; Yaroslavsky et al., 2002); (c) an unspecified/unknown factor not taken into account by the model; see (Figure 4 of Senova et al., 2017). Brain slice temperatures increased with the duration of light stimulation reaching a steady state after approximately 5 s. Such an increase in temperature is associated with a reduction in firing. Interestingly, we found that prolonged light stimulation of MCs produced a persistent membrane hyperpolarization associated with a decline in firing. As pointed out before, it is unlikely that these effects are due to tissue warming (~1°C) associated with long-lasting LED stimulation. Neither can they be due to prolonged warming (10 s), as V_m hyperpolarization and the strong decline in firing were not observed when bath temperatures were increased in the absence of light (see Figure 3a). This suggests a

direct effect of light on neuronal physiology when prolonged light stimulation is used. Membrane hyperpolarization and declining firing could be due to a slow recovery of physiological activity after light stimulation or to a persistent neuronal alteration, possibly due to phototoxicity. It has been proposed that vestiges of nonvisual photoreceptors in the mammalian brain can affect neuronal physiology (Fernandes et al., 2013; Kojima et al., 2011). Our results suggest that activation of encephalopsin could participate in this reduction in MC firing during visible light stimulation (Figure 5). However, the statistical evidence is weak (Bayes factor = 1.14; $p = 0.032$) and more robust results are required to support this evidence. Moreover, we did not observe any light-induced modifications of firing in the Purkinje cells, a neuronal type that strongly expresses encephalopsin (Blackshaw & Snyder, 1999). Our results cannot exclude the possibility of visible light-activated encephalopsins acting on neuronal parameters other than firing activity, as well as the possible role of these opsins when stimulated by ultraviolet light (Kojima et al., 2011).

4.2 | Biophysical explanation for the effect of light

The effect of light on membrane properties and action potential parameters were investigated with MCs.

LED-stimulation generated an outward current producing a small but consistent membrane hyperpolarization, an increase in AP latency and a decrease in AP amplitude. Moreover, our exploratory analysis suggests that light stimulation increases the AP rising slope, reduces AP duration and increases the postspike AHP. Assuming that the observed effects are due to light-induced temperature modifications, it is worth discussing the present results by taking into account the effects produced by temperature variations on neuronal physiology as reported in the literature. A temperature increase has shown to affect neuronal V_{rest} in different ways, depending on the brain structure and the animal species. In guinea pig hippocampal CA1 pyramidal neurons held at different temperatures (27°C or 37°C), no significant modifications of V_{rest} were observed (Thompson, Masukawa, & Prince, 1985), while in mouse hippocampal neurons, heating from 30°C to 41°C produced a membrane depolarization between 0.8 and 1.5 mV/°C, depending on the neuronal type recorded (Kim & Connors, 2012). Conversely, a temperature increase from 12 to 31°C in a rat visual cortex produced a membrane hyperpolarization of -1.3 ± 0.09 mV/°C (Volgushev, Vidyasagar, Chistiakova, & Eysel, 2000; Volgushev, Vidyasagar, Chistiakova, Yousef, et al., 2000), a result similar to ours with MCs. This result is comparable with the estimated voltage/temperature modification in the present study (-0.6 mV/0.34°C = -1.7 mV/°C). A temperature increase was also shown to affect AP shape in a similar way to that produced by LED-stimulation of MCs. In particular, a decrease in AP amplitude and duration with increasing temperature was observed in cortical and hippocampal neurons (Thompson et al., 1985; Volgushev, Vidyasagar, Chistiakova, Yousef, et al., 2000), as well as an increase in AP latency (Volgushev, Vidyasagar, Chistiakova, Yousef, et al., 2000), rising slope (Thompson et al., 1985), and a decrease in spike threshold (Volgushev, Vidyasagar, Chistiakova, Yousef, et al., 2000). The biophysical mechanisms associated with temperature changes were minutely analyzed by Volgushev et al. who suggest that the modification in V_{rest} is mainly due to an increase in the ratio for the permeability of the potassium and sodium leak channels (Volgushev, Vidyasagar, Chistiakova, Yousef, et al., 2000). It should be noted that a temperature dependent increase in the activity of the Na^+-K^+ pump could also contribute to the observed membrane hyperpolarization (Bates & Mackillop, 1985). On the other hand the modification of AP shape with changing temperature has been ascribed to an increase in amplitude, duration, and steepness of voltage dependent potassium currents and to an increase in amplitude but a decrease in the width of voltage-dependent sodium currents (Volgushev, Vidyasagar, Chistiakova, Yousef, et al., 2000). Similar mechanisms could explain the effect of light on the AP shape in MCs, as well as the observed increase in the fast AHP, mainly due to the activation of voltage-dependent potassium channels in these neurons (Duménieu et al., 2015).

Even though evaluating the effect of light on synaptic transmission was behind the objectives of the present study and requires further investigation, a consistent decrease in putative spontaneous glutamatergic activity was observed in several recorded MCs. A reduction in excitatory synaptic activity could be the consequence of the decrease in spontaneous firing on neighboring MCs and tufted cells as well as the consequence of the reduction in their AP duration and amplitude (Geiger & Jonas, 2000; Rama et al., 2015). A direct effect of heat or light on neurotransmitter release probability and/or postsynaptic-receptor activation, could also be implicated in the observed effect (Leszkiewicz & Aizenman, 2003; Volgushev, Vidyasagar, Chistiakova, & Eysel, 2000).

The reported effects of light on MC membrane potential, AP proprieties and synaptic activity could all account for the observed reduction in spontaneous and evoked firing activity produced by LED stimulation. Indeed, the outward current so generated would bring the membrane potential away from spike threshold and, although our experimental design did not allow us to evidence this, would probably result in reduced membrane resistance with a consequent reduction in neuronal excitability. This latter hypothesis is in line with the reported reduction in membrane resistance produced by a temperature increase (Thompson et al., 1985; Volgushev, Vidyasagar, Chistiakova, Yousef, et al., 2000). The increase in AP latency and AHP amplitude would also promote a reduction in firing

in MCs (Duménieu et al., 2015). Finally, the apparent reduction in glutamatergic transmission and in particular the recurrent synaptic excitation, will also lead to a reduction in MC firing (Salin, Lledo, Vincent, & Charpak, 2001).

We found that LED-stimulation affects both firing activity and AHP amplitude in different and even opposing ways, depending on the neuronal type. Interestingly the light-induced decrease in AHP that we observed in mouse CA1 pyramidal cells is reminiscent of the temperature-induced decrease in the AHP observed in guinea pig CA1 neurons (Thompson et al., 1985). In the latter report the AHP reduction was associated with a decrease in firing adaptation. In the present study we did not evaluate the effect of light on CA1 firing adaptation, focalizing our attention only on the average firing activity, but the raw traces of our experiments are available at https://osf.io/kp34r/. Interesting too the exploratory analysis suggests that, in MCs, LED- stimulation increases AHP amplitude following a single AP (Figure 10d) but not a long depolarizing step (Figure 12). If confirmed these results suggest that light would act differentially on the potassium channels participating in early and medium AHP (Sah & Faber, 2002). The heterogeneity of the action of light on different neuronal types and parameters is reminiscent of the heterogeneous effect produced by temperature modification reported in the literature and discussed previously and could be due to differences in the experimental conditions and/or the biophysical characteristics of the different neuronal types (Kim & Connors, 2012).

5 | CONCLUSIONS

The results of the present study have three main implications.

The first concerns the ability of optical stimulation, in the range used for optogenetic applications, to affect the neuronal physiology of wild-type neurons. Our results are in agreement with a previous report showing the sensitivity of prefrontal cortex neurons to light- stimulation in vivo (Stujenske et al., 2015). It has been argued that the parameters used in this study (30 s of 5–10 mW continuous LED-stimulation) that led to a temperature increase in 1–2°C, are not representative of those commonly used in optogenetics experiments (Senova et al., 2017). However, even more canonical stimulation patterns, that is, pulsed light at a reduced duty cycle, can still produce tissue warming between 0.1 and 0.8°C in vivo (Senova et al., 2017; Stujenske et al., 2015). These temperature modifications are sufficiently large to affect the firing activity of some neuronal types recorded in the present study. Thus, control tests on wild-type animals/neurons should be mandatory to confirm the specificity of the observed effects in optogenetic experiments.

The second implication concerns the sensitivity of some neuronal types to very small variations in tissue temperature, with less than 0.1°C sufficient to modify the firing activity of MCs. Since the brain is submitted to daily physiological temperature fluctuations that can reach a few degrees Celsius (Andersen & Moser, 1995), our results raise the question of whether, and how, the possible modifications in firing activity produced by physiological temperature fluctuations have an impact on cognitive functions.

The third implication concerns a possible therapeutic application of optical stimulation. The potential of optogenetics to treat certain brain pathologies has been documented in animal models (Bentley et al., 2013; Vann & Xiong, 2016), but its application in humans is limited by the need to express exogenous opsins. Our demonstration of the sensitivity to light in naive neurons, not limited by this constraint, suggests that light stimulation alone could be used to inactivate or activate selective brain regions during pathological manifestations. As blue-light delivered in the ear canal of healthy humans appears to penetrates the skull and modifies the event-related potential recorded with an EEG (Sun et al., 2016), visible light could potentially be used as a noninvasive tool to study human brain activity for therapeutic or research purposes, but further investigations are necessary to better elucidate the action of light at cellular and cognitive levels.

ACKNOWLEDGEMENTS

This work was supported by the CNRS, Inserm, and Lyon 1 University. We thank: Nicolas Fourcaud-Trocmé and Samuel Garcia for helping produce the scripts for data analysis; Jean-Christophe Comte for helpful suggestions and Emilie Mathian for her contribution to the preliminary experiments.

COMPETING INTERESTS

The authors declare no competing financial interests.

AUTHOR CONTRIBUTIONS

K.Ait Ouares performed the experiment with Purkinje neurons. C. Beurrier supervised the experiments with MSNs, analysed the data and cowrote the article. M. Canepari supervised the Purkinje and CA1 neurons, analysed the data and cowrote the article. G. Laverne performed the MSN experiments. N. Kuczewski performed the olfactory bulb and CA1 neuron experiments, analysed the data, and cowrote the article.

DATA ACCESSIBILITY

Raw data and analyses are accessible on the Open Science Framework web site (https://osf.io/mrw93/, https://doi.org/10.17605/osf.io/mrw93).

ORCID

Nicola Kuczewski http://orcid.org/0000-0003-1615-6344

REFERENCES

Ait Ouares, K., Jaafari, N., & Canepari, M. (2016). A generalised method to estimate the kinetics of fast Ca(2 +) currents from Ca(2 +) imaging experiments. *Journal of Neuroscience Methods*, *268*, 66–77. https://doi.org/10.1016/j.jneumeth.2016.05.005

Andersen, P., & Moser, E. I. (1995). Brain temperature and hippocampal function. *Hippocampus*, *5*, 491–498. https://doi.org/10.1002/(ISSN)1098-1063

Arvanitaki, A., & Chalazonitis, N. (n.d.) Excitatory and inhibitory processes initiated by light and infrared radiations in single identifiable nerve cells (Giant Ganglion Cells of Aplysia).

Banghart, M., Borges, K., Isacoff, E., Trauner, D., & Kramer, R. H. (2004). Light-activated ion channels for remote control of neuronal firing. *Nature Neuroscience*, *7*, 1381–1386. https://doi.org/10.1038/nn1356

Bates, D. A., & Mackillop, W. J. (1985). The effect of hyperthermia on the sodium-potassium pump in Chinese hamster ovary cells. *Radiation Research*, *103*, 441–451. https://doi.org/10.2307/3576766

Bean, B. P. (2007). The action potential in mammalian central neurons. *Nature Reviews Neuroscience*, *8*, 451–465. https://doi.org/10.1038/nrn2148

Bentley, J. N., Chestek, C., Stacey, W. C., & Patil, P. G. (2013). Optogenetics in epilepsy. *Neurosurgical Focus*, *34*, E4. https://doi.org/10.3171/2013.3.FOCUS1364

Blackshaw, S., & Snyder, S. H. (1999). Encephalopsin: A novel mammalian extraretinal opsin discretely localized in the brain. *Journal of Neuroscience*, *19*, 3681–3690. https://doi.org/10.1523/JNEUROSCI.19-10-03681.1999

Boyden, E. S., Zhang, F., Bamberg, E., Nagel, G., & Deisseroth, K. (2005). Millisecond-timescale, genetically targeted optical control of neural activity. *Nature Neuroscience*, *8*, 1263–1268. https://doi.org/10.1038/nn1525

Canepari, M., Willadt, S., Zecevic, D., & Vogt, K. E. (2010). Imaging inhibitory synaptic potentials using voltage sensitive dyes. *Biophysical Journal*, *98*, 2032–2040. https://doi.org/10.1016/j.bpj.2010.01.024

Christie, I. N., Wells, J. A., Southern, P., Marina, N., Kasparov, S., Gourine, A. V., & Lythgoe, M. F. (2013). fMRI response to blue light delivery in the naïve brain: Implications for combined optogenetic fMRI studies. *NeuroImage*, *66*, 634–641. https://doi.org/10.1016/j.neuroimage.2012.10.074

Deisseroth, K. (2015). Optogenetics: 10 years of microbial opsins in neuroscience. *Nature Neuroscience*, *18*, 1213–1225. https://doi.org/10.1038/nn.4091

Deng, W., Goldys, E. M., Farnham, M. M. J., & Pilowsky, P. M. (2014). Optogenetics, the intersection between physics and neuroscience: Light stimulation of neurons in physiological conditions. *American Journal of Physiology: Regulatory, Integrative and Comparative Physiology*, *307*, R1292–R1302.

Duménieu, M., Fourcaud-Trocmé, N., Garcia, S., & Kuczewski, N. (2015) Afterhyperpolarization (AHP) regulates the frequency and timing of action potentials in the mitral cells of the olfactory bulb: Role of olfactory experience. *Physiological Reports*, *3*, 1–19. https://doi.org/10.14814/phy2.12344.

Faul, F., Erdfelder, E., Lang, A.-G., & Buchner, A. (2007). G*Power 3: A flexible statistical power analysis program for the social, behavioral, and biomedical sciences. *Behavior Research Methods*, *39*, 175–191. https://doi.org/10.3758/BF03193146

Fenno, L., Yizhar, O., & Deisseroth, K. (2011). The development and application of optogenetics. *Annual Review of Neuroscience*, *34*, 389–412. https://doi.org/10.1146/annurev-neuro-061010-113817

Fernandes, A. M., Fero, K., Driever, W., & Burgess, H. A. (2013). Enlightening the brain: Linking deep brain photoreception with behavior and physiology. *BioEssays*, *35*, 775–779. https://doi.org/10.1002/bies.201300034

Garcia, S., & Fourcaud-Trocmé, N. (2009). OpenElectrophy: An electrophysiological data- and analysis-sharing framework. *Frontiers in Neuroinformatics*, *3*, 14.

Geiger, J. R., & Jonas, P. (2000). Dynamic control of presynaptic Ca(2 +) inflow by fast-inactivating K(+) channels in hippocampal mossy fiber boutons. *Neuron*, *28*, 927–939. https://doi.org/10.1016/S0896-6273(00)00164-1

Gradinaru, V., Zhang, F., Ramakrishnan, C., Mattis, J., Prakash, R., Diester, I., … Deisseroth, K. (2010). Molecular and cellular approaches for diversifying and extending optogenetics. *Cell*, *141*, 154–165. https://doi.org/10.1016/j.cell.2010.02.037

Hodgkin, A. L., & Huxley, A. F. (1952). A quantitative description of membrane current and its application to conduction and excitation in nerve. *Journal of Physiology*, *117*, 500–544. https://doi.org/10.1113/jphysiol.1952.sp004764

Johansson, J. D. (2010). Spectroscopic method for determination of the absorption coefficient in brain tissue. *Journal of Biomedial Optics*, *15*, 057005. https://doi.org/10.1117/1.3495719

Kerby, D.S. (2014). The simple difference formula: An approach to teaching nonparametric correlation. *Comprehensive Psychiatry*, *3*, 11.IT.3.1. https://doi.org/10.2466/11.IT.3.1

Kim, J. A., & Connors, B. W. (2012). High temperatures alter physiological properties of pyramidal cells and inhibitory interneurons in hippocampus. *Frontiers in Cellular Neuroscience*, *6*, 27.

Kojima, D., Mori, S., Torii, M., Wada, A., Morishita, R., & Fukada, Y. (2011). UV-sensitive photoreceptor protein OPN5 in humans and mice. *PLoS ONE*, *6*, e26388. https://doi.org/10.1371/journal.pone.0026388

Leszkiewicz, D. N., & Aizenman, E. (2003). Reversible modulation of GABA(A) receptor-mediated currents by light is dependent on the redox state of the receptor. *European Journal of Neuroscience*, *17*, 2077–2083. https://doi.org/10.1046/j.1460-9568.2003.02656.x

Nissilä, J., Mänttäri, S., Särkioja, T., Tuominen, H., Takala, T., Timonen, M., & Saarela, S. (2012). Encephalopsin (OPN3) protein abundance in the adult mouse brain. *Journal of Comparative Physiology A*, *198*, 833–839. https://doi.org/10.1007/s00359-012-0754-x

Platkiewicz, J., & Brette, R. (2010). A threshold equation for action potential initiation. *PLoS Computational Biology*, *6*, e1000850.

Rama, S., Zbili, M., Bialowas, A., Fronzaroli-Molinieres, L., Ankri, N., Carlier, E., … Debanne, D. (2015). Presynaptic hyperpolarization induces a fast analogue modulation of spike-evoked transmission mediated by axonal sodium channels. *Nature Communications*, *6*, 10163. https://doi.org/10.1038/ncomms10163

Rungta, R. L., Osmanski, B.-F., Boido, D., Tanter, M., & Charpak, S. (2017). Light controls cerebral blood flow in naive animals. *Nature Communications*, *8*, 14191. https://doi.org/10.1038/ncomms14191

Sah, P., & Faber, E. S. L. (2002). Channels underlying neuronal calcium-activated potassium currents. *Progress in Neurobiology*, *66*, 345–353. https://doi.org/10.1016/S0301-0082(02)00004-7

Salin, P. A., Lledo, P. M., Vincent, J. D., & Charpak, S. (2001). Dendritic glutamate autoreceptors modulate signal processing in rat mitral cells. *Journal of Neurophysiology*, *85*, 1275–1282. https://doi.org/10.1152/jn.2001.85.3.1275

Senova, S., Scisniak, I., Chiang, C.-C., Doignon, I., Palfi, S., Chaillet, A., … Pain, F. (2017). Experimental assessment of the safety and potential efficacy of high irradiance photostimulation of brain tissues. *Scientific Reports*, *7*, 43997. https://doi.org/10.1038/srep43997

Shapiro, M. G., Priest, M. F., Siegel, P. H., & Bezanilla, F. (2013). Thermal mechanisms of millimeter wave stimulation of excitable cells. *Biophysical Journal*, *104*, 2622–2628. https://doi.org/10.1016/j.bpj.2013.05.014

Stujenske, J. M., Spellman, T., & Gordon, J. A. (2015). Modeling the spatiotemporal dynamics of light and heat propagation for in vivo optogenetics. *Cell Reports*, *12*, 525–534. https://doi.org/10.1016/j.celrep.2015.06.036

Sun, L., Peräkylä, J., Kovalainen, A., Ogawa, K. H., Karhunen, P. J., & Hartikainen, K. M. (2016). Human brain reacts to transcranial extraocular light. *PLoS ONE*, *11*, e0149525. https://doi.org/10.1371/journal.pone.0149525

Thompson, S. M., Masukawa, L. M., & Prince, D. A. (1985). Temperature dependence of intrinsic membrane properties and synaptic potentials in hippocampal CA1 neurons in vitro. *Journal of Neuroscience*, *5*, 817–824. https://doi.org/10.1523/JNEUROSCI.05-03-00817.1985

Ting, J. T., Daigle, T. L., Chen, Q., & Feng, G. (2014). Acute brain slice methods for adult and aging animals: Application of targeted patch clamp analysis and optogenetics. *Methods in Molecular Biology*, *1183*, 221–242. https://doi.org/10.1007/978-1-4939-1096-0

Vann, K. T., & Xiong, Z.-G. (2016). Optogenetics for neurodegenerative diseases. *International Journal of Physiology, Pathophysiology and Pharmacology*, *8*, 1–8.

Vogt, K. E., Gerharz, S., Graham, J., & Canepari, M. (2011a). High-resolution simultaneous voltage and Ca2 + imaging. *Journal of Physiology*, *589*, 489–494. https://doi.org/10.1113/jphysiol.2010.200220

Vogt, K. E., Gerharz, S., Graham, J., & Canepari, M. (2011b). Combining membrane potential imaging with L-glutamate or GABA photorelease. *PLoS ONE*, *6*, e24911. https://doi.org/10.1371/journal.pone.0024911

Volgushev, M., Vidyasagar, T. R., Chistiakova, M., & Eysel, U. T. (2000). Synaptic transmission in the neocortex during reversible cooling. *Neuroscience*, *98*, 9–22. https://doi.org/10.1016/S0306-4522(00)00109-3

Volgushev, M., Vidyasagar, T. R., Chistiakova, M., Yousef, T., & Eysel, U. T. (2000). Membrane properties and spike generation in rat visual cortical cells during reversible cooling. *Journal of Physiology*, *522*(Pt 1), 59–76. https://doi.org/10.1111/j.1469-7793.2000.0059m.x

Williams, S. C. P., & Deisseroth, K. (2013). Optogenetics. *Proceedings of the National Academy of Sciences of the United States of America*, *110*, 16287. https://doi.org/10.1073/pnas.1317033110

Yaroslavsky, A. N., Schulze, P. C., Yaroslavsky, I. V., Schober, R., Ulrich, F., & Schwarzmaier, H. J. (2002). Optical properties of selected native and coagulated human brain tissues in vitro in the visible and near infrared spectral range. *Physics in Medicine & Biology*, *47*, 2059–2073. https://doi.org/10.1088/0031-9155/47/12/305

SUPPORTING INFORMATION

Additional supporting information may be found online in the Supporting Information section at the end of the article.

How to cite this article: Ait Ouares K, Beurrier C, Canepari M, Laverne G, Kuczewski N. Opto nongenetics inhibition of neuronal firing. *Eur J Neurosci*. 2018;00:1–21. https://doi.org/10.1111/ejn.14251

Adv Exp Med Biol, in press

Imaging Native Calcium Currents in Brain Slices

Karima Ait Ouares[a,b], **Nadia Jaafari**[a,b] , **Nicola Kuczewski**[c] and **Marco Canepari**[a,b,d]

[a] Univ. Grenoble Alpes, CNRS, LIPhy, F-38000 Grenoble, France
[b] Laboratories of Excellence, Ion Channel Science and Therapeutics, France.
[c] Centre de Recherche en Neurosciences de Lyon, INSERM U1028/CNRS UMR5292, Université Lyon1, Lyon, France
[d] Institut National de la Santé et Recherche Médicale (INSERM), France.

Address of the submitting and corresponding author
Marco Canepari, Laboratoire Interdisciplinaire de Physique (UMR 5588), Bat. E45, 140 avenue de la physique, Domaine univ., 38402 St Martin d'Hères cedex, France. Email: marco.canepari@univ-grenoble-alpes.fr

Short Title: Imaging Native Calcium Currents

34

35

36

Abstract

Imaging techniques may overcome the limitations of electrode techniques to measure locally not only membrane potential changes, but also ionic currents. Here, we review a recently developed approach to image native neuronal Ca^{2+} currents from brain slices. The technique is based on combined fluorescence recordings using low-affinity Ca^{2+} indicators possibly in combination with voltage sensitive dyes. We illustrate how the kinetics of a Ca^{2+} current can be estimated from the Ca^{2+} fluorescence change and locally correlated with the change of membrane potential, calibrated on an absolute scale, from the voltage fluorescence change. We show some representative measurements from the dendrites of CA1 hippocampal pyramidal neurons, from olfactory bulb mitral cells and from cerebellar Purkinje neurons. We discuss the striking difference in data analysis and interpretation between Ca^{2+} current measurements obtained using classical electrode techniques and the physiological currents obtained using this novel approach. Finally, we show how important is the kinetic information on the native Ca^{2+} current to explore the potential molecular targets of the Ca^{2+} flux from each individual Ca^{2+} channel.

Keywords:

Calcium currents

Calcium imaging

Voltage sensitive dyes imaging

CA1 hippocampal pyramidal neuron

Olfactory bulb mitral cell

Purkinje neuron

Brain slices

Action potential

Synaptic potential

Biophysical modeling

1. Introduction

Optical measurements have been historically designed to monitor the electrical activity of the nervous system, a task where the use of electrode techniques has clear limitations (1). In the last two decades, the development of new organic voltage sensitive dyes (VSD), in parallel with the progress of devices to excite and detect fluorescence (2), allowed optical recordings of sub-cellular membrane potential (V_m) changes < 1 mV with a signal-to-noise ratio (S/N) comparable to that of patch clamp recordings (3). This achievement suggested that voltage imaging can be used to investigate voltage-dependent proteins, in particular voltage-gated ion channels, in their physiological environment. The principal function of an ion channel is to allow an ion flux through a membrane, i.e. to produce an ionic current. Thus, the study of the biophysics of ion channels is routinely performed by measurements of ionic currents in single-electrode or two-electrode voltage clamp (4). A way to investigate the biophysics of isolated native ion channels is to perform excised patches from *ex-vivo* membranes (5). Alternatively, ion channels can be expressed in foreign cells such as oocytes or mammalian cell lines (6) and studied by using patch clamp techniques (7). Yet, the physiological role and function of voltage-gated ion channels must be investigated in their natural environment, i.e. in their native cellular compartment and during physiological changes of V_m. To this purpose, the voltage clamp electrode approach has serious limitations for several reasons. First, the ionic current is measured by maintaining the cell at a given artificial V_m and even if the cell is dynamically clamped the V_m change is never a physiological signal (8). Second, the current measured with the electrode is the summation of the filtered currents from all different cellular regions, including remote regions where V_m is unclamped, and no information is available on the site of origin of the current (9). Third, different ionic currents contribute to the physiological change of V_m producing a functional coupling among the different ion channels (10). Thus, a single native ionic current must be pharmacologically isolated from the total current mediated by the other channels, but the block of these channels will make the V_m change non-physiological.

In the last few years, we designed a novel approach to measure physiological Ca^{2+} currents from neurons in brain slices (11). The method is based on fast Ca^{2+} optical measurements using low-affinity indicators that can be combined with sequential (12) or simultaneous (13) V_m optical recordings. The latter measurements can be calibrated in mV (14) using cell-specific protocols. Individual cells are loaded with Ca^{2+} and V_m indicators using a patch clamp recording. In contrast to voltage-clamp current measurements, the current approach permits independent recordings of the V_m change and of the Ca^{2+} influx, i.e. the study of voltage gating during physiological V_m changes. Since the Ca^{2+} current is reconstructed by the measurement of Ca^{2+} locally binding to an indicator, this approach provides information on channels in different areas of the cell with a spatial resolution as good as the optical recording allows. Finally, the Ca^{2+} current is recorded without blocking all Na^+ and K^+ channels that are necessary to produce the physiological V_m change. The principle of obtaining an optical measurement of a fast Ca^{2+} current is based on the analysis of the dye-Ca^{2+} binding reaction in a cell, a scenario initially studied by Kao and Tsien (15). According to their theoretical estimates

and to our recent empirical measurements (16), the relaxation time of the dye-Ca^{2+} binding reaction is less than 200 µs for low-affinity indicators with equilibrium constant (K_D) ≥ 10 µM such as Oregon Green BAPTA-5N (OG5N, K_D = 35 µM, 17) or Fura-FF (K_D = 10 µM, 18). Therefore, a fast Ca^{2+} current with duration of a few milliseconds can be reliably tracked by low-affinity indicators if fluorescence is acquired at sufficiently high speed. The goal of this methodological article is to provide an exhaustive tool for those scientists aiming at performing this type of measurement. The next section addresses in detail the problem of extracting the Ca^{2+} current kinetics from Ca^{2+} fluorescence measurements under different cellular buffering conditions. The following section is devoted to the technical aspects of how to set up combined V_m and Ca^{2+} optical measurements and to calibrate V_m signals on an absolute scale. We then illustrate some examples of combined V_m and Ca^{2+} current measurements and we finally discuss how to correctly interpret the results and how to use this information to significantly advance our knowledge on Ca^{2+} channels function. All data shown here were from experiments performed at the Laboratoire Interdisciplinaire de Physique and approved by the Isere prefecture (Authorisation n. 38 12 01). These experiments were performed at 32-34°C using brain slices from 21-40 postnatal days old C57Bl6 mice of both genders.

2. Extracting Ca^{2+} current kinetics from Ca^{2+} fluorescence measurements

2.1 Biophysical foundations of Ca^{2+} currents imaging

An optical measurement of a Ca^{2+} signal is ultimately a measurement of the Ca^{2+} indicator bound to Ca^{2+} ions, which is proportional to the Ca^{2+} fractional change of fluorescence ($\Delta F/F_0$) if the indicator is not saturated. If the kinetics of the Ca^{2+}-binding reaction of the indicator is slower than the kinetics of the Ca^{2+} source, and imaging is performed at higher rate, the time-course of Ca^{2+} $\Delta F/F_0$ essentially tracks the kinetics of the chemical reaction. Alternatively, if the kinetics of the Ca^{2+}-binding reaction is faster than the kinetics of the Ca^{2+} source, the Ca^{2+} $\Delta F/F_0$ signal tracks the kinetics of the Ca^{2+} source. It follows that the equilibration (or relaxation) time of the Ca^{2+}-indicator binding reaction is a crucial variable to use the technique to investigate the biophysics and the physiology of the Ca^{2+} source. The relaxation of the Ca^{2+}- binding reactions for early indicators was studied by Kao and Tsien (15) who established that the rate of association for all these molecules is limited by diffusion leading to an association constant of ~$6 \cdot 10^8$ $M^{-1}s^{-1}$. Thus, both the equilibrium constant (K_D) and the equilibrium time are determined by the dissociation constant, i.e. the lower is the affinity of the indicator the shorter is its equilibrium time. We have empirically demonstrated that indicators with K_D ≥ 10 µM such as OG5N or FuraFF have relaxation time < 200 µs (16). Since the kinetics of activation and deactivation of voltage-gated Ca^{2+} channels (VGCCs) during physiological changes of V_m (for instance action potentials), is governed by the kinetics of the V_m transient, it follows that the relaxation time for those indicators is shorter than the duration of the Ca^{2+} influx. Hence, since Ca^{2+} binds to the indicator linearly in time, the Ca^{2+} $\Delta F/F_0$ is proportional to the integral of the Ca^{2+} influx, i.e. to the

integral of the Ca^{2+} current. In the cell, however, Ca^{2+} simultaneously binds to proteins that form the endogenous buffer and this binding is competing with the binding to the indicator. An endogenous buffer can be, in principle, at least as fast as the indicator in equilibrating. In this case, only a fraction of Ca^{2+} is bound to the indicator, but this fraction is proportional to the total Ca^{2+} entering the cell and therefore to the integral of the Ca^{2+} current. Alternatively, an endogenous buffer can equilibrate over a time scale that is longer than the duration of the Ca^{2+} current. In this case, Ca^{2+} first binds to the dye and later to the endogenous buffer, implying that part of Ca^{2+} moves from the indicator to the endogenous buffer during its relaxation time. Under this condition, the Ca^{2+} $\Delta F/F_0$ is not linear with the integral of the Ca^{2+} current over this time scale. To clarify this important concept we make use of two simple computer simulations shown in Fig. 1, produced by a model that takes into account the chemical reactions as well as an extrusion mechanism re-establishing the initial Ca^{2+} conditions over a time scale >100 ms. We analyse what hypothetically can happen if a Ca^{2+} current with Gaussian shape occurs in a cell filled with 2 mM OG5N. In the first simulation (Fig. 1a), the cell has only 1 mM of a fast endogenous buffer behaving with the same association constant of the indicator and K_D = 10 µM. In the second simulation (Fig. 1b), the cell has additional 400 µM of a slower endogenous buffer with association rate ~3 times slower than that of the indicator and K_D = 0.2 µM. In the first case, the time derivative of the Ca^{2+} $\Delta F/F_0$ signal matches the kinetics of the Ca^{2+} current (Fig. 1a). In contrast, in the presence of the slower buffer, the time derivative of the Ca^{2+} $\Delta F/F_0$ signal has a negative component and does not match the kinetics of the Ca^{2+} current (Fig. 1b). In the next two paragraphs, we present the analysis strategies that can be applied to extract the kinetics of Ca^{2+} currents from Ca^{2+} imaging recordings.

2.2 The case of linearity between Ca^{2+} influx and Ca^{2+} fluorescence changes

The proteins expressed in a cell determine whether or not the time course of the Ca^{2+} $\Delta F/F_0$ signal is linear with the kinetics of the Ca^{2+} current. As previously demonstrated (11), in the case of linear behaviour, the Ca^{2+} $\Delta F/F_0$ signal must reach its peak and remain constant for a few milliseconds afterwards, i.e. for the entire duration of the current. As shown in the simulation of Fig. 1a, the kinetics of Ca^{2+} extrusion producing a slow decrease of the Ca^{2+} $\Delta F/F_0$ signal has negligible effect on the time derivative. Thus, the estimate of the Ca^{2+} current kinetics is reliably obtained by the calculation of the time derivative of the Ca^{2+} $\Delta F/F_0$ signal. This calculation, however, requires the signal noise to be smaller than the signal change between two consecutive samples. The classical way to achieve this necessary condition is to apply to the Ca^{2+} $\Delta F/F_0$ signal a “smoothing algorithm”, i.e. a temporal filter that reduces the noise of the signal with minimal distortion of its kinetics. At 20 kHz acquisition rate, we have found that the Savitky-Golay algorithm (19) is an optimal filtering tool permitting noise reduction of the signal without significant temporal distortion using time-windows of up to 20-30 samples (11). The applicability of this strategy has however limitations, i.e. if the signal or the region of measurement are too small, or if the light is too dim, the smoothing of the signal might not be sufficient to reduce the noise down to the level permitting calculation of the time derivative. In this

case, the alternative strategy to apply consists in fitting the raw or the filtered Ca^{2+} $\Delta F/F_0$ signal with a model function obtaining a noiseless curve that mimics the time course of the Ca^{2+} $\Delta F/F_0$ signal. A simple choice of function that resembles the time course of the Ca^{2+} $\Delta F/F_0$ transient is the sigmoid. In particular, we found that the product of three sigmoid functions always provides an excellent fit of the Ca^{2+} $\Delta F/F_0$ signal associated with a backpropagating action potential in CA1 hippocampal pyramidal neurons (16). As shown in the example of Fig. 2a both strategies are faithful in correctly calculating the time derivative of the $\Delta F/F_0$ signal. In this example, a CA1 hippocampal pyramidal neuron was filled with 2 mM OG5N and the dendritic Ca^{2+} $\Delta F/F_0$ signal associated with a backpropagating action potential was recorded at 20 kHz and averaged over 16 trials. This high sampling frequency was necessary to avoid signal aliasing and therefore distortion of the kinetics of the current. The filtering strategy is the straightforward approach that enables the calculation of the time derivative, but it produces a curve with noise. The noise can be reduced (if possible) by increasing the number of trials to average or by enlarging the dendritic area from where fluorescence is averaged. The fitting strategy is less direct but it produces a noiseless curve and it is therefore the only possible approach when the noise of the Ca^{2+} $\Delta F/F_0$ signal is above a certain level, as quantitatively estimated in an original report (16). In particular, this is the case when the current must be extracted from single trials or when the recording is obtained from small or relatively dim regions.

2.3 The case of nonlinearity between Ca^{2+} influx and Ca^{2+} fluorescence changes

The method of estimating the kinetics of a Ca^{2+} current by calculating the Ca^{2+} $\Delta F/F_0$ time derivative fails when Ca^{2+} unbinds from the indicator over a time scale that is longer than the current duration, but sufficiently short to distort the estimate of Ca^{2+} influx dynamics by fluorescence measurement. In other words, this method fails when the Ca^{2+} $\Delta F/F_0$ signal decays rapidly, after correction for bleaching, generating a negative component in its time derivative. Such a situation occurs, for example, where slow buffering is produced by Calbindin-D28k (20,21) and Parvalbumin (22,23). As shown in the example of Fig. 2b, the Ca^{2+} $\Delta F/F_0$ signal associated with a climbing fibre excitatory postsynaptic potential (EPSP), recorded at 5 kHz from a dendritic region and averaged over four trials, decays rapidly after its maximum resulting in a negative component of its time derivative. The distortion from the linear behaviour produced by the slow buffers can be compensated by taking into account the kinetics of Ca^{2+} unbinding from the indicator. We have recently developed a successful method to achieve this goal (24). The strategy is based on fitting the decay time of the Ca^{2+} $\Delta F/F_0$ signal with the result of a computer simulation of a model with a slow buffer. Initially the input current is the Gaussian function fitting the rising phase of the time derivative (that is still a good approximation of the initial part of the current). The kinetic parameters and the concentration of the slow buffer are set to obtain the best fit of the decay phase of the Ca^{2+} $\Delta F/F_0$ signal. Then, the kinetics of the Ca^{2+} current is obtained as summation of four Gaussian functions that maximise the match between the result of the computer simulation and the experimental Ca^{2+} $\Delta F/F_0$ signal. Although this new method provides only an indirect approximation of the kinetics of the Ca^{2+} current, this

information is crucial at understanding the activation and deactivation of different types of VGCCs. In the dendrites of PNs, for instance, different Ca^{2+} current kinetics components are associated with the activation of P/Q-type VGCCs (25) and T-type Ca^{2+} channels (26) that can be in principle separated by pharmacological block of one component. Thus, the extrapolation of a curve that approaches the kinetics of the Ca^{2+} current can be used to quantitatively investigate the variability of channels activation at different dendritic sites, the modulation of channel activation due to physiological activity or to pharmacological action. Finally, it is important to say that such a strategy can be extended to estimate slower Ca^{2+} currents where the fitting procedure can be applied to the slower decay time due to Ca^{2+} extrusion (27).

3. Combining membrane potential and Ca^{2+} Imaging

3.1 Setting up combined voltage and Ca^{2+} fluorescence measurements

To combine V_m and Ca^{2+} optical measurements, the VSD and the Ca^{2+} indicator must have minimal overlap in the emission spectra. Water soluble voltage indicators with different excitation and emission spectra have been recently developed (28). In particular, the red-excitable and IR emitting VSD ANBDQPTEA (or PY3283) is suitable for coupling with other optical techniques (29). Nevertheless, the most used VSDs for single cell applications are still JPW3028 (30) and the commercially available JPW1114 (18). These indicators have wide excitation spectrum in the blue/green region and they emit mainly in the red region. We have previously demonstrated that both indicators can be optimally combined with Fura indicators that are excited in the UV region and emit in the short green region (12). In this case, VSDs were excited at 543 nm using a laser and Fura indicators were excited at 385 nm using a light emitting diode (LED) as shown in the scheme of Fig.3a. Alternatively, simultaneous voltage and Ca^{2+} imaging can be achieved using Oregon Green, Calcium Green or Fluo Ca^{2+} indicators using blue light (470 – 490 nm) to excite both VSDs and Ca^{2+} indicators (31). Simultaneous imaging of JPW1114 and Oregon Green BAPTA-5N (OG5N) was adopted to obtain the first combined measurement of V_m and Ca^{2+} currents using the configuration of Fig.3b. This type of measurement, however, has several disadvantages. First, OG5N fluorescence has a small tail component in the red region (31) which can be negligible or not depending on the ratio of the two dyes at each site as well as on the ratio between the two signals. Thus, for example, it works in proximal dendrites of CA1 pyramidal neurons for signals associated with action potentials (11), where V_m fluorescence is stronger than Ca^{2+} fluorescence, but it does not in distal dendrites of cerebellar Purkinje neurons (PNs, data not shown), where V_m fluorescence is weaker than Ca^{2+} fluorescence. A second disadvantage is that the JPW1114 signal at 470 nm excitation is ~4 times smaller than that at 532 nm excitation. If simultaneous recordings are not critical, one can replace them with sequential recordings obtained by alternating 470 nm and 532 nm excitation as used in a recent study (32). Finally, a third disadvantage is that JPW1114 absorbs more in the blue range than

in the green range, i.e. it exhibits toxic effects after fewer exposures. A crucial technical aspect to take into consideration while setting up combined voltage and Ca^{2+} fluorescence measurements is the ability to record the two signals simultaneously at high speed. To this purpose, the company RedShirtImaging (Decantur, GA) has developed a dual-head version of the SMQ NeuroCCD (Fig. 3c). This camera permits simultaneous image acquisitions from both heads at 5-20 kHz, i.e. at the required speed. A demagnifier developed by Cairn Research Ltd (Faversham, UK) allows adjusting the size of the image before it is split in two images at the emission wavelengths of the two dyes. Thus, the alignment of the two heads of the camera allows obtaining, at each precise region of interest, the V_m and the Ca^{2+} signal.

2.2 Calibrating membrane potential fluorescence transients

The calibration of V_m optical signals on an absolute scale (in mV) is crucial to analyse the gating of Ca^{2+} channels at the same locations where Ca^{2+} recordings are performed. This is not, however, straightforward. Indeed, the fractional change of VSD fluorescence is proportional to V_m (33), but the linear coefficient between these two quantities depends on the ratio between the inactive dye and the active dye that varies from site to site. The inactive dye is bound to membranes that do not change potential and contributes only to the resting fluorescence, while the active dye is bound to the plasma membrane and contributes to the resting fluorescence, but also carries the signal. In particular, in experiments utilising intracellular application of the dye, inactive dye is the dye that binds to intracellular membranes and organelles. Since the sensitivity of recording varies from site to site, a calibration can be achieved only if a calibrating electrical signal that has known amplitude at all locations is available. Such a signal is different in different systems. In mitral cells of the olfactory bulb, the amplitude of an action potential is the same in the whole apical dendrite and it can be used to create a sensitivity profile of the measuring system (34). Another type of calibrating electrical signal can be a slow electrical change spreading with minimal attenuation over relatively long distances. Such a signal can be used to reliably calibrate VSD signals in PNs (18). An example of this type of calibration is reported in Fig. 4a. Starting from the resting V_m, that we assume nearly uniform over the entire cell, long current hyperpolarising or depolarising current pulses are injected to the soma *via* the patch pipette and the change in V_m is recorded. As shown by direct dendritic patch recording, the dendrite is hyperpolarised by the same amount of the soma (35). Thus, the measurement of somatic hyperpolarisation can be used as voltage reference to calibrate the dendritic VSD fractional change of fluorescence (VSD $\Delta F/F_0$) optical signal, as shown in Fig. 4a. In contrast, a depolarisation step attenuates along the dendrite. A third type of calibrating signal is a uniform depolarisation over the entire dendritic tree using L-glutamate photolysis from 4-Methoxy-7-nitroindolinyl-caged-L-glutamate (MNI-glutamate) (14). This calibration procedure is applicable to all membrane expressing a relatively large number of glutamate receptors, i.e. to dendrites with high densities of excitatory synapses. The calibration is based on the principle that if the ionotropic glutamate receptor becomes the dominant conductance in a particular neuronal compartment, its reversal potential will determine the membrane

potential of the compartment. Thus, in the area where dominance of glutamate receptor conductance is obtained, the resulting V_m change will be the same and can be used to calibrate VSD signals. An example of this protocol to calibrate backpropagating action potentials in CA1 hippocampal pyramidal neurons is shown in Fig. 4b. The VSD $\Delta F/F_0$ signal associated with the backpropagating AP at different sites of the apical dendrites is variable and cannot be directly correlated with the absolute change of V_m. In the presence of 1 µM TTX, to block action potentials, L-glutamate is photoreleased to saturate glutamate receptors over the whole field of view. Since the recording is performed starting from the resting V_m, the size of the VSD $\Delta F/F_0$ corresponds to this potential in the whole illuminated area where V_m reaches the reversal potential of 0 mV. Thus, this information is used to extrapolate the V_m at each dendritic site.

4. Examples of combined voltage and Ca^{2+} current imaging

4.1 Ca^{2+} currents associated with backpropagating action potentials in CA1 hippocampal pyramidal neurons and in olfactory bulb mitral cells

In many neurons, action potentials generated in the axon hillock adjacent to the soma do not only propagate along the axon to reach neurotransmitter release terminals, but also backpropagate throughout dendrites to signal cell activation at the sites where the neuron receives the synaptic inputs. At least part of this information is given by the fast Ca^{2+} transients produced by activation of VGCCs caused by the dendritic depolarisation associated with the action potential. The analysis that can be performed using the present imaging method is therefore crucial at understanding signal processing in individual neurons, as well as the specific role and function of the diverse VGCCs activated in dendrites. The propagation of the action potential and the consequent activation of VGCCs may be very different in different neuronal systems. In CA1 hippocampal pyramidal neurons, action potentials attenuate along the dendrite and activate both high-voltage activated (HVA) and low-voltage activated (LVA) VGCCs (36, 37). We have very recently demonstrated that HVA-VGCCs and LVA-VGCCs operate synergistically to stabilise Ca^{2+} signals during burst firing (32). Somatic and dendritic action potentials, at nearly physiological temperature, have 1-4 ms duration as in the example shown in Fig. 5a. In agreement with this, the kinetics of the Ca^{2+} current is similar to that of the action potential, with a peak delayed by a few hundred milliseconds from the peak of the action potential. In total contrast to the CA1 hippocampal pyramidal neuron, in olfactory bulb mitral cells the action potential does not attenuate along the dendrites (38). In addition, as shown in the representative example of Fig. 5b, the somatic and dendritic action potential at near physiological temperature (32-34 °C) has duration < 1 ms. Thus, in this system, the activation and deactivation of VGCCs is also faster leading to a Ca^{2+} current with shorter duration and shorter delay from the V_m waveform peak. This preliminary comparison between the two cases indicates that the role of VGCCs, activated by the action potential, is different in different systems. For example, Ca^{2+} currents

with delays of ~100 µs in presynaptic terminal where the function of this signal is to trigger neurotransmitter release (39). Here, the kinetics of the Ca^{2+} current was obtained by calculating the time derivative of the Ca^{2+} $\Delta F/F_0$ signal fit (16). VGCCs contribute to the shape of the action potential directly and indirectly by activating K^+ channels, but also provide a precise time-locked Ca^{2+} transient capable to select fast-activated Ca^{2+} binding proteins. The possibility to locally investigate, using combined V_m and Ca^{2+} current optical measurements, the physiological occurrence of Ca^{2+} signals mediated by VGCCs will contribute enormously, in the near future, to the understanding of complex signal processing in neurons.

4.2 Ca^{2+} currents associated with climbing fibre EPSPs in cerebellar Purkinje neurons

In contrast to pyramidal neurons of the cortex and hippocampus, and to olfactory bulb mitral cells, somatic/axonal action potentials in PNs do not actively propagate in the dendrites (40). The dendrites of PNs, however, express P/Q-type HVA-VGCCs (25) and T-type LVA-VGCCs (26) that are activated by the dendritic depolarisation produced by climbing fibre EPSPs. As shown in the example of Fig. 6, the shape of the dendritic V_m, calibrated in Fig. 4a is quite different in the soma and in the dendrite, mainly reflecting the absence of Na^+ action potentials in the dendrite. In this system, the low-affinity Ca^{2+} indicator used to estimate the Ca^{2+} current was Fura-FF, since the larger Ca^{2+} signal produced by OG5N contaminated the optical V_m measurement. The prominent dendritic depolarisation produces a biphasic Ca^{2+} current, which is in this case obtained by applying our recent generalised method (24). The fast and sharp component is nearly concomitant to the short period in which V_m > -40 mV and it is therefore likely mediated by HVA-VGCCs. The slower and more persistent component is instead mostly concomitant to the whole depolarisation transient and is therefore likely mediated by LVA-VGCCs, as demonstrated by selectively blocking T-type VGCCs (unpublished data not shown). The analysis of Ca^{2+} signalling associated with the climbing fibre EPSP is crucial for the understanding of synaptic plasticity in PNs (41). Yet, while the role of the Ca^{2+} transient associated with the climbing fibre EPSP has been postulated to be auxiliary to the principal Ca^{2+} signal mediated by parallel fibre EPSPs, these first measurements of the Ca^{2+} current kinetics elucidate a quite precise timing of occurrence of the Ca^{2+} source that may eventually provide a less ambiguous explanation of the precise function of this spread dendritic depolarisation. In summary, the examples illustrated in this section show the potentials of this novel optical method in providing physiological information not available by using electrode techniques.

5. Data interpretation and future prospective

The method described here has been developed to overcome the limitations of single-electrode or two-electrode voltage clamp techniques permitting the analysis of physiological Ca^{2+} currents of native Ca^{2+} channels. Indeed, in contrast to patch-clamp recordings, these Ca^{2+} optical currents can

be measured in conditions of a physiological change of V_m and the measured currents are confined to the sites where they are recorded, as shown in apical dendrites of hippocampal pyramidal neurons (32). The additional information on local V_m change, necessary to correlate the behaviour of the conductance with its biophysical properties, is obtained by combining VSD imaging. In cases of linear behaviour between Ca^{2+} influx and Ca^{2+} fluorescence changes the kinetics of the Ca^{2+} current can be extracted by calculating the time derivative of the Ca^{2+} $\Delta F/F_0$ signal using low-affinity Ca^{2+} indicators (11, 16). In the case of nonlinear behaviour between Ca^{2+} influx and Ca^{2+} fluorescence, produced by Ca^{2+}-binding proteins with slower kinetics with respect to the Ca^{2+} current, the kinetics of the Ca^{2+} current can be still correctly estimated by taking into account the faster unbinding of Ca^{2+} from the low-affinity indicator (24). In this last section we address the question of how data, obtained using this technique, should be interpreted. In Ca^{2+} current recordings from channels expressed in heterologous systems using voltage clamp, V_m is controlled artificially and its change is therefore independent of the channel deactivation. Under physiological conditions, Ca^{2+} channels contribute to the V_m change directly, through the ion flux, and indirectly by regulating other conductances. It follows that the channel deactivation changes the V_m waveform. We have shown that in CA1 hippocampal pyramidal neurons this phenomenon produces a modulation of LVA-VGCCs by HVA-VGCCs (32). More in general, a Ca^{2+} current mediated by diverse VGCCs is always the result of a synergy among all different ion channels contributing to the V_m waveform. It follows that in a Ca^{2+} current optical measurement, a single component of the current cannot be extracted simply by blocking the underlying channel, since this block may affect the residual current as well. This evidence has important implications in the study of transgenic animals carrying Ca^{2+} channel mutations. In this case, a certain phenotype is likely to result from the combined modification of function of many different channels, rather than from the specific Ca^{2+} influx component, making the study of these animals as models for disease challenging. In summary, the investigation of the role and function of individual Ca^{2+} channels must be performed in the global context of activation of all channels participating to the local V_m waveform.

Another important aspect of data interpretation is the relation of the kinetics of Ca^{2+} current with the putative molecular targets of Ca^{2+} ions entering the cell. While importance is normally given to possible molecular coupling between the Ca^{2+} channel and the Ca^{2+} binding protein, the kinetics of the Ca^{2+} current can be a potent selector of the molecular pathway which is activated. To illustrate this important concept we make use of computer simulations using the same theoretical framework for simple Ca^{2+}-binding dynamics that we already used in the past (42). We imagine the possible activation of two proteins: a “fast” protein with $K_{ON} = 5.7 \cdot 10^8$ $M^{-1}s^{-1}$ and $K_D = 10$ µM, expressed at the concentration of 500 µM; and a “slow” protein with $K_{ON} = 4 \cdot 10^8$ $M^{-1}s^{-1}$ and $K_D = 0.4$ µM, expressed at the concentration of 100 µM. In the first case, shown in Fig. 7a, the cell is receiving a fast Ca^{2+} current with ~ 2 ms total duration which binds first to the fast protein and later to the slow protein. In the second case, shown in Fig. 7b, the cell is receiving a slower Ca^{2+} current that is smaller in amplitude but that carries approximately the same amount of Ca^{2+}. In this case the slow protein binds to Ca^{2+} with a slower kinetics but the amount of the fast protein binding to Ca^{2+} is less than half with respect

to the first case. These simulations indicate that the ability to activate for a molecular pathway triggered by the fast protein strongly depends on the kinetics of the Ca^{2+} current. Thus, the approach described here should drastically improve our understanding of the physiological function of Ca^{2+} channels by providing the possibility to explore the biophysics of native channels during physiological activity locally within the complex neuronal architecture. The examples of combined V_m and Ca^{2+} current optical measurements from CA1 hippocampal pyramidal neurons, olfactory bulb mitral cells and PNs reported here are representative of the types of exploration that can be performed using this novel approach.

Acknowledment

This work was supported by the *Agence Nationale de la Recherche* through three grants: 1. Grant *WaveFrontImag*, program number ANR-14-CE17-0006-01; 2. Labex *Ion Channels Science and Therapeutics*, program number ANR-11-LABX-0015; 3. National Infrastructure France Life Imaging "Noeud Grenoblois" ; and by the *Federation pour la recherché sur le Cerveau* (FRC) through the grant *Espoir en tête* (in partnership with Rotary France).

References

[1] Braubach O, Cohen LB, Choi Y (2015) Historical Overview and General Methods of Membrane Potential Imaging. Adv Exp Med Biol 859: 3-26

[2] Davies R, Graham J, Canepari M (2013) Light sources and cameras for standard in vitro membrane potential and high-speed ion imaging. J Microsc 251: 5-13

[3] Canepari M, Willadt S, Zecevic D, Vogt KE (2010) Imaging Inhibitory Synaptic Potentials Using Voltage Sensitive Dyes. Biophys J 98: 2032-2040

[4] Sakmann, B, Neher E (1986) Patch clamp techniques for studying ionic channels in excitable membranes. Annu Rev Physiol 46: 455-472

[5] Gray R, Johnston D (1985) Rectification of single GABA-gated chloride channels in adult hippocampal neurons. J Neurophysiol 54: 134-142

[6] Lester HA (1988) Heterologous expression of excitability proteins: route to more specific drugs? Science 241: 1057-1063

|7] Guy HR, Conti F (1990) Pursuing the structure and function of voltage-gated channels. Trends Neurosci 13: 201-206

[8] Antic SD (2016) Simultaneous recordings of voltage and current waveforms from dendrites. J Physiol 594: 2557-2558.

[9] Williams SR, Mitchell SJ (2008) Direct measurement of somatic voltage clamp errors in central neurons. Nat Neurosci 11: 790-798.

[10] Hodgkin AL, Huxley AF (1952) Currents carried by sodium and potassium ions through the membrane of the giant axon of Loligo. J Physiol 116: 449-472.

[11] Jaafari N, De Waard M, Canepari M (2014) Imaging Fast Calcium Currents beyond the Limitations of Electrode Techniques. Biophys J 107: 1280-1288

[12] Canepari M, Vogt K, Zecevic D (2008) Combining voltage and calcium imaging from neuronal dendrites. Cell Mol Neurobiol 58: 1079-1093

[13] Vogt KE, Gerharz S, Graham J, Canepari M (2011a) High-resolution simultaneous voltage and Ca^{2+} imaging. J Physiol 589: 489-494

[14] Vogt KE, Gerharz S, Graham J, Canepari M (2011b) Combining membrane potential imaging with L-glutamate or GABA photorelease. PLoS ONE 6: e24911

[15] Kao JP, Tsien RY (1988) Ca2+ binding kinetics of fura-2 and azo-1 from temperature-jump relaxation measurements. Biophys J 53: 635-639

[16] Jaafari N, Marret E, Canepari M (2015) Using simultaneous voltage and calcium imaging to study fast Ca2+ channels. Neurophotonics 2: 021010

[17] Canepari M, Odgen D (2006) Kinetic, pharmacological and activity-dependent separation of two Ca^{2+} signalling pathways mediated by type 1 metabotropic glutamate receptors in rat Purkinje neurons. J Physiol 573: 65-82

[18] Canepari M, Vogt, KE (2008) Dendritic Spike Saturation of Endogenous Calcium Buffer and Induction of Postsynaptic Cerebellar LTP. PLoS ONE 3: e4011

[19] Savitzky A, Golay MJE (1964) Smoothing and Differentiation of Data by Simplified Least Squares Procedures. Anal Chem 36: 1627-1639

[20] Nägerl UV, Novo D, Mody I, Vergara JL (2000) Binding kinetics of calbindin-D(28k) determined by flash photolysis of caged Ca(2+). Biophys J 79: 3009-3018

[21] Airaksinen MS, Eilers J, Garaschuk O, Thoenen H, Konnerth A, Meyer M (1997) Ataxia and altered dendritic calcium signalling in mice carrying a targeted nullmutation of the calbindin D28k gene. Proc Natl Acad Sci USA 94: 1488-1493

[22] Lee SH, Schwaller B, Neher E (2000) Kinetics of Ca2+ binding to parvalbumin in bovine chromaffin cells: implications for [Ca2+] transients of neuronal dendrites. J Physiol 525: 419-432

[23] Schmidt H, Stiefel KM, Racay P, Schwaller B, Eilers J (2003) Mutational analysis of dendritic Ca2+ kinetics in rodent Purkinje cells: role of parvalbumin and calbindin D28k. J Physiol 551: 13-32

[24] Ait Ouares K, Jaafari N, Canepari M (2016) A generalised method to estimate the kinetics of fast Ca^{2+} currents from Ca^{2+} imaging experiments. J Neurosci Methods 268: 66-77

[25] Usowicz MM, Sugimori M, Cherksey B, Llinás R (1992) P-type calcium channels in the somata and dendrites of adult cerebellar Purkinje cells. Neuron 9: 1185-1199

[26] Isope P, Hildebrand ME, Snutch TP (2012) Contributions of T-type voltage-gated calcium channels to postsynaptic calcium signaling within Purkinje neurons. Cerebellum 11: 651-665

[27] Miyakawa H, Lev-Ram V, Lasser-Ross N, Ross WN (1992) Calcium transients evoked by climbing fiber and parallel fiber synaptic inputs in guinea pig cerebellar Purkinje neurons. J Neurophysiol 68: 1178-1189

[28] Yan P, Acker CD, Zhou WL, Lee P, Bollensdorff C, Negrean A, Lotti J, Sacconi L, Antic SD, Kohl P, Mansvelder HD, Pavone FS, Loew LM (2012) Palette of fluorinated voltage-sensitive hemicyanine dyes. Proc Natl Acad Sci USA 109: 20443-20448

[29] Willadt S, Canepari M, Yan P, Loew LM, Vogt KE (2014) Combined optogenetics and voltage sensitive dye imaging at single cell resolution. Front Cell Neurosci 8: 311

[30] Antic SD (2003) Action potentials in basal and oblique dendrites of rat neocortical pyramidal neurons. J Physiol 550: 35-50

[31] Bullen A, Saggau P (1998) Indicators and optical configuration for simultaneous high-resolution recording of membrane potential and intracellular calcium using laser scanning microscopy. Pflügers Arch 436: 788–796

[32] Jaafari N, Canepari M (2016) Functional coupling of diverse voltage-gated Ca(2+) channels underlies high fidelity of fast dendritic Ca(2+) signals during burst firing. J Physiol 594: 967-983

[33] Loew LM, Simpson LL (1981) Charge-shift probes of membrane potential: a probable electrochromic mechanism for p-aminostyrylpyridinium probes on a hemispherical lipid bilayer. Biophys J 34: 353-365

[34] Djurisic M, Antic S, Chen WR, Zecevic D (2004) Voltage imaging from dendrites of mitral cells: EPSP attenuation and spike trigger zones. J Neurosci 24: 6703-6714

[35] Roth A, Häusser M (2001) Compartmental models of rat cerebellar Purkinje cells based on simultaneous somatic and dendritic patch-clamp recordings. J Physiol 535: 445-472

[36] Spruston N, Schiller Y, Stuart G, Sakmann B (1995) Activity-dependent action potential invasion and calcium influx into hippocampal CA1 dendrites. Science 268: 297-300

[37] Canepari M, Djurisic M, Zecevic D (2007) Dendritic signals from rat hippocampal CA1 pyramidal neurons during coincident pre- and post-synaptic activity: a combined voltage- and calcium-imaging study. J Physiol 580: 463-484

[38] Bischofberger J, Jonas P (1997) Action potential propagation into the presynaptic dendrites of rat mitral cells. J Physiol 504: 359-365

[39] Sabatini BL, Regerh WG (1996) Timing of neurotransmission at fast synapses in the mammalian brain. Nature 384: 170-172.

[40] Stuart G, Häusser M (1994) Initiation and spread of sodium action potentials in cerebellar Purkinje cells. Neuron 13: 703-712

[41] Vogt KE, Canepari M (2010) On the induction of postsynaptic granule cell-Purkinje neuron LTP and LTD. Cerebellum 9: 284-290

[42] Canepari M, Mammano F (1999) Imaging neuronal calcium fluorescence at high spatio-temporal resolution. J. Neurosci. Methods 1999; 87:1 -11

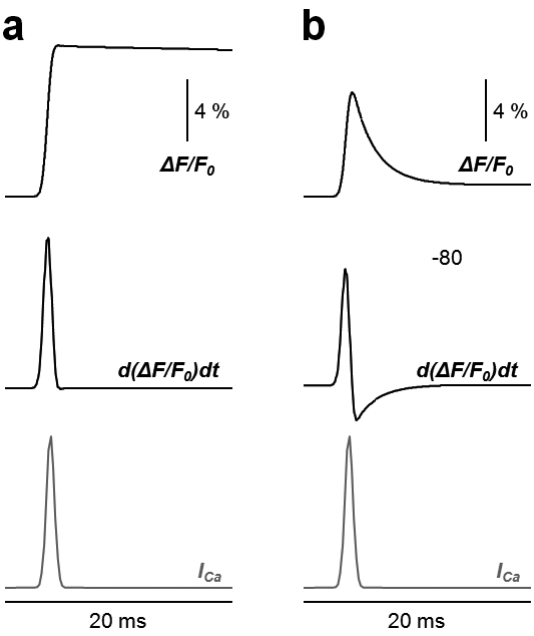

Fig. 1. Simulation of hypothetical Ca^{2+} $\Delta F/F_0$ signals from 2 mM OG5N in the presence of endogenous Ca^{2+} buffers. (**a**) Simulation of $\Delta F/F_0$ signal (top trace) following a Ca^{2+} current with simple Gaussian kinetics (I_{Ca}, gray trace on the bottom) in the presence of 1 mM of a fast endogenous Ca^{2+} buffer with same association constant of the Ca^{2+} indicator ($5.7 \cdot 10^8$ $M^{-1}s^{-1}$) and K_D = 10 µM. The kinetics of the $\Delta F/F_0$ time derivative (middle trace) matches the kinetics of the Ca^{2+} current. (**b**) Same as in the previous panel but in this case in the presence of additional 400 µM of a slower buffer with association constant equal to $2 \cdot 10^8$ $M^{-1}s^{-1}$ and K_D = 0.2 µM. The kinetics of the $\Delta F/F_0$ time derivative (middle trace) does not matches the kinetics of the Ca^{2+} current.

537

538

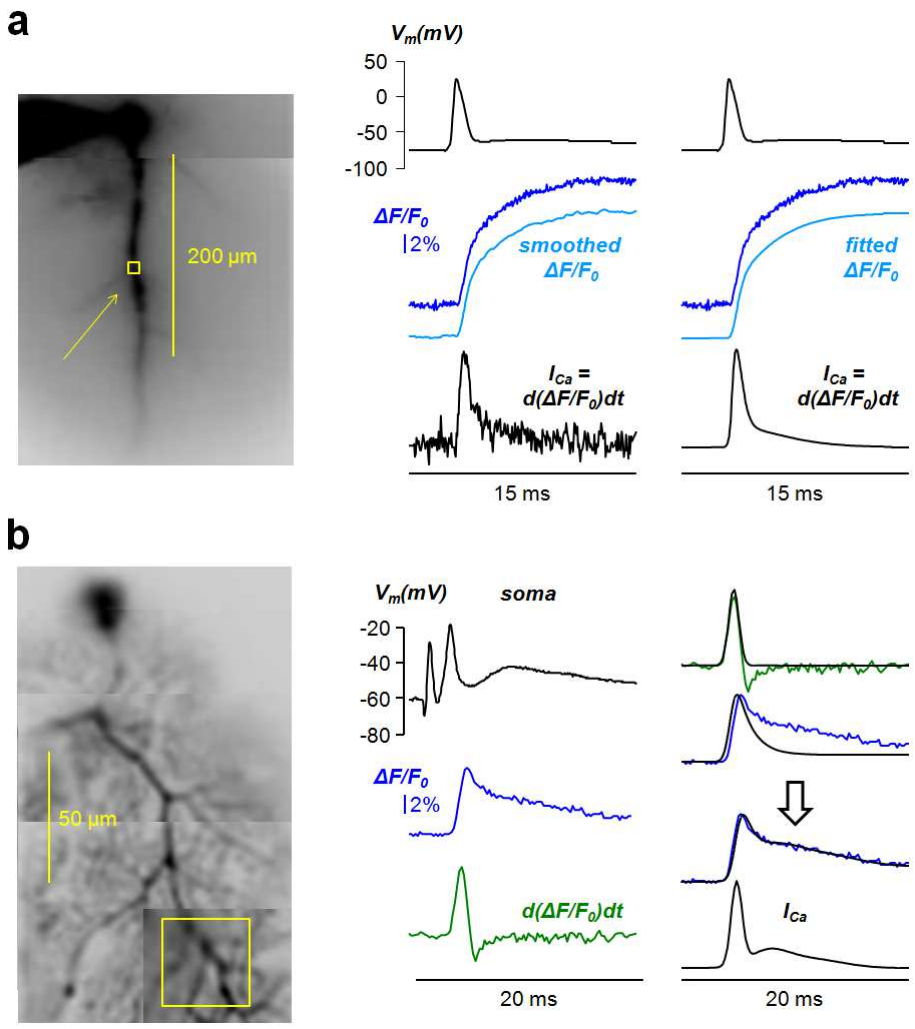

Fig. 2. Different strategies to estimate the kinetics of a Ca^{2+} current (**a**) On the left, fluorescence image of CA1 hippocampal pyramidal neuron filled with 2 mM OG5N with a small region of the apical dendrite outlined and indicated by the arrow. On the right, somatic V_m change associated with an action potential (top black traces) and Ca^{2+} $\Delta F/F_0$ signal in the indicated region (blue trace). The $\Delta F/F_0$ signal is either smoothed with a Savitky-Golay algorithm (left) or fitted with a 3-sigmoid function (right). The Ca^{2+} current kinetics (I_{Ca}) is then estimated by calculating the time derivative of the processed $\Delta F/F_0$ signal. The kinetics of the current is the same using the two strategies, but the curve obtained with the strategy of data fitting is noiseless. Data, recorded at 20 kHz, were from averages of 16 trials. (**b**) On the left, fluorescence image of PN filled with 2 mM OG5N with square region of interest outlined. On the right, somatic V_m change associated with a climbing fibre EPSP (top-left black trace) and Ca^{2+} $\Delta F/F_0$ signal in the indicated region (blue traces). The time derivative of the Ca^{2+} $\Delta F/F_0$ signal (green traces) does not match the kinetics of the current. To estimate the kinetics of the current we use a strategy that consists in matching the result of a computer simulation to the Ca^{2+} $\Delta F/F_0$ signal using an optimised two-buffer model (24). We start from the Gaussian function fitting the rising phase of the $\Delta F/F_0$ time derivative (top-right black trace). We then correct the current with three additional Gaussian components until a match of the computer simulation with the Ca^{2+} $\Delta F/F_0$ signal is obtained (process indicated by the arrow. The curve producing this match (I_{Ca}, bottom-right black

trace) is the estimate of the Ca^{2+} current kinetics. Data, recorded at 5 kHz, were from averages of 4 trials.

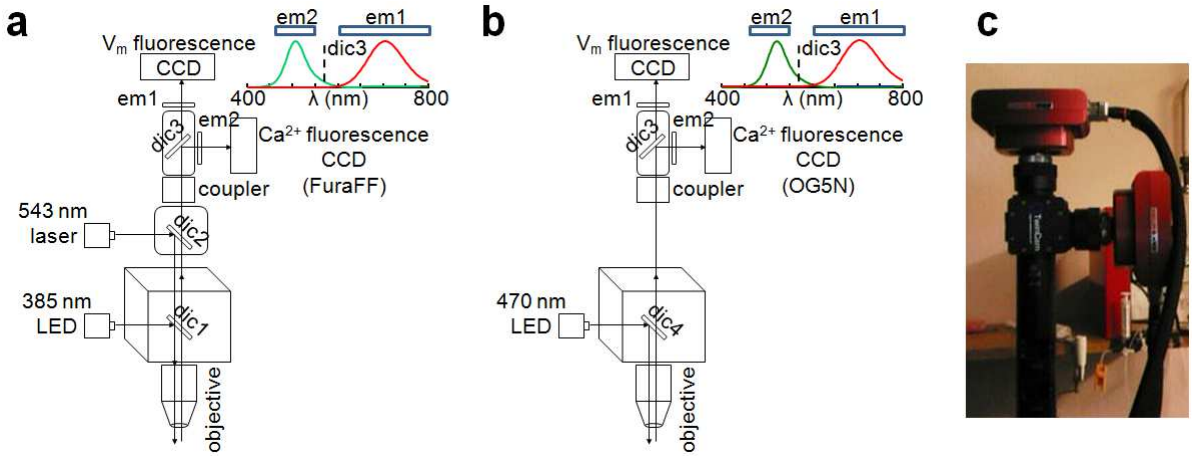

Fig. 3. Configurations and camera for combined voltage and Ca^{2+} fluorescence measurements. (**a**) Schematic drawing of the apparatus for simultaneous voltage and Ca^{2+} imaging using the VSD JPW1114 and the Ca^{2+} indicator FuraFF (13); 385 nm LED light via the epifluorescence port of a commercial microscope is reflected by a 506 nm long-pass dichroic mirror (dic1); 543 nm laser light via the top of the microscope is reflected by a dual-band dichroic mirror transmitting wavelengths between 493 nm and 530 nm and wavelengths longer than 574 nm (dic2); the fluorescence images of the two dyes are demagnified and separated by a 565 nm long-pass dichroic mirror (dic3); The V_m image and the Ca^{2+} images are filtered by a 610 nm long-pass (em1) and by a 510±42 nm band-pass filter (em2) respectively, then acquired by two CCD cameras; the emission spectra of FuraFF (green) and JPW1114 (red) are shown on the top-right. (**b**) Schematic drawing of the apparatus for simultaneous voltage and Ca^{2+} imaging using the VSD JPW1114 and the Ca^{2+} indicator OG5N (11); 470 nm LED light via the epifluorescence port of a commercial microscope is reflected by a 495 nm long-pass dichroic mirror (dic4); the fluorescence images of the two dyes are demagnified and and processed as in the previous configuration; the emission spectra of OG5N (green) and JPW1114 (red) are shown on the top-right. (**c**) The dual NeuroCCD camera designed by RedshirtImaging for this type of measurement.

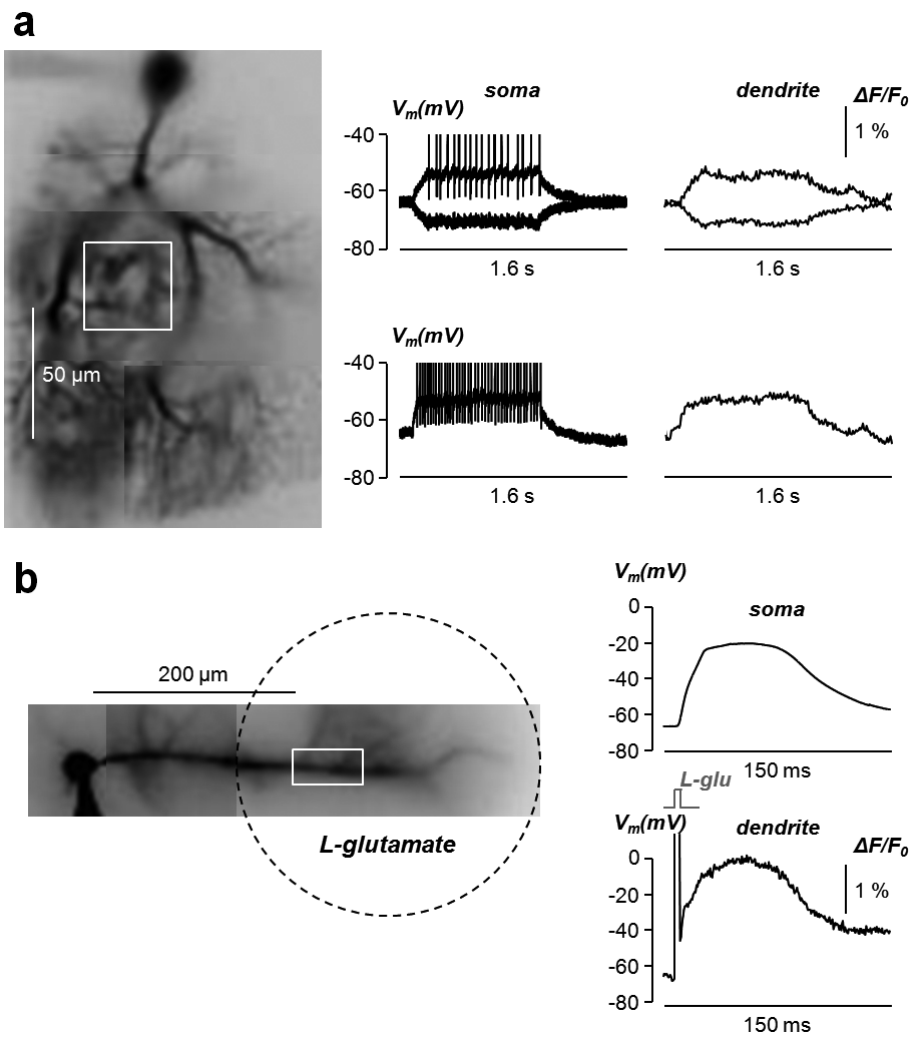

Fig. 4. Calibration methods for dendritic V_m optical signals. (**a**) On the left, fluorescence image of PN with square region of interest outlined. On the right, somatic V_m change associated with long hyperpolarising or depolarising steps and associated dendritic VSD $\Delta F/F_0$ signals in the region of interest; the hyperpolarising step spreads to the dendrites with negligible attenuation (35) and is used to calibrate the VSD $\Delta F/F_0$ signals; the weak depolarising step on the top also spreads with minimal attenuation, but the associated somatic action potentials do not propagate into the dendrites; in contrast, the strong depolarising step on the bottom attenuates. (**b**) On the left, fluorescence image of CA1 hippocampal pyramidal neuron with rectangular region, 200-250 µm from the soma, outlined. On the right, somatic V_m change associated with L-glutamate photorelease from MNI-glutamate (14) in the area limited by the dotted line and in the presence of 1 µM tetrodotoxin blocking action potentials; the dendritic VSD $\Delta F/F_0$ signal is reported on the bottom; the saturating L-glutamate concentration depolarises the illuminated area from the resting V_m (~-70 mV) to the reversal potential of AMPA receptors (0 mV). All calibrations were from single trials.

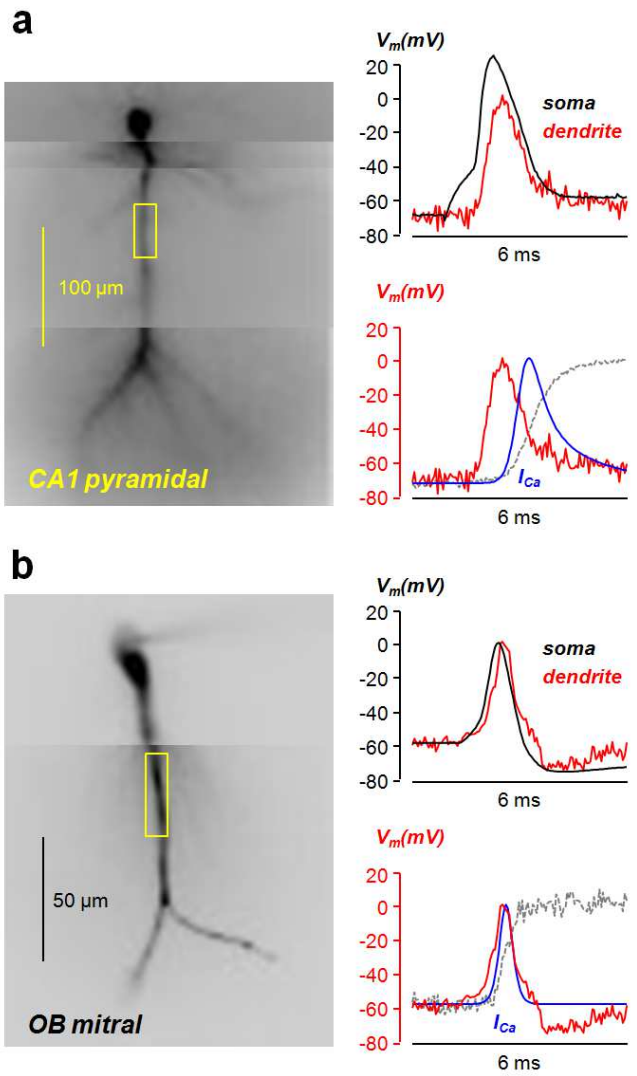

Fig. 5. Ca^{2+} currents associated with backpropagating action potentials in CA1 hippocampal pyramidal neurons and in olfactory bulb (OB) mitral cells (**a**) On the left, fluorescence image of CA1 hippocampal pyramidal neuron filled with JPW1114 and 2 mM OG5N with a region of the apical dendrite outlined. On the right, somatic V_m change associated with an action potential (black trace) in the soma and in the dendritic region. The associated Ca^{2+} current kinetics, obtained with the fitting strategy from the raw Ca^{2+} signal (dashed gray trace), is shown in the bottom. (**b**) On the left, fluorescence image of OB cell filled with JPW1114 and 2 mM OG5N with a region of the principal dendrite outlined. On the right, somatic V_m change associated with an action potential in the soma (black trace) and in the dendritic region (red trace). The associated Ca^{2+} current kinetics, obtained with the fitting strategy from the raw Ca^{2+} signal (dashed gray trace), is shown in the bottom (blue trace) superimposed to the dendritic action potential (red trace). Data, recorded at 20 kHz, were from averages of 4 trials. All experiments were performed at 32-34 °C.

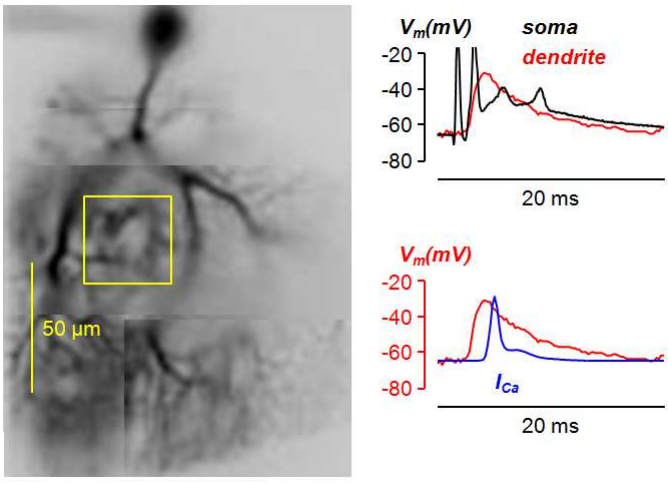

Fig. 6. Ca^{2+} currents associated with climbing fibre EPSPs in cerebellar Purkinje neurons. On the left, fluorescence image of PN filled with JPW1114 and 2 mM Fura-FF with a region of the dendrite outlined. On the right, somatic V_m change associated with climbing fibre EPSP (black trace) in the soma and in the dendritic region. The associated Ca^{2+} current kinetics, obtained with the generalised method (24), is shown in the bottom. Data, recorded at 5 kHz, were from averages of 4

trials. Experiments were performed at 32-34 °C.

601

602

603

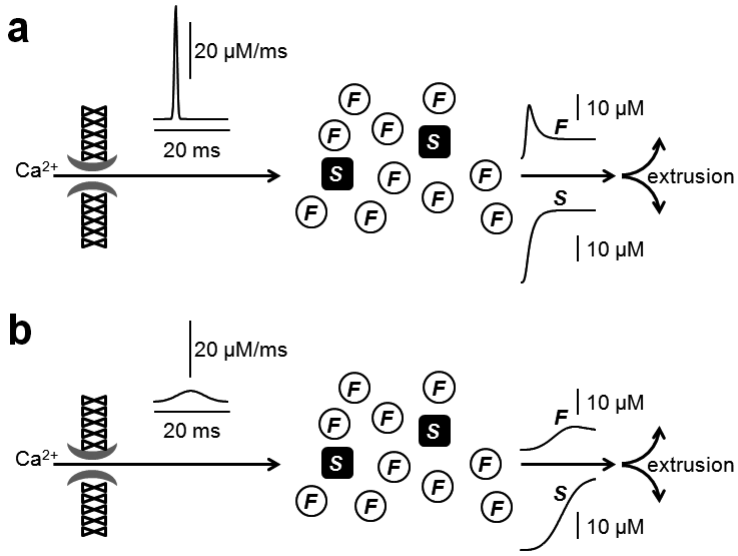

Fig. 7. Simulated activation of two different Ca^{2+}-binding proteins by Ca^{2+} currents. (**a**) In a cell containing 500 µM of a fast (*F*) buffer with $K_{ON} = 5.7 \cdot 10^8$ $M^{-1}s^{-1}$ and K_D = 10 µM, and 100 µM of a slow (*S*) buffer with $K_{ON} = 4 \cdot 10^8$ $M^{-1}s^{-1}$ and K_D = 0.4 µM, the curves on the right report the binding to Ca^{2+} of the *F* and *S* proteins following the fast Ca^{2+} current reported on the left. (**b**) Same as in the previous panel but following the fast Ca^{2+} current reported on the left.

604

605